Title

Analysis of Curved Nonprismatic Reinforced and Prestressed Concrete Box Girder Bridges

Author

Choudhury, Deepak

Publication Date

1986-12-01

REPORT NO.
UCB/SEMM-86/13

STRUCTURAL ENGINEERING
MECHANICS AND MATERIALS

ANALYSIS OF CURVED NONPRISMATIC REINFORCED AND PRESTRESSED CONCRETE BOX GIRDER BRIDGES

BY

DEEPAK CHOUDHURY

Prepared under the sponsorship of
U.S. - Spain Joint Committee for
Scientific and Technological Cooperation
Project No. CCA8309-012

DECEMBER 1986

DEPARTMENT OF CIVIL ENGINEERING
UNIVERSITY OF CALIFORNIA
BERKELEY, CALIFORNIA

TECHNICAL REPORT STANDARD TITLE PAGE

1. Report No.	2. Government Accession No.	3. Recipient's Catalog No.

4. Title and Subtitle
ANALYSIS OF CURVED NONPRISMATIC REINFORCED AND PRESTRESSED CONCRETE BOX GIRDER BRIDGES

5. Report Date
December 1986

6. Performing Organization Code

7. Author(s)
Deepak Choudhury

8. Performing Organization Report No.
UCB/SEMM-86/13

9. Performing Organization Name and Address
Department of Civil Engineering
University of California
Berkeley, California 94720

10. Work Unit No.

11. Contract or Grant No.
CCA8309-012

12. Sponsoring Agency Name and Address
U.S.-Spain Joint Committee for
Scientific and Technological Cooperation
Paseo del Prado, 28-5 planta
28014 Madrid, Spain

13. Type of Report and Period Covered
Final Report

14. Sponsoring Agency Code

15. Supplementary Notes

16. Abstract

A numerical procedure for the analysis of curved nonprismatic reinforced and prestressed concrete box girder bridges is presented. Both linear elastic analysis and nonlinear material analysis up to ultimate are considered.

Thin-walled beam theory and the finite element method are combined to develop a curved nonprismatic thin-walled box beam element. The cross section of the element is a rectangular single-cell box with side cantilevers. The axis of the element is curved in plan. The cross sectional dimensions vary along the element axis. Eight displacement degrees of freedom, including transverse distortion and longitudinal warping of the cross section, are considered at each of the three element nodes. Small displacements and small strains are assumed in the element formulation.

Prestressing, consisting of post-tensioned bonded tendons in the longitudinal direction, is considered. The tendons are idealized as straight prestressing steel segments between the nodes of the box beam elements. Friction and anchorage slip losses are considered.

For nonlinear material analysis, the uniaxial stress-strain curves of concrete, reinforcing steel and prestressing steel are modelled. The shear and the transverse flexural responses of the box beam cross section are modelled using trilinear constitutive relationships based on cracking, yielding and ultimate stages. Effect of load reversal is considered. A composite system of concrete and longitudinal reinforcing steel filaments is constructed in order to account for varied material properties within the element cross section. Tension stiffening effect between concrete and longitudinal steel is considered.

The nonlinear equilibrium equations are solved using an incremental method combined with unbalanced load iterations. Load control and displacement control solution strategies are included in the numerical procedure. A path-independent state determination scheme is used. The nonlinear analysis procedure is capable of tracing the structural response throughout the elastic, inelastic and ultimate load ranges.

The theory is incorporated into two computer programs, LAPBOX and NAPBOX. Various numerical examples of linear elastic analysis and nonlinear material analysis are presented demonstrating the applicability and the capabilities of the proposed method. Comparisons with other analytical and experimental results are made.

17. Key Words
Structural Engineering,
Prestressed concrete, box girder bridge,
Curved bridge, nonprismatic bridge,
Thin-walled beam, finite element,
Nonlinear analysis, computer program.

18. Distribution Statement
Unlimited

19. Security Classif. (of this report)	20. Security Classif. (of this page)	21. No. of Pages	22. Price
Unclassified	Unclassified	232	

Form DOT F 1700.7 (8-69)

Department of Civil Engineering
Structural Engineering Mechanics and Materials

Report No. UCB/SEMM-86/13

ANALYSIS OF CURVED NONPRISMATIC REINFORCED AND PRESTRESSED CONCRETE BOX GIRDER BRIDGES

by

Deepak Choudhury

Faculty Investigator: A.C. Scordelis

Prepared under the sponsorship of
U.S.-Spain Joint Committee for
Scientific and Technological Cooperation
Project No. CCA8309-012

College of Engineering
Office of Research Services
University of California
Berkeley, California

December 1986

ANALYSIS OF CURVED NONPRISMATIC REINFORCED AND PRESTRESSED CONCRETE BOX GIRDER BRIDGES

Deepak Choudhury

Doctor of Philosophy Civil Engineering

ABSTRACT

A numerical procedure for the analysis of curved nonprismatic reinforced and prestressed concrete box girder bridges is presented. Both linear elastic analysis and nonlinear material analysis up to ultimate are considered.

Thin-walled beam theory and the finite element method are combined to develop a curved nonprismatic thin-walled box beam element. The cross section of the element is a rectangular single-cell box with side cantilevers. The axis of the element is curved in plan. The cross sectional dimensions vary along the element axis. Eight displacement degrees of freedom, including transverse distortion and longitudinal warping of the cross section, are considered at each of the three element nodes. Small displacements and small strains are assumed in the element formulation.

Prestressing, consisting of post-tensioned bonded tendons in the longitudinal direction, is considered. The tendons are idealized as straight prestressing steel segments between the nodes of the box beam elements. Friction and anchorage slip losses are considered.

For nonlinear material analysis, the uniaxial stress-strain curves of concrete, reinforcing steel and prestressing steel are modelled. The shear and the transverse flexural responses of the box beam cross section are modelled using trilinear constitutive relationships based on cracking, yielding and ultimate stages. Effect of load reversal is considered. A composite system of concrete and longitudinal reinforcing steel filaments is constructed in order to account for varied material properties within the element cross section. Tension stiffening effect between concrete and longitudinal steel is considered.

The nonlinear equilibrium equations are solved using an incremental method combined with unbalanced load iterations. Load control and displacement control solution strategies are included in the numerical procedure. A path-independent state determination scheme is used. The nonlinear analysis procedure is capable of tracing the structural response throughout the elastic, inelastic and ultimate load ranges.

The theory is incorporated into two computer programs, LAPBOX and NAPBOX. Various numerical examples of linear elastic analysis and nonlinear material analysis are presented demonstrating the applicability and the capabilities of the proposed method. Comparisons with other analytical and experimental results are made.

A. C. Scordelis
Chairman of Committee

ACKNOWLEDGEMENTS

The author wishes to express his sincere gratitude to Prof. A. C. Scordelis for his invaluable guidance and constant encouragement throughout the course of this work. He would also like to thank Prof. G. H. Powell and Prof. B. N. Parlett for serving on the Dissertation Committee.

This research was sponsored by the U.S.-Spain Joint Committee for Scientific and Technological Cooperation. The computer center at the University of California, Berkeley, provided the facilities for the numerical work.

Finally, the patience, understanding and encouragement of the author's wife have played a major role in the completion of this work.

TABLE OF CONTENTS

1. INTRODUCTION

1.1 General

Reinforced and prestressed concrete box girder bridges have gained importance as economic and esthetic solutions for the overcrossings, undercrossings, separation structures and viaducts found in today's highway system. These bridges can be simple span or continuous structures (Fig. 1.1a). Transverse diaphragms are placed at the end and interior support sections, and sometimes additional diaphragms are used between the supports. Design and esthetic considerations often call for longitudinal variations in the bridge depth. In plan, the bridge can have a straight or curved geometry (Fig. 1.1b). Sometimes part of the bridge may be straight, and part of it may be curved. The width of the bridge can also vary longitudinally. The typical cross section of such a box girder bridge consists of a top slab and a bottom slab connected monolithically by vertical webs to form a cellular or box-like structure. In some cases, sloping or curved exterior webs are also used. Either single-cell or multi-cell cross sections may be used, depending on the span, the width or the construction method. This study is, however, limited to single-cell cross sections with vertical webs (Fig. 1.1c). The thickness of the slabs and/or the webs are often varied along the bridge axis in order to obtain an efficient design.

Prestressing, consisting primarily of post-tensioned tendons in the longitudinal direction, is used in concrete box girder bridges in order to increase maximum span, control behavior and limit weight. Transverse post-tensioning is sometimes used in order to provide the load carrying capabilities of the deck economically, and also to obtain a more durable deck.

The complex spatial nature of a curved box girder bridge with a variable cross section (nonprismatic) makes it difficult to accurately predict the structural response to a general loading case. The presence of prestressing further complicates the analysis. Even with the assumption of homogeneous linear elastic material, the accurate analysis of such a structure remains a formidable challenge to the engineer.

Highway bridges are being subjected to increasing vehicular loads and traffic densities. A better understanding of the overload behavior of these bridges beyond the working stress range is thus necessary. Also, in order to assess the degree of safety against failure, an accurate estimate of the ultimate load has to be made. However, when reinforced and prestressed concrete bridge structures are loaded beyond the working stress range, analytical models based on the assumption of homogeneous linear elastic material cannot be justified. The effects of nonhomogeneity of the material, concrete cracking and nonlinearities in the stress-strain relationships of concrete, reinforcing steel and prestressing steel need to be considered. And this requires a nonlinear analysis procedure.

1.2 Review of Analytical Methods

A number of different methods are available for the analysis of box girder bridges. The choice of a particular method is usually dictated by the geometric complexity of the bridge and the design quantities that are desired. A review of the different analytical methods for concrete box girder bridges has been presented by Scordelis [1] with reference to a large number of computer programs developed at the University of California, Berkeley. Other reviews can be found in [2, 3]. Kristek [2] has discussed the theoretical bases of some of the methods. Maisel and Roll [3] have presented a comparative study of the various methods available for the analysis of straight prismatic single-cell box girders. In order to form the basis for the selection of the analytical method to be used in the present study, a brief review of the different methods is given below.

1.2.1 Folded Plate Elasticity Method

A multi-cell prismatic box girder bridge can be modelled as a folded plate system made up of longitudinal plate elements interconnected at joints along their longitudinal edges, and simply supported at both ends by diaphragms which are only rigid in their own planes. Any joint loading with arbitrary longitudinal distribution can be resolved into its Fourier series components, and a direct stiffness analysis can be performed for each harmonic component of

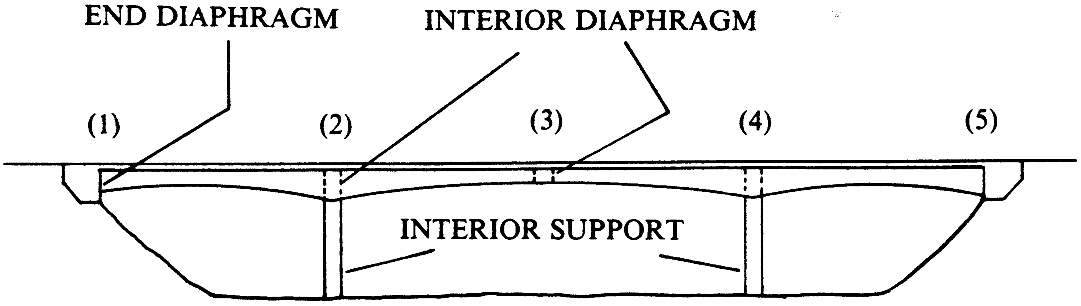

(a) ELEVATION

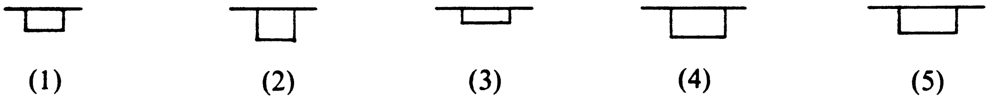

(b) CROSS SECTIONS

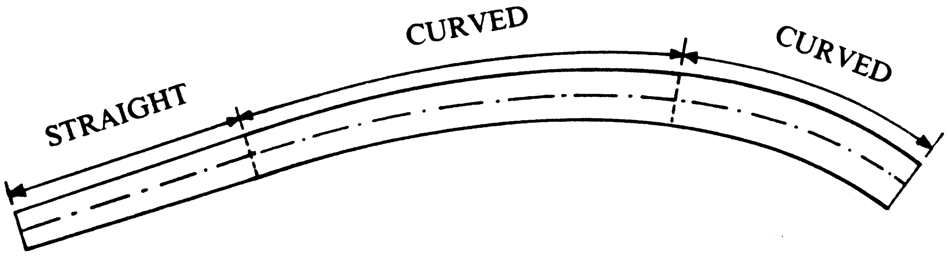

(c) PLAN

FIG. 1.1 CURVED NONPRISMATIC BOX GIRDER BRIDGE

the loading. The final results can then be obtained by superposing the results for all harmonics used to represent the loading.

The analysis for each harmonic load is simplified by the fact that for a straight or a circularly curved bridge, the response quantities (displacements and internal forces) also have harmonic variations in the longitudinal direction. Since each harmonic is completely defined by its amplitude, analysis of the three-dimensional bridge structure is reduced to a two-dimensional problem in the transverse direction. Application of the direct stiffness approach to such a system results in a banded well-conditioned stiffness matrix. Furthermore, due to the repetitive nature of the solution technique for multiple harmonics, this method takes full advantage of the capabilities of a digital computer.

In its basic form, this method is limited to simply supported box girders without interior diaphragms. Formulas based on the theory of elasticity are used to define the membrane and plate bending actions of the folded plate system. Within the scope of assumptions of the theory of elasticity, results obtained with the folded plate elasticity method represent the exact solution for linear elastic analysis of a box girder bridge, and hence they are often used to assess the accuracy of other methods. The method was first used at the University of California, Berkeley, to develop the computer program MULTPL (1965) [1, 4, 5] for straight single span bridges, simply supported at the two ends. Since then the method has been extended to continuous span bridges with interior diaphragms by combining the direct stiffness harmonic analysis with a force method of analysis. The computer programs MUPDI [1, 4, 6], MUPDI3 [1, 7] and MUPDI4 [8], developed at the University of California, Berkeley, are part of the continuing effort on the extension of the folded plate elasticity method.

The shortcomings of the folded plate elasticity method are its limitation to prismatic structures with either straight or circularly curved plan geometries, and the large computational effort required when concentrated loads dictate the use of a large number of harmonics in the Fourier series representation. Furthermore, this method cannot be extended to nonlinear analysis since the principle of superposition is used to obtain the final results from the harmonic components.

1.2.2 Finite Strip Method

The finite strip method is basically a transition between the folded plate elasticity method and the finite element method. The straight or circularly curved bridge is discretized only in the transverse direction into longitudinal finite strips. A direct stiffness harmonic analysis is performed as in the folded plate elasticity method. However, the properties of the finite strips corresponding to each harmonic are evaluated based on assumed displacement distributions across the strip width, rather than on the theory of elasticity. Thus the solution converges to the exact theory of elasticity solution only with mesh refinement.

The finite strip method is particularly suited to the analysis of orthotropic and circularly curved plate elements for which direct application of the theory of elasticity becomes too involved. The method was introduced in 1968 by Cheung [9]. It has been used to develop the computer programs MULSTR [10, 11], CURSTR [12, 13], CURDI [1, 14], CURDIP [1, 15] and CURDI4 [8] at the University of California, Berkeley.

Though the finite strip method has broader applicability as compared to the folded plate elasticity method, it is still limited to prismatic structures with either straight or circularly curved plan geometries. And the principle of superposition inherent in the direct stiffness harmonic analysis precludes the extension of this method to nonlinear analysis.

1.2.3 Grillage Analogy

Two- and three-dimensional grillage analogies, consisting primarily of flexural members, have been used in the past to approximate the behavior of cellular structures. Hambly has summarized various grillage models in [16].

A three-dimensional grillage, consisting of longitudinal beam elements, transverse diaphragm elements, transverse bending frames, and specially developed torsional shear panels, was used by Seible [17, 18, 19] for nonlinear analysis of multi-cell reinforced concrete box girders of arbitrary plan geometry and constant depth. Nonlinearities considered were material nonlinearities inherent in reinforced concrete members under short term loading, such as cracking of concrete, yielding of reinforcement, and formation of plastic hinges due to flexure and shear. Simple trilinear models, based on numerous experimental investigations, were used to approximate the member end force-deformation relationships for the various elements of the grillage. Prestressing was not considered.

1.2.4 Finite Element Method

The finite element method is the most powerful and versatile numerical tool of all the available methods. A box girder bridge of arbitrary plan geometry and variable cross section can be modelled as an assembly of finite elements interconnected at nodal points. These finite elements may be one-dimensional beam-type elements, two-dimensional plate or shell elements, or even three-dimensional solids. For each finite element, a stiffness matrix, which approximates the behavior in the continuum, is developed based on assumed displacement or stress patterns. A direct stiffness approach is then used to obtain the nodal displacements and thence the internal stresses in the finite elements. Results obtained from a finite element analysis usually satisfy compatibility, but not necessarily equilibrium. Equilibrium can, however, be satisfied to the desired degree by adequate mesh refinement.

Many special purpose finite element programs are available for the analysis of box girder bridges. These programs take advantage of the repetitive and special nature of box girders in order to minimize the required amount of input preparation, execution time and core storage in the computer, and the amount of post-processing necessary for meaningful interpretation of results. Two such special purpose programs developed at the University of California, Berkeley, for linear elastic analysis of box girder bridges are FINPLA2 [1, 20] and CELL4 [8]. Both programs use specially developed two-dimensional plate elements to model the bridge superstructure. Jirousek et al. [21] have presented a macro-element having the form of transversal slices of the bridge. Each macro-element is formed using two types of special purpose elements: a thick shell element and an assembly element. These macro-elements can be used to model a curved nonprismatic box girder bridge.

For medium and long span box girders, the transverse behavior of the structure can be characterized adequately by fewer parameters than the longitudinal bahavior. A discrete subdivision in the longitudinal direction only, i.e., a subdivision into beam-type elements, is thus a logical choice for such structures. Beam-type elements, which are usually based on thin-walled beam theory [22], have been used by several investigators [23, 24, 25] for linear elastic analysis of box girder bridges. These elements are capable of capturing the dominant structural actions, but at considerably reduced computational effort. The computer program SEGAN [26, 27] for curved prestressed segmental bridges, developed at the University of California, Berkeley, is based on such a model.

Many finite element formulations have been extended to include nonlinear analysis capabilities. Beam, plate and shell elements have been used at the University of California, Berkeley, for nolinear geometric, material and time-dependent analysis of prestressed concrete frames [28, 29], prestressed concrete slabs and panels [30], and reinforced concrete shells with edge beams [31, 32]. Conceivably, either one-, two- or three-dimensional elements can be used for nonlinear analysis of box girder bridges. However, the simplicity and reduced computational effort inherent in a beam-type element make it particularly suitable for nonlinear analysis, which requires much greater central processor time and storage space in the computer than linear elastic analysis.

1.3 Objective and Scope

The objective of the present study is to develop an efficient numerical procedure for linear elastic analysis and nonlinear material analysis of curved nonprismatic reinforced and prestressed concrete box girder bridges. Prediction of the overall response of the structure, rather than local behavior, is aimed at.

A finite element formulation based on thin-walled beam theory is used to develop a curved nonprismatic thin-walled box beam element. The cross section of the element is a rectangular single-cell box with side cantilevers. The axis of the element is curved in plan, and the cross sectional dimensions vary along the element axis. Transverse distortion and longitudinal warping of the cross section are included in the element formulation. Prestressing, consisting of post-tensioned bonded tendons in the longitudinal direction, is considered. Friction and anchorage slip losses are accounted for.

Nonlinearities in the uniaxial stress-strain curves of concrete, reinforcing steel and prestressing steel are considered. The shear and the transverse flexural responses of the box beam cross section are represented by trilinear constitutive relationships based on cracking, yielding and ultimate stages. Tension stiffening effect between concrete and longitudinal steel and the effect of load reversal are considered. The nonlinear analysis procedure is designed to trace the structural response throughout the elastic, inelastic and ultimate load ranges.

The theory is incorporated into two computer programs, LAPBOX and NAPBOX. Various numerical examples of linear elastic analysis and nonlinear material analysis up to ultimate are presented demonstrating the applicability and the capabilities of the proposed method. Comparisons with other analytical and experimental results are made.

2. CURVED NONPRISMATIC THIN-WALLED BOX BEAM ELEMENT

2.1 General

The basic differential equations governing thin-walled box beams have been derived by Vlasov [22] and extended by Dabrowski [33] and numerous other authors. Several investigators have combined thin-walled beam theory and the finite element technique to develop thin-walled box beam elements. Bazant and El Nimeiri [23] formulated a skew-ended nonprismatic thin-walled beam element for analyzing box girders curved or straight in space taking into account longitudinal warping and transverse distortion. Though the element itself was straight, full continuity in the case of a curved girder was achieved by means of the skewed ends. Van Zyl [26, 27] adopted this element for analyzing curved segmentally erected prestressed concrete box girder bridges. Zhang and Lyons [25] developed a curved nonprismatic thin-walled box beam element for the analysis of single- or multi-cell box girders curved in space. Transverse distortion and longitudinal warping were taken into account.

In the present study, certain aspects of the formulations used by Bazant and El Nimeiri [23] and Zhang and Lyons [25] are combined to develop a new curved nonprismatic thin-walled box beam element based on the displacement formulation of the finite element method. Small displacements and small strains are assumed in the formulation. The element is formulated in such a way as to facilitate its extension to nonlinear analysis. In this chapter, the detailed theoretical derivation of this element to be used for linear elastic and nonlinear analysis of curved nonprismatic box girder bridges is presented.

2.2 Geometry of the Element

The geometry of the three-node thin-walled box beam element (Fig. 2.1a) is similar to that considered by Zhang and Lyons [25]. The axis of the element lies in the global X-Y plane and may be curved. The element has two end nodes i and j and an interior node o situated on the axis. The cross section of the element perpendicular to its axis is a rectangular single-cell thin-walled box with side cantilevers (Fig. 2.1b). A local rectangular coordinate system (x, y, z) along the curved axis is used in the element formulation. The local z axis is the axis of symmetry of the cross section and coincides with the direction of the global Z axis. The local x axis is tangential to the element axis in the direction of node i towards node j. The local y axis is defined by a right handed orthogonal system. The y-z plane then defines the plane of the cross section. In addition, a natural coordinate ξ is defined along the element axis which has its origin at node o and varies between -1 at node i and +1 at node j (Fig. 2.1a).

The walls of the box cross section will hereafter be referred to by the names indicated in Fig. 2.1b, in which all dimensions are to the mid-thickness of the walls. The two walls parallel to the z axis and located respectively at positive and negative y coordinates are referred to as "left web" and "right web." The two walls parallel to the y axis and located between the webs are referred to as "top flange", if located at a greater (in an algebraic sense) z coordinate, and "bottom flange", otherwise. The two walls parallel to the y axis on either side of the top flange and located respectively at positive and negative y coordinates are referred to as "left cantilever" and "right cantilever."

The dimensions of the box cross section in Fig. 2.1b are defined by its width a, depth b ($= b_1 + b_2$), width of cantilever flanges f, thickness of top flange t_t, thickness of bottom flange t_b, thickness of each web t_w and thickness of each cantilever flange t_c. The distances b_1 and b_2 from the y axis to the top flange and bottom flange respectively are measured positive as shown in Fig. 2.1b. All the dimensions a, b_1, b_2, f, t_t, t_b, t_w and t_c can vary along the length of the element.

The shape functions N_k associated with each node, which are used later (Sec. 2.3.2) to define the longitudinal distribution of displacements, are

$$N_1 = \frac{1}{2}(\xi^2 - \xi) \tag{2.1a}$$

$$N_2 = (1 - \xi^2) \tag{2.1b}$$

$$N_3 = \frac{1}{2}(\xi^2 + \xi) \tag{2.1c}$$

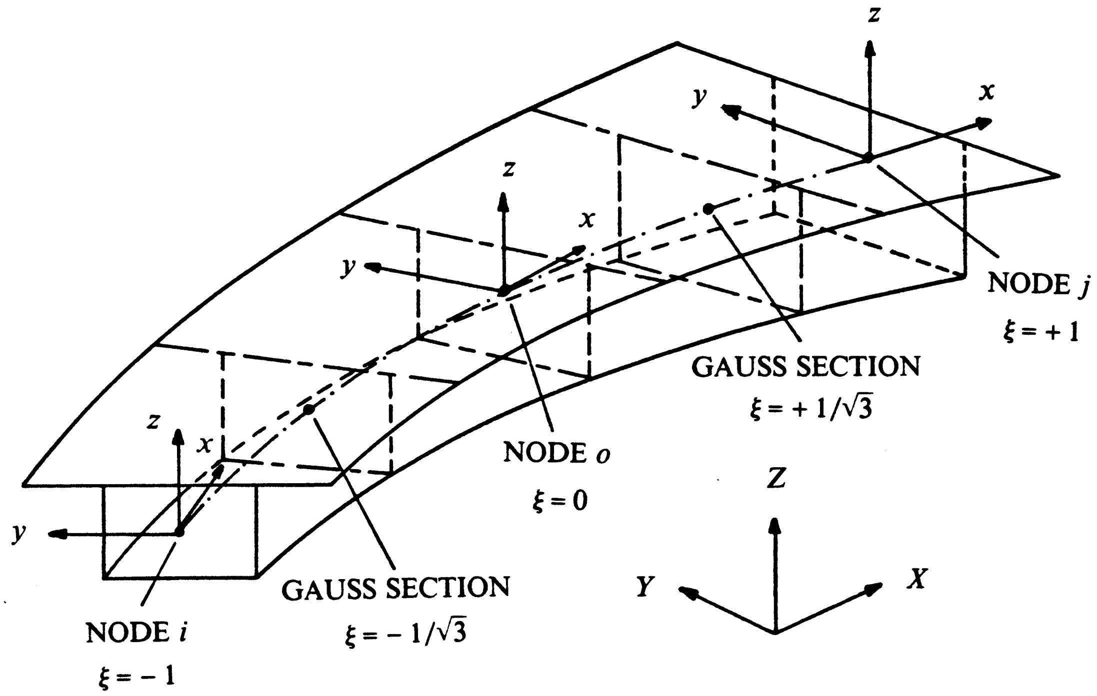

(a) ISOMETRIC VIEW

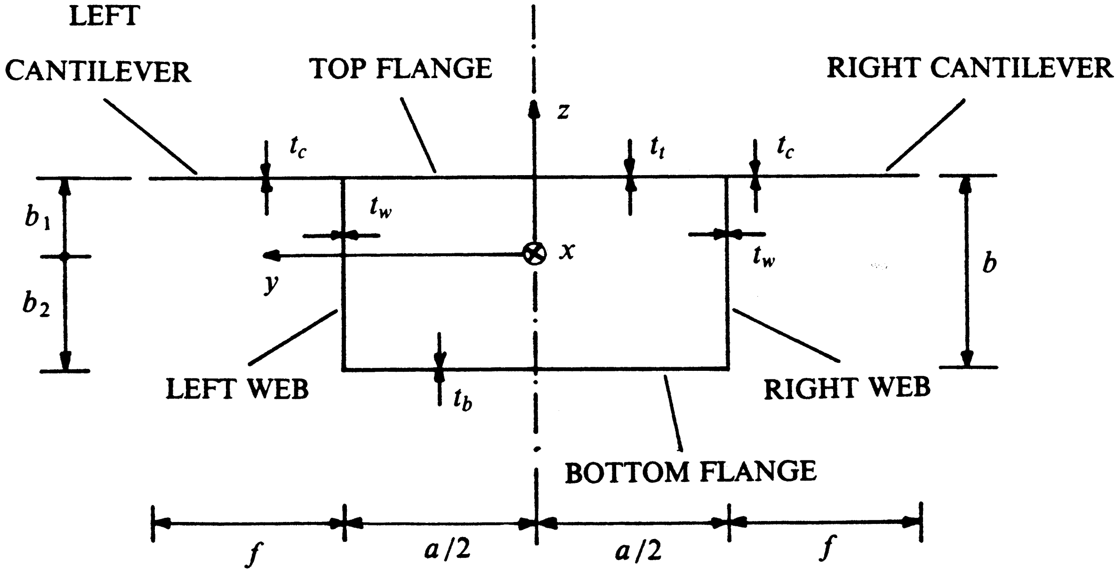

(b) CROSS SECTION

FIG. 2.1 CURVED NONPRISMATIC THIN-WALLED BOX BEAM ELEMENT where subscript 1 refers to node i, 2 refers to node o and 3 refers to node j. Now if $(X_k, Y_k, 0)$, $k = 1, 2, 3$, are the global coordinates of the three nodes, the global coordinates $(X_0, Y_0, 0)$ of any point on the element axis are obtained from an isoparametric mapping as

$$X_0 = \sum_{k=1}^{3} N_k X_k \tag{2.2a}$$

$$Y_0 = \sum_{k=1}^{3} N_k Y_k \tag{2.2b}$$

Similarly, the cross sectional dimensions at any point along the element axis are taken as

$$a = \sum_{k=1}^{3} N_k a_k \tag{2.3a}$$

$$b_1 = \sum_{k=1}^{3} N_k b_{1_k} \tag{2.3b}$$

$$b_2 = \sum_{k=1}^{3} N_k b_{2_k} \tag{2.3c}$$

$$f = \sum_{k=1}^{3} N_k f_k \tag{2.3d}$$

$$t_t = \sum_{k=1}^{3} N_k t_{t_k} \tag{2.3e}$$

$$t_b = \sum_{k=1}^{3} N_k t_{b_k} \tag{2.3f}$$

$$t_w = \sum_{k=1}^{3} N_k t_{w_k} \tag{2.3g}$$

$$t_c = \sum_{k=1}^{3} N_k t_{c_k} \tag{2.3h}$$

where $a_k, b_{1_k}, b_{2_k}, f_k, t_{t_k}, t_{b_k}, t_{w_k}$ and t_{c_k} are the nodal values of the cross sectional dimensions.

The unit tangent vector along the element local x direction at any point on the element axis is given by

$$\underset{\sim}{e}_x = \frac{1}{\lambda_0}\begin{Bmatrix} X_0' \\ Y_0' \\ 0 \end{Bmatrix} \tag{2.4}$$

where

$$X_0' = \sum_{k=1}^{3} N_k' X_k \tag{2.5a}$$

$$Y_0' = \sum_{k=1}^{3} N_k' Y_k \tag{2.5b}$$

$$\lambda_0 = \sqrt{(X_0')^2 + (Y_0')^2} \tag{2.5c}$$

and a prime denotes differentiation with respect to ξ.

Now, since the local z axis coincides with the global Z axis, i.e.,

$$\underset{\sim}{e}_z = \begin{Bmatrix} 0 \\ 0 \\ 1 \end{Bmatrix} \tag{2.6}$$

the unit vector along the local y direction is simply

$$\underset{\sim}{e}_y = \underset{\sim}{e}_z \times \underset{\sim}{e}_x = \frac{1}{\lambda_0}\begin{Bmatrix} -Y_0' \\ X_0' \\ 0 \end{Bmatrix} \tag{2.7}$$

With the local coordinate system (x, y, z) determined as above, the location of any point within the element is uniquely represented by the coordinates (ξ, y, z). The corresponding global coordinates (X, Y, Z) are given by the mapping

$$X = X_0 - \frac{Y_0'}{\lambda_0} y \tag{2.8a}$$

$$Y = Y_0 + \frac{X_0'}{\lambda_0} y \tag{2.8b}$$

$$Z = z \tag{2.8c}$$

2.3 Displacement Field

2.3.1 Displacement Variations Within the Cross Section

At any point along the element axis, eight generalized displacement degrees of freedom are defined in the local coordinate system [23]. These are

$$\underline{v} = < v_1, v_2, v_3, v_4, u_1, u_2, u_3, u_4 >^T \tag{2.9}$$

where $\underline{v}$ is the vector of generalized displacements in the local coordinate system; u_1, v_2, v_3 are respectively the rigid body translations of the cross section in the x, y, and z directions; v_1, u_3, u_2 are respectively the rigid body rotations of the cross section about the x, y, and z axes; v_4 is the transverse distortional mode of the cross section; and u_4 is the longitudinal warping mode of the cross section.

The displacement distributions within the cross section can be represented in terms of the generalized displacements as follows:

$$u(\xi, y, z) = \sum_{k=1}^{4} u_k(\xi)\phi_k(y, z) \tag{2.10a}$$

$$v(\xi, y, z) = \sum_{k=1}^{3} v_k(\xi)\psi_k(y, z) + v_4(\xi)\psi_4(\xi, y, z) \tag{2.10b}$$

$$w(\xi, y, z) = \sum_{k=1}^{3} v_k(\xi)\chi_k(y, z) + v_4(\xi)\chi_4(\xi, y, z) \tag{2.10c}$$

where u, v, w are the displacements of a general point within the element in the local x, y, z directions respectively; and the functions ϕ_k, ψ_k, χ_k define the transverse displacement distributions within the cross section. The dependence of ψ_4 and χ_4 on ξ arises from the assumed nonprismaticity of the element as explained later.

Making use of Eq. (2.9), Eq. (2.10) can be written in matrix notation as

$$\underline{u} = \underline{C}\,\underline{v} \tag{2.11}$$

where

$$\underline{u} = \begin{Bmatrix} u \\ v \\ w \end{Bmatrix} \tag{2.12}$$

$$\underline{C} = \begin{bmatrix} 0 & 0 & 0 & 0 & \phi_1 & \phi_2 & \phi_3 & \phi_4 \\ \psi_1 & \psi_2 & \psi_3 & \psi_4 & 0 & 0 & 0 & 0 \\ \chi_1 & \chi_2 & \chi_3 & \chi_4 & 0 & 0 & 0 & 0 \end{bmatrix} \tag{2.13}$$

The transverse displacement distributions corresponding to the rigid body modes of the cross section are simply given by:

$$\phi_1 = 1 \; ; \quad \phi_2 = -y \; ; \quad \phi_3 = z \tag{2.14a}$$

$$\psi_1 = -z \; ; \quad \psi_2 = 1 \; ; \quad \psi_3 = 0 \tag{2.14b}$$

$$\chi_1 = y \; ; \quad \chi_2 = 0 \; ; \quad \chi_3 = 1 \tag{2.14c}$$

The transverse distributions of displacements due to longitudinal warping and transverse distortion of the cross section are unique to thin-walled box beam elements and deserve some discussion.

A unit generalized displacement u_4 corresponding to longitudinal warping of the cross section is shown in Fig. 2.2a. The cross section warps out of its plane but its projection on the $y-z$ plane remains unchanged. Only u displacements result and these vary linearly along each side of the box cross section. From Fig. 2.2a it is evident that the distribution of the u displacements within the cross section is given by

$$\phi_4 = yz \tag{2.15}$$

A unit generalized displacement v_4 corresponding to transverse distortion of the cross section is shown in Fig. 2.2b. The cross section distorts in its own plane, resulting in v and w displacements. The component of the displacement tangential to the walls of the box is taken as constant along each side of the box. The displacement component normal to the walls of the box is derived by analyzing the cross section as a continuous frame subjected to the imposed displacements at its corners shown in Fig. 2.2b, as suggested by Bazant and El

Nimeiri [23]. The slope deflection method is used thus neglecting shear deformations. The distributions within the cross section of the v and w displacements in the local y and z directions due to a unit transverse distortion v_4 are then given by:

$$\psi_4 = b_1 \text{ , for top flange and cantilevers} \tag{2.16a}$$

$$\psi_4 = - b_2 \text{ , for bottom flange} \tag{2.16b}$$

$$\psi_4 = - b_2 - \theta_b(z + b_2) + \frac{(z + b_2)^2}{b^2}[\theta_t(b_1 - z) + \theta_b(b + b_1 - z)$$

$$+ b + 2(b_1 - z)] \text{ , for webs} \tag{2.16c}$$

$$\chi_4 = \frac{1}{2}(3 - \theta_t)y - \frac{2}{a^2}(1 - \theta_t)y^3 \text{ , for top flange} \tag{2.17a}$$

$$\chi_4 = \frac{1}{2}(3 - \theta_b)y - \frac{2}{a^2}(1 - \theta_b)y^3 \text{ , for bottom flange} \tag{2.17b}$$

$$\chi_4 = \frac{a}{2} \text{ , for left web} \tag{2.17c}$$

$$\chi_4 = - \frac{a}{2} \text{ , for right web} \tag{2.17d}$$

$$\chi_4 = \theta_t y + \frac{a}{2}(1 - \theta_t) \text{ , for left cantilever} \tag{2.17e}$$

$$\chi_4 = \theta_t y - \frac{a}{2}(1 - \theta_t) \text{ , for right cantilever} \tag{2.17f}$$

where θ_t and θ_b are as shown in Fig. 2.2b and are obtained as

$$\theta_t = 1 - \frac{2t_w^6a^2 + 6t_w^3t_b^3ab}{2t_t^3t_w^3ab + 3t_t^3t_b^3b^2 + t_w^6a^2 + 2t_w^3t_b^3ab} \tag{2.18a}$$

$$\theta_b = 1 - \frac{2t_w^6a^2 + 6t_w^3t_t^3ab}{2t_t^3t_w^3ab + 3t_t^3t_b^3b^2 + t_w^6a^2 + 2t_w^3t_b^3ab} \tag{2.18b}$$

It is seen from above that ψ_4 and χ_4 depend on the natural coordinate ξ since the cross sectional dimensions vary along the length of the element according to Eq. (2.3).

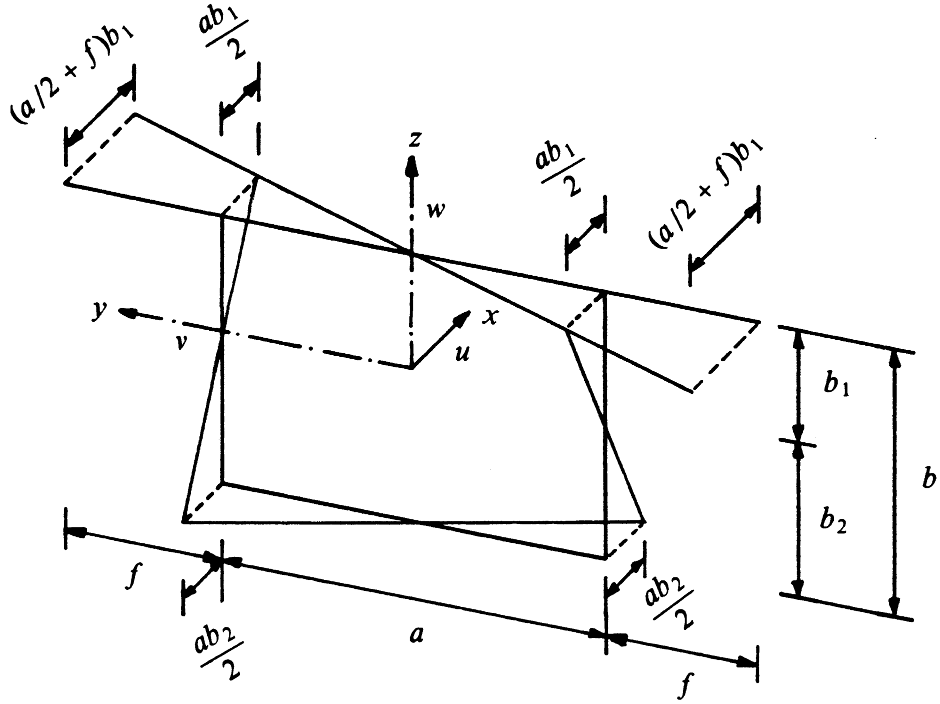

(a) UNIT LONGITUDINAL WARPING

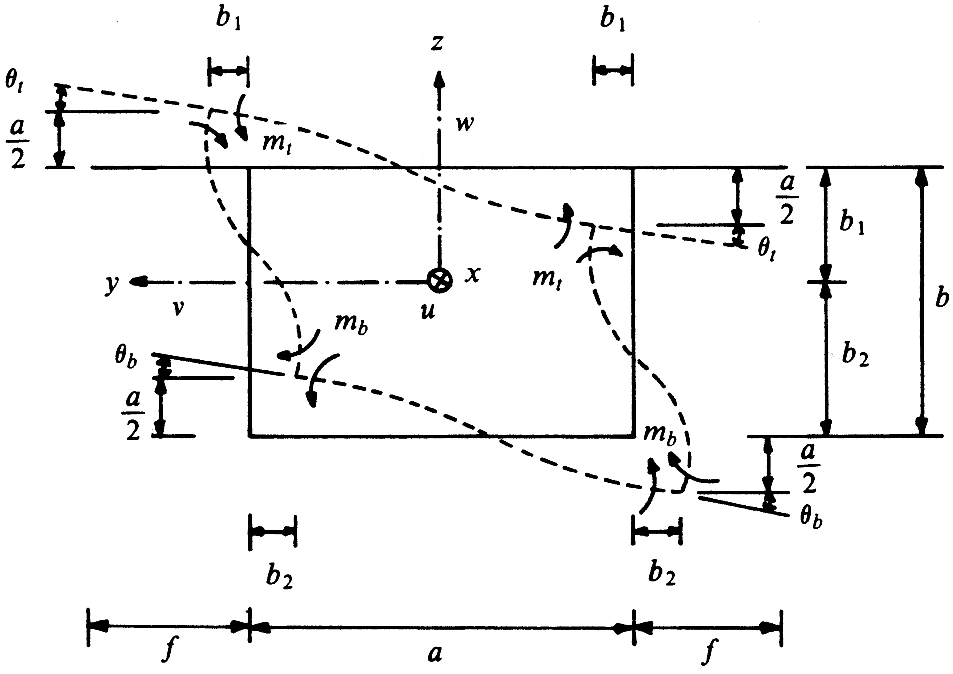

(b) UNIT TRANSVERSE DISTORTION

FIG. 2.2 UNIT GENERALIZED LONGITUDINAL WARPING AND TRANSVERSE DISTORTION DISPLACEMENTS

Bazant and El Nimeiri [23] observed that the two deformation modes u_4 and v_4 of the cross section are sufficient to characterize the global behavior of long single-cell box girders under study herein. A greater number of deformation modes, however, would be required for the analysis of short or multi-cell box girders. Even in the case of long single-cell box girders, more accurate solutions can be sought by increasing the number of terms in Eq. (2.10), as was done by Mikkola and Paavola in [24]. It is however believed that the inclusion of the two deformation modes of the cross section, u_4 and v_4, provides sufficient accuracy for most practical purposes.

2.3.2 Displacement Variations Along the Length of the Element

Let $\underline{v}^g$ be the vector of generalized displacements in the global coordinate system at any point along the element axis. Then

$$\underline{v}^g = < V_1, V_2, V_3, v_4, U_1, U_2, U_3, u_4 >^T \tag{2.19}$$

where U_1, V_2, V_3 are respectively the rigid body translations of the cross section in the global X, Y, Z directions; and V_1, U_3, U_2 are respectively the rigid body rotations of the cross section about a system of global X, Y, Z axes passing through the origin of the local coordinate system. The transverse distortion v_4 and the longitudinal warping u_4 of the cross section remain in the local coordinate system.

Then with the local coordinate system defined by Eqs. (2.4) through (2.7), the transformation between the generalized local displacements, $\underline{v}$, and the generalized global displacements, $\underline{v}^g$, is obtained as

$$\underline{v} = \underline{T}\,\underline{v}^g \tag{2.20}$$

$$\underline{T} = \frac{1}{\lambda_0}\begin{bmatrix} X_0' & 0 & 0 & 0 & 0 & 0 & Y_0' & 0 \\ 0 & X_0' & 0 & 0 & -Y_0' & 0 & 0 & 0 \\ 0 & 0 & \lambda_0 & 0 & 0 & 0 & 0 & 0 \\ 0 & 0 & 0 & \lambda_0 & 0 & 0 & 0 & 0 \\ 0 & Y_0' & 0 & 0 & X_0' & 0 & 0 & 0 \\ 0 & 0 & 0 & 0 & 0 & \lambda_0 & 0 & 0 \\ -Y_0' & 0 & 0 & 0 & 0 & 0 & X_0' & 0 \\ 0 & 0 & 0 & 0 & 0 & 0 & 0 & \lambda_0 \end{bmatrix} \qquad (2.21)$$

Next we define $\underline{r}$ as the vector of nodal values of the generalized displacements in the global coordinate system. In other words, $\underline{r}$ represents the twenty-four generalized global displacement degrees of freedom of the element. Then,

$$\underline{r} = \begin{Bmatrix} \underline{r}_1 \\ \underline{r}_2 \\ \underline{r}_3 \end{Bmatrix} \qquad (2.22)$$

where $\underline{r}_1, \underline{r}_2, \underline{r}_3$ are the nodal values of the generalized global displacements at nodes i, o, j, respectively.

Then making use of the shape functions in Eq. (2.1), the global displacements $\underline{v}^g$ at any point along the element axis are obtained in terms of the nodal values $\underline{r}$ by interpolation as follows.

$$\underline{v}^g = \underline{N}\,\underline{r} \qquad (2.23)$$

$$\underline{N} = [\underline{N}_1, \underline{N}_2, \underline{N}_3] \qquad (2.24a)$$

$$\underline{N}_k = N_k \underline{I}\ , \quad k = 1, 2, 3 \qquad (2.24b)$$

where $\underline{I}$ is the 8×8 identity matrix.

Let U, V and W be the displacements of a general point within the element in global X, Y and Z directions respectively. Then if $\underline{U}$ is the vector of these global displacements,

$$\underline{U} = \begin{Bmatrix} U \\ V \\ W \end{Bmatrix} = \underline{\Theta}\,\underline{u} \tag{2.25}$$

$$\underline{\Theta} = [\underline{e}_x, \underline{e}_y, \underline{e}_z] = \frac{1}{\lambda_0}\begin{bmatrix} X_0' & -Y_0' & 0 \\ Y_0' & X_0' & 0 \\ 0 & 0 & \lambda_0 \end{bmatrix} \tag{2.26}$$

where $\underline{\Theta}$ is the matrix of direction cosines of the local x, y, z axes.

Finally, combining Eqs. (2.11), (2.20), (2.23) and (2.25),

$$\underline{U} = \underline{A}\,\underline{r} \tag{2.27}$$

$$\underline{A} = \underline{\Theta}\,\underline{C}\,\underline{T}\,\underline{N} \tag{2.28}$$

Carrying out the matrix multiplications in Eq. (2.28),

$$\underline{A} = [\underline{A}_1, \underline{A}_2, \underline{A}_3] \tag{2.29a}$$

$$\underline{A}_k = N_k \begin{bmatrix} 0 & 0 & 0 & -\dfrac{\psi_4 Y_0'}{\lambda_0} & 1 & -\dfrac{X_0' y}{\lambda_0} & z & \dfrac{X_0' yz}{\lambda_0} \\ -z & 1 & 0 & \dfrac{\psi_4 X_0'}{\lambda_0} & 0 & -\dfrac{Y_0' y}{\lambda_0} & 0 & \dfrac{Y_0' yz}{\lambda_0} \\ \dfrac{X_0' y}{\lambda_0} & 0 & 1 & \chi_4 & 0 & 0 & \dfrac{Y_0' y}{\lambda_0} & 0 \end{bmatrix}, \quad k = 1, 2, 3 \tag{2.29b}$$

where all quantities are as defined previously.

The matrix $\underline{A}$, given by Eq. (2.29) above, which relates the global displacements, $\underline{U}$, to the generalized global displacement degrees of freedom of the element, $\underline{r}$, through Eq. (2.27), completely defines the displacement field within the element.

2.4 Definition of Strains and Stresses

In the present formulation, three generalized strain components ϵ_x, γ_{xs} and v_4 are of interest. The generalized stresses corresponding to these strains are σ_x, τ_{xs} and w_4. ϵ_x and σ_x are the usual normal strain and normal stress in the direction of the local x axis. γ_{xs} and τ_{xs} are the usual shear strain and shear stress acting in the plane of the cross section along the walls of the box. The positive direction of the local s coordinate along the walls of the cross section is shown in Fig. 2.3. Also shown in Fig. 2.3 are the positive components of $\epsilon_x, \gamma_{xs}, \sigma_x, \tau_{xs}$. Then,

$$\epsilon_x = \frac{\partial u}{\partial x} \tag{2.30}$$

$$\gamma_{xs} = \left[\frac{\partial u}{\partial y} + \frac{\partial v}{\partial x}\right]\cos\alpha + \left[\frac{\partial u}{\partial z} + \frac{\partial w}{\partial x}\right]\sin\alpha \tag{2.31}$$

where

$$\alpha = \pi \text{ , for top flange and cantilevers} \tag{2.32a}$$

$$\alpha = 0 \text{ , for bottom flange} \tag{2.32b}$$

$$\alpha = \pi/2 \text{ , for left web} \tag{2.32c}$$

$$\alpha = -\pi/2 \text{ , for right web} \tag{2.32d}$$

The generalized strain component v_4 is the transverse distortion of the cross section itself as defined previously in Fig. 2.2b. The generalized strain v_4 and the associated generalized stress w_4 represent the strain energy contribution due to the transverse bending of the walls of the box cross section. It should be noted here that v_4 represents the generalized strain of an entire cross section of the element, unlike ϵ_x and γ_{xs} which represent strains at a point in the element. The generalized stress w_4 associated with v_4 is defined in a virtual work sense as the internal work per unit length of the element done by the flexural stresses, arising from transverse bending of the walls of the cross section, due to a unit virtual generalized strain v_4.

For linear elastic isotropic material, the generalized stress-strain relationships are given by

$$\sigma_x = E\epsilon_x \tag{2.33}$$

$$\tau_{xs} = G\gamma_{xs} \tag{2.34}$$

$$w_4 = Dv_4 \tag{2.35}$$

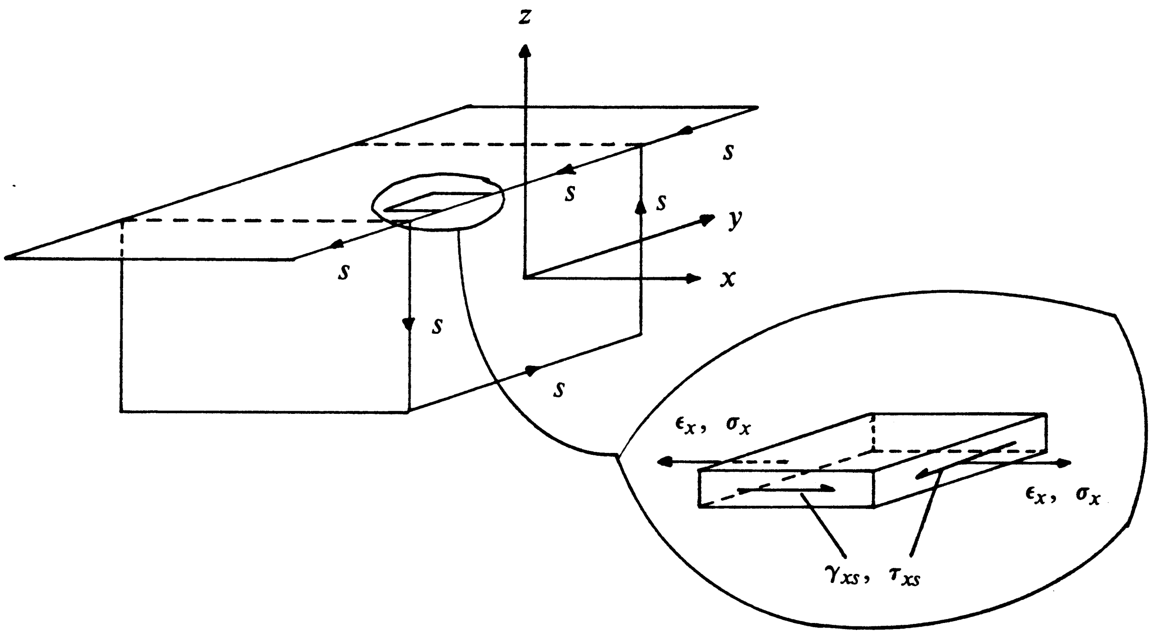

FIG. 2.3 POSITIVE STRAIN AND STRESS COMPONENTS

where E is the modulus of elasticity, $G = \dfrac{E}{2(1 + \nu)}$ is the shear modulus, ν is the Poisson's ratio, and D is a generalized rigidity.

In order to determine the generalized rigidity D, the transverse bending moments per unit length at the top and bottom corners of the box beam cross section, m_t and m_b respectively (Fig. 2.2b), due to a unit transverse distortion v_4, need to be found. Using the flexural rigidity $\dfrac{Et^3}{12(1 - \nu^2)}$ of plates [34] to represent the bending stiffness of the walls of the cross section, m_t and m_b are obtained from the slope deflection method as

$$m_t = \frac{Et_t^3}{2(1 - \nu^2)a}(1 - \theta_t) \tag{2.36}$$

$$m_b = \frac{Et_b^3}{2(1 - \nu^2)a}(1 - \theta_b) \tag{2.37}$$

Then applying the principle of virtual displacements,

$$w_4 = 4(m_t + m_b)v_4 \tag{2.38}$$

Hence,

$$D = \frac{2E}{(1 - \nu^2)a}[t_t^3(1 - \theta_t) + t_b^3(1 - \theta_b)] \tag{2.39}$$

2.5 Generalized Internal Forces

It is of interest to identify the generalized internal forces at a cross section corresponding to the generalized displacements $\underline{v}$ in the local coordinate system. Let

$$\underline{S} = \langle Q_1, Q_2, Q_3, Q_4, P_1, P_2, P_3, P_4\rangle^T \tag{2.40}$$

be the vector of generalized internal forces in the local coordinate system at a cross section along the axis of the element. Then, from the principle of virtual displacements,

$$Q_k = \int_A (\psi_k \cos\alpha + \chi_k \sin\alpha)\tau_{xs}\, dA \ , \quad k = 1, 2, 3, 4 \tag{2.41a}$$

$$P_k = \int_A \phi_k \sigma_x\, dA \ , \quad k = 1, 2, 3, 4 \tag{2.41b}$$

where Q_1 is the torque; Q_2 and Q_3 are the shear forces in the y and z directions respectively; P_1 is the normal force; P_2 and P_3 are the bending moments about the z and y axes respectively; Q_4 is the distortional moment with dimension $force \times length$; and P_4 is the warping bimoment with dimension $force \times length^2$.

2.6 Strain-Displacement Relationships

The strain-displacement relationship corresponding to the generalized strain v_4 is easily obtained from Eqs. (2.19),(2.23) and (2.24) to be

$$v_4 = \underline{B}_v \, \underline{r} \tag{2.42}$$

where

$$\underline{B}_v = < \underline{B}_{v_1}, \underline{B}_{v_2}, \underline{B}_{v_3} > \tag{2.43a}$$

$$\underline{B}_{v_k} = N_k < 0, 0, 0, 1, 0, 0, 0, 0 > , \quad k = 1, 2, 3 \tag{2.43b}$$

In order to establish the strain-displacement relationships corresponding to ϵ_x and γ_{xs}, the derivatives of the local displacements $\underline{u}$ with respect to the local x, y, z axes, occurring in Eqs. (2.30) and (2.31), must be determined. The process is the same as the one used in the formulation of thick shell elements [35].

First, the derivatives of the global displacements $\underline{U}$ with respect to the global X, Y, Z axes are obtained through the transformation

$$\begin{bmatrix} \frac{\partial U}{\partial X} & \frac{\partial V}{\partial X} & \frac{\partial W}{\partial X} \\ \frac{\partial U}{\partial Y} & \frac{\partial V}{\partial Y} & \frac{\partial W}{\partial Y} \\ \frac{\partial U}{\partial Z} & \frac{\partial V}{\partial Z} & \frac{\partial W}{\partial Z} \end{bmatrix} = \underline{J}^{-1} \begin{bmatrix} \frac{\partial U}{\partial \xi} & \frac{\partial V}{\partial \xi} & \frac{\partial W}{\partial \xi} \\ \frac{\partial U}{\partial y} & \frac{\partial V}{\partial y} & \frac{\partial W}{\partial y} \\ \frac{\partial U}{\partial z} & \frac{\partial V}{\partial z} & \frac{\partial W}{\partial z} \end{bmatrix} \tag{2.44}$$

where the Jacobian matrix $\underline{J}$ is defined as

$$\underline{J} = \begin{bmatrix} \dfrac{\partial X}{\partial \xi} & \dfrac{\partial Y}{\partial \xi} & \dfrac{\partial Z}{\partial \xi} \\ \dfrac{\partial X}{\partial y} & \dfrac{\partial Y}{\partial y} & \dfrac{\partial Z}{\partial y} \\ \dfrac{\partial X}{\partial z} & \dfrac{\partial Y}{\partial z} & \dfrac{\partial Z}{\partial z} \end{bmatrix} \tag{2.45}$$

The Jacobian matrix $\underline{J}$ is calculated from the coordinate mapping in Eq. (2.8) and is then inverted to give

$$\underline{J}^{-1} = \frac{1}{\lambda} \begin{bmatrix} X_0'/\lambda_0 & -Y_0' - (X_0'/\lambda_0)'y & 0 \\ Y_0'/\lambda_0 & X_0' - (Y_0'/\lambda_0)'y & 0 \\ 0 & 0 & \lambda \end{bmatrix} \tag{2.46}$$

where the determinant of $\underline{J}$, λ, is given by

$$\lambda = \lambda_0 - y(X_0'Y_0'' - Y_0'X_0'')/\lambda_0^2 \tag{2.47}$$

It may be noted here that the second term in Eq. (2.47) above arises due to the curved nature of the element. For a straight element, $\lambda = \lambda_0$.

The derivatives of the global displacements $\underline{U}$ with respect to the ξ, y, z axes occurring in Eq. (2.44) are found from Eqs. (2.27) and (2.29).

Next, the global derivatives of displacements $\underline{U}$ are transformed to the local derivatives of displacements $\underline{u}$ by a standard operation.

$$\begin{bmatrix} \dfrac{\partial u}{\partial x} & \dfrac{\partial v}{\partial x} & \dfrac{\partial w}{\partial x} \\ \dfrac{\partial u}{\partial y} & \dfrac{\partial v}{\partial y} & \dfrac{\partial w}{\partial y} \\ \dfrac{\partial u}{\partial z} & \dfrac{\partial v}{\partial z} & \dfrac{\partial w}{\partial z} \end{bmatrix} = \underline{\Theta}^T \begin{bmatrix} \dfrac{\partial U}{\partial X} & \dfrac{\partial V}{\partial X} & \dfrac{\partial W}{\partial X} \\ \dfrac{\partial U}{\partial Y} & \dfrac{\partial V}{\partial Y} & \dfrac{\partial W}{\partial Y} \\ \dfrac{\partial U}{\partial Z} & \dfrac{\partial V}{\partial Z} & \dfrac{\partial W}{\partial Z} \end{bmatrix} \underline{\Theta} \tag{2.48}$$

where $\underline{\Theta}$ is as defined in Eq. (2.26).

The derivatives in Eqs. (2.30) and (2.31) can then be calculated to give the following strain-displacement relationships.

$$\epsilon_x = \underline{B}_\epsilon \underline{r} \tag{2.49}$$

$$\underline{B}_\epsilon = <\underline{B}_{\epsilon_1}, \underline{B}_{\epsilon_2}, \underline{B}_{\epsilon_3}> \tag{2.50a}$$

$$\underline{B}_{\epsilon_k}^T = \frac{1}{\lambda}\left\{\begin{array}{c} -N_k' Y_0' z/\lambda_0 \\ N_k' Y_0'/\lambda_0 \\ 0 \\ N_k \psi_4 (Y_0' X_0'' - X_0' Y_0'')/\lambda_0^2 \\ N_k' X_0'/\lambda_0 \\ -N_k' y \\ N_k' X_0' z/\lambda_0 \\ N_k' yz \end{array}\right\}, \quad k = 1, 2, 3 \tag{2.50b}$$

$$\gamma_{xs} = \underline{B}_\gamma \underline{r} \tag{2.51}$$

$$\underline{B}_\gamma = <\underline{B}_{\gamma_1}, \underline{B}_{\gamma_2}, \underline{B}_{\gamma_3}> \tag{2.52a}$$

$$\underline{B}_{\gamma_k}^T = \frac{1}{\lambda}\left\{\begin{array}{c} -N_k Y_0' \sin\alpha + N_k' X_0' (y\sin\alpha - z\cos\alpha)/\lambda_0 \\ N_k' X_0' \cos\alpha/\lambda_0 \\ N_k' \sin\alpha \\ N_k(\chi_4' \sin\alpha + \psi_4' \cos\alpha) + N_k'(\chi_4 \sin\alpha + \psi_4 \cos\alpha) \\ -N_k' Y_0' \cos\alpha/\lambda_0 \\ -N_k \lambda_0 \cos\alpha \\ N_k X_0' \sin\alpha + N_k' Y_0' (y\sin\alpha - z\cos\alpha)/\lambda_0 \\ N_k(\lambda_0 z\cos\alpha + \lambda y \sin\alpha) \end{array}\right\}, k = 1, 2, 3 \tag{2.52b}$$

2.7 Element Stiffness Matrix

Using the principle of virtual displacements, the equations of equilibrium for the element in the global coordinate system are obtained as

$$\underline{R} = \underline{K}\,\underline{r} \tag{2.53}$$

where $\underline{R}$ is the vector of generalized equivalent nodal forces corresponding to the generalized nodal displacements $\underline{r}$, and $\underline{K}$ is the element stiffness matrix of order 24×24 expressed as

$$\underline{K} = \int_{-1}^{1}\int_A \underline{B}_\epsilon^T E\, \underline{B}_\epsilon \lambda\, dA\ d\xi + \int_{-1}^{1}\int_A \underline{B}_\gamma^T G\, \underline{B}_\gamma \lambda\, dA\ d\xi + \int_{-1}^{1} \underline{B}_v^T D\, \underline{B}_v \lambda_0\, d\xi \tag{2.54}$$

In Eq. (2.54) above, $\lambda\, dA\ d\xi = \lambda\, dy\ dz\ d\xi$ is the differential volume of the element, and $\lambda_0\, d\xi$ is the differential arc length along the axis of the element.

The integrations in Eq. (2.54) with respect to ξ are done numerically using two-point Gauss quadrature (Fig. 2.1a). This is found to eliminate the "spurious shear stiffness" usually associated with beam and shell element formulations including shear deformations. Spurious shear effects relative to the torsional, distortional and warping degrees of freedom are also eliminated by this reduced order of integration.

The integrations over the area of the cross section in Eq. (2.54) are done separately for each web, flange and cantilever. Two different numerical approaches are used for linear elastic and nonlinear analysis.

In a linear elastic analysis, E and G are constants. Furthermore, consistent with thin-walled beam theory, it is assumed that λ, $\underline{B}_\epsilon$ and $\underline{B}_\gamma$ are constant over the thickness of the walls of the cross section. Thus four Gauss points at the mid-thickness of the walls are used along the s direction (Fig. 2.3) of each web, flange and cantilever. This achieves exact integration over the area of the webs where the integrands involve polynomials in z of highest order 6. For the flanges and the cantilevers, however, the integrands involve rational functions in y and hence four-point Gauss quadrature is only an approximation. In the special case of a straight element, the integrands for the flanges and the cantilevers involve polynomials in y of highest order 2 and four-point Gauss quadrature does achieve exact integration. For practical instances of curved bridges, four-point Gauss quadrature is found to be adequate for the flanges and the cantilevers.

The integration scheme over the area of the box cross section used for nonlinear analysis is discussed later in Chapters 5 and 6.

2.8 Equivalent Nodal Forces

The vector of equivalent nodal forces, $\underline{R}$, appearing in Eq. (2.53), consists of nodal values of forces in the X, Y, Z directions, moments about the X, Y, Z axes, distortional moment and warping bimoment. $\underline{R}$ in general can represent load effects due to concentrated forces, distributed forces, body forces, initial strains and prestressing. The calculation of equivalent nodal forces due to prestressing is discussed in Chapter 3. The effects of initial strains, due possibly to temperature changes, creep and shrinkage of concrete and relaxation of prestressing steel, are not considered in the present study. Calculation of equivalent nodal forces due to concentrated forces, distributed element forces and dead load is discussed here.

2.8.1 Concentrated Forces

If $\underline{F} = <F_X, F_Y, F_Z>^T$ is a concentrated force vector acting on the element at location (ξ, y, z), its contribution to the nodal force vector is calculated as

$$\underline{R} = \underline{A}^T \underline{F} \tag{2.55}$$

where $\underline{A}$ is as defined in Eq. (2.29).

2.8.2 Distributed Element Forces

In this study consideration of distributed element forces is limited to those acting in the Z direction on the flanges or the side cantilevers. If p is the uniform force per unit area of projection on the $X-Y$ plane, acting in the Z direction over the length of the element, on either the top flange, the cantilever flanges or the bottom flange, the equivalent nodal force vector is calculated as

$$\underline{R} = \int_{-1}^{1} \int_{y_1}^{y_2} \underline{A}^T <0, 0, p>^T \lambda \, dy \, d\xi \tag{2.56}$$

where y_1 and y_2, generally dependent on ξ, define the limits in the y direction between which the pressure p acts. In Eq. (2.56), the integration with respect to y is carried out explicitly while two-point Gauss quadrature (Fig.2.1a) is used in the ξ direction. Further discussion on distributed element forces can be found in Sec. 7.2.1.

2.8.3 Dead Load

Dead load effects are represented by means of equivalent nodal forces calculated as follows

$$\underline{R} = \int_{-1}^{1} \int_{A} \underline{A}^T \underline{w} \lambda \, dA \, d\xi \tag{2.57}$$

where $\underline{w} = < w_X, w_Y, w_Z >^T$ is the body force vector due to dead load, and $| \underline{w} | = w$ is the unit weight of the element. The above formulation recognizes that in the general case, the vertical axis may be arbitrarily oriented with respect to the global X, Y, Z axes. In Eq. (2.57), two-point Gauss quadrature (Fig. 2.1a) is used for the integration with respect to ξ, and the area integral is evaluated explicitly.

2.9 Assembly of Equilibrium Equations for Structure

A typical rectangular single-cell box girder bridge is shown in Fig. 2.4. The bridge is supported at S1, S2 and S3, and has interior diaphragms at D1 and D2. A set of global rectangular X, Y, Z axes is defined for the structure. The cross section of the bridge (Fig. 2.4b) perpendicular to the reference axis has a local z axis of symmetry, and the direction of this z axis always coincides with the direction of the global Z axis, which is usually the vertical axis. The global $X-Y$ plane, which is usually the horizontal plane, is perpendicular to the Z axis. The reference axis of the bridge (Fig. 2.4a,c) is defined as the locus of the points of intersection of the global $X-Y$ plane and the local z axis of symmetry of the cross section. This reference axis thus lies in the $X-Y$ plane and is, in general, arbitrarily curved. The cross sectional dimensions of the bridge (Fig. 2.4b) can vary arbitrarily along the reference axis.

For the purpose of analysis, the bridge is discretized in the longitudinal direction into a finite number of box beam elements. An odd number of element nodes NN are located along the reference axis at locations S1, D1, S2, D2, S3 and between them. The ith box beam element is then automatically defined as spanning nodes $2i - 1, 2i, 2i + 1$.

If the global X, Y coordinates and the cross sectional dimensions are specified at the nodes, the geometry of each box beam element can be determined from Eqs. (2.2) and (2.3). In general, at a node common to two elements, the directions of the element x axis determined from Eq. (2.4) for the two adjacent elements will not be the same. In other words, full compatibility between adjacent elements at a node will not be obtained unless the reference axis of the bridge has a linear or quadratic variation in the $X-Y$ plane. However, in the common case of a circularly curved bridge with practical element subdivisions, the discrepancies between the element x axes at common nodes are found to be negligible and hence inconsequential.

For each element, the stiffness matrix is calculated from Eq. (2.54) and then assembled in a standard manner to give the stiffness matrix of the entire structure in the global (X, Y, Z) coordinate system. The diaphragm and support stiffnesses are then added to the appropriate terms of the structure stiffness matrix corresponding to the nodes at which they are located, as discussed later in Sec. 2.10. The resulting structure stiffness matrix is banded with a half band width of 24 and a square dimension of $8 \times NN$.

The nodal force vector for the entire structure is similarly assembled in the global coordinate system by summing the contributions from each element. For a linear elastic analysis, the equilibrium equations of the structure can then be directly solved for the generalized nodal displacements. The solution of the equilibrium equations for nonlinear analysis is more involved and is discussed later in Chapter 6.

2.10 Boundary Conditions

Boundary conditions are specified at the supported nodes of the structure by means of support springs. Eight springs are provided corresponding to the eight generalized degrees of freedom at a supported node. The translational and rotational spring stiffnesses are specified relative to a coordinate system (A, B, Z) which is obtained by rotating the global coordinate system (X, Y, Z) by an arbitrary angle θ about the Z axis (Fig. 2.5). The warping and distortional spring stiffnesses are always specified relative to the local coordinate system at the node. Thus by appropriately specifying the angle θ and the support spring stiffnesses, any kind of boundary conditions can be simulated at the supported nodes. Interior unsupported diaphragms, such as D1 and D2 in Fig. 2.4, can be represented as supported nodes with non-zero spring stiffnesses for the distortional and/or warping degrees of freedom only.

The support spring stiffness matrix $\underline{k}_s$ in the (A, B, Z) coordinate system can be written

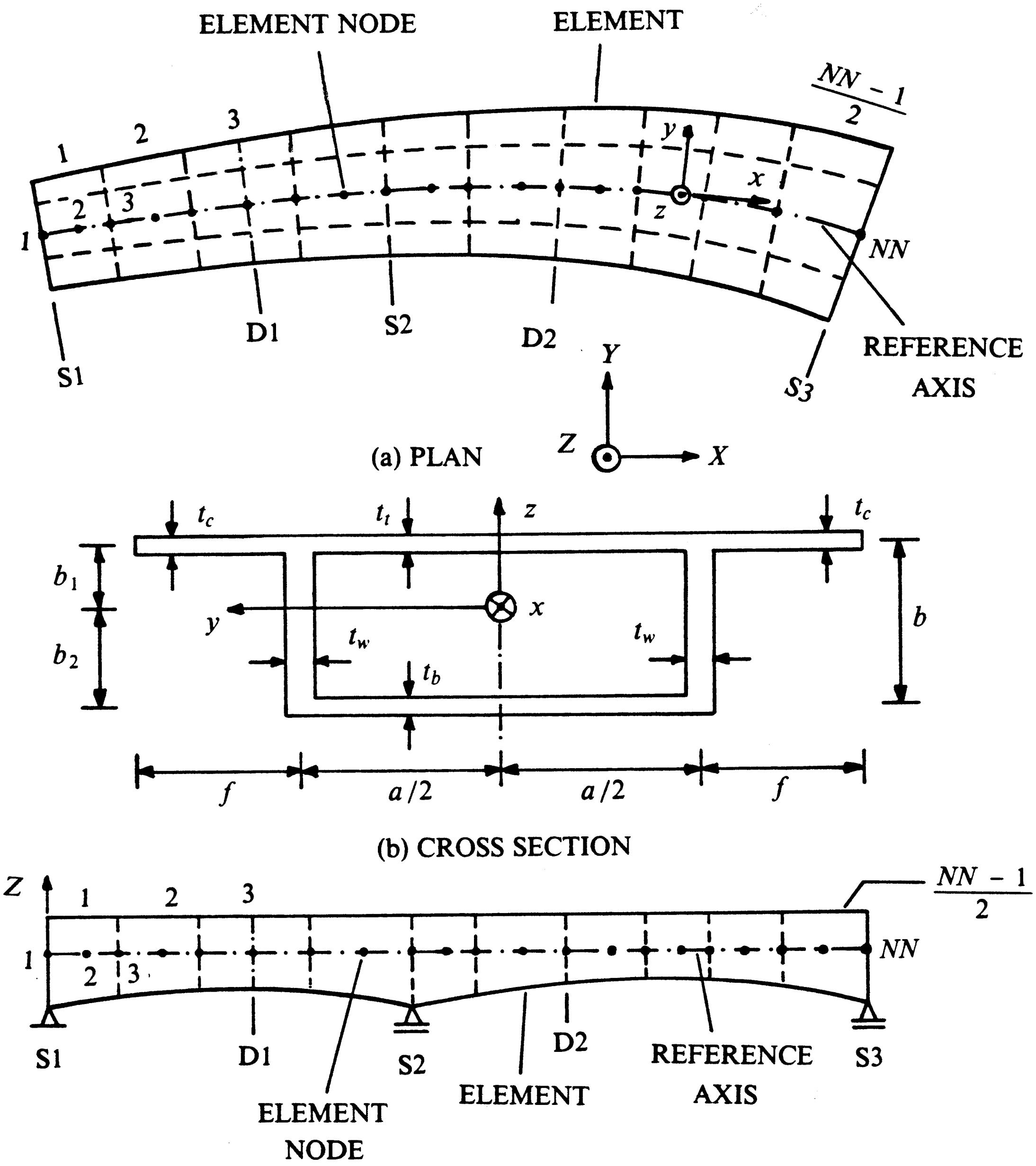

FIG. 2.4 DISCRETIZATION OF TYPICAL BOX GIRDER BRIDGE INTO BOX BEAM ELEMENTS

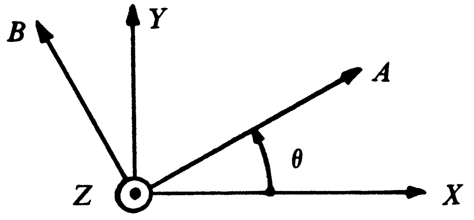

FIG. 2.5 ORIENTATION OF SUPPORT SPRINGS

as

$$\underset{\sim}{k_s} = \text{diag}\,[k_1, k_2, k_3, k_4, k_5, k_6, k_7, k_8] \tag{2.58}$$

where k_5, k_2, k_3 are respectively the translational spring stiffnesses in the A, B, Z directions; k_1, k_7, k_6 are respectively the rotational spring stiffnesses about the A, B, Z axes; k_4 is the transverse distortional spring stiffness; and k_8 is the longitudinal warping spring stiffness.

The support spring stiffness matrix $\underset{\sim}{K_s}$ in the global (X, Y, Z) coordinate system is then obtained from the transformation

$$\underset{\sim}{K_s} = \underset{\sim}{T}^T \underset{\sim}{k_s} \underset{\sim}{T} \tag{2.59}$$

in which the transformation matrix $\underset{\sim}{T}$ is given by

$$\underset{\sim}{T} = \begin{bmatrix} c & 0 & 0 & 0 & 0 & 0 & s & 0 \\ 0 & c & 0 & 0 & -s & 0 & 0 & 0 \\ 0 & 0 & 1 & 0 & 0 & 0 & 0 & 0 \\ 0 & 0 & 0 & 1 & 0 & 0 & 0 & 0 \\ 0 & s & 0 & 0 & c & 0 & 0 & 0 \\ 0 & 0 & 0 & 0 & 0 & 1 & 0 & 0 \\ -s & 0 & 0 & 0 & 0 & 0 & c & 0 \\ 0 & 0 & 0 & 0 & 0 & 0 & 0 & 1 \end{bmatrix} \tag{2.60}$$

where $c = \cos\theta$ and $s = \sin\theta$.

After the equilibrium equations of the structure are solved, the support reactions $\underset{\sim}{R_s} = \langle R_1, R_2, R_3, R_4, R_5, R_6, R_7, R_8 \rangle^T$ in the (A, B, Z) coordinate system are calculated from

$$\underset{\sim}{R_s} = -\underset{\sim}{k_s} \underset{\sim}{T} \underset{\sim}{r} \tag{2.61}$$

where $\underset{\sim}{r}$ is the vector of generalized displacements at the supported node in the global coordinate system.

In the general case when θ is not equal to zero, the transformation in Eq. (2.59) can result in large off-diagonal terms in $\underset{\sim}{K_s}$ corresponding to the translational and rotational degrees of freedom in the X, Y directions. This can cause the structure stiffness matrix to be ill-conditioned. Whether the equilibrium equations will be solved correctly will depend upon the precision used as well as the magnitude of the large off-diagonal terms relative to the other terms of the stucture stiffness matrix. Thus care must be exercised in choosing the magnitudes of the translational and rotational spring stiffnesses in the A, B directions when these directions do not coincide with the X, Y directions.

2.11 Recovery of Strains and Stresses

An integral part of any finite element analysis is the recovery of strains and stresses. After the nodal displacements are obtained from the solution of the equilibrium equations, the strain-displacement relationships in Eq. (2.42), (2.49) and (2.51) can be used to find the strains at any point in the element. The corresponding stresses are then determined from the constitutive relationships.

The locations at which the strains and the stresses should be recovered in a finite element have been the subject of some discussion. It has been observed that at certain unique points within a finite element, the stresses have higher accuracy than at any other points. In analysis involving numerically integrated elements, experience has shown that the integration points are the optimal stress sampling points [36, 37]. For the 3-node isoparametric box beam element developed in the present investigation, these optimal locations are the two Gauss sections ($\xi = \pm 1/\sqrt{3}$) along the element axis (Fig. 2.1a). The nodes, which are the most practical output locations for stresses, appear to be the worst locations for sampling stresses.

Thus, in the present study, strains and stresses are recovered at the two Gauss sections of the box beam element. If nodal values are desired, then a simple linear extrapolation from Gauss sections should be made. Such extrapolations have been discussed by Hinton and Campbell [37] and Hinton et al. [38].

The locations at which strains and stresses are recovered in a linear elastic analysis, of course, have no influence on the solution for the nodal displacements. The use of the optimal sampling points simply enables one to obtain strains and stresses which have the same degree of accuracy as the nodal displacements. However, the locations of strain and stress sampling points have wider implications in nonlinear analysis. In a nonlinear analysis the solution does depend on the recovered internal strains and stresses which are used in the state determination phase (Chapter 6). From the above discussion it is apparent that the two Gauss sections should also be used to monitor the element states in a nonlinear analysis.

3. PRESTRESSING

3.1 General

Prestressing is used in concrete box girder bridges in order to increase maximum span, control behavior and limit weight. Post-tensioned tendons are generally used, both in the longitudinal direction where their use can result in more slender girders and longer maximum spans, and in some cases in the transverse direction where their use can reduce the number of webs required and increase the width of the cantilever top slabs, resulting in a more efficient cross section.

In the present study, only post-tensioned tendons in the longitudinal direction are considered. For linear elastic analysis of the structure under prestressing, the effect of prestress is represented by a set of equivalent nodal loads, and these are treated as a separate load case on the structure. The prestressing load case can be combined with other load cases for determination of total stresses and displacements. For the analysis at transfer of prestress in a nonlinear analysis, the prestressing is similarly represented by a set of equivalent nodal loads, and the structure is analyzed as an ordinary reinforced concrete one. The contribution of the prestressing steel to the overall structural stiffness is neglected since, at this stage, the steel is unbonded. For the subsequent application of external loads, the prestressing steel is assumed to be bonded to the concrete (i.e., grouted) and the prestressing steel stiffnesses are included in the overall structural stiffness.

This chapter describes aspects of the prestressing analysis which are common to linear elastic analysis and nonlinear analysis. These include discretization of the tendon, definition of tendon profile, determination of tendon forces, and calculation of the equivalent nodal force vector due to prestress. The basic approach for prestressing analysis presented in this chapter is similar to the one used by Scordelis et al. in [8]. Certain other aspects of prestressing analysis that are relevant only to nonlinear analysis are presented later in Chapters 5 and 6.

3.2 Tendon Discretization

For prestressing analysis only, the definition of the term "top flange" introduced in Sec. 2.2 is broadened to include the cantilever flanges in addition to the portion of the top flange located between the webs. Each prestressing steel tendon is then defined to have a given longitudinal profile at the mid-thickness of either the left web, the right web, the top flange or the bottom flange, initial tensioning force, and a constant cross sectional area along its length. Stressing may be done from one or both ends. Discretization of flange and web tendons is shown in Fig. 3.1. In order to describe a wide range of general tendon profiles, the actual curved tendon is approximated by subdivision into piece-wise linear segments intersecting at tendon points. The tendon points are located at the nodes of the box beam elements the tendon spans (Fig. 3.1). Thus the two ends of the tendon must be located at element nodes. The discretized geometry is then completely defined by the set of global X, Y, Z coordinates of the tendon points, all of which must lie within the walls of the box beam elements.

The tendon is discretized into $(n - 1)$ straight segments defined by n tendon points (Fig. 3.1). Each of these straight tendon segments spans between two consecutive nodes of a curved box beam element with certain eccentricities with respect to the element axis at the nodes. Thus compatibility between the tendon segments and the box beam elements is enforced only at the nodes. Each prestressing tendon segment is assumed to have a constant prestress force. If these segment forces are known, whose determination is discussed later (Sec. 3.4), the effect of prestress is completely represented by a set of forces acting at the box beam element nodes.

3.3 Definition Of Tendon Profile

In order to determine the global X, Y, Z coordinates of the tendon points, the longitudinal profile of the tendon within the wall (top flange, bottom flange, left web or right web) in which it is located must be defined. If the tendon is located in the left web ($y = a/2$) or the right web ($y = - a/2$), the local y coordinates of the tendon points are already known from the geometry of the bridge, and hence the global X and Y coordinates can be

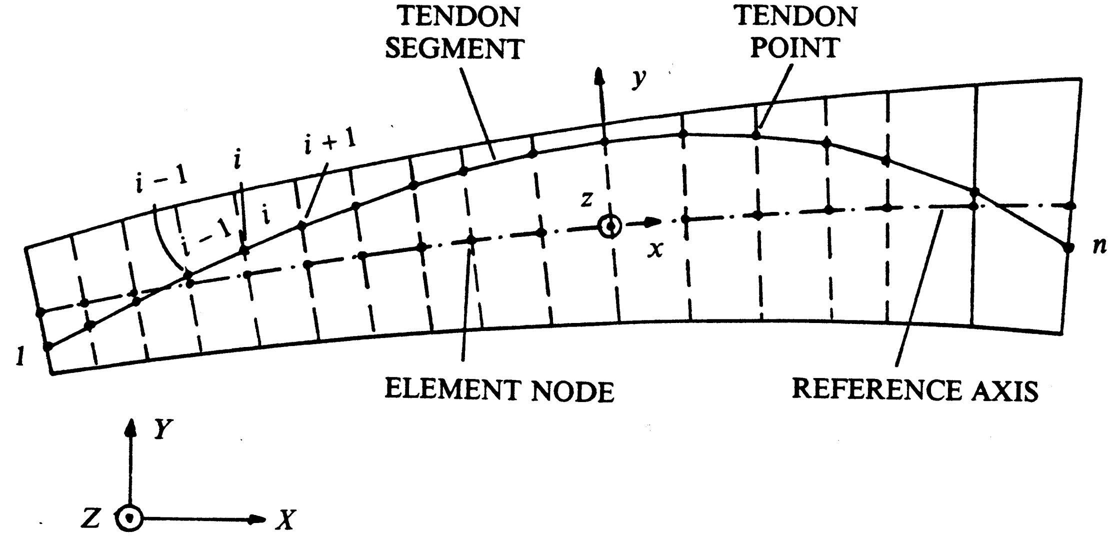

(a) PLAN OF TENDON IN TOP OR BOTTOM FLANGE

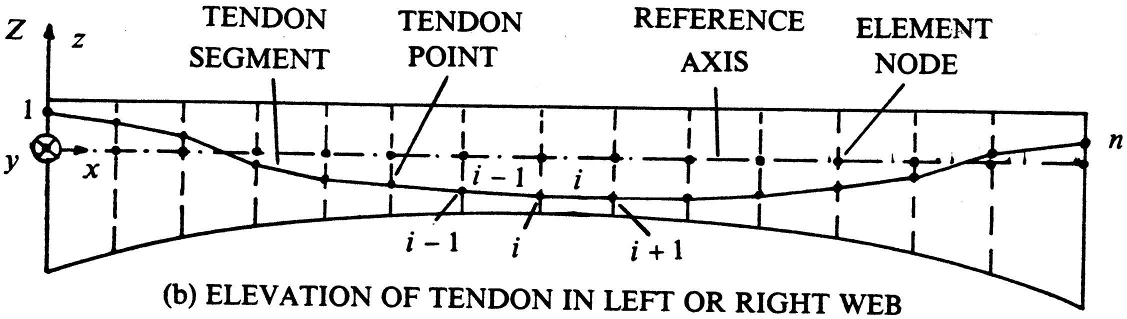

(b) ELEVATION OF TENDON IN LEFT OR RIGHT WEB

FIG. 3.1 TENDON DISCRETIZATION

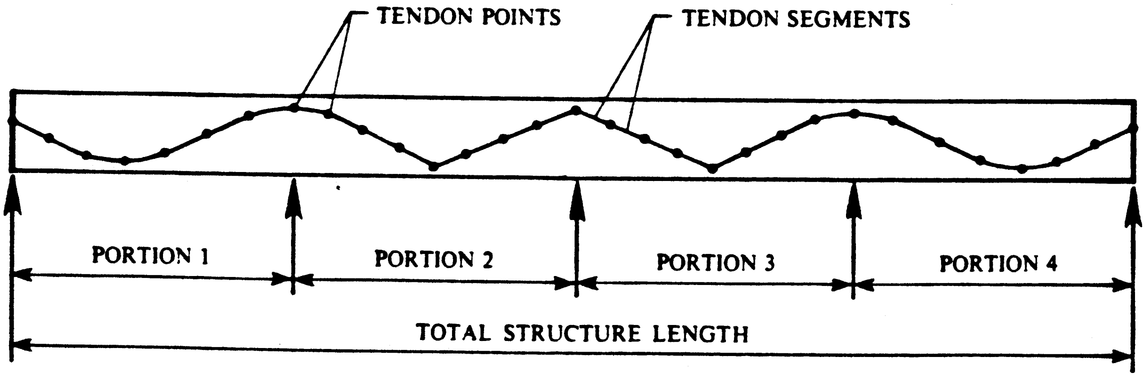

FIG. 3.2 DEFINITION OF TENDON PROFILE (From Ref. [8])

determined from Eq. (2.8). Then the tendon profile need to be specified only in terms of the global Z (or local z) coordinates of the tendon points (Fig. 3.1b). If the tendon is located in the top flange ($Z = b_1$) or the bottom flange ($Z = -b_2$), the Z coordinates of the tendon points are already known from the geometry of the bridge. Then the tendon profile need to be specified only in terms of the local y coordinates of the tendon points (Fig. 3.1a), which can be used in Eq. (2.8) to calculate the global X and Y coordinates. In either case, it is seen from Eq. (2.8) that the direction cosines X_0'/λ_0 and Y_0'/λ_0 of the element x axis must be known at the tendon point nodes. It was mentioned in Sec. 2.9, however, that in general at a node common to two box beam elements, the directions of the element x axis determined for the two adjacent elements will not be the same. The average direction is thus used in calculating the global X, Y coordinates of the tendon points from Eq. (2.8).

To specify tendon profiles, the length of the bridge spanned by the tendon is first divided into portions which usually correspond to the actual physical spans of the bridge between supports (Fig. 3.2). The ends of each portion correspond to tendon points and thus are required to be located at element nodes. Then the tendon profile in each portion is defined either directly or parametrically. In the direct definition, the ordinates of the tendon profile at the tendon points are specified directly. In the parametric definition, the tendon profile is generated as a series of parabolic and/or linear segments based on a few simple specified parameters. In either case, the actual tendon profile is discretized as a series of straight segments.

It would seem from Fig. 3.2 that portion 1 requires a considerably finer subdivision into segments than portion 2 to define the tendon geometry accurately. Care should however be taken in discretizing straight tendons into long segments, particularly in curved bridges where radial forces are distributed along the length of the tendon even when the tendon appears straight when viewed from some directions. In such cases, short segments should be used. The choice of the box beam element subdivision can thus be dictated by the tendon discretization.

3.3.1 Direct Definition Of Tendon Profile

The conceptually simplest approach for definition of tendon profiles is to directly specify the required y coordinates (for flanges) or z coordinates (for webs) of the n tendon points used for the discretization. However, in the general case of a curved nonprismatic bridge, this approach requires tremendous computational effort. For most typical tendon profiles, this task can be avoided by generating the tendon profile parametrically.

In some cases where nontypical tendon profiles are used, it may be necessary to directly specify the tendon geometry. With careful selection of tendon portions, and with use of parametric generation in portions where it is possible, direct specification of tendon geometry can be minimized.

3.3.2 Parametric Definition Of Tendon Profile

Prestressing tendon profiles in most concrete box girder bridges consist of combinations of parabolas "draped" between the supports. In special cases, other geometries may be used, which can generally be specified as combinations of several parabolic and/or straight segments. In the present study, generation of this type of tendon profile based on a minimum number of tendon geometry parameters is considered.

Let L be the length of one span or portion of the tendon. For a tendon located in one of the webs, this span length is measured along the line of intersection of the curved webs and the X-Y plane. For a tendon located in one of the flanges, the length L is measured along the curved centerline (mid-width line) of the flange. It should be noted that for webs, the span length is always measured along a line curved in the X-Y plane. But for flanges in a bridge with variable depth, the span length is measured along a line curved in space. The tendon profile within a span is then specified by means of the following parameters (Fig. 3.3):

YZLT - Local y (for flanges) or z (for webs) coordinate of tendon profile at left end of span.

YZLP - Local y (for flanges) or z (for webs) coordinate of tendon profile at point of

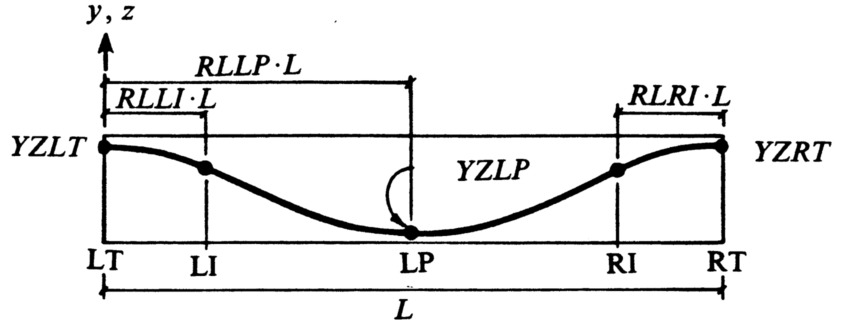

FIG. 3.3 DEFINITION OF TENDON GEOMETRY PARAMETERS (From Ref. [8])

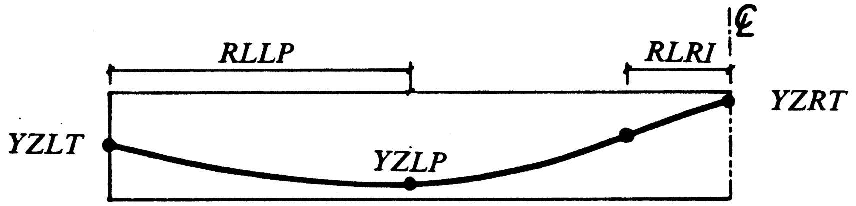

(a) CASE 1: LEFT SPAN OF TWO-SPAN BRIDGE (*RLLI* = 0)

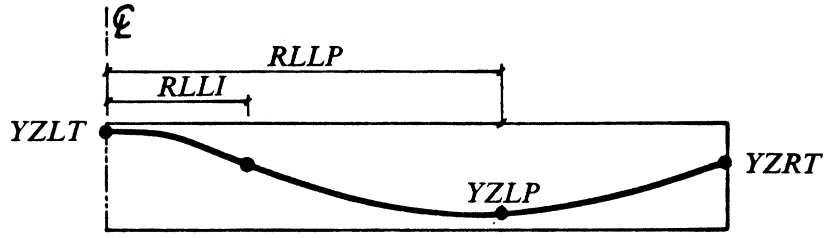

(b) CASE 2: RIGHT SPAN OF TWO-SPAN BRIDGE (*RLRI* = 0)

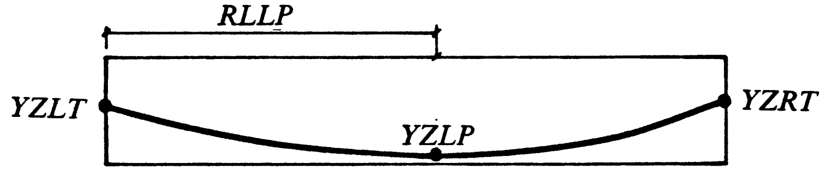

(c) CASE 3: SIMPLE SPAN (*RLLI* = *RLRI* = 0)

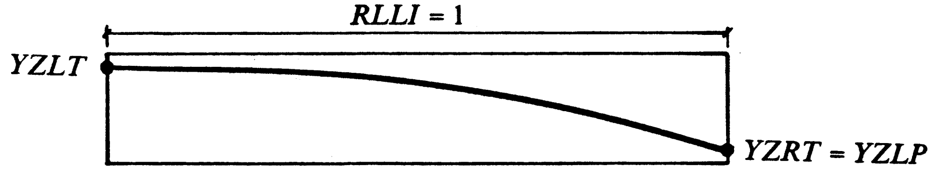

(d) CASE 4: CANTILEVER SPAN (*RLLI* = *RLLP* = 1, *RLRI* = 0)

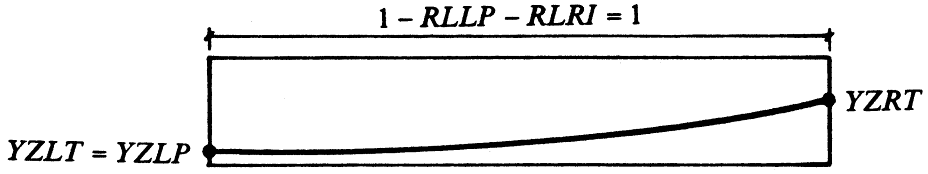

(e) CASE 5: CANTILEVER SPAN (*RLLI* = *RLLP* = *RLRI* =0)

FIG. 3.4 DEFINITION OF SOME TYPICAL TENDON GEOMETRIES (From Ref. [8])

zero tendon slope (low point).

YZRT - Local y (for flanges) or z (for webs) coordinate of tendon profile at right end of span.

RLLI - Fraction of span length from left end of span to left tendon inflection point.

RLLP - Fraction of span length from left end of span to point of zero tendon slope.

RLRI - Fraction of span length from right tendon inflection point to right end of span.

These parameters provide enough information to generate a profile made up of four parabolic segments with zero slope at locations LT, LP and RT, and tangent intersections at LI, LP and RI. The zero slopes at ends LT and RT guarantee tangent intersections with neighboring spans. For curved spans, this profile is developed onto the actual span geometry.

Many other tendon profiles can be generated by proper specification of the above parameters. Some typical tendon profiles commonly found in prestressed concrete box girder bridges that can be generated with the above parameters are shown in Fig. 3.4. In special cases, it is possible to use more than one portion to represent one physical span of the bridge. This technique allows generation of very complex tendon geometries.

3.4 Calculation Of Tendon Segment Forces

In the analysis for prestress, the variation of the stress in the prestressing steel along the tendon profile is an important consideration since the behavior of prestressed concrete box girders is largely dependent on the effective amount of prestress acting on them. The force distribution along the length of the tendon and the resulting equivalent nodal forces on the structure are influenced by short and long term prestress losses. Short term losses take place at the time of stressing and are due to two major causes : friction between the tendon and the duct during the jacking (stressing) operation, and slippage of the anchorage during transfer of the prestressing force from the jack to the anchorage assembly. Long term losses take place during the life of the structure and are due to creep and shrinkage of the concrete and relaxation of the prestressing steel. In the present study, long term losses are simply specified as a fraction of the initial prestress.

3.4.1 Friction Losses

Due to friction between the tendon and the duct during jacking, the tendon force at the jacking end is greater than the tendon force at some distance away from the jacking end (Fig. 3.5a). This friction loss can be considered in two parts : the length or wobble effect and the curvature effect. The length effect is the amount of friction loss that would occur in a straight tendon due to duct imperfections and construction practice, and is dependent on the coëfficient of friction, the length of the tendon, and the workmanship and method used in aligning the duct. The curvature effect results from the intended curvature of the tendons, and is dependent on the coefficient of friction and the total angle change between the jacking end and the point under consideration.

The tendon force P_s at a distance s from the jacking end is commonly expressed as

$$P_s = P_0 e^{-(\mu\alpha + Ks)} \tag{3.1}$$

where P_0 = tendon force at jacking end; μ = curvature friction coefficient; α = cumulative angle (in radians) by which the tangent to the tendon profile has changed between the jacking end and location s; K = wobble friction coefficient; s = distance along tendon from jacking end to point considered. The derivation of Eq. (3.1) can be found in most text books on prestressed concrete. The values of μ and K have been established by experiments and are summarized in [39, 40].

In the tendon discretization used in this study (Fig. 3.1), the angle changes are concentrated at the $(n - 2)$ interior tendon points, and the length is defined by the lengths of the $(n - 1)$ tendon segments. Thus the curvature losses are lumped at the tendon points and the wobble losses are distributed over each tendon segment (Fig. 3.5b). The friction loss expression in Eq. (3.1) must be reformulated in accordance with this approximation. The first

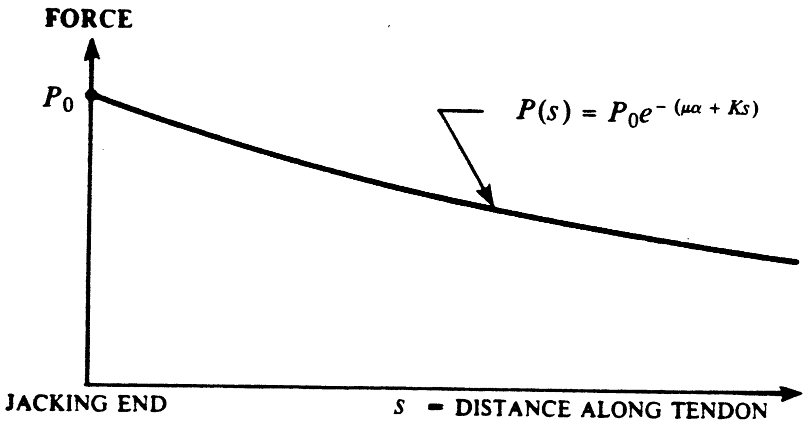

(a) ACTUAL TENDON FORCE PROFILE

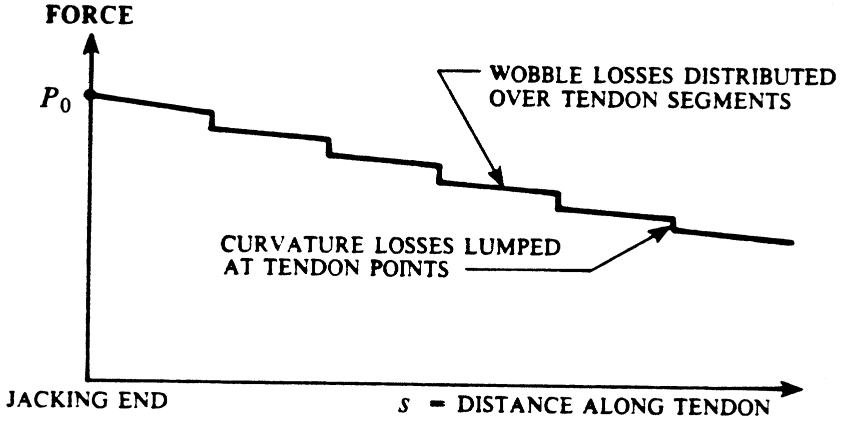

(b) DISCRETIZED TENDON FORCE PROFILE

FIG. 3.5 TENDON FORCE PROFILE UNDER JACKING (From Ref. [8])

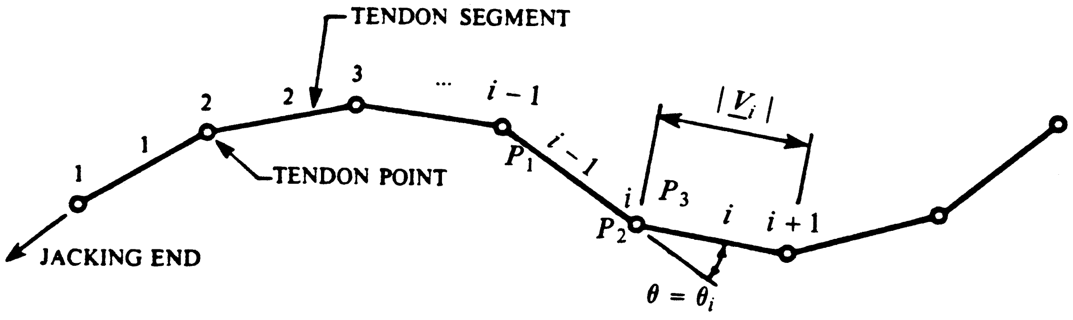

FIG. 3.6 CALCULATION OF FRICTION LOSSES (From Ref. [8])

step is to derive expressions for the length of each tendon segment and the angle change in space at each interior tendon point.

Define vectors $\underline{V}_{i-1}$ and $\underline{V}_i$ from tendon point i to $i - 1$ and from i to $i + 1$ respectively.

$$\underline{V}_{i-1} = \begin{Bmatrix} X_{i-1} - X_i \\ Y_{i-1} - Y_i \\ Z_{i-1} - Z_i \end{Bmatrix} \; ; \qquad \underline{V}_i = \begin{Bmatrix} X_{i+1} - X_i \\ Y_{i+1} - Y_i \\ Z_{i+1} - Z_i \end{Bmatrix} \tag{3.2}$$

where (X_i, Y_i, Z_i) are the global coordinates of tendon point i.

The angle θ_i in space between tendon segments i and $i - 1$ at tendon point i can be found from

$$\cos \theta_i = \frac{\underline{V}_{i-1} \cdot \underline{V}_i}{|\underline{V}_{i-1}| \; |\underline{V}_i|} \tag{3.3}$$

where the dot denotes scalar product of two vectors and $|\underline{V}_i|$ denotes the length of vector $\underline{V}_i$ and hence of segment i.

The force at each end of each tendon segment can be expressed in terms of these lengths and angle changes (Fig. 3.6). The force at one end of a segment in terms of the force at the other end is expressed as

$$P_2 = P_1 e^{-K|\underline{V}|} \tag{3.4}$$

while the force at one side of a tendon point in terms of the force at the other side is expressed as

$$P_3 = P_2 e^{-\mu\theta} \tag{3.5}$$

where the locations of P_1, P_2 and P_3 relative to the jacking end are shown in Fig. 3.6.

These expressions are evaluated for each tendon segment and each interior tendon point to arrive at the discretized tendon force profile during jacking shown in Fig. 3.5b.

3.4.2 Anchorage Slip Losses

Anchorage slip losses take place when the jacking force is transferred from the jack to the permanent tendon anchorage assembly. The anchorage assembly typically displaces up to 3/8 inch during this operation, resulting in a change in stress over a length of the tendon near the anchorage (Fig. 3.7).

The change in stress and the length over which it is effective can be derived from fundamental principles. If Δ_a is the anchorage slip and L_a is the length along the tendon affected by the anchorage slip,

$$\Delta_a = \int_0^{L_a} \Delta\epsilon \, ds \tag{3.6}$$

where $\Delta\epsilon$ is the decrease in the tendon strain due to anchorage slip. This results in the "mirror image" type tendon force change over the length L_a shown in Fig. 3.7.

A graphical interpretation of the fundamental principles may be taken in order to arrive at the computational approach used in this study. The area of region *ABC* of the tendon force diagram in Fig. 3.7 must equal the anchorage slip Δ_a multiplied by the axial rigidity $E_p A_p$ of the tendon.

$$\text{Area } (ABC) = E_p A_p \Delta_a \tag{3.7}$$

The tendon segments are scanned starting at the jacking end in order to locate point *C* in Fig. 3.7 that satisfies the above equality. After this point is located, all tendon forces between the jacking end and the point *C* are modified to reflect the "mirrored" profile.

3.4.3 Influence Of Stressing Procedure

In a real bridge structure, two different jacking procedures may be used for stressing the tendons : jacking from one of the two ends, or jacking from both ends. When the tendon is stressed from both ends, the controlling anchorage must be determined for each tendon segment (Fig. 3.8). The procedure used is as follows. First, the segment forces are determined under jacking at tendon end *A* as discussed in Secs. 3.4.1 and 3.4.2. Next, the

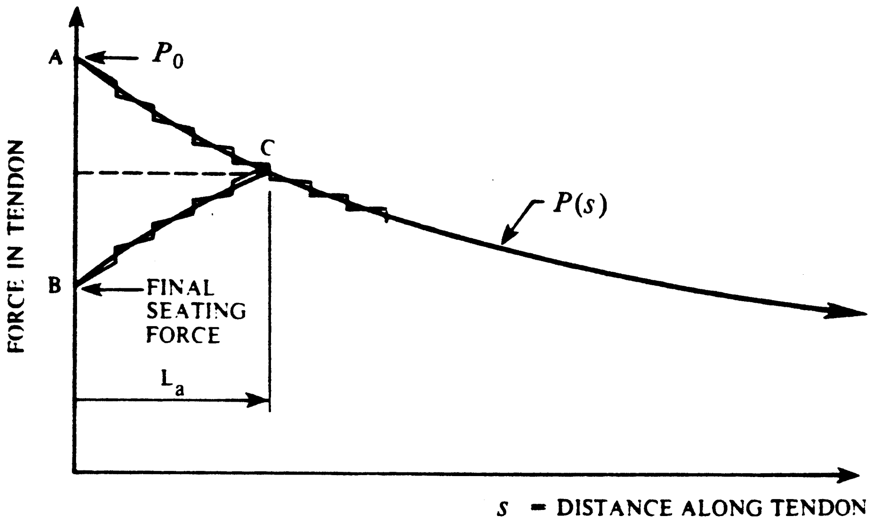

FIG. 3.7 ANCHORAGE SLIP LOSSES (From Ref. [8])

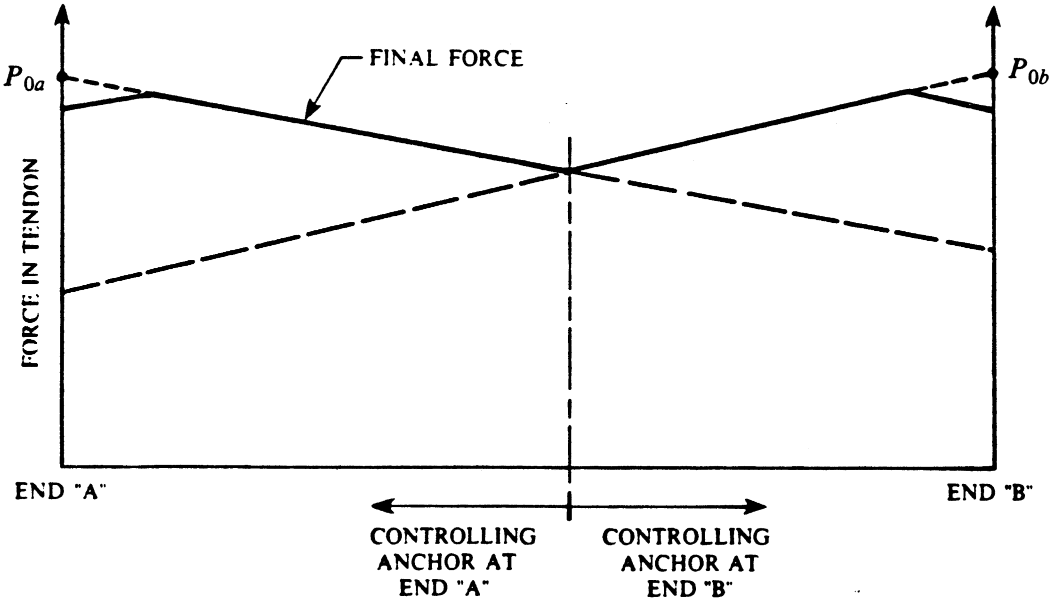

FIG. 3.8 JACKING FROM BOTH ENDS (From Ref. [8])

same procedure is initiated for jacking from tendon end *B*, but as each segment force is computed it is compared with the force already existing due to jacking from tendon end *A*. When it is found that the force already existing in the segment (from end *A* jacking) is higher than the force computed for end *B* jacking, the end *B* jacking procedure is terminated. This method closely approximates the physical situation in the actual tendon.

3.4.4 Final Tendon Forces

After the force is computed at each end of each tendon segment, an average force is computed in each tendon segment which is then used for computing the equivalent nodal loads. One of two methods can be used for computing this average force. Method *A* is applicable to tendons with smooth profiles, while method *B* is applicable to harped tendons with concentrated angle changes. The differences in computed forces from the two methods are generally small and have the greatest influence near the anchorages.

Consider a tendon with a smooth arbitrarily curved profile (Fig. 3.9). The actual tendon force profile is a smooth curve (Fig. 3.9b). The computed tendon force profile (Fig. 3.9c) has curvature friction losses lumped at the tendon points and wobble friction losses distributed over the tendon segments. The best estimate of the actual tendon force profile from this computed force profile is found by connecting the plotted average forces at the tendon points with straight lines (Fig. 3.9c). The constant force in each tendon segment can then be found by averaging the segment end force values from this smoothed profile (Fig. 3.9d). This approach is used in averaging method *A* and is recommended for smoothly curved tendon profiles.

Consider a harped tendon with concentrated angle changes in its profile (Fig. 3.10). The actual tendon force profile is the same as the computed force profile, it is piece-wise linear with steps at the harp points (Fig. 3.10b). The constant force in each tendon segment can be found by averaging the segment end force values from this unsmoothed force profile (Fig. 3.10c). This approach is used in averaging method *B* and is recommended for harped tendon profiles.

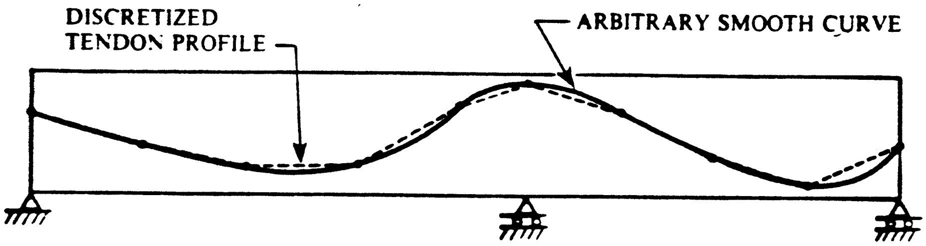

(a) STRUCTURE AND TENDON GEOMETRY

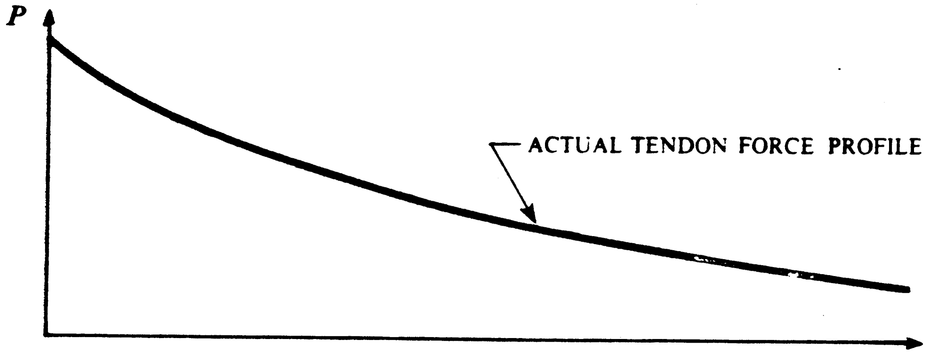

(b) ACTUAL TENDON FORCE PROFILE

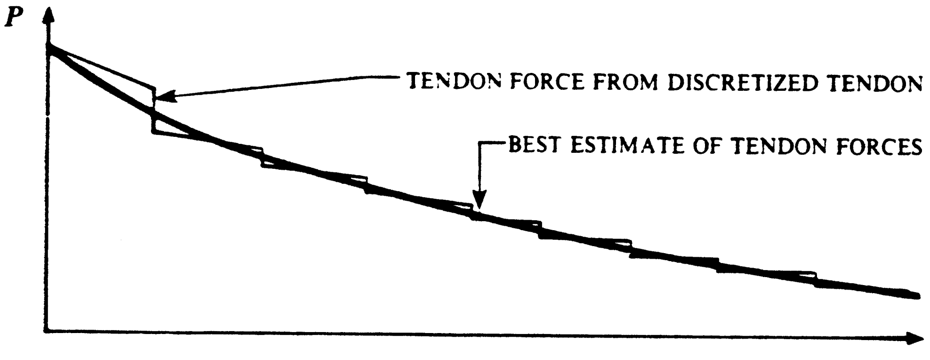

(c) BEST ESTIMATE OF TENDON FORCE PROFILE

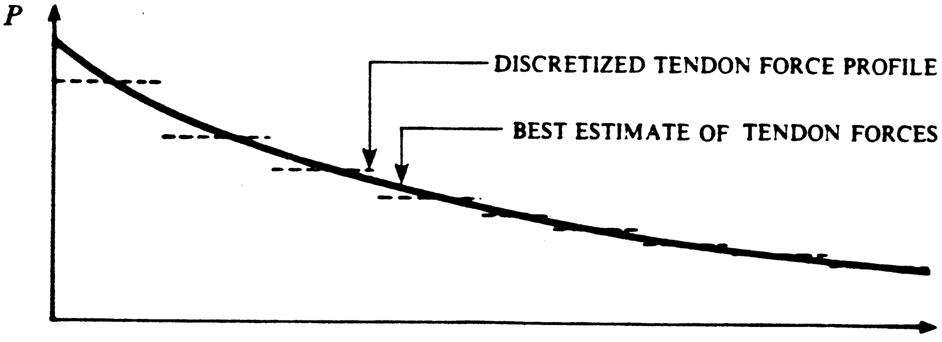

(d) DISCRETIZED FORCE PROFILE USED IN ANALYSIS

FIG. 3.9 SEGMENT FORCES IN A SMOOTHLY CURVED TENDON (From Ref. [8])

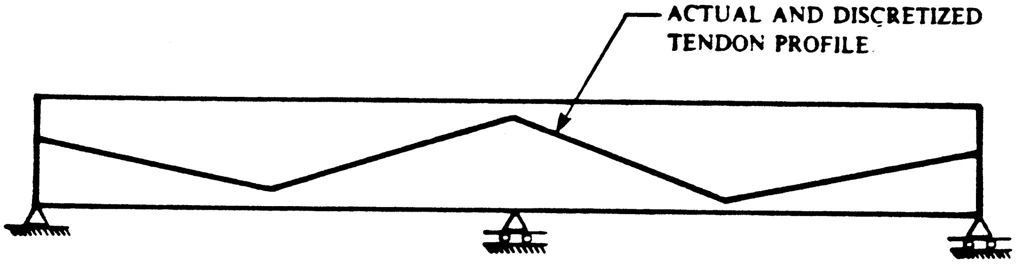

(a) STRUCTURE AND TENDON GEOMETRY

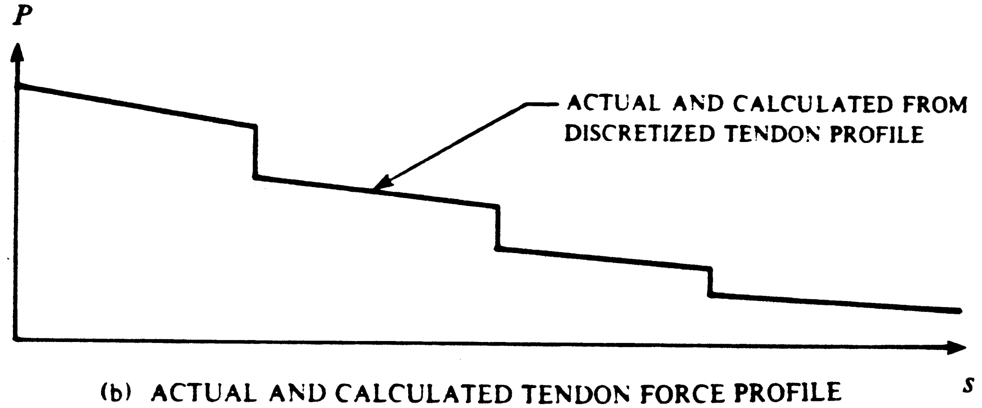

(b) ACTUAL AND CALCULATED TENDON FORCE PROFILE

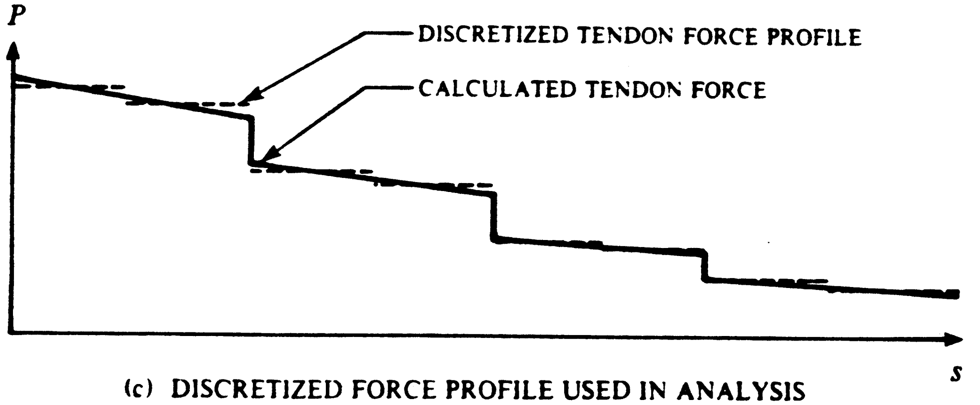

(c) DISCRETIZED FORCE PROFILE USED IN ANALYSIS

FIG. 3.10 SEGMENT FORCES IN A HARPED TENDON (From Ref. [8])

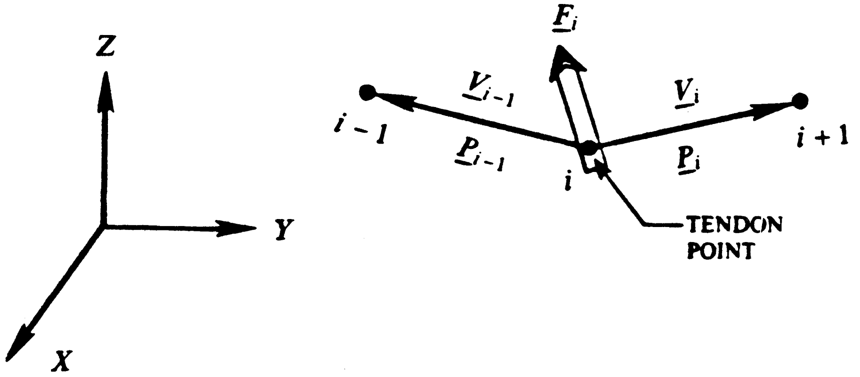

FIG. 3.11 EQUIVALENT LOAD AT TENDON POINT (From Ref. [8])

3.5 Equivalent Nodal Force Vector

Once the forces in all the tendon segments are known, the resultant forces acting on the structure at each tendon point can be found. Consider tendon point i where tendon segments $i - 1$ and i are connected (Fig. 3.11). The tendon force vectors $\underline{P}_{i-1}$ and $\underline{P}_i$ at tendon point i are given by

$$\underline{P}_{i-1} = P_{i-1}\frac{\underline{V}_{i-1}}{|\underline{V}_{i-1}|} \tag{3.8a}$$

$$\underline{P}_{i} = P_{i}\frac{\underline{V}_{i}}{|\underline{V}_{i}|} \tag{3.8b}$$

where P_{i-1} and P_i are the magnitudes of the tendon forces in segments $i - 1$ and i respectively, and $\underline{V}_{i-1}$ and $\underline{V}_i$ are as defined in Eq. (3.2).

Then the resultant force vector $\underline{F}_i$ acting on the structure at tendon point i is obtained from simple vector addition as

$$\underline{F}_i = \underline{P}_{i-1} + \underline{P}_i \tag{3.9}$$

Omitting the subscript, the force vector $\underline{F}$ of Eq. (3.9) is referred to the fixed global coordinate system (X, Y, Z) with components

$$\underline{F} = \begin{Bmatrix} F_X \\ F_Y \\ F_Z \end{Bmatrix} \tag{3.10}$$

With the y and z eccentricities of the tendon points with respect to the box beam element axis known, the eight generalized nodal force components at the tendon point nodes corresponding to the force vector $\underline{F}$ can be calculated using Eq. (2.55). These generalized nodal force components are assembled for the entire structure to give the equivalent prestressing nodal force vector for the structure.

4. LINEAR ELASTIC ANALYSIS - NUMERICAL EXAMPLES

The theory presented in Chapters 2 and 3 has been incorporated into a computer program LAPBOX for linear elastic analysis of curved nonprismatic reinforced and prestressed concrete box girders. The details of the computer program LAPBOX are given in Chapter 7. Input guidelines and sample input data are given in Appendices A and B.

In order to demonstrate the applicability of the proposed method and the capabilities of the computer program LAPBOX, five numerical examples of linear elastic analysis are presented in this chapter. The relative accuracy of the proposed method is examined by comparison with other analytical and/or experimental results. The last example illustrates how some of the capabilities of the program LAPBOX can be used to analyze practical box girder bridges of complex geometries.

4.1 Example 4.1 - Straight Simply Supported Box Girder

For the first example, a straight simply supported box girder is analyzed. The purpose of this example is to demonstrate the capability of the thin-walled box beam element to capture the torsional and distortional effects inherent in single-cell box girders. The results from LAPBOX are compared with a folded plate harmonic analysis based on the theory of elasticity (Sec. 1.2.1).

4.1.1 Structure Details and Analytical Modelling

The structure geometry and loading are shown in Fig. 4.1. The structure is simply supported and torsionally restrained at the two ends. Diaphragms, rigid in their planes but perfectly flexible perpendicular to their planes, are assumed at the supported ends. Thus the two end cross sections are fixed against transverse distortion but are free to warp longitudinally. Modulus of elasticity E = 432,000 kip/ft^2 and Poisson's ratio $\nu = 0$ are assumed.

The loading consists of a vertical force couple at midspan (Fig. 4.1a). In terms of the equivalent loads for the box beam element, this loading translates into a torque and a transverse distortional moment of 3 kip·ft each. While the torsional component can only be equilibrated at the end supports, the effects of the self-equilibrating distortional component should damp out away from midspan. To investigte this effect, two box cross sections of different wall thicknesses, t = 0.1 ft and 0.5 ft, are considered (Fig. 4.1b). The dead load of the structure is not included in the analyses.

Making use of the symmetry of the structure and the loading about midspan, only half the span is analyzed with LAPBOX using 10 box beam elements of equal length. The harmonic folded plate analysis results used for comparison were obtained by Seible [17] using a computer program MULTPL [1, 4, 5]. A total of 100 odd harmonics were employed and a longitudinal uniform distribution of the concentrated forces over 1 ft was assumed.

4.1.2 Presentation and Discussion of Results

Due to the nature of the loading considered, all displacement and stress results are antisymmetric about the $X-Z$ plane. The longitudinal distribution of the vertical displacements along one of the webs is shown in Fig. 4.2a. The vertical web displacements for LAPBOX were obtained by summing the contributions from the twist and the transverse distortion of the cross sections. In Fig. 4.2b, the longitudinal bending moments along one girder are shown. Each girder is assumed to be comprised of one web and half the width of the top and bottom flanges. The girder bending moments for LAPBOX were obtained from the warping bimoment output. It may be noted that the warping stresses are associated only with the distortional component of the loading since theoretically there is no torsional warping for a square cross section. Close agreement exists between the harmonic folded plate solution and the thin-walled box beam model. The effect of the wall thickness can be seen in Fig. 4.2b where the longitudinal girder moments damp out more quickly for the box with the thicker walls.

The longitudinal distributions of the web shears and the transverse bending moments per unit length at the four corners of the box have been plotted in Fig. 4.3. The web shears,

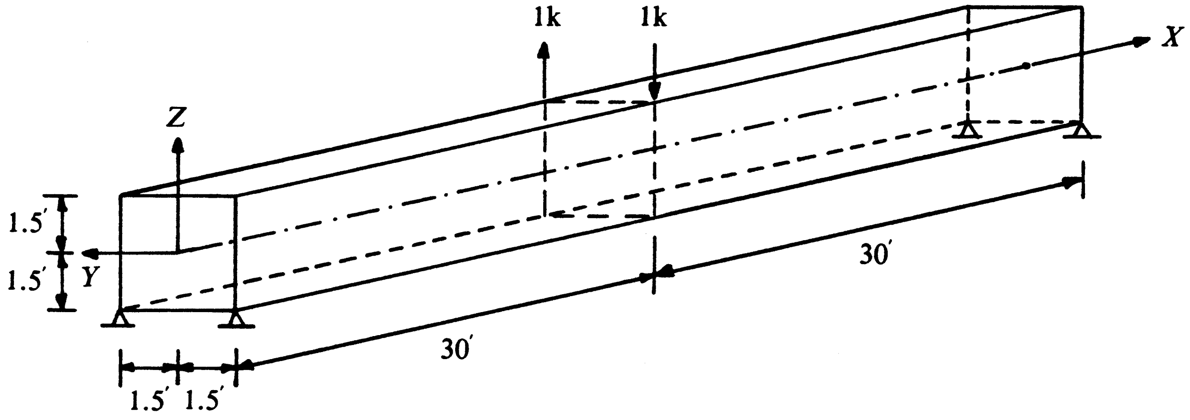

(a) ISOMETRIC VIEW

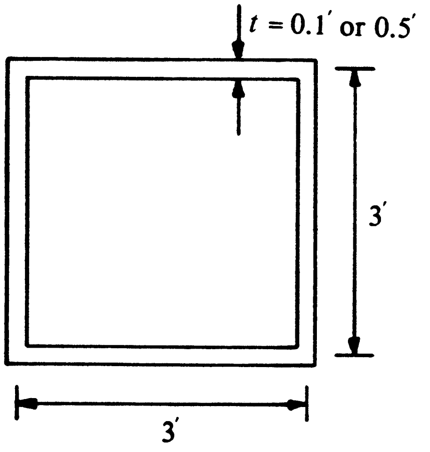

(b) CROSS SECTION

FIG. 4.1 EXAMPLE 4.1 - STRAIGHT SIMPLY SUPPORTED BOX GIRDER

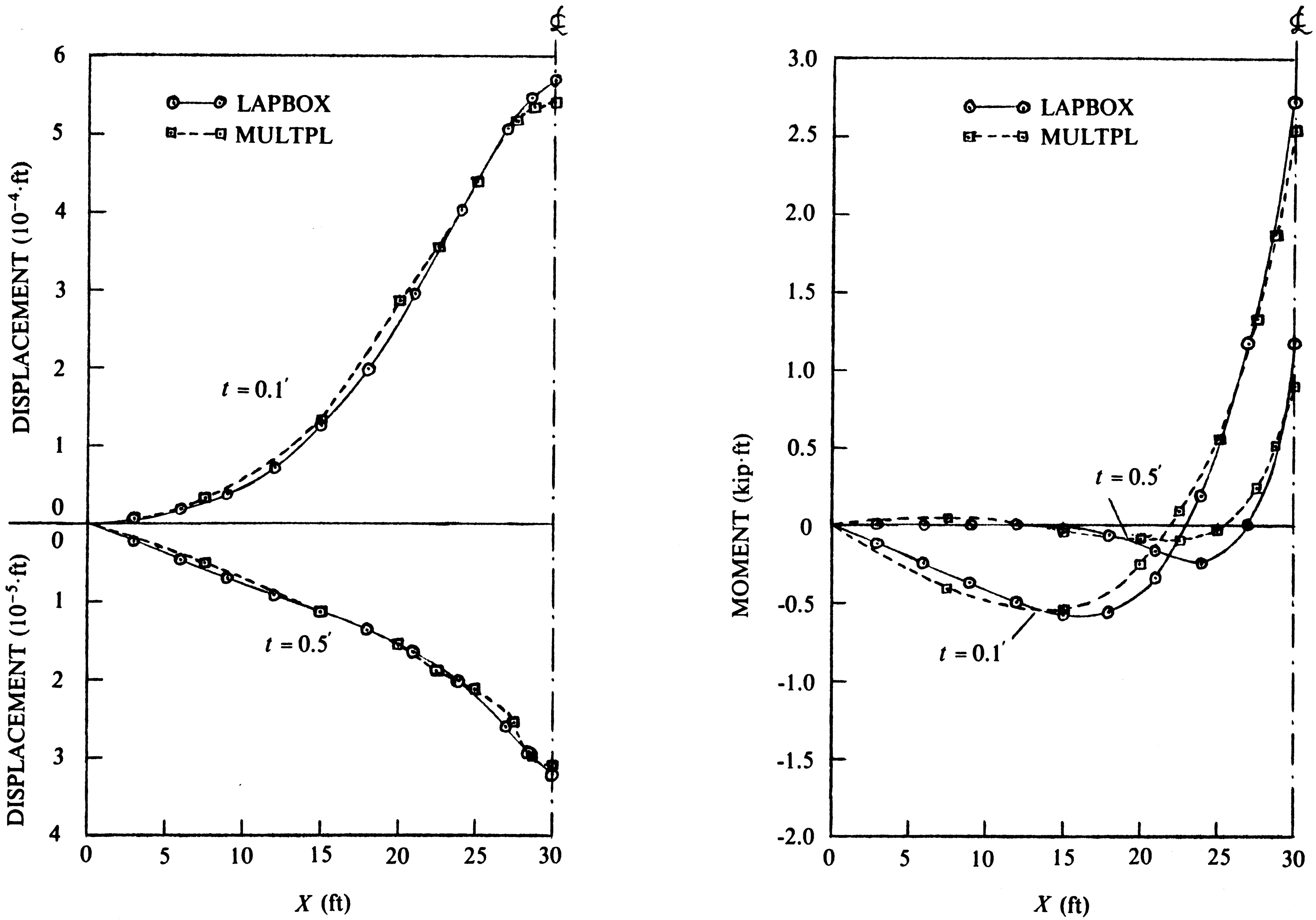

(a) VERTICAL WEB DISPLACEMENTS

(b) LONGITUDINAL GIRDER MOMENTS

FIG. 4.2 EXAMPLE 4.1 - LONGITUDINAL DISTRIBUTIONS OF VERTICAL WEB DISPLACEMENTS AND LONGITUDINAL GIRDER MOMENTS

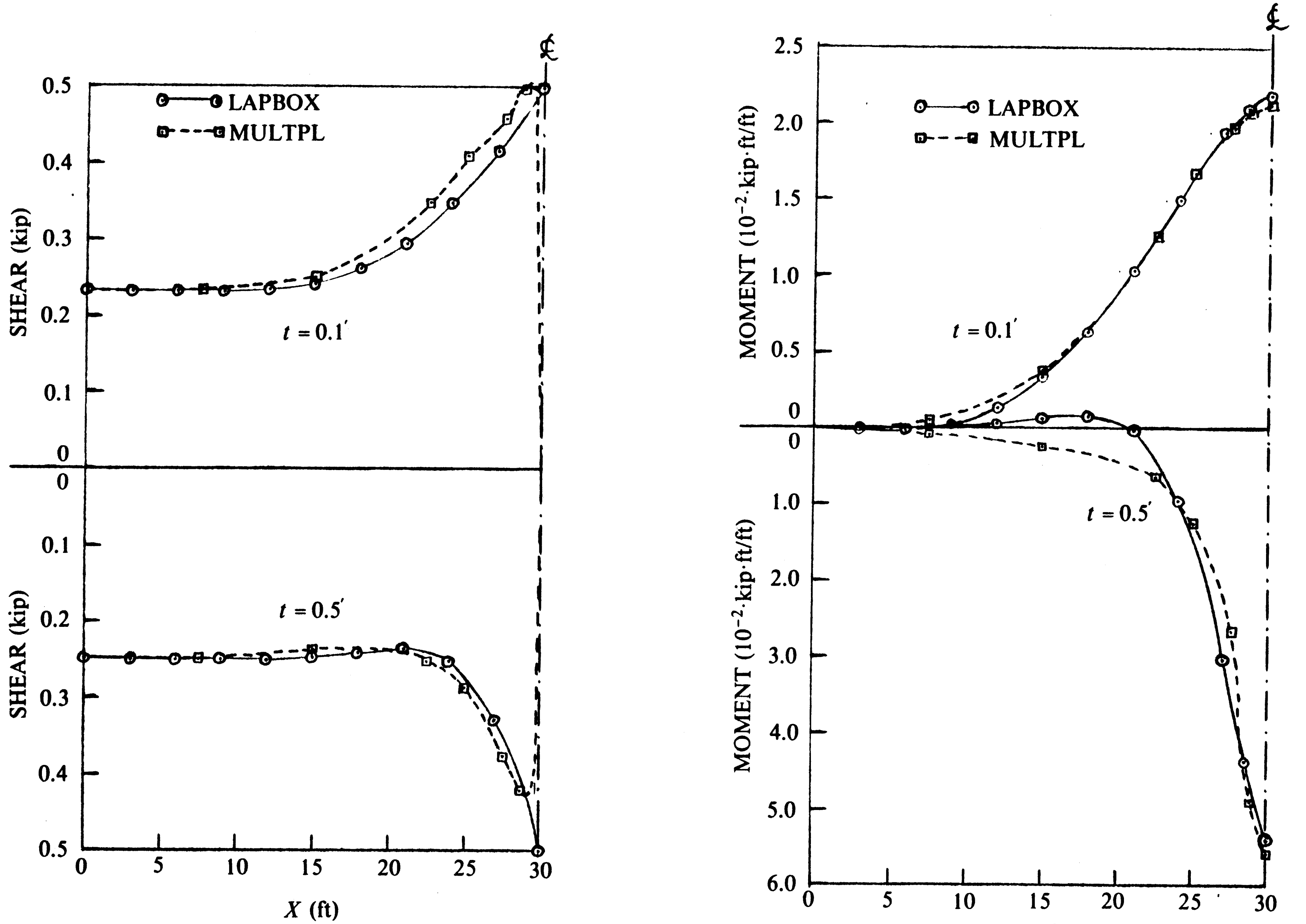

(a) WEB SHEARS

(b) TRANSVERSE BENDING MOMENTS

FIG. 4.3 EXAMPLE 4.1 - LONGITUDINAL DISTRIBUTIONS OF WEB SHEARS AND TRANSVERSE BENDING MOMENTS

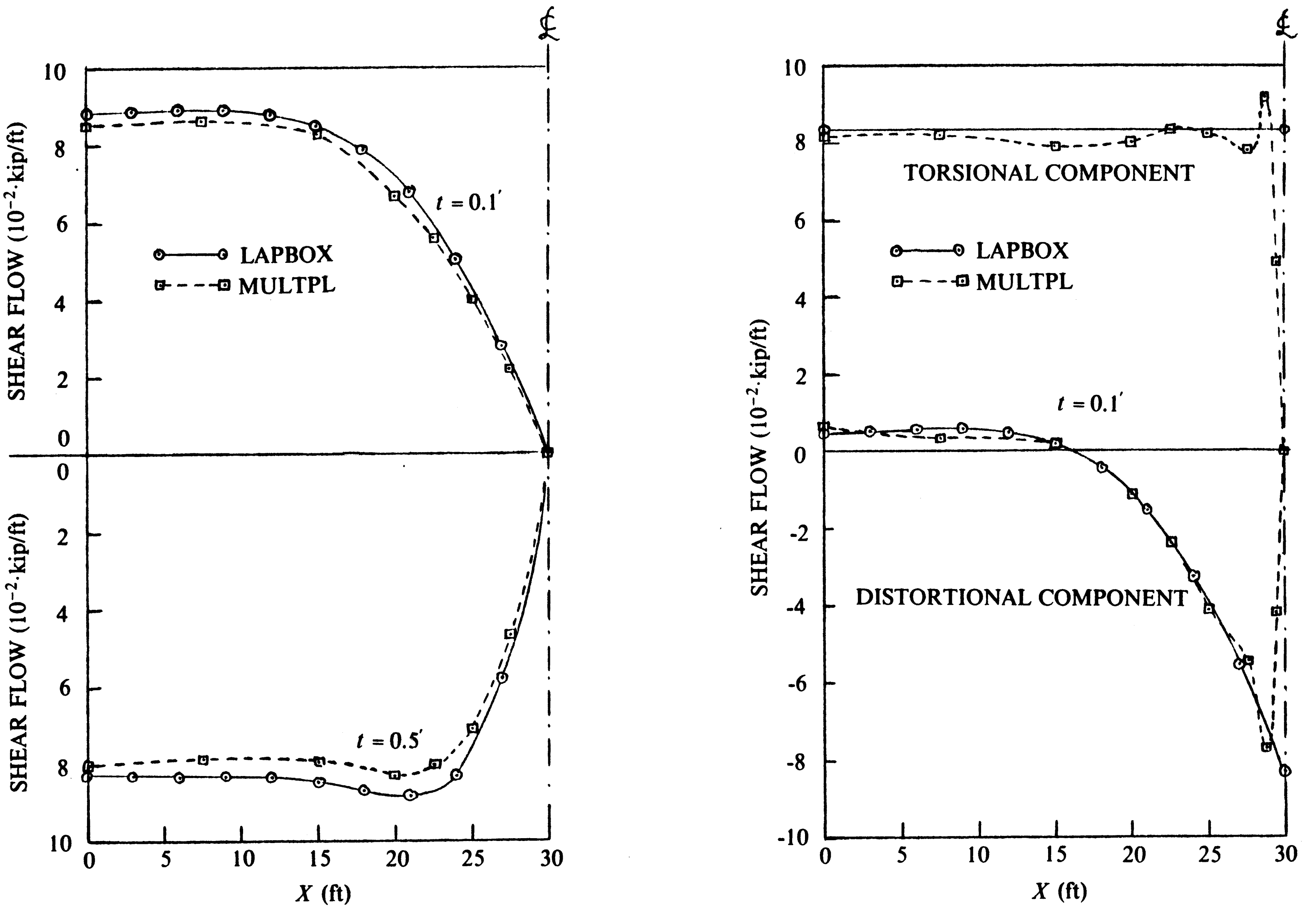

(a) SHEAR FLOW IN FLANGES

(b) TORSIONAL AND DISTORTIONAL COMPONENTS OF SHEAR FLOW

FIG. 4.4 EXAMPLE 4.1 - LONGITUDINAL DISTRIBUTIONS OF SHEAR FLOW IN TOP AND BOTTOM FLANGES

which were obtained by superposing the torsional and distortional shear components, are highest near midspan. Near the supports, the effect of the distortional loading damps out, and the web shears are primarily due to the torsional loading. Again, if allowance is made for the fact that in LAPBOX the loads were concentrated at midspan while in MULTPL the loads were distributed over a small length, the agreement between the two methods of analysis can be considered very good.

Fig. 4.4 shows the longitudinal distributions of shear flow in the top and the bottom flanges. While Fig. 4.4a depicts the shear flow for the two wall thicknesses, a separation of the total shear flow into its torsional and distortional components is shown in Fig. 4.4b for the wall thickness of $t = 0.1$ ft only. The distortional component of the shear damps out quickly towards the supports, while the torsional component is as expected virtually constant over the span. The present method (LAPBOX) is again seen to capture the torsional and distortional behavior of the box accurately.

4.2 Example 4.2 - Curved Simply Supported Box Girder

The next example is a simply supported box girder circularly curved in plan (Fig. 4.5). The capability of the proposed method to analyze curved box girders is demonstrated through this example. Comparisons are made with the finite strip method (Sec. 1.2.2).

The overall dimensions of the structure (Fig. 4.5) are the same as those considered in Example 4.1 (Fig. 4.1). The axis of the girder is however curved now with a radius of curvature $R = 38.2$ ft. Only one wall thickness of $t = 0.1$ ft is considered. The box girder is again simply supported and restrained against twist and transverse distortion at the two ends. No warping restraint is provided anywhere. Modulus of elasticity $E = 432{,}000$ kip/ft^2 and Poisson's ratio $\nu = 0$ are again assumed.

The loading consists of a vertical concentrated load of 1 kip at midspan (Fig. 4.5c). Dead load is not included. Two different load cases corresponding to two different transverse positions of the concentrated load are considered:

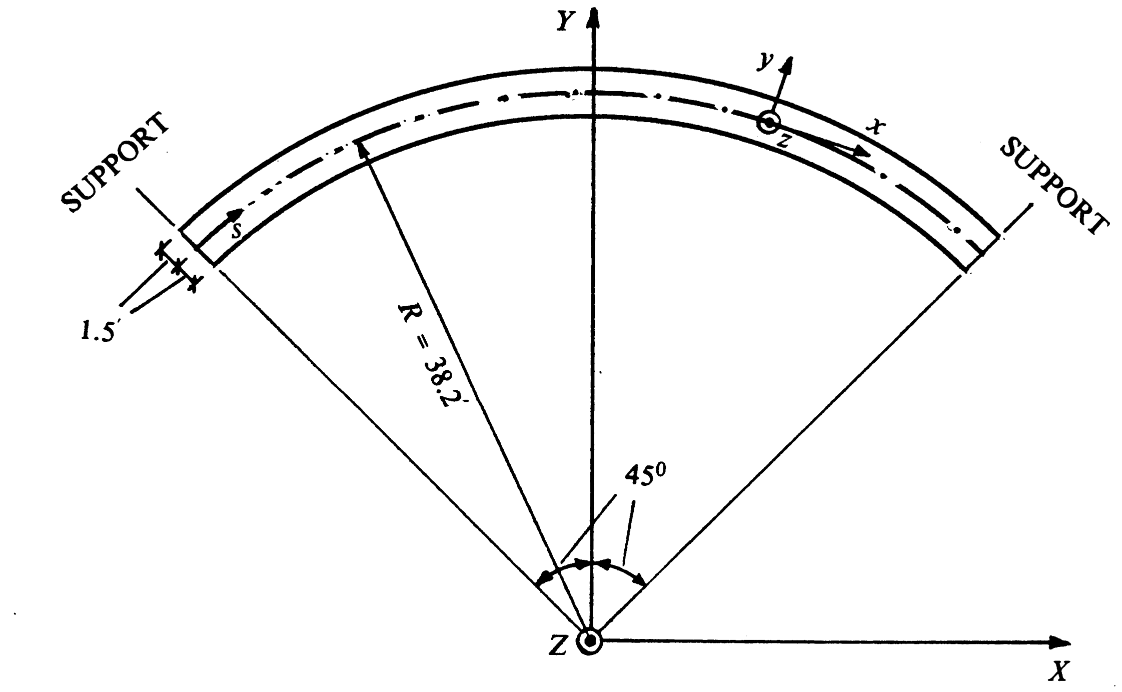

(a) PLAN

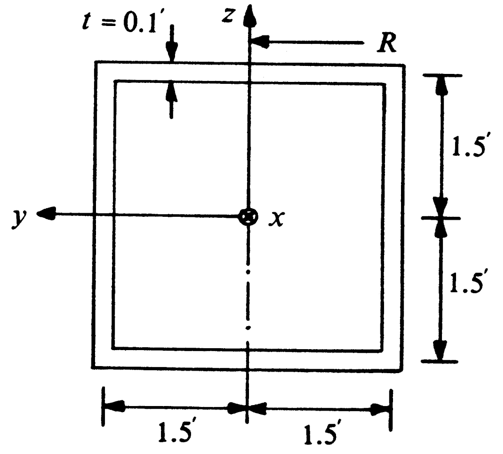

(b) CROSS SECTION

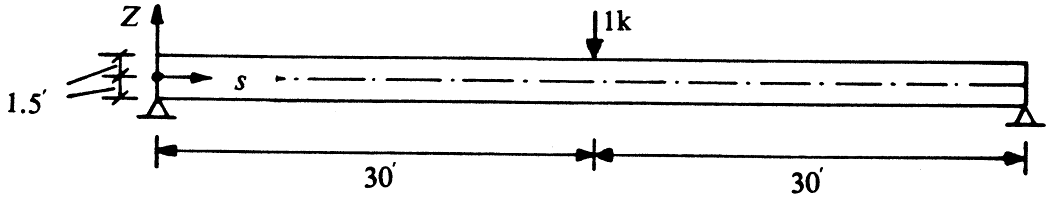

(c) LONGITUDINAL SECTION ALONG CENTERLINE

FIG. 4.5 EXAMPLE 4.2 - CURVED SIMPLY SUPPORTED BOX GIRDER

TABLE 4.1 EXAMPLE 4.2 - VERTICAL WEB DISPLACEMENTS

LOAD CASE	SECTION LOCATION *s* (ft)	INNER WEB DISPLACEMENTS		OUTER WEB DISPLACEMENTS	
		LAPBOX (ft)	CURDI4 (ft)	LAPBOX (ft)	CURDI4 (ft)
INNER WEB LOADING	7.5; 52.5	0.0087	0.0087	0.0089	0.0089
	15; 45	0.0163	0.0163	0.0165	0.0165
	22.5; 37.5	0.0217	0.0216	0.0217	0.0217
	30	0.0237	0.0237	0.0235	0.0235
OUTER WEB LOADING	7.5; 52.5	0.0089	0.0089	0.0092	0.0092
	15; 45	0.0166	0.0165	0.0170	0.0170
	22.5; 37.5	0.0217	0.0217	0.0223	0.0223
	30	0.0235	0.0235	0.0243	0.0243

TABLE 4.2 EXAMPLE 4.2 - LONGITUDINAL GIRDER MOMENTS

LOAD CASE	SECTION LOCATION *s* (ft)	INNER GIRDER MOMENTS		OUTER GIRDER MOMENTS	
		LAPBOX (ft)	CURDI4 (ft)	LAPBOX (ft)	CURDI4 (ft)
INNER WEB LOADING	7.5; 52.5	2.51 (49.6%)	2.52 (49.7%)	2.55 (50.4%)	2.55 (50.3%)
	15; 45	5.09 (51.3%)	5.09 (51.2%)	4.84 (48.7%)	4.85 (48.8%)
	22.5; 37.5	8.05 (55.8%)	8.04 (55.7%)	6.37 (44.2%)	6.40 (44.3%)
	30	11.79 (64.3%)	11.66 (63.7%)	6.56 (35.7%)	6.65 (36.3%)
OUTER WEB LOADING	7.5; 52.5	3.03 (55.4%)	3.03 (55.3%)	2.44 (44.6%)	2.45 (44.7%)
	15; 45	6.10 (56.7%)	6.09 (56.6%)	4.65 (43.3%)	4.67 (43.4%)
	22.5; 37.5	8.83 (56.6%)	8.82 (56.5%)	6.76 (43.4%)	6.79 (43.5%)
	30	9.92 (50.0%)	9.95 (50.2%)	9.93 (50.0%)	9.85 (49.8%)

(1) The concentrated load is positioned over the inner web at midspan.

(2) The concentrated load is positioned over the outer web at midspan.

Due to symmetry, only half the structure is analyzed using 16 curved box beam elements of equal length. For the finite strip analysis, a computer program CURDI4, developed recently by Scordelis et al. [8], is used. The cross section is modelled with 16 finite strips. 100 odd harmonics are included in the analysis.

Since the single concentrated load constitutes primarily a flexural loading, only the vertical web displacements and the longitudinal girder moments are compared in Tables 4.1 and 4.2 respectively. The percentage distribution of the total section moment to each girder is also shown in Table 4.2. Excellent agreement between the box beam element results (LAPBOX) and the finite strip results (CURDI4) can be noted in Tables 4.1 and 4.2 for both load cases. The different responses of the girder to the different load cases are captured accurately by the box beam model. The somewhat larger discrepancies between LAPBOX and CURDI4 results for the girder moments at midspan are due to the error in the approximation of the concentrated load by a finite number (100) of harmonic components in the CURDI4 analysis.

4.3 Example 4.3 - Tapered Box Girder

The accuracy of the proposed method in predicting the response of nonprismatic structures is examined by analyzing a tapered box girder model studied both analytically and experimentally by Kristek [41].

The geometry of the PVC-N model is shown in Fig. 4.6a,b. The cross section has constant width and wall thickness, but its height varies parabolically. The girder is fixed into the supports. Thus in the LAPBOX analysis, all eight displacement degrees of freedom are restrained at the supports. Kristek [41] did not report the material properties. Modulus of elasticity of $E = 500{,}000$ psi and Poisson's ratio of $\nu = 0.33$, which are believed to be representative of PVC-N models, are used.

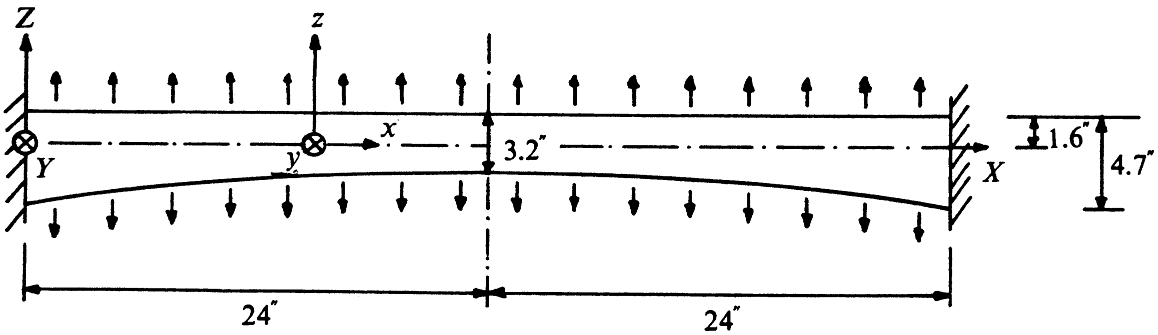

(a) ELEVATION

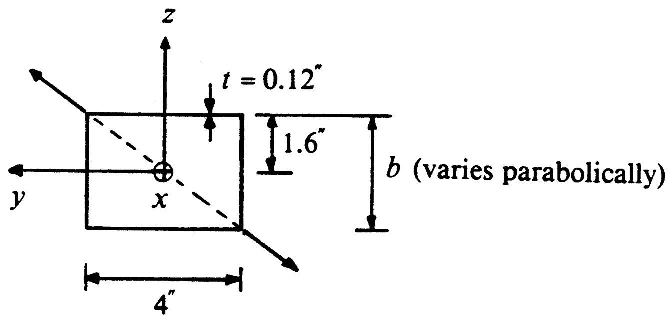

(b) CROSS SECTION

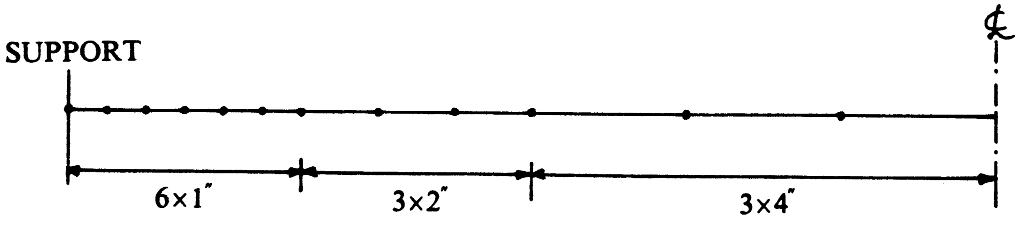

(c) ELEMENT SUBDIVISION

FIG. 4.6 EXAMPLE 4.3 - TAPERED BOX GIRDER

The girder is loaded in the direction of the diagonal of the cross sections by a pair of distributed loads which has a constant vertical component of 0.7 lb/in. (Fig. 4.6a,b). This loading represents a uniform transverse distortional moment per unit length along the span of the girder.

Again because of symmetry only half the span is analyzed using 12 nonprismatic box beam elements. The element subdivision is shown in Fig. 4.6c. A finer mesh is used near the supports where the rate of variation of the cross sectional depth is higher.

In Table 4.3, the vertical displacements at one of the corners of the box cross section obtained from LAPBOX are compared with the analytical and experimental values reported by Kristek [41]. Agreement is generally found to be good, in particular between LAPBOX and Kristek's analytical method.

4.4 Example 4.4 - Curved Simply Supported Prestressed Concrete Bridge

This example illustrates the analysis of a curved prestressed concrete box girder bridge of practical dimensions with LAPBOX. The accuracy of the box beam element in predicting the response under prestressing and dead load is examined. The results obtained with LAPBOX are compared with those obtained with the computer program CURDI4 [8], which is based on finite strip theory.

4.4.1 Structure Details and Analytical Modelling

The geometry of the bridge is shown in Fig. 4.7. It is a typical two-lane bridge with a total top deck width of 30 ft and a single simple span of 162 ft measured along the centerline (s direction). The bridge is circularly curved in plan with a radius of $R = 162$ ft to the centerline. Simple support conditions are assumed at the ends where rigid diaphragms prevent the transverse distortion of the cross sections. It is further assumed that the end diaphragms are perfectly flexible perpendicular to their planes so that they do not restrain longitudinal warping.

TABLE 4.3 EXAMPLE 4.3 - VERTICAL DISPLACEMENTS AT BOX CORNERS

SECTION LOCATION X (in.)	EXPERIMENTAL DISPLACEMENTS FROM Ref. [41] (in.)	ANALYTICAL DISPLACEMENTS FROM Ref. [41] (in.)	ANALYTICAL DISPLACEMENTS FROM LAPBOX (in.)
4; 44	0.00075	0.00068	0.00108
8; 40	0.00351	0.00332	0.00313
12; 36	0.00556	0.00541	0.00542
16; 32	0.00741	0.00739	0.00740
20; 28	0.00859	0.00869	0.00871
24	0.00907	0.00916	0.00916

TABLE 4.4 EXAMPLE 4.4 - VERTICAL CENTERLINE DISPLACEMENTS

SECTION LOCATION s (ft)	DISPLACEMENTS DUE TO DEAD LOAD		DISPLACEMENTS DUE TO PRESTRESSING	
	LAPBOX (ft)	CURDI4 (ft)	LAPBOX (ft)	CURDI4 (ft)
8.1; 153.9	-0.1082	-0.1103	0.0742	0.0734
16.2; 145.8	-0.2134	-0.2169	0.1461	0.1453
24.3; 137.7	-0.3128	-0.3176	0.2138	0.2131
32.4; 129.6	-0.4039	-0.4099	0.2758	0.2752
40.5; 121.5	-0.4848	-0.4918	0.3304	0.3299
48.6; 113.4	-0.5535	-0.5613	0.3764	0.3761
56.7; 105.3	-0.6085	-0.6170	0.4130	0.4128
64.8; 97.2	-0.6486	-0.6576	0.4396	0.4393
72.9; 89.1	-0.6731	-0.6823	0.4556	0.4554
81	-0.6813	-0.6906	0.4609	0.4608

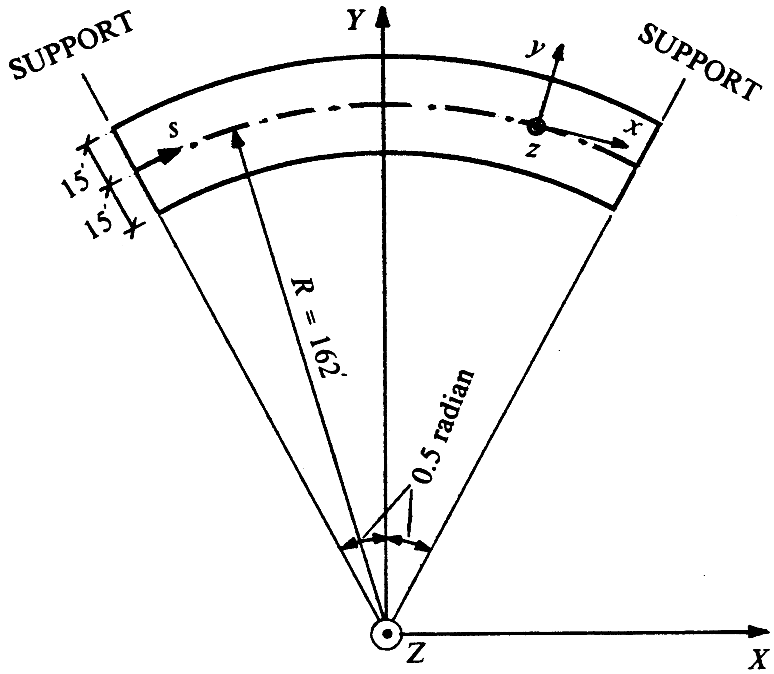

(a) PLAN

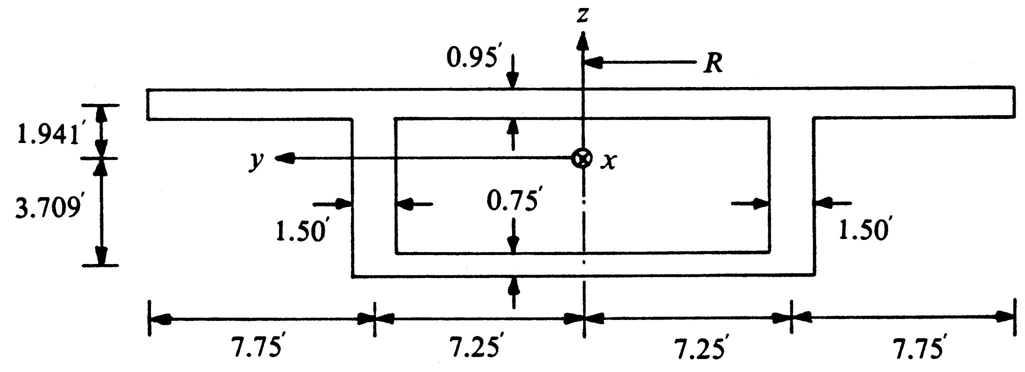

(b) CROSS SECTION

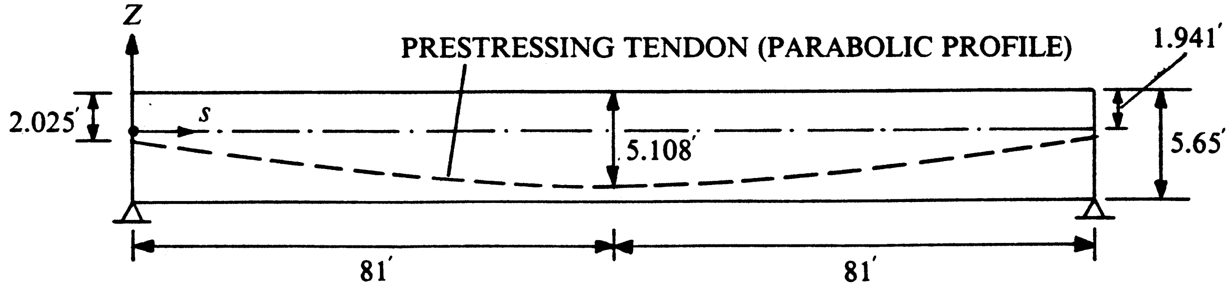

(c) LONGITUDINAL SECTION ALONG CENTERLINE

FIG. 4.7 EXAMPLE 4.4 - CURVED SIMPLY SUPPORTED PRESTRESSED CONCRETE BRIDGE

The following concrete material properties are assumed : modulus of elasticity E = 518,400 kip/ft^2; Poisson's ratio $\nu = 0.15$. A unit weight density of $w = 155$ pcf is used for the dead load calculations.

The prestressing in the bridge consists of two tendons in the longitudinal direction, one in each web. The cross sectional area of each tendon is $A_p = 0.157$ ft^2. Each tendon has a vertical parabolic profile (Fig. 4.7c) measured along the curved webs. The tendons are stressed symmetrically from both ends of the bridge with a jacking force of 4266 kip per web. Wobble friction coefficient of $K = 0.0002$/ft, curvature friction coefficient of $\mu = 0.25$/radian, and anchorage slip of $\Delta_a = 0.0156$ ft at each jacking end are assumed. The modulus of elasticity of the prestressing steel is taken as $E_p = 4{,}032{,}000$ kip/ft^2. Long term losses are not considered.

The bridge is analyzed for two different load cases :

(1) Dead Load

(2) Prestressing

Due to symmetry of the structure and the loadings, only half the bridge is analyzed using 20 curved box beam elements of equal length. The origin of local x, y, z axes of the cross section (Fig. 4.7b) is taken at the centroid which is located at a depth of 1.941 ft from the mid-thickness of the top flange. The dead load and prestressing are represented by equivalent loads at the box beam element nodes generated automatically within the program LAPBOX.

32 finite strips are used in modelling the cross section for the CURDI4 [8] analysis. 100 odd harmonics are employed to represent the variations in the longitudinal direction.

4.4.2 Presentation and Discussion of Results

Some of the results obtained for the two load cases from LAPBOX and CURDI4 are summarized in Table 4.4 and Figs. 4.8 and 4.9. The vertical centerline displacements at various locations s along the span are given in Table 4.4. The CURDI4 results in Table 4.4

TABLE 4.5 EXAMPLE 4.5 - PRESTRESSING TENDON DATA

TENDON NO.	JACKING FORCE (kip)	LOCATION OF END A		LOCATION OF END B		LOCATION(S) OF ZERO TENDON SLOPE	
		s (ft)	*z* (ft)	*s* (ft)	*z* (ft)	*s* (ft)	*z* (ft)
1, 2	300	0	-2.470	120	-4.044	60	-6.357
3, 4	700	420	-3.646	560	-2.410	490	-6.278
5, 6	600	180	-2.473	340	-2.463	260	-3.500
7, 8	2500	80	-3.343	200	-1.710	120; 160	-0.500
9, 10	3000	320	-1.840	440	-3.283	360; 400	-0.500
11, 12	1000	40	-2.911	240	-1.710	80; 200	-0.500
13, 14	1250	280	-1.710	480	-4.089	320; 440	-0.500

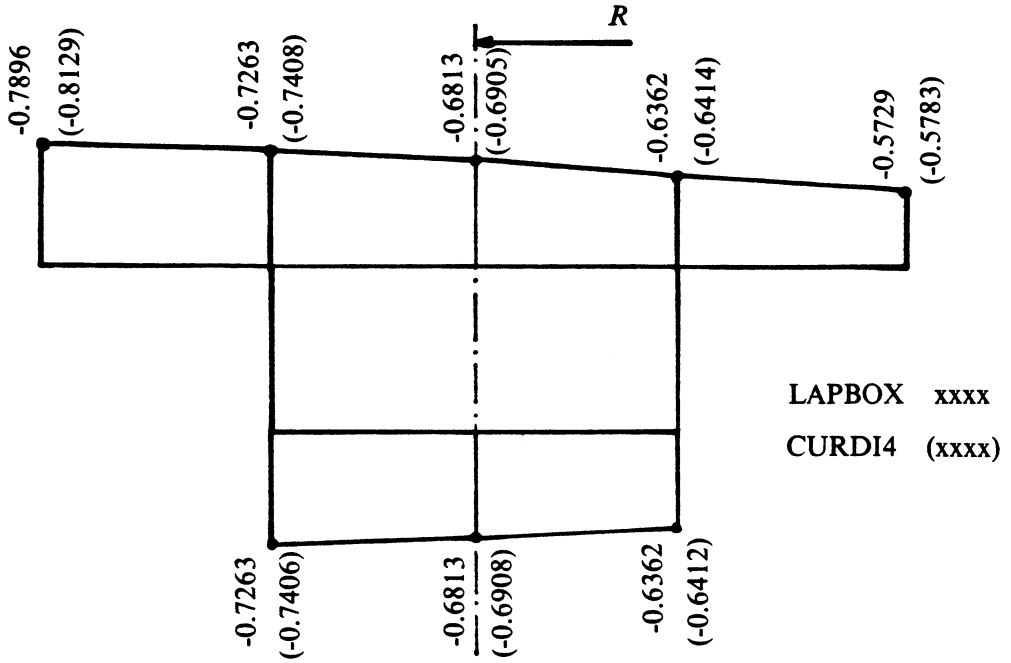

(a) DEAD LOAD

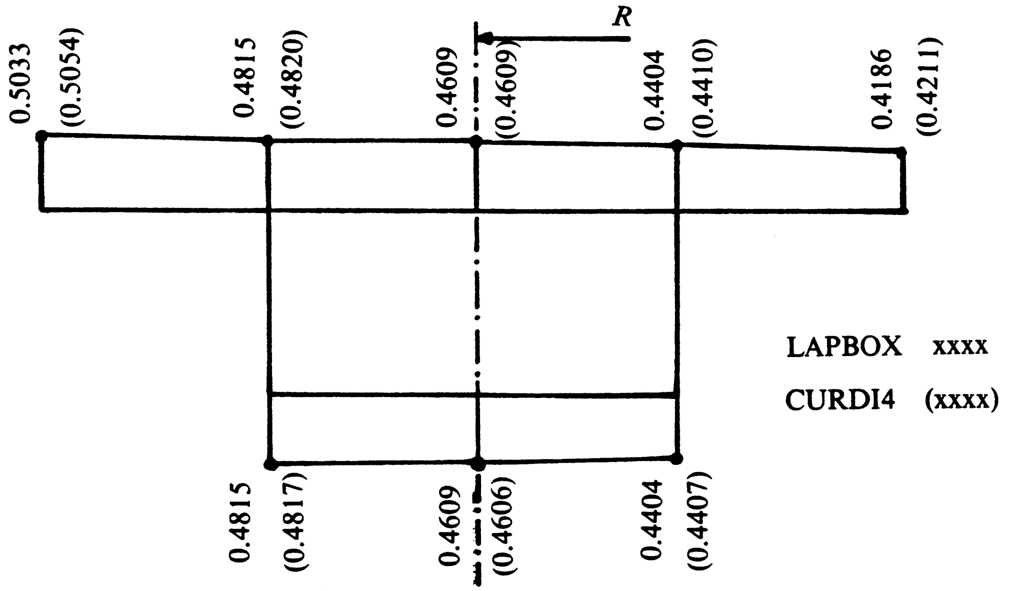

(b) PRESTRESSING

FIG. 4.8 EXAMPLE 4.4 - TRANSVERSE DISTRIBUTIONS OF VERTICAL DISPLACEMENTS (ft) AT MIDSPAN

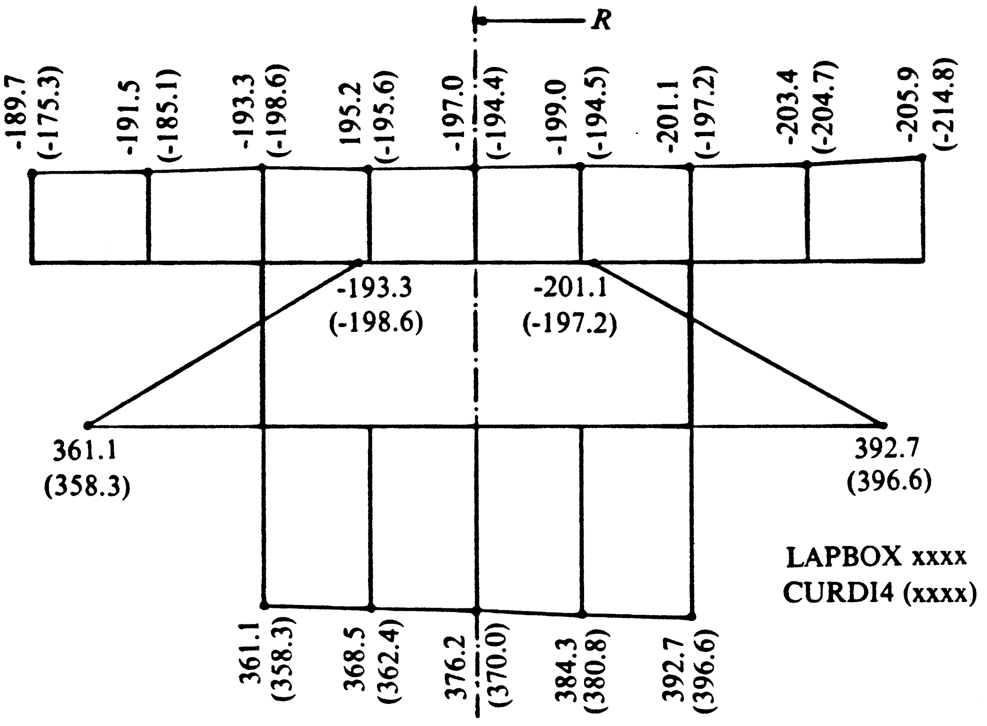

(a) DEAD LOAD

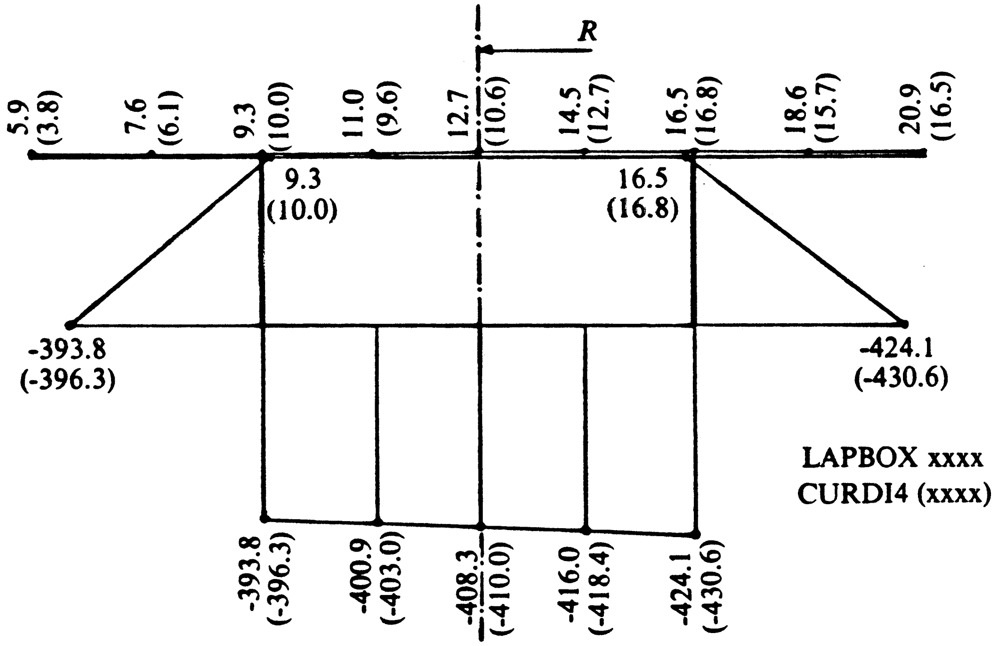

(b) PRESTRESSING

FIG. 4.9 EXAMPLE 4.4 - TRANSVERSE DISTRIBUTIONS OF LONGITUDINAL NORMAL STRESSES σ_x (kip/ft^2) NEAR MIDSPAN were obtained by averaging the centerline displacements of the top and bottom flanges which were practically the same (Fig. 4.8). The vertical displacements in the direction of the Z axis (Fig. 4.7) are taken to be positive. Good agreement between the results from the LAPBOX and CURDI4 analyses can be noted in Table 4.4. In fact, for the prestressing load case, the agreement is excellent. The smaller displacements predicted by LAPBOX for the dead load case are primarily due to the fact that the box beam elements cannot capture the transverse bending of the side cantilevers due to their self-weight. But the differences are small.

The transverse distributions of the vertical displacements at midspan for dead load and prestressing are shown in Fig. 4.8. As expected, the outer web deflects more than the inner web. The agreement between LAPBOX and CURDI4 is again found to be good particularly for the prestressing load case.

In LAPBOX, internal stresses and integrated force resultants are recovered at the two Gauss sections of each element which are considered to be the optimal locations (Sec. 2.11). The transverse distributions of the longitudinal normal stresses at the Gauss section nearest to midspan (s = 80.144 ft) are shown in Fig. 4.9. Tensile stresses are taken to be positive in Fig. 4.9. The longitudinal normal stresses are approximately constant across the width of the bridge indicating primarily flexural behavior. For the dead load case, elementary beam theory gives stresses of -195.5 kip/ft^2 and 373.5 kip/ft^2 at the top and bottom flanges respectively. The LAPBOX results agree quite well with the CURDI4 results obtained at the same cross section, the largest discrepancies being at the tips of the side cantilevers.

For the dead load analysis, the following support reactions were obtained from LAPBOX.

Distortional moment (M_d) = – 351.8 kip·ft

Vertical force (V_z) = 707.2 kip

Torque (M_x) = 10,881.4 kip·ft

The distortional moment is a generalized force quantity and does not represent a statical force resultant. The vertical force and the torque obtained from LAPBOX, on the other hand, are exactly the same as those obtained by applying statics to the circularly curved bridge which is statically determinate for symmetric loadings. This indicates that the geometry of a circularly curved bridge can be modelled very accurately as a series of parabolically curved box beam elements.

It is of interest to compare the integrated force resultants at Gauss sections obtained from LAPBOX with the corresponding values required to satisfy equilibrium. Two Gauss sections, one nearest to the support (s = 0.856 ft) and the other nearest to midspan (s = 80.144 ft) are considered. The following values were obtained from LAPBOX for the dead load case.

At Gauss section nearest to support:

Bending moment (M_y) = 659.7 kip·ft

Vertical shear (V_z) = 699.7 kip

Torque (M_x) = 10,877.0 kip·ft

At Gauss section nearest to midspan:

Bending moment (M_y) = 32,026.8 kip·ft

Vertical shear (V_z) = 7.5 kip

Torque (M_x) = 171.8 kip·ft

The section forces obtained by considering equilibrium under the applied dead load and the support reactions are found to be the same as the LAPBOX results above. This justifies the selection of the Gauss sections for recovery of stresses in the box beam element.

4.5 Example 4.5 - Three-Span Curved Nonprismatic Prestressed Concrete Bridge

This example is used to demonstrate the versatility of the proposed method in analyzing a complex prestressed concrete box girder bridge of curved plan geometry and variable cross section. The input data for the computer program LAPBOX used to obtain the results of this example are given in Appendix B. A careful study of this example along with the input data should be very useful to a potential user of LAPBOX.

4.5.1 Structure Details and Analytical Modelling

A hypothetical three-span continuous prestressed concrete box girder bridge (Fig. 4.10) is analyzed. In plan (Fig. 4.10a), the bridge has a straight span of 140 ft between supports S1 and S2, and two circularly curved spans of 240 ft between supports S2 and S3, and 180 ft between supports S3 and S4. The radius of the circularly curved spans is $R = 500$ ft to the centerline. For convenience, a coordinate s is defined along the centerline with its origin at S1 and directed towards S4. At each of the four supports of the bridge, vertical movement, twist and transverse distortion of the cross section are prevented.

The cross section of the bridge is shown in Fig. 4.10b. The width of both the box section and the cantilever flanges vary linearly along the length of the bridge. The depth of the box section and the thickness of the bottom flange also vary. The thickness of the webs as well as the thickness of the top flange and the cantilever flanges are however constant along the length. The following equations define the variation of the cross sectional dimensions a, f, b, t_b (all in ft) in terms of the s coordinate.

$$a = 12 + s/100\,, \quad \text{for } 0 \le s \le 560'$$

$$f = 4 + 9s/2800\,, \quad \text{for } 0 \le s \le 560'$$

$$\begin{aligned} b &= 6 + s/70\,, && \text{for } 0 \le s \le 140' \\ &= 52/3 - s/15\,, && \text{for } 140' \le s \le 200' \\ &= 4\,, && \text{for } 200' \le s \le 320' \\ &= -\,52/3 + s/15\,, && \text{for } 320' \le s \le 380' \\ &= 110/9 - s/90\,, && \text{for } 380' \le s \le 560' \end{aligned}$$

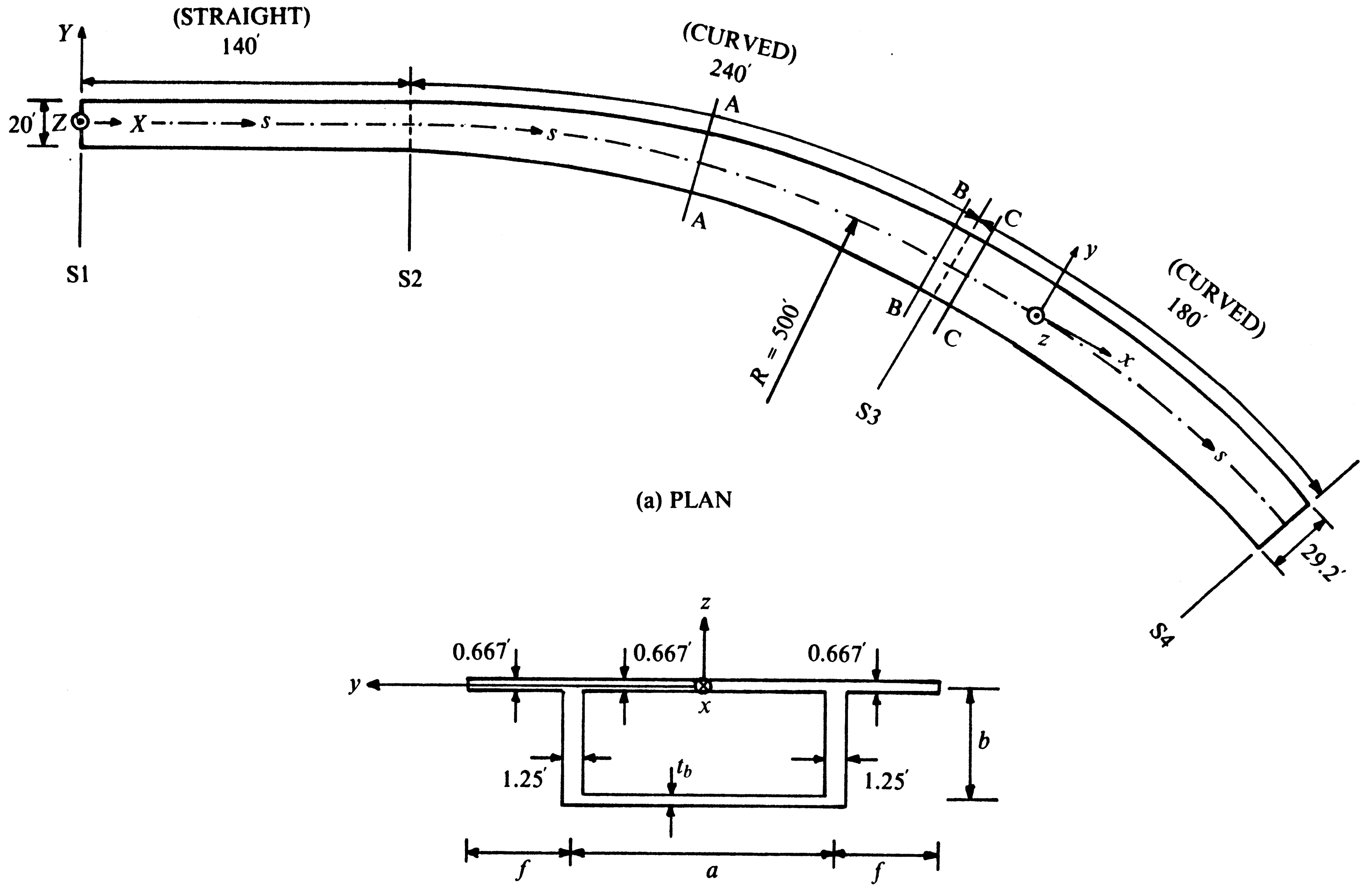

(a) PLAN

a, f, b, t_b vary

(b) CROSS SECTION

FIG. 4.10 EXAMPLE 4.5 - THREE-SPAN CURVED NONPRISMATIC PRESTRESSED CONCRETE BRIDGE

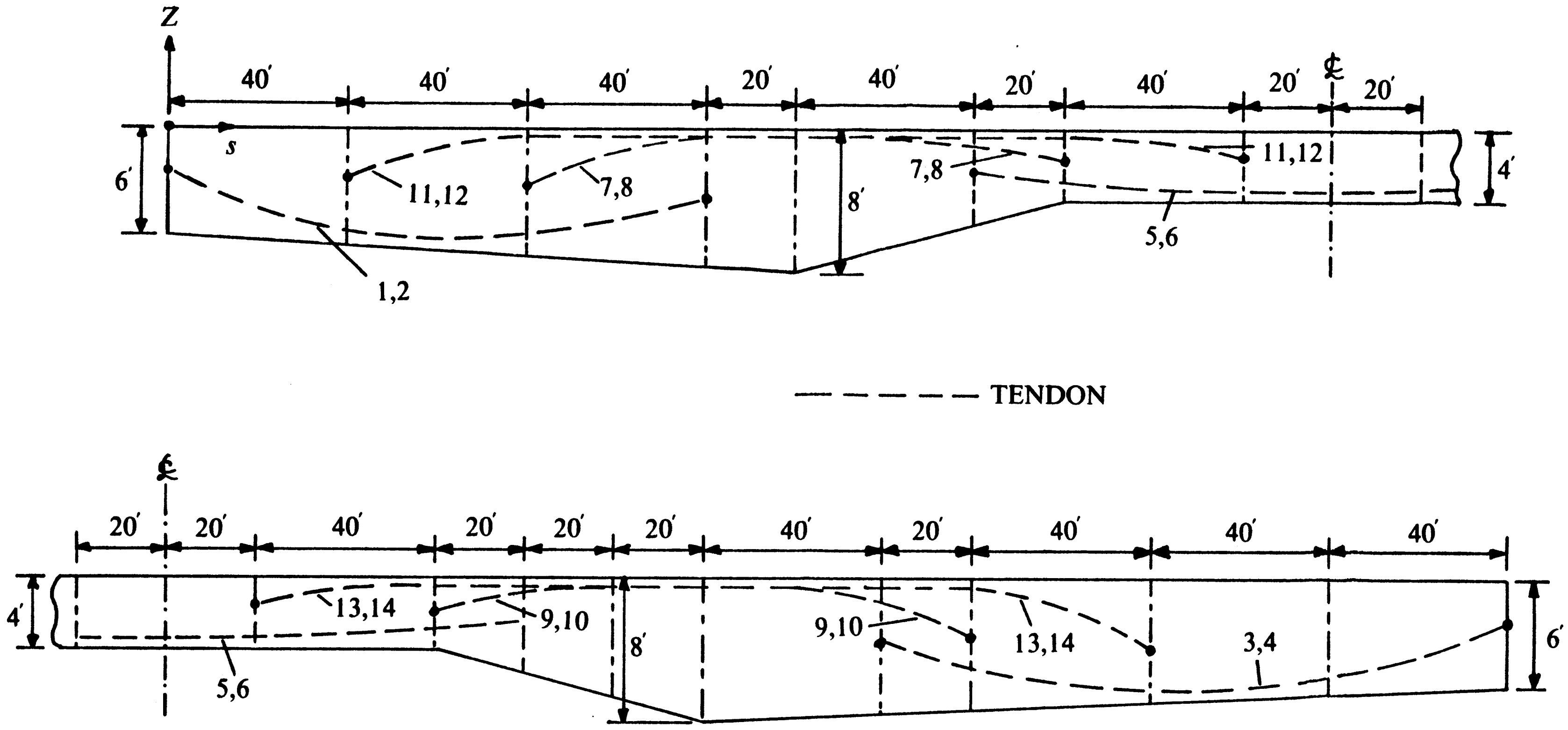

(c) LONGITUDINAL SECTION ALONG CENTERLINE

FIG. 4.10 EXAMPLE 4.5 - THREE-SPAN CURVED NONPRISMATIC PRESTRESSED CONCRETE BRIDGE

$$\begin{aligned} t_b &= 3/5 + s/200\,, \quad \text{for } 0 \le s \le 140' \\ &= 67/30 - s/150\,, \quad \text{for } 140' \le s \le 260' \\ &= -\,37/30 + s/150\,, \quad \text{for } 260' \le s \le 380' \\ &= 25/9 - 7s/1800\,, \quad \text{for } 380' \le s \le 560' \end{aligned}$$

Modulus of elasticity $E = 608{,}256$ kip/ft^2 and Poisson's ratio $\nu = 0.18$ are assumed for the concrete. The unit weight density of the structure is taken as $w = 160$ pcf.

The bridge is prestressed with 14 different tendons, 7 in each web (Fig. 4.10c). The jacking forces and the geometry data of each tendon are given in Table 4.5. Tendon numbers 1 through 6 each has a vertical profile along its span consisting of one parabolic segment. Each of the other 8 tendons has two parabolic segments connected by a linear segment in the middle. All the tendons are stressed simultaneously from both ends. Wobble friction coefficient of $K = 0.0002$/ft, curvature friction coefficient of $\mu = 0.2$/radian, and anchorage slip of $\Delta_a = 0$ are assumed. The modulus of elasticity and the cross sectional area of the tendons are not required for the analysis since the anchorage slip is assumed to be zero.

A total of four different load cases are considered. They may be summarized as follows:

Case 1 - Uniform line load of 1 kip/ft along the centerline of the bridge (Fig. 4.11a). This loading is used to carry out equilibrium checks on the LAPBOX results.

Case 2 - Dead load of the bridge due to a unit weight density of 160 pcf.

Case 3 - Prestressing.

Case 4 - Uniform live load of 0.15 kip/ft^2 over the full width of the top deck and between $s = 180$ ft and 340 ft (Fig. 4.11b).

The bridge is analyzed using 56 curved nonprismatic box beam elements, each 10 ft long. The origin of the local x, y, z axes of the cross section (Fig. 4.10b) is taken at the mid-thickness of the top flange. The uniform line load of 1 kip/ft for load case 1 is simulated as a uniform pressure of 10^{10} kip/ft^2 on the top flange uniformly distributed over a width of 10^{-10} ft at the centerline. All load cases are represented by equivalent nodal loads generated automatically within the program LAPBOX.

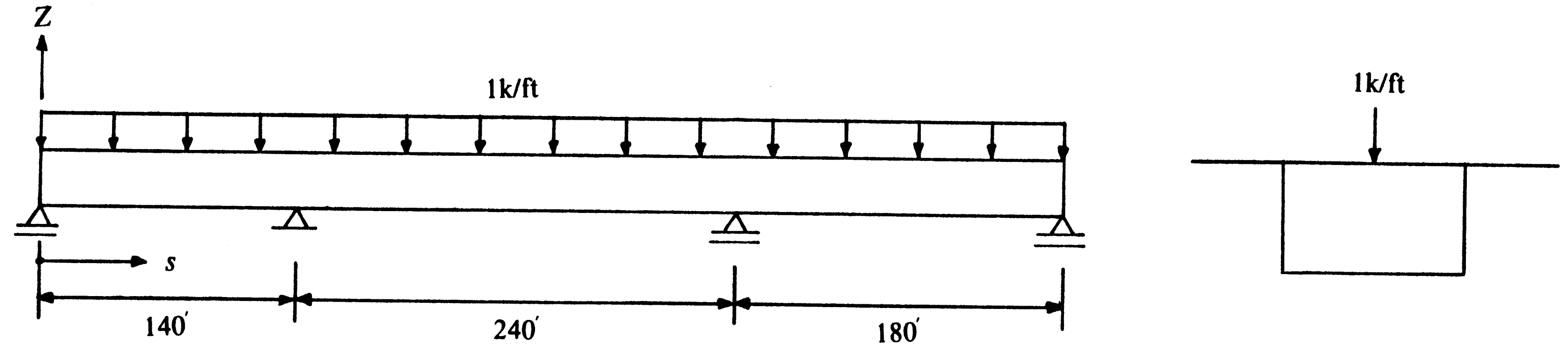

(a) LOAD CASE 1 - UNIFORM LINE LOAD

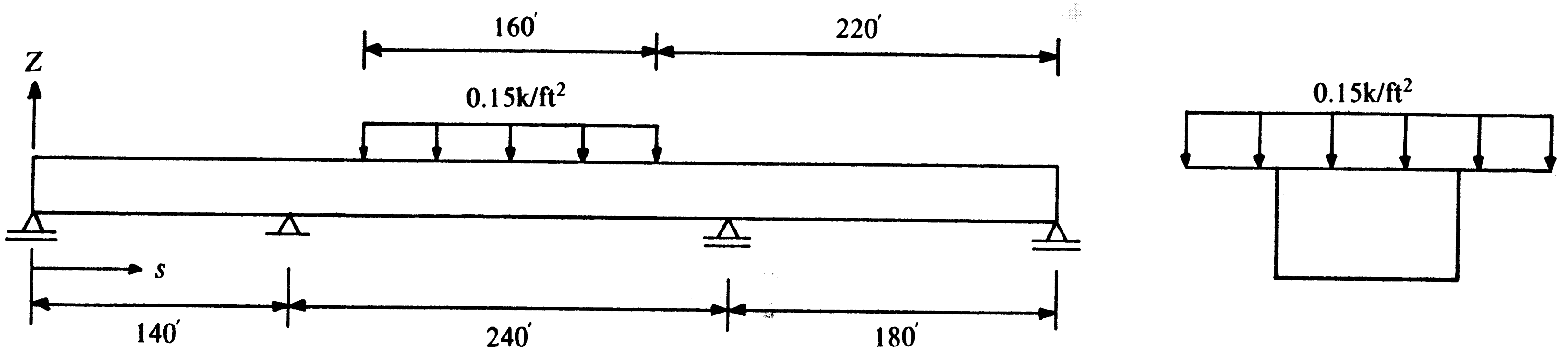

(b) LOAD CASE 2 - UNIFORM DISTRIBUTED LIVE LOAD

FIG. 4.11 EXAMPLE 4.5 - LOAD CASES 1 AND 4

An additional analysis is performed for load case 4 with the computer program SAP IV [42] using one-dimensional (straight) beam elements. 56 beam elements, each spanning 10 ft (measured along the actual axis of the bridge), are used. Each element is prismatic so that the nonprismatic bridge can only be modelled approximately by using different cross sectional properties for each element. The distributed live load is represented by statically equivalent concentrated loads at the nodes.

4.5.2 Presentation and Discussion Of Results

From the large amount of output obtained from the analyses, a few selected results are tabulated and plotted for the four load cases.

Table 4.6 gives a summary of the support reactions obtained from LAPBOX for all load cases. In the last two columns of Table 4.6, the total sum of all the vertical reactions is compared with the applied load calculated by hand from the actual loading and geometry of the structure. The agreement is perfect which is indicative of the high accuracy with which the box beam elements can be used to model the geometry and loading of a curved nonprismatic bridge. The support reactions obtained from the SAP IV analysis for load case 4 are also shown in Table 4.6. The agreement between the LAPBOX and the SAP IV results are good, particularly for the vertical reactions.

To perform equilibrium checks, load case 1 of 1 kip/ft uniform line load along the centerline is considered. The vertical shear V_z, bending moment M_y and torque M_x at the Gauss section AA (s = 262.113 ft) near midspan, and the two Gauss sections BB (s = 377.887 ft) and CC (s = 382.113 ft) near support S3 (Fig. 4.10a), obtained by statics from the support reactions (Table 4.6) and the applied external load (Fig. 4.11a), and then with LAPBOX from the integration of the internal stresses at these same sections, are shown in Table 4.7. Excellent agreement can be noted. In fact, the small discrepancies are possibly due to round-off errors which would imply that the internal force resultants obtained with LAPBOX satisfy statics exactly.

TABLE 4.6 EXAMPLE 4.5 - SUMMARY OF SUPPORT REACTIONS

LOAD CASE	FORCE QUANTITY	SUPPORT S1	SUPPORT S2	SUPPORT S3	SUPPORT S4	TOTAL VERTICAL REACTION (kip)	TOTAL APPLIED LOAD (kip)
LINE LOAD	Distortional Moment M_d (kip·ft)	0.0	132.8	343.8	-17.3	—	—
	Vertical Force V_z (kip)	32.9	223.8	246.5	56.8	560.0	560.0
	Torque M_x (kip·ft)	-0.5	-151.9	-443.6	119.2	—	—
DEAD LOAD	Distortional Moment M_d (kip·ft)	-0.2	782.4	2233.6	-125.1	—	—
	Vertical Force V_z (kip)	237.8	1491.9	1853.2	493.8	4076.7	4076.7
	Torque M_x (kip·ft)	-2.8	-867.9	-2026.8	1545.0	—	—
PRE-STRESS	Distortional Moment M_d (kip·ft)	-0.1	260.1	572.3	14.6	—	—
	Vertical Force V_z (kip)	-30.8	26.4	34.2	-29.8	0.0	0.0
	Torque M_x (kip·ft)	-1.6	-1103.6	-1954.8	-267.3	—	—
LIVE LOAD (LAPBOX)	Distortional Moment M_d (kip·ft)	-0.1	430.3	1035.3	8.0	—	—
	Vertical Force V_z (kip)	-116.2	404.0	385.2	-90.5	582.5	582.5
	Torque M_x (kip·ft)	-1.6	-322.9	-2359.2	-860.3	—	—
LIVE LOAD (SAP IV)	Vertical Force M_z (kip)	-115.7	403.4	385.2	-90.4	582.5	582.5
	Torque M_x (kip·ft)	0	-344.2	-2384.0	-848.0	—	—

TABLE 4.7 EXAMPLE 4.5 - COMPARISON OF EXTERNAL AND INTERNAL SECTION FORCES (LOAD CASE 1 : 1 kip/ft LINE LOAD)

SECTION	FORCE QUANTITY	EXTERNAL STATICS	INTERNAL LAPBOX
AA s = 262.113 ft	Shear, V_z (kip)	5.4	5.4
	Moment, M_y (kip·ft)	1621.0	1621.0
	Torque, M_x (kip·ft)	19.8	19.8
BB s = 377.887 ft	Shear, V_z (kip)	121.2	121.2
	Moment, M_y (kip·ft)	5717.8	5717.8
	Torque, M_x (kip·ft)	196.6	196.5
CC s = 382.113 ft	Shear, V_z (kip)	121.1	121.1
	Moment, M_y (kip·ft)	5718.0	5718.2
	Torque, M_x (kip·ft)	197.6	197.0

The longitudinal variations of the vertical centerline displacements (positive upwards) for load cases 2 (dead load), 3 (prestressing) and 4 (live load) are shown in Fig. 4.12. The plotted values for load case 4 represent both the LAPBOX and the SAP IV analyses, which predicted practically the same vertical displacements. The transverse distributions of vertical displacements at the middle of the interior span ($s = 260$ ft) are shown in Fig. 4.13 for the same three load cases. The vertical displacements are larger at the outer web than at the inner web with almost a linear variation across the bridge width indicating a twist of the cross section with little transverse distortion.

Longitudinal variations of bending moment M_y for dead load, prestressing and live load are shown in Figs. 4.14, 4.15 and 4.16 respectively. It may be noted that the total moments (primary + secondary) are shown for the prestressing load case (Fig. 4.15). The locations of the discontinuities in the prestressing moment diagram correspond to the jacking ends of the tendons. The live load moments (Fig. 4.16) obtained from the LAPBOX and the SAP IV analyses are found to agree closely.

Finally, the longitudinal variations of the vertical shear force V_z for dead load and live load are shown in Fig. 4.17. The shears plotted in Fig. 4.17 were obtained from the integrated force resultants at the Gauss sections output by LAPBOX. The values at the supports were obtained by extrapolating from the Gauss sections. The live load shears obtained with SAP IV were practically the same as those obtained with LAPBOX, and hence they are not shown separately.

The close agreement between the LAPBOX and the SAP IV results for the live load case indicates that the longitudinal flexural behavior of the bridge was not affected significantly by transverse distortion and longitudinal warping of the cross sections. However, ordinary beam theory (SAP IV) cannot predict the transverse distribution of stresses and the transverse flexural moments (not reported) which can be obtained from thin-walled beam theory (LAPBOX).

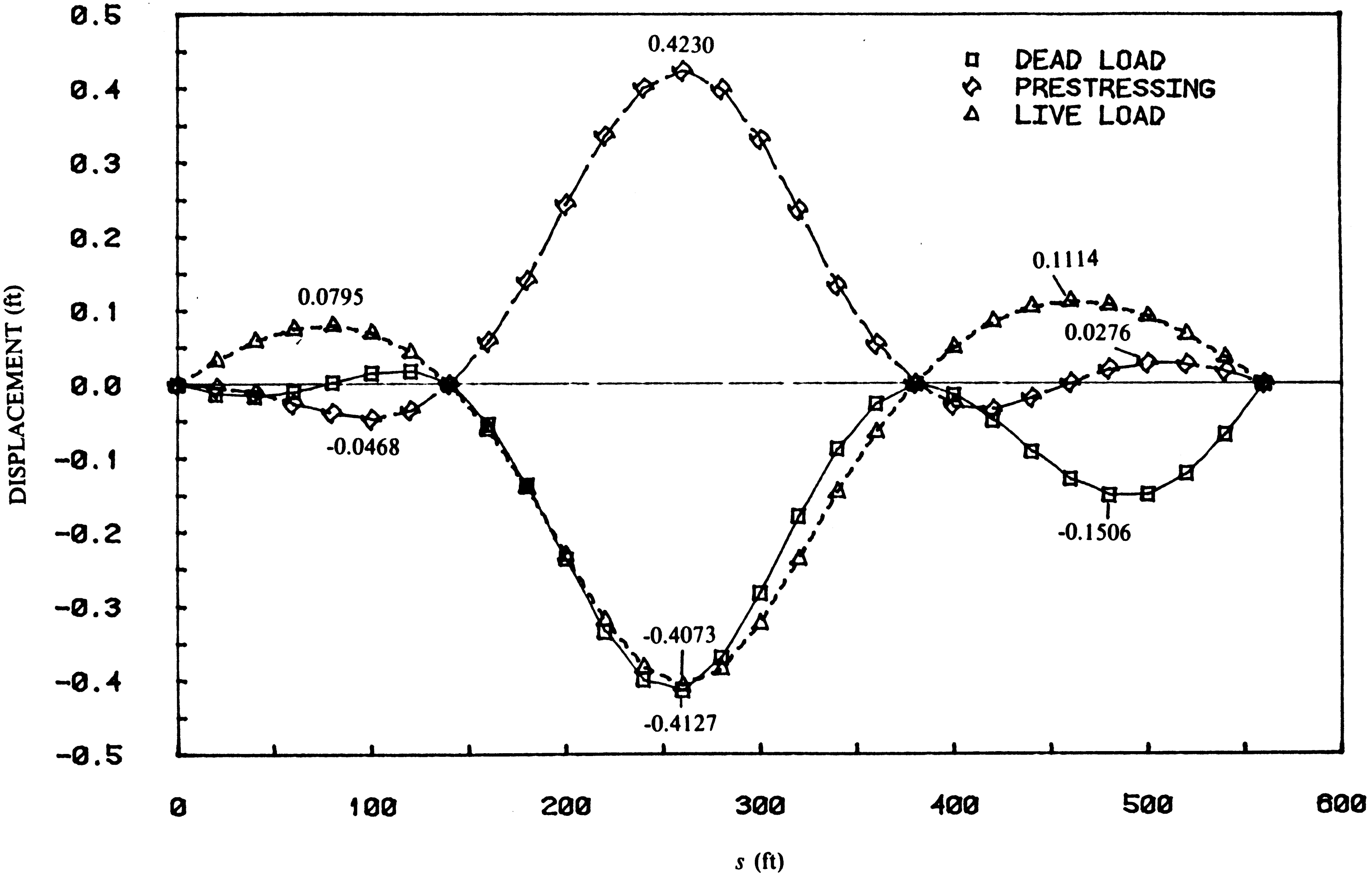

FIG. 4.12 EXAMPLE 4.5 - LONGITUDINAL DISTRIBUTIONS OF VERTICAL CENTERLINE DISPLACEMENTS

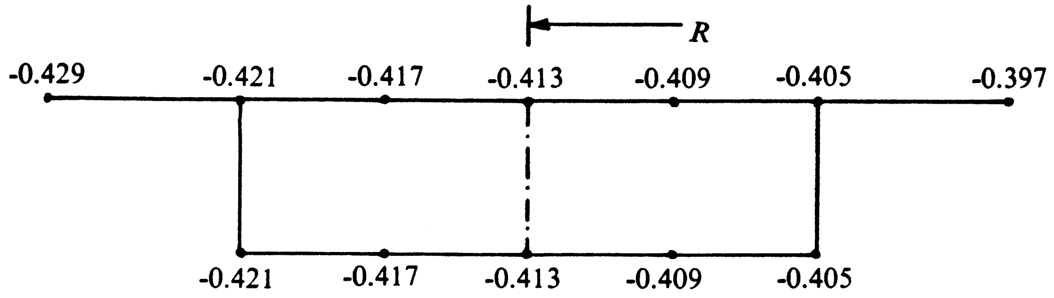

(a) DEAD LOAD

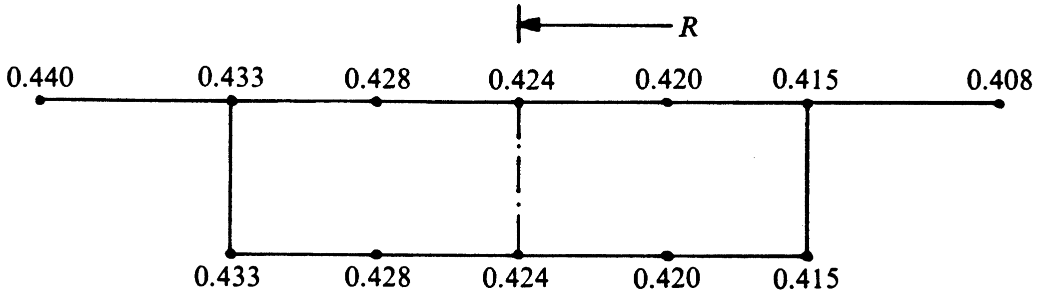

(b) PRESTRESSING

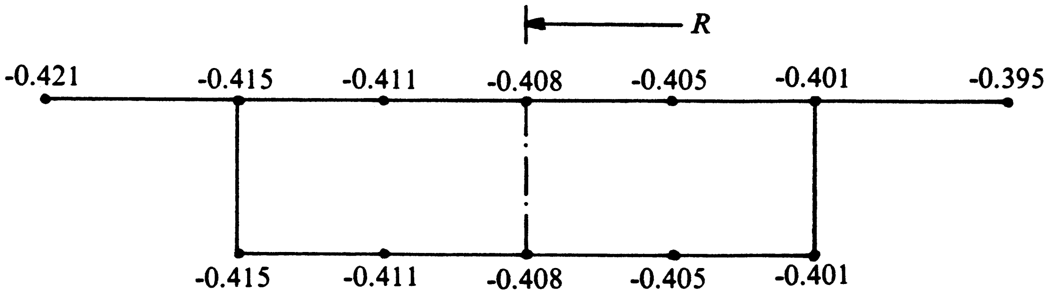

(c) LIVE LOAD

FIG. 4.13 EXAMPLE 4.5 - TRANSVERSE DISTRIBUTIONS OF VERTICAL DISPLACEMENTS (ft) @ s = 260 ft

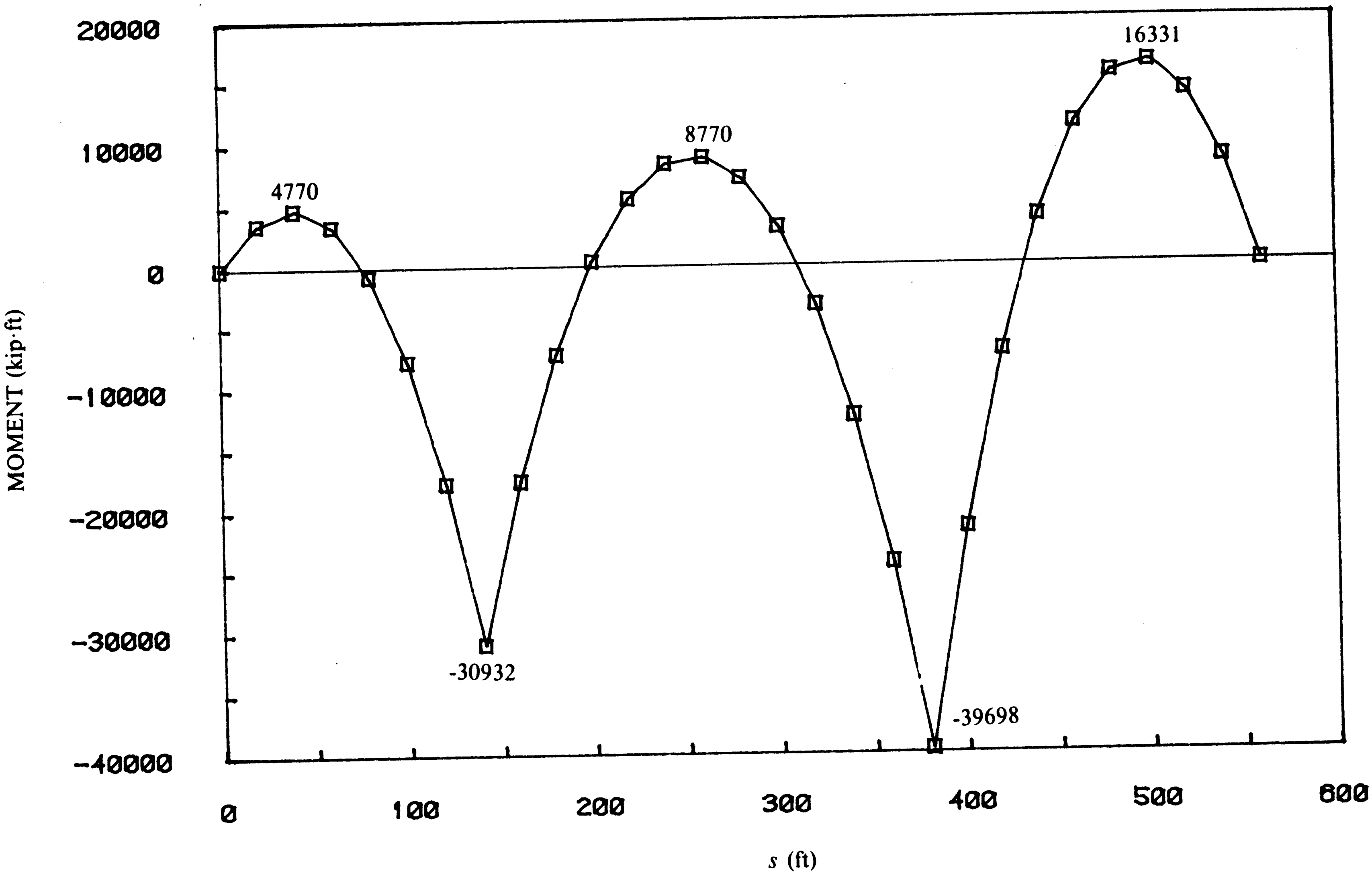

FIG. 4.14 EXAMPLE 4.5 - LONGITUDINAL DISTRIBUTION OF BENDING MOMENT M_y DUE TO DEAD LOAD

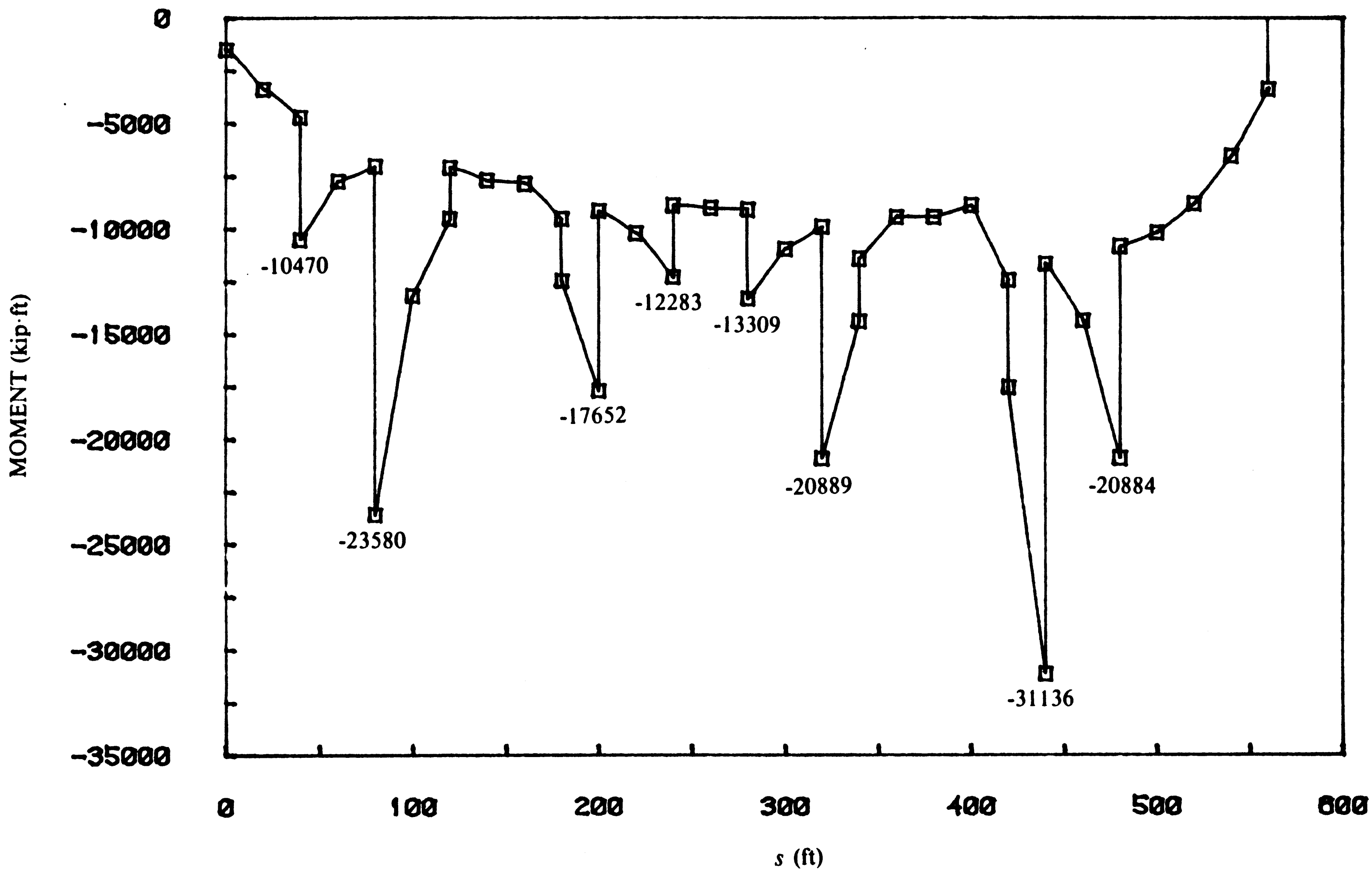

FIG. 4.15 EXAMPLE 4.5 - LONGITUDINAL DISTRIBUTION OF BENDING MOMENT M_y DUE TO PRESTRESSING

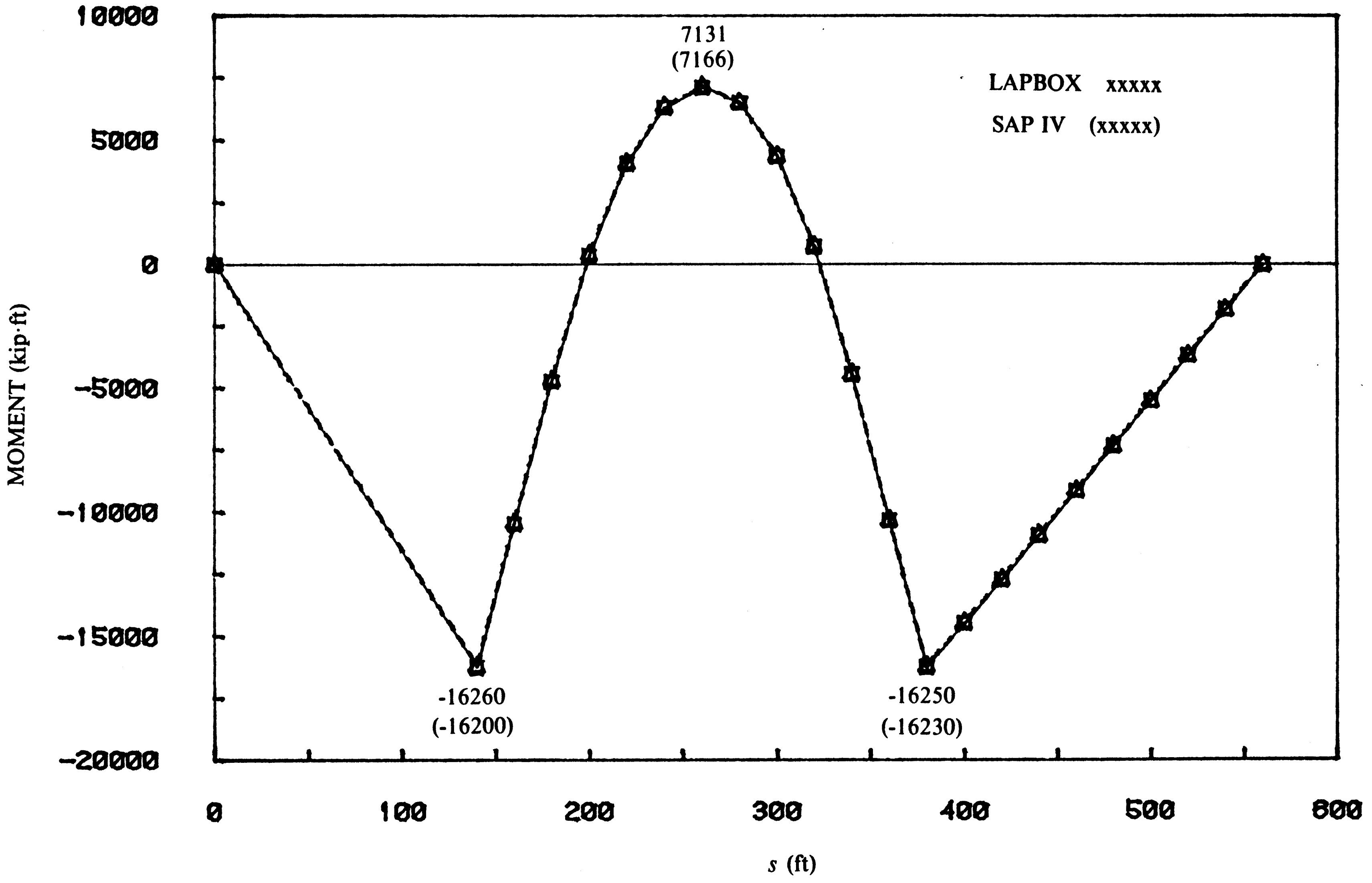

FIG. 4.16 EXAMPLE 4.5 - LONGITUDINAL DISTRIBUTION OF BENDING MOMENT M_y DUE TO LIVE LOAD

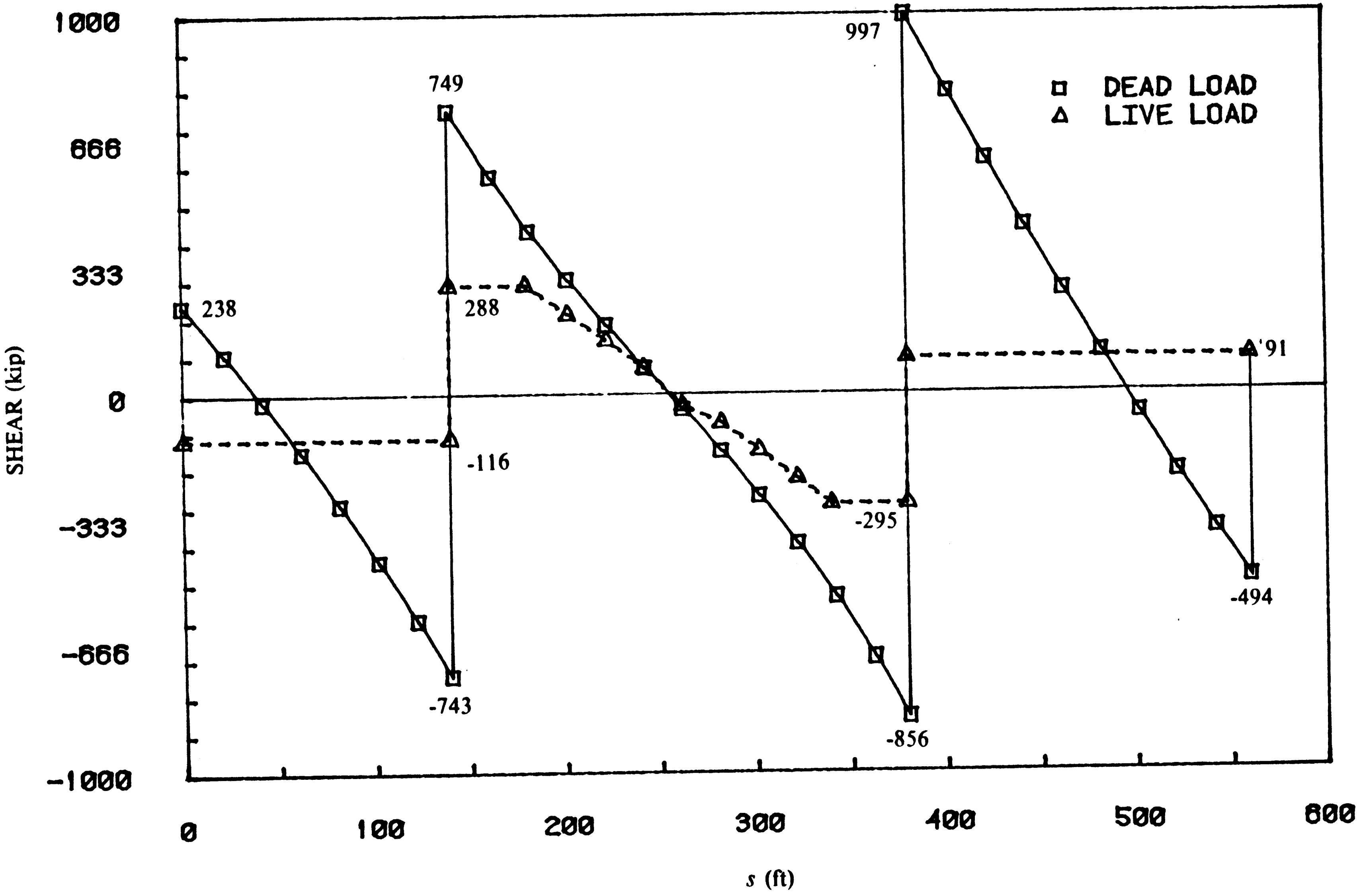

FIG. 4.17 EXAMPLE 4.5 - LONGITUDINAL DISTRIBUTION OF VERTICAL SHEAR V_z DUE TO DEAD LOAD AND LIVE LOAD

4.6 Concluding Remarks

The five numerical examples discussed in this chapter have demonstrated the capabilities of the proposed method for linear elastic analysis of curved nonprismatic reinforced and prestressed concrete box girders. Comparisons of results obtained from the proposed method with results from other analytical and experimental models showed that the proposed method is capable of capturing the dominant actions in single-cell box girders quite accurately.

The simplicity, accuracy and reduced computional effort inherent in the proposed curved nonprismatic thin-walled box beam element make it extremely well suitable for an extension to capture nonlinear effects.

5. NONLINEAR CONSTITUTIVE MODELS

5.1 General

The nonlinearity in the response of reinforced and prestressed concrete box girder bridges is primarily due to material nonlinearities. Geometric nonlinearities are negligible for most practical bridges and hence are not considered in the present study. Material nonlinearities arise due to the nonlinear nature of the short-time constitutive relationships for concrete, reinforcing steel and prestressing steel, and also due to time-dependent and environmental effects of aging, creep and shrinkage of concrete, relaxation of prestressing steel, and temperature changes. The time-dependent and environmental effects influence deflections and stresses at service loads but usually have little influence on the response of the bridge to overloads or ultimate loads. Since the present study is concerned with the ultimate load analysis of reinforced and prestressed concrete box girders, only the nonlinearities in the short-time constitutive relationships are considered.

Both concrete and steel exhibit various nonlinear material properties. The stress-strain relationship of concrete is not only nonlinear, but it differs in compression and tension. Tensile cracking is one of the most important factors which contribute to the nonlinear behavior of reinforced concrete structures. Reinforcing steel generally exhibits symmetrical nonlinear stress-strain relationships in tension and compression. Prestressing steel is used exclusively in tension, and its stress-strain relationship is also nonlinear, and the shape of its stress-strain curve is different from that of reinforcing steel.

Another nonlinear factor to be noted is the unloading and reloading characteristics of concrete and steel. Although the effects of dynamic loadings such as seismic load or wind load are not considered in this study, the effects of live load history are considered in a quasi-static manner. Thus a simple mathematical model for unloading and reloading is developed to study the effects of load reversal.

As was done for linear elastic analysis, a reinforced or prestressed concrete box girder bridge is discretized in a nonlinear analysis into a finite number of curved nonprismatic box beam elements. This was described previously in Sec. 2.9. But the box beam elements can no longer be assumed to be composed of homogeneous material. They must be considered as reinforced concrete elements composed of concrete, and reinforcing steel in the longitudinal and transverse directions. Moreover, the prestressing tendons must be considered an integral part of the structure. As described previously in Chapter 3, the prestressing tendons are discretized into straight prestressing steel segments between tendon points located at the nodes of the reinforced concrete box beam elements. It is thus necessary to model the nonlinear constitutive relationships for the reinforced concrete box beam element and the prestressing steel segment.

5.2 Reinforced Concrete Box Beam Element

A reinforced concrete box beam element is composed of concrete with longitudinal and transverse reinforcing steel. A typical cross section is shown in Fig. 5.1. Perfect bond is assumed to exist between the concrete and the reinforcing steel so that the displacement field within the element can be considered continuous. The transverse reinforcing steel is assumed to be perpendicular to the element axis.

The constitutive relationships for a reinforced concrete box beam element between the generalized strains ϵ_x, γ_{xs}, v_4 and stresses σ_x, τ_{xs}, w_4, introduced in Sec 2.4, will in reality be coupled in addition to being nonlinear. The various mechanisms contributing to the response of reinforced concrete structures, however, make it difficult to accurately model this coupling. The global behavior of most reinforced and prestressed concrete box girder bridges under practical loading conditions is usually dominated by the longitudinal flexural response. Though the coupling terms in the constitutive relationships affect local behavior, their influence on the overall response of the structure is believed to be much less significant. Thus in this study, it is assumed that the constitutive relationships are uncoupled, and the $\sigma_x - \epsilon_x$, $\tau_{xs} - \gamma_{xs}$ and $w_4 - v_4$ relationships are modelled independently.

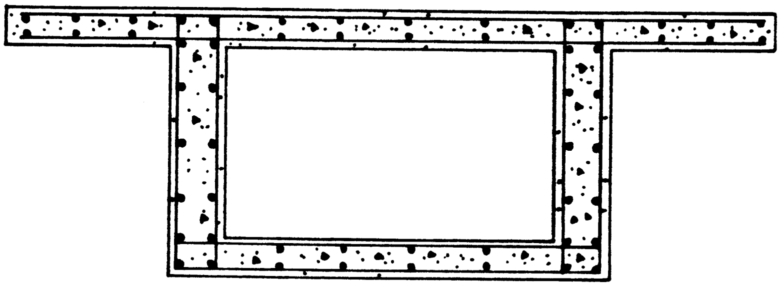

FIG. 5.1 TYPICAL REINFORCED CONCRETE BOX BEAM CROSS SECTION

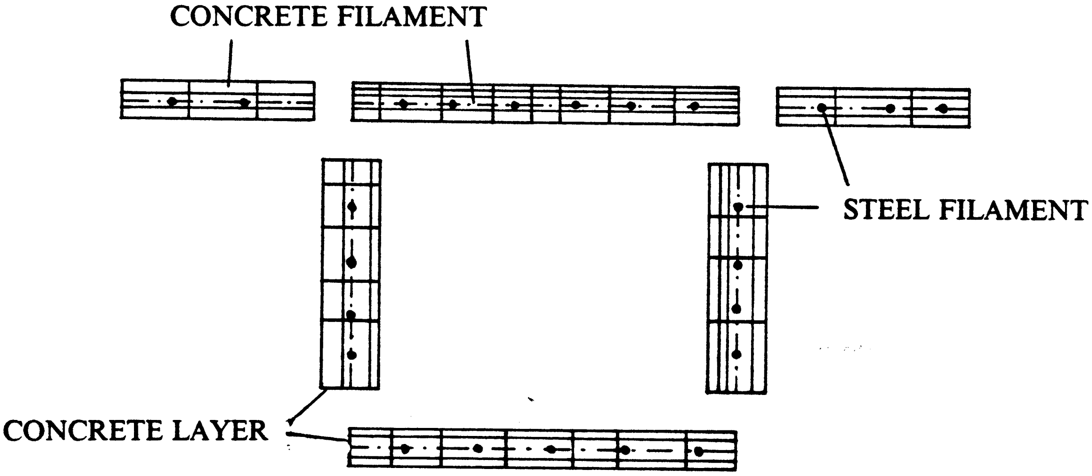

FIG. 5.2 BOX CROSS SECTION IDEALIZED AS CONCRETE AND LONGITUDINAL REINFORCING STEEL FILAMENTS

5.2.1 $\sigma_x - \epsilon_x$ Relationship

The response of the reinforced concrete box beam element under longitudinal normal strains and stresses plays a dominant part in the overall behavior of the structure. It is thus necessary to model this response accurately.

A composite filament system consisting of concrete and longitudinal reinforcing steel filaments is constructed in order to account for varied material properties within the cross section of the box beam element (Fig. 5.2). Each wall of the box cross section is subdivided into discrete concrete layers, and each layer is further subdivided into discrete concrete filaments. The number of concrete layers and the number of concrete filaments per layer can vary from wall to wall. The longitudinal reinforcing steel filaments are located at the mid-thickness of the cross section walls. The number of steel filaments can vary from wall to wall, and within a wall the spacing between filaments can vary.

Though in the linear elastic analyses sufficient accuracy was obtained by monitoring the longitudinal strains and stresses only at the mid-thickness of the cross section walls, in a nonlinear analysis more than one concrete layer may be necessary to accurately model the varied concrete response across the thickness of a wall. For the longitudinal reinforcing steel, however, one layer at the mid-thickness of each wall provides sufficient accuracy.

Each concrete and steel filament in a cross section is assumed to be in a state of uniaxial stress. The geometric and material properties of each filament are referred to its mid-point. Then any integration over the cross section of a box beam element associated with longitudinal normal strains and stresses, such as the first integral in Eq. (2.54) required to evaluate the element stiffness matrix, can be performed filament by filament as follows :

$$\int_A \phi_\epsilon \, dA = \sum_{i=1}^{n_c} \phi_{\epsilon_i} A_{c_i} + \sum_{i=1}^{n_s} \phi_{\epsilon_i} A_{s_i} \tag{5.1}$$

where ϕ_ϵ is a function of material and geometric properties related to axial deformations; n_c and n_s are respectively the number of concrete and longitudinal steel filaments; A_c and A_s are respectively the cross sectional areas of concrete and longitudinal steel filaments.

In the following sections, the necessary constitutive relationships for concrete and longitudinal reinforcing steel filaments are modelled. Also, the interaction between concrete and reinforcing steel due to "tension stiffening" effect is considered.

5.2.1a Concrete

The mathematical model for concrete employed in the present study is the one used by Kang and Scordelis [28, 29] to study planar reinforced and prestressed concrete frames. The model, shown in Fig. 5.3, is an extension of the widely used mathematical formula suggested by Hognestad [43] for concrete in compression. The ascending part of the compressive stress-strain curve is described by the following equation

$$\sigma_c = f_c'' \frac{\epsilon_c}{\epsilon_0}\left(2 - \frac{\epsilon_c}{\epsilon_0}\right) \tag{5.2}$$

in which the strain ϵ_0 corresponding to the maximum compressive stress f_c'' is given by

$$\epsilon_0 = 2\frac{f_c''}{E_{ci}} \tag{5.3}$$

where E_{ci} is the initial tangent modulus. By differentiating Eq. (5.2), the tangent modulus E_{tc} is obtained.

$$E_{tc} = \frac{d\sigma_c}{d\epsilon_c} = E_{ci}\left(1 - \frac{\epsilon_c}{\epsilon_0}\right) \tag{5.4}$$

The descending part of the compressive stress-strain curve is a straight line given by the equation

$$\sigma_c = f_c''\left[1 - (1 - \beta)\frac{\epsilon_c - \epsilon_0}{\epsilon_{cu} - \epsilon_0}\right] \tag{5.5}$$

where β is the ratio of the stress at the ultimate compressive strain ϵ_{cu} to the maximum compressive stress f_c''. Hognestad [43] suggested values of $\beta = 0.85$ and $\epsilon_{cu} = 0.0038$. In the present study, values of β and ϵ_{cu} are specified directly thus allowing for flexibilty in modelling different concrete properties. By differentiating Eq. (5.5), the tangent modulus for the descending branch is obtained as

$$E_{tc} = -\frac{(1-\beta)f_c''}{\epsilon_{cu} - \epsilon_0} \tag{5.6}$$

Maximum compressive stress f_c'' is given by a fraction of the compressive strength f_c' determined from tests on standard cylinders.

$$f_c'' = r_c f_c' \tag{5.7}$$

Hognestad suggested a value of $r_c = 0.85$ for prismatic members based on numerous tests of concentrically loaded columns, but many investigators also use $r_c = 1$.

In tension, the slope of the stress-strain curve (Fig. 5.3) is assumed to be constant and the same as the initial tangent modulus E_{ci}. Then the tensile stress-strain relationship can be expressed as

$$\sigma_c = E_{ci}\epsilon_c \quad \leq f_t \tag{5.8a}$$

$$E_{tc} = E_{ci} \tag{5.8b}$$

where f_t is the tensile strength of the concrete assumed to have the value of the modulus of rupture in this study.

Ideally, the values of the initial tangent modulus E_{ci} and the tensile strength f_t should be determined from tests. However, in the absence of test data, empirical formulae such as Eqs. (5.9) and (5.10) below, recommended by ACI Committee 209 [44], can be used.

$$E_{ci} = 33(w^3 f_c')^{1/2} \text{ psi} \tag{5.9}$$

$$f_t = r_t(w f_c')^{1/2} \text{ psi} \tag{5.10}$$

where f_c' is the compressive strength in psi, w is the unit weight of concrete in pcf, and parameter r_t has a value between 0.6 and 1.0.

The load reversal model utilized in this study is also shown in Fig. 5.3. The following assumptions are made in this model.

1. The slope of the load reversal path in the stress-strain curve is the same as the initial tangent modulus E_{ci}.

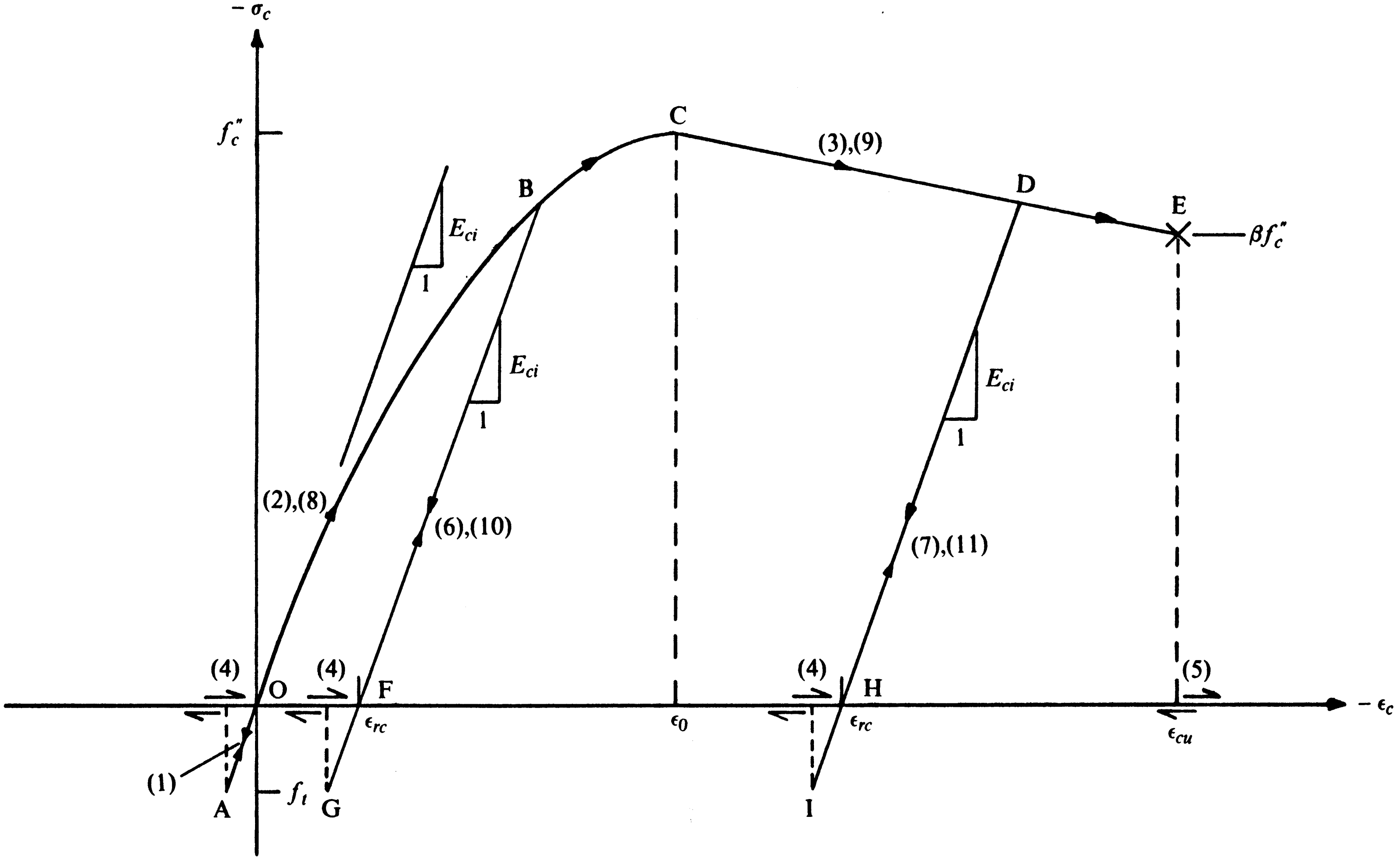

FIG. 5.3 CONSTITUTIVE MODEL FOR CONCRETE FILAMENT

2. Tensile failure or cracking of concrete occurs when the tensile stress exceeds the tensile strength f_t.

3. Compressive failure or crushing of concrete occurs when the compressive strain exceeds the ultimate compressive strain ϵ_{cu}.

4. Once concrete is cracked, it cannot take any tensile stress again. But it can take compressive stress after closing of the crack.

5. Once concrete is crushed, it cannot take any compressive or tensile stress again.

In the present study 11 different concrete material states (Fig. 5.3) are defined for the purpose of tracing primary loading, unloading and reloading paths in the stress-strain curve and for evaluating the stress σ_c and the tangent modulus E_{tc}. In the following description of the 11 different concrete material states, concrete is defined as yielded when the compressive strain exceeds ϵ_0, the strain corresponding to the maximum compressive stress f_c''.

(1) In primary tension (path OA or AO)

(2) In compression, not yielded (path OC)

(3) In compression, yielded (path CE)

(4) Crack open

(5) Crushed

(6) In load reversal path from state 2 (path BG or GB)

(7) In load reversal path from state 3 (path DI or ID)

(8) In compression, not yielded and previously cracked (path OC or BC)

(9) In compression, yielded and previously cracked (path CE or DE)

(10) In load reversal path from state 2 or 8 and previously cracked (path BF or FB)

(11) In load reversal path from state 3 or 9 and previously cracked (path DH or HD)

The constitutive model for concrete used in the present study can now be summarized in the following equations.

For state 1,

$$\sigma_c = E_{ci}\epsilon_c \ ; \ E_{tc} = E_{ci} \tag{5.11}$$

For states 2 and 8,

$$\sigma_c = f_c''\frac{\epsilon_c}{\epsilon_0}(2 - \frac{\epsilon_c}{\epsilon_0}) \ ; \ E_{tc} = E_{ci}(1 - \frac{\epsilon_c}{\epsilon_0}) \tag{5.12}$$

For states 3 and 9,

$$\sigma_c = f_c''\left[1 - (1 - \beta)\frac{\epsilon_c - \epsilon_0}{\epsilon_{cu} - \epsilon_0}\right] \ ; \ E_{tc} = -\frac{(1 - \beta)f_c''}{\epsilon_{cu} - \epsilon_0} \tag{5.13}$$

For states 6, 7, 10 and 11,

$$\sigma_c = E_{ci}(\epsilon_c - \epsilon_{rc}) \ ; \ E_{tc} = E_{ci} \tag{5.14}$$

For states 4 and 5,

$$\sigma_c = 0 \ ; \ E_{tc} = 0 \tag{5.15}$$

In Eq. (5.14) above, ϵ_{rc} is the residual strain due to unloading, as shown by points F and H in Fig. 5.3.

5.2.1b Reinforcing Steel

To model the constitutive relationship of the reinforcing steel, the same simple bilinear model used by Kang [28] and Chan [31] is employed in this study. As shown in Fig. 5.4, four parameters are needed to define the stress-strain curve: the initial modulus up to yielding E_{s1}; the second modulus after yielding E_{s2}; the yield stress f_y; and the ultimate strain ϵ_{su}.

The slope of the load reversal path in Fig. 5.4 is assumed to be the same as the initial modulus E_{s1}. Failure is assumed to occur when the steel strain exceeds the ultimate strain ϵ_{su}.

The model can be used to simulate strain hardening with Bauschinger effect or elastic-perfectly plastic behavior.

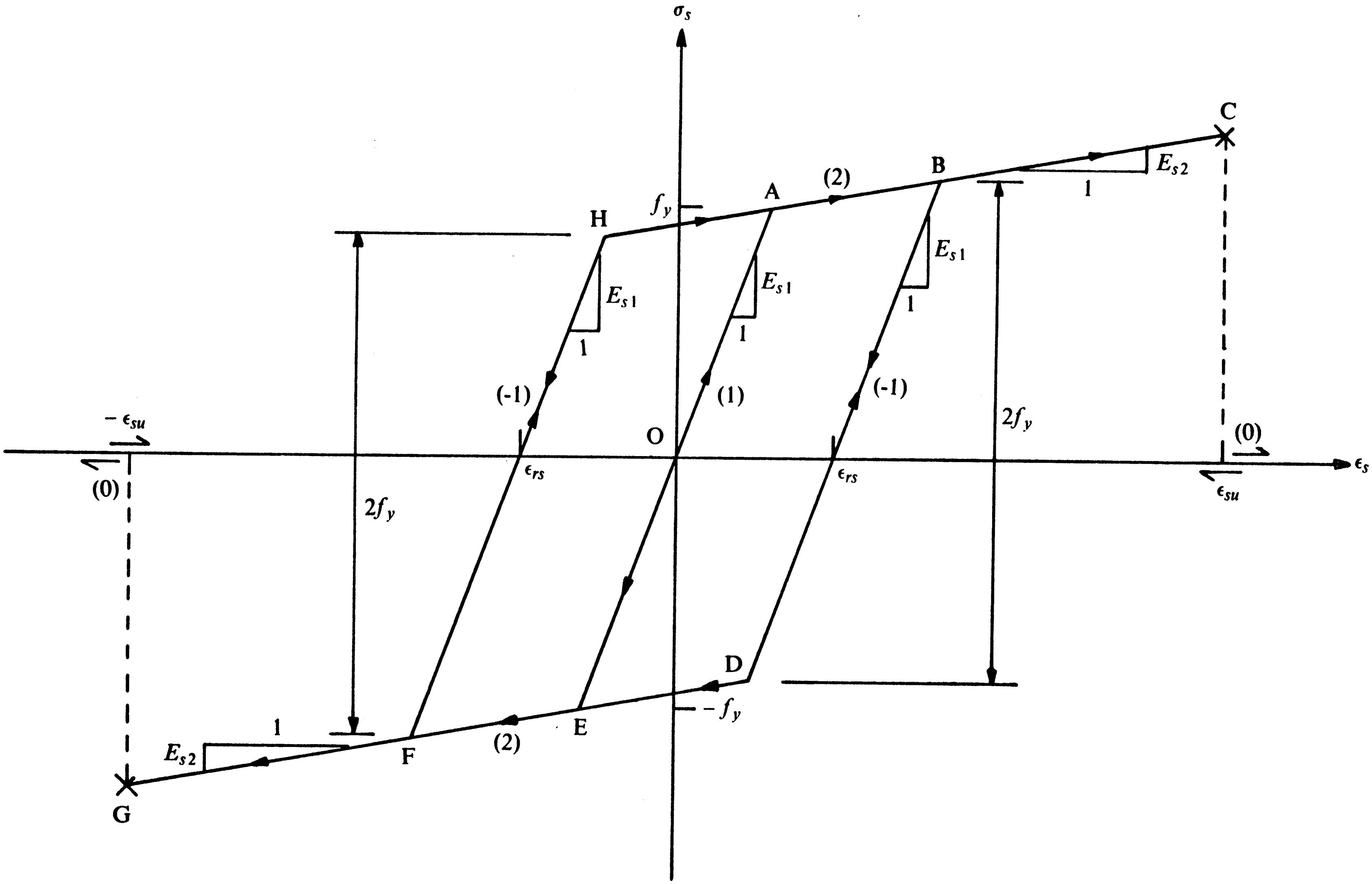

FIG. 5.4 CONSTITUTIVE MODEL FOR REINFORCING STEEL FILAMENT

Four different material states are defined in Fig. 5.4. These are described below along with the corresponding equations for the stress σ_s and the tangent modulus E_{ts}.

(1) In primary tension or compression (path AE or EA)

$$\sigma_s = E_{s1}\epsilon_s \ ; \ E_{ts} = E_{s1} \tag{5.16}$$

(2) Yielded (path HC or DG)

$$\sigma_s = E_{s2}\epsilon_s \pm f_y(1 - \frac{E_{s2}}{E_{s1}}) \ ; \ E_{ts} = E_{s2} \tag{5.17}$$

(-1) In load reversal path from state 2 (path BD, DB, FH or HF)

$$\sigma_s = E_{s1}(\epsilon_s - \epsilon_{rs}) \ ; \ E_{ts} = E_{s1} \tag{5.18}$$

where ϵ_{rs} is the residual strain due to unloading, as shown in Fig. 5.4.

(0) Failed

$$\sigma_s = 0 \ ; \ E_{ts} = 0 \tag{5.19}$$

5.2.1c Tension Stiffening

The low tensile strength of concrete, which is usually only about one-tenth of its compressive strength, is one of its most important properties. Cracking occurs when the tensile strength of concrete is exceeded, and this is a major factor affecting the behavior of reinforced concrete members. Thus an important consideration in the analysis of reinforced concrete members is the influence of concrete cracking on member stiffness.

The phenomenon of concrete cracking is complicated by the presence of reinforcing steel. The basic mechanism is illustrated in Fig. 5.5 for a reinforced concrete element under uniaxial tension. When the concrete reaches its tensile strength at randomly distributed weak sections, primary cracks will form. At these cracks, the stress in the concrete drops to zero while the steel carries the entire load. Between the cracks, however, concrete still carries some tensile stress due to the bond between concrete and reinforcing steel. This is often referred to as the "tension stiffening" effect. As the load is increased secondary cracks will form with the result that the portion of the load carried by the concrete, and thus the average stress in the concrete, will decrease. Finally, the bond between the concrete and the steel will completely deteriorate and the steel will carry all the load.

Two basically different approaches have been used by previous investigators to model the tension stiffening effect. One approach is to relate average tensile stress to average strain by means of an unloading stress-strain relationship for cracked concrete in tension. Scanlon [45] used a stepped piecewise linear unloading relationship. A similar approach was used by Lin and Scordelis [46], however with a smooth unloading curve. The steel and concrete stresses obtained from this approach are estimates of the average stresses (Fig. 5.5). At the actual crack, the steel stress is therefore always underestimated, while the concrete stress is overestimated since it should be zero.

The second approach is to ignore the concrete after cracking and to use an increased stiffness for the reinforcing steel. This approach was used by Gilbert and Warner [47] and Poston et al. [48], among others. The steel stress obtained from this approach should be a reasonably good estimate of the maximum steel stress at a crack, while the concrete stress, which is zero, is exact at a crack.

Gilbert and Warner [47] investigated both approaches and concluded that modelling the tension stiffening effect by modifying the stress-strain relationship for the reinforcing steel is not only simpler to incorporate, but also computationally more efficient. Furthermore, results obtained from this approach were at least as good as those obtained from the use of an unloading curve for concrete.

In this study, a modification of the steel-referred method used by Poston et al. [48] is adopted. The model is illustrated in Fig. 5.6 for a reinforced concrete element subjected to monotonically increasing axial tension. In Fig. 5.6, $\epsilon_y = f_y / E_{s1}$ is the yield strain of reinforcing steel, and $\epsilon_{ct} = f_t / E_{ci}$ is the cracking strain of concrete. The parameter α which defines the tension stiffening effect is given by the following two equations taken from [48].

$$\alpha = \frac{k'}{\rho} \ , \ \rho \geq 0.5\% \tag{5.20}$$

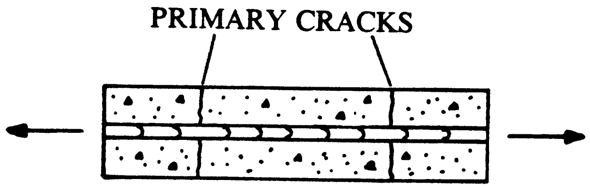

(a) REINFORCED CONCRETE ELEMENT

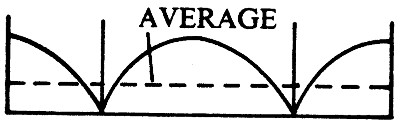

(b) CONCRETE STRESS

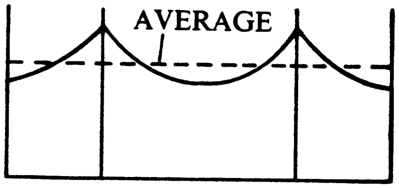

(c) STEEL STRESS

FIG. 5.5 STRESS DISTRIBUTIONS IN A CRACKED REINFORCED CONCRETE ELEMENT

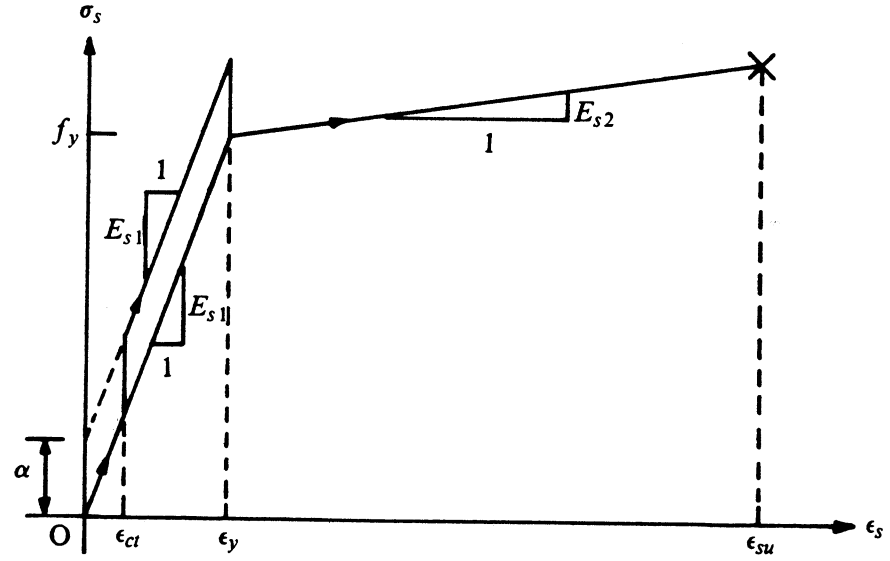

FIG. 5.6 TENSION STIFFENING MODEL FOR MONOTONIC LOADING

$$\alpha = \frac{k'}{0.005}(2 - \frac{\rho}{0.005}) \ , \ \rho \le 0.5\% \tag{5.21}$$

where ρ is the reinforcement ratio and k' is a tension stiffening coefficient with dimension *force/length*^{2}. Poston et al. used a value of $k' = 57$ psi. For the present application, the reinforcement ratio ρ is based on the longitudinal steel area and is calculated separately for each wall of the box cross section.

Certain modifications of the model in Fig. 5.6 are necessary to account for the possibility of load reversal. Consider a reinforced concrete element (Fig. 5.7a) subjected to the quasi-static load history in Fig. 5.7b. The element is initially loaded in compression giving rise to compressive stresses in concrete and reinforcing steel corresponding to point A in Fig. 5.7c, d. For generality, the reinforcing steel is assumed to have yielded in compression. Upon unloading, the compressive stresses in concrete and steel decrease elastically until at point B, when the compressive strain in the element equals the residual concrete strain ϵ_{rc}, the concrete stress reaches zero. Upon further unloading, the concrete stress becomes tensile while the steel stress remains compressive. Then at point C concrete cracks. After cracking, the concrete stress drops to zero, while the steel stress reflects the tension stiffening effect.

It is apparent from Fig. 5.7d that in order to incorporate load reversal in the tension stiffening model of Fig. 5.6, the origin of the reinforcing steel stress-strain curve has to be shifted from point D to point B. Such a modified stress-strain curve for the reinforcing steel is shown in Fig. 5.8. If the concrete crack is closing, the secant stiffness corresponding to the largest value of $(\epsilon_s - \epsilon_{rc})$ attained during the load history is used. This is illustrated graphically in Fig. 5.8. Crack opening occurs along path ABC, while crack closing occurs along path BO.

As can be seen from Fig. 5.8, the tension stiffening effect is assumed to be negligible when $(\epsilon_s - \epsilon_{rc})$ exceeds ϵ_y. Furthermore, it is assumed that there is no tension stiffening effect if the concrete has been previously crushed.

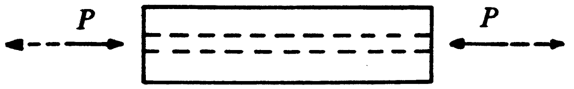

(a) REINFORCED CONCRETE ELEMENT

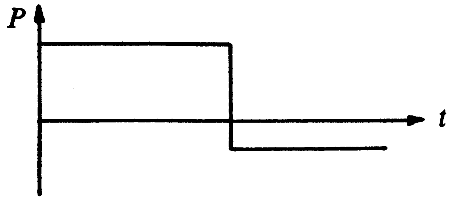

(b) LOAD HISTORY

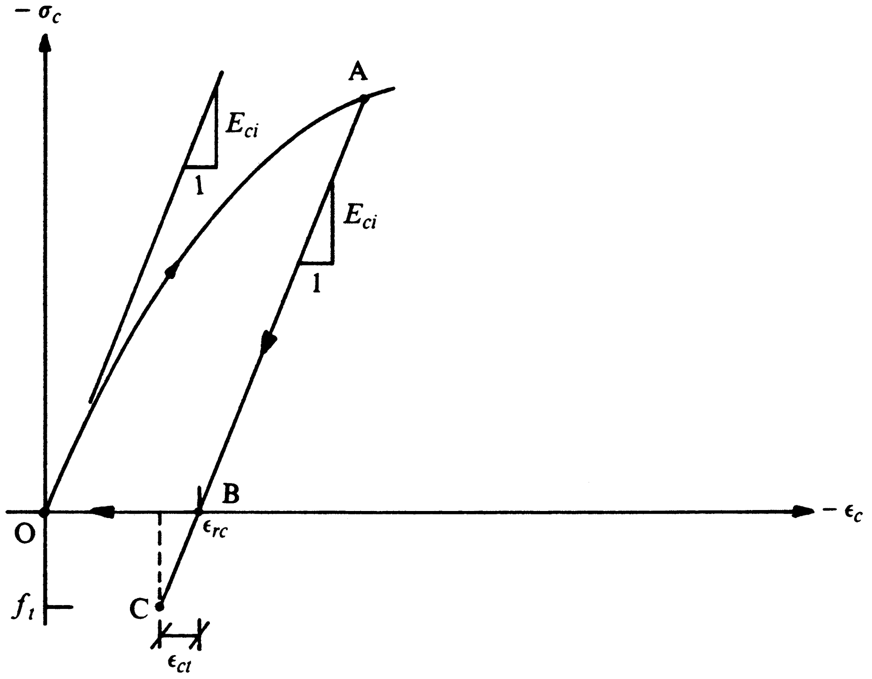

(c) CONCRETE STRESS-STRAIN HISTORY

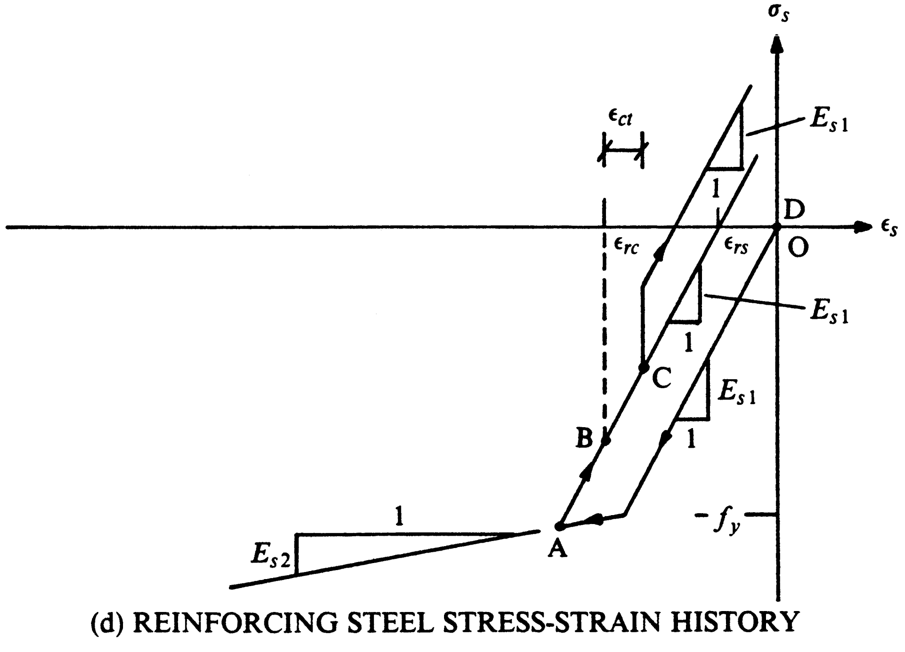

(d) REINFORCING STEEL STRESS-STRAIN HISTORY

FIG. 5.7 TENSION STIFFENING WITH LOAD REVERSAL

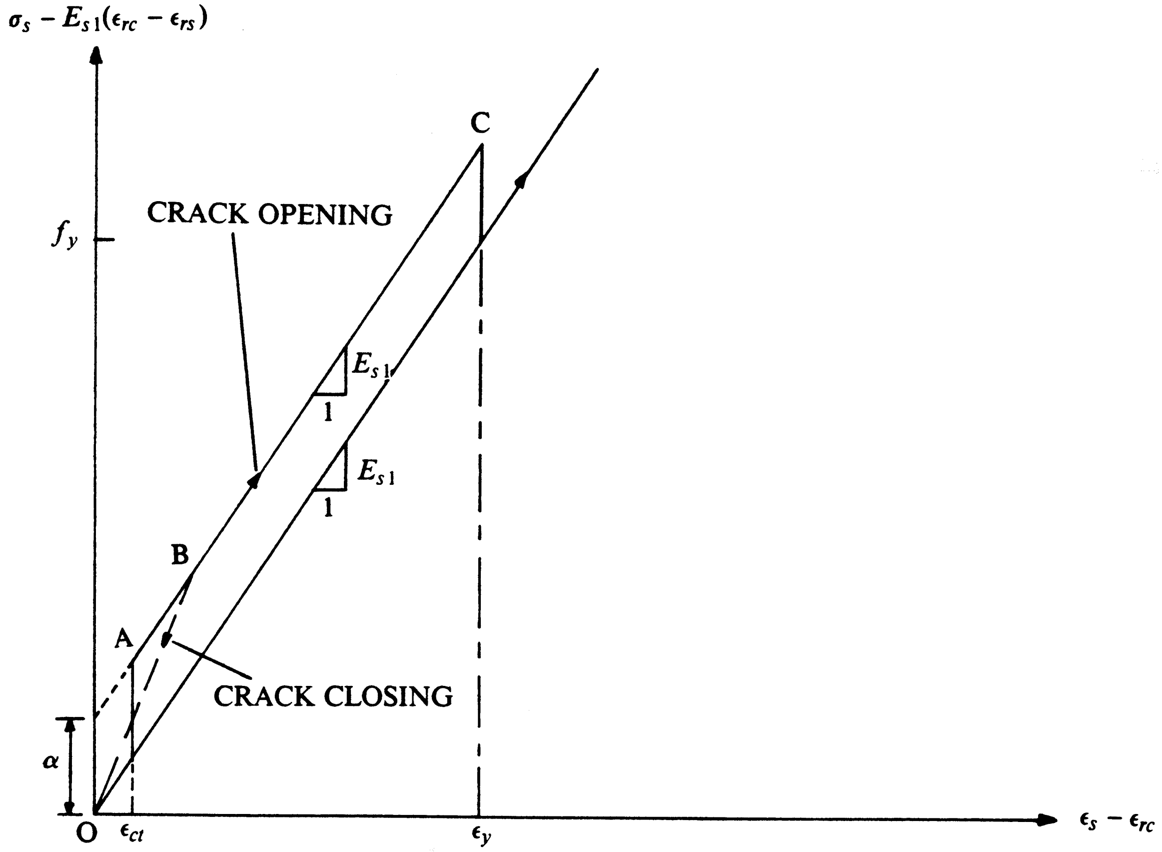

FIG. 5.8 MODIFIED STRESS-STRAIN CURVE FOR REINFORCING STEEL FILAMENT INCLUDING TENSION STIFFENING EFFECT WITH LOAD REVERSAL

5.2.2 $\tau_{xs} - \gamma_{xs}$ Relationship

A study of the shear strain-displacement relationship in Eqs. (2.51) and (2.52) reveals that the shear strains are constant along the webs of the box beam cross section, but vary as rational functions of y along the flanges and the side cantilevers. The variation of the shear strains along the flanges and the cantilevers arises due to the curved nature of the box beam element. For curved bridges encountered in practice, the effect of bridge curvature on the shear strain distributions along the flanges and the cantilevers, predicted by Eq. (2.52), will be small. Hence in the present study, for the evaluation of element properties related to shear deformations, the cross section of the reinforced concrete box beam element is subdivided into the left web, the right web, the bottom flange, and the top flange including the side cantilevers, as shown in Fig. 5.9. Each of these four walls is assumed to be in a state of constant shear. The geometric and material properties of each wall are referred to its mid-point. Then any integration over the cross section associated with shear deformations, such as the second integral in Eq. (2.54) required to evaluate the element stiffness matrix, can be performed as follows.

$$\int_A \phi_\gamma \, dA = \phi_{\gamma_t} A_t + \phi_{\gamma_b} A_b + \phi_{\gamma_l} A_l + \phi_{\gamma_r} A_r \tag{5.22}$$

where ϕ_γ is a function of material and geometric properties related to shear deformations; A is cross sectional area; and the subscripts t, b, l and r refer to top flange including side cantilevers, bottom flange, left web and right web respectively.

It is then necessary to model the shear stress-strain relationships for the individual walls of the box cross section. In a reinforced concrete member subjected to shear, three major events occur. While the reinforced concrete member initially acts like a homogeneous material, the first major event occurs when the concrete cracks. The second major event occurs when the reinforcing steel yields, and the third and final event takes place when the member actually fails due to crushing of concrete. The above findings naturally apply only to under-reinforced members where yielding of the reinforcement occurs well before crushing of concrete. Only this type of under-reinforced members is considered in this study. These three major events suggest a trilinear model for the shear response of reinforced concrete members.

5.2.2a Trilinear Model

A typical trilinear model used to represent the shear stress-strain relationship in the present study is shown in Fig. 5.10. The initial response is assumed to be linear elastic until concrete cracks at a shear stress of τ_{cr}. The initial shear stiffness G_i for this linear elastic branch is taken as

$$G_i = \frac{E_{ci}}{2(1 + \nu)} \tag{5.23}$$

where E_{ci} is the initial tangent modulus of concrete defined previously in Sec. 5.2.1a, and ν is the Poisson's ratio of concrete whose value varies between 0.16 and 0.30 for normal weight concrete.

Numerous experimental and theoretical investigations define the cracking shear in a reinforced concrete member in different ways. In the present study, the cracking shear stress τ_{cr} is taken to be the same as the shear resistance of concrete in a reinforced concrete member. The shear stresses along the walls of the box beam cross section will in general be due to the combined effects of bending, torsion, distortion and warping. Thus far, it has not been possible to account for all the factors affecting the shear resistance of concrete under such combined effects. It is, however, generally accepted that the major factor affecting the shear resistance of concrete is its tensile strength. Thus in this study, the shear resistance of concrete, and hence the cracking shear stress τ_{cr}, is simply assumed to depend solely on the concrete properties, and is specified directly for each different concrete in the structure. It is suggested that τ_{cr} be specified as a fraction of the tensile strength of concrete f_t. The simple conservative expression

$$\tau_{cr} = 2\sqrt{f_c'} \text{ psi} \tag{5.24}$$

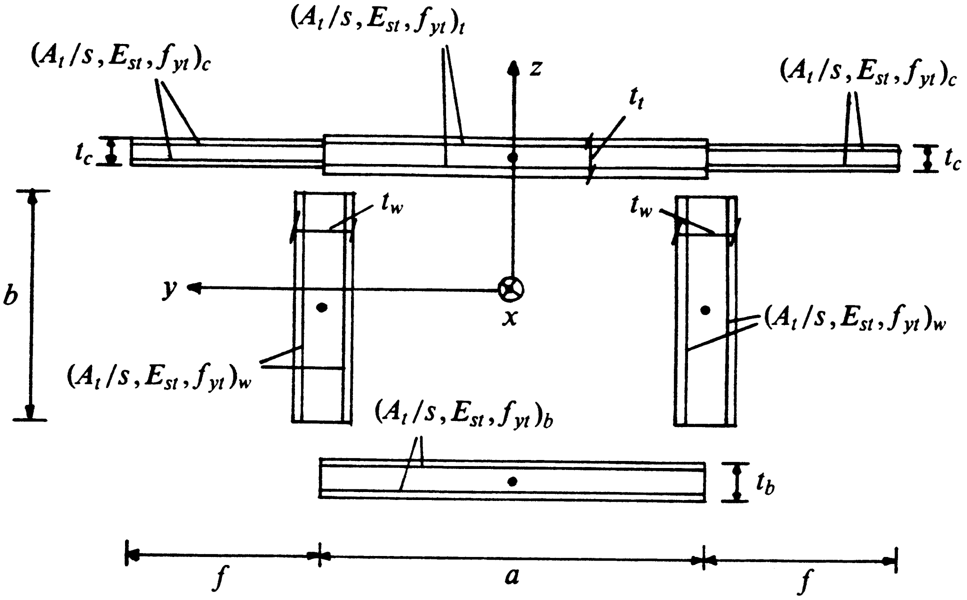

FIG. 5.9 IDEALIZATION OF BOX BEAM CROSS SECTION FOR EVALUATION OF SHEAR RESPONSE

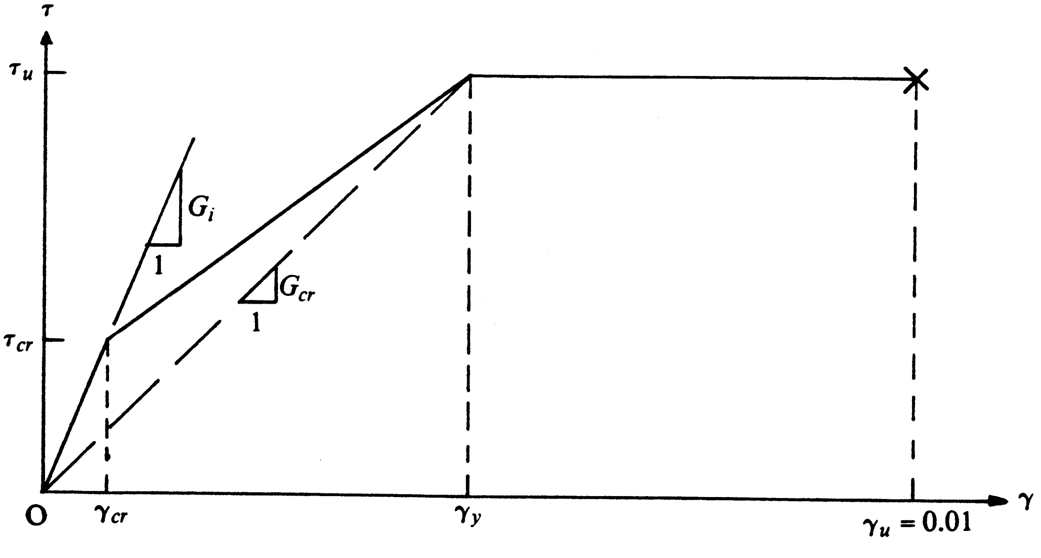

FIG. 5.10 TRILINEAR MODEL FOR SHEAR STRESS-STRAIN RELATIONSHIP

recommended by the AASHTO [49] and ACI [50] codes for reinforced concrete beams in flexure can be used as a guideline.

The cracked shear stiffness G_{cr} (Fig. 5.10) used in the present study is based on the 45^0 truss analogy. The truss is assumed to consist of rigid chords in the longitudinal direction, shear reinforcement in the transverse direction, and 45^0 diagonal concrete struts. Then applying a unit shear deformation to the truss model, the associated shear stiffness is determined from the elongation and shortening of the stirrups (transverse reinforcing steel) and concrete struts respectively. The cracked shear stiffness obtained thus can be expressed as

$$G_{cr} = \frac{\rho_t}{1 + 4n\rho_t} E_{st} \tag{5.25}$$

where $\rho_t = A_t/st$ is the transverse reinforcement ratio; $n = E_{st}/E_{ci}$ is the modular ratio; E_{st} is the modulus of elasticity of the transverse steel; A_t is the area of the transverse reinforcement; s is the spacing of the transverse reinforcement; and t is the thickness of the wall of the box cross section under consideration. A detailed derivation of Eq. (5.25) can be found in [51].

A comparison of Eqs. (5.23) and (5.25) indicates that the cracked shear stiffness is approximately 10 to 30% of the initial uncracked shear stiffness, depending on the amount of transverse reinforcement provided. This highlights the importance of considering the effect of cracking on the shear stiffness of reinforced concrete members.

The ultimate shear stress τ_u in Fig. 5.10 is obtained as a sum of the shear resistance of concrete and the shear resistance of the transverse reinforcement [49, 50].

$$\tau_u = \tau_{cr} + \rho_t f_{yt} \tag{5.26}$$

where τ_{cr} is the shear resistance of concrete, assumed to be the same as the cracking shear stress; $\rho_t f_{yt}$ is the shear resistance of the transverse reinforcement determined from the 45^0 truss analogy; and f_{yt} is the yield stress of the transverse reinforcing steel.

Experiments have indicated that the ultimate shear strain γ_u in reinforced concrete members usually lies between 0.01 and 0.02. In the present study, a conservative value of

$\gamma_u = 0.01$ is used, as shown in Fig. 5.10. Shear failure in the walls of the box cross section is assumed to occur when the shear strain exceeds γ_u.

The trilinear shear stress-strain relationship in Fig. 5.10 is completely defined by the parameters G_i, τ_{cr}, G_{cr}, τ_u and γ_u discussed above. The cracking shear strain γ_{cr} and the yield shear strain γ_y indicated in Fig. 5.10 are given by:

$$\gamma_{cr} = \frac{\tau_{cr}}{G_i} \tag{5.27}$$

$$\gamma_y = \frac{\tau_u}{G_{cr}} \tag{5.28}$$

In the above formulation, evaluation of the cracked shear stiffness G_{cr} and the ultimate shear stress τ_u involves the transverse reinforcement area per unit longitudinal length A_t/s, and the material properties E_{st}, f_{yt} of the transverse steel. These are specified separately for each wall of the box section, as shown in Fig. 5.9. Since the top flange and the side cantilevers are idealized as one member for the evaluation of shear properties, the possible variation of A_t/s, E_{st}, f_{yt}, as well as the wall thickness t, between the top flange and the side cantilevers must be considered in the evaluation of G_{cr} and τ_u. This is done by determining G_{cr} and τ_u separately for the top flange and the side cantilevers, and then using the area-weighted mean values.

5.2.2b Superposition Model for Load Reversal

In order to facilitate the mathematical formulation of load reversal in shear, the trilinear response shown in Fig. 5.10 is modelled as a superposition of two components, each exhibiting elastic-perfectly plastic behavior (Fig. 5.11a). This approach was used by Chan [31] to model load reversal for a trilinear torque-twist relationship.

The initial stiffnesses G_1 and G_2 for the two components in Fig. 5.11a are found by solving the simulataneous equations

$$G_1\gamma_{cr} + G_2\gamma_{cr} = \tau_{cr} \tag{5.29a}$$

$$G_1\gamma_{cr} + G_2\gamma_y = \tau_u \tag{5.29b}$$

The solutions are

$$G_1 = G_i - G_2 \tag{5.30}$$

$$G_2 = \frac{\tau_u - \tau_{cr}}{\gamma_y - \gamma_{cr}} \tag{5.31}$$

The yield stresses for the two components are then

$$\tau_{y1} = G_1\gamma_{cr} \tag{5.32}$$

$$\tau_{y2} = G_2\gamma_y \tag{5.33}$$

The parameters G_1, G_2, τ_{y1}, τ_{y2} expressed above completely define the two components in Fig. 5.11a. The slope of the load reversal path in each component is assumed to be the same as its initial stiffness. The resulting trilinear response for shear with load reversal, which is obtained by superposing the two components in Fig. 5.11a, is shown in Fig. 5.11b.

Five different material states are defined in Fig. 5.11b. These are described below along with the corresponding equations for the stress τ and the tangent stiffness G_t. In the following equations, γ_{r1} and γ_{r2} are the residual shear strains due to unloading for the two components in Fig. 5.11a.

(1) In primary loading or unloading prior to cracking (path OA or AO)

$$\tau = G_i\gamma \ ; \ G_t = G_i \tag{5.34}$$

(2) Cracked but not yielded (path AC, JK or FH)

$$\tau = \pm\tau_{y1} + G_2(\gamma - \gamma_{r2}) \ ; \ G_t = G_2 \tag{5.35}$$

(3) Yielded (path CE)

$$\tau = \pm\tau_u \ ; \ G_t = 0 \tag{5.36}$$

(-1) In load reversal path from state 2 or 3 (path BJ, JB, DF or FD)

$$\tau = G_1(\gamma - \gamma_{r1}) + G_2(\gamma - \gamma_{r2}) \ ; \ G_t = G_i \tag{5.37}$$

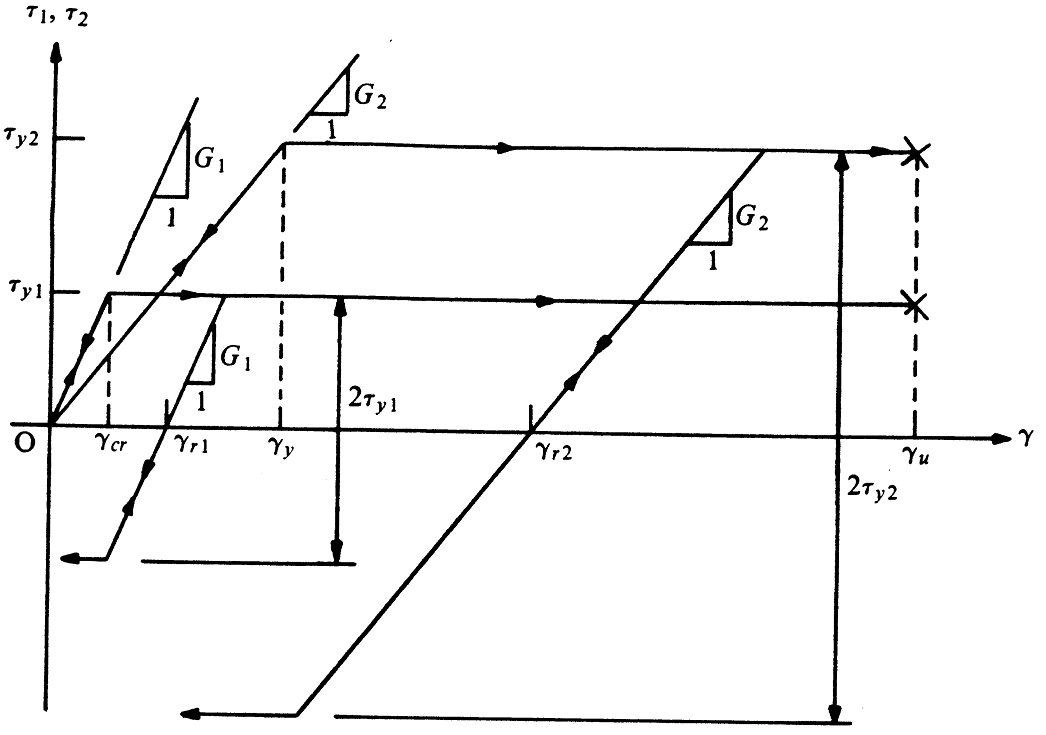

(a) SUPERPOSITION MODEL FOR LOAD REVERSAL

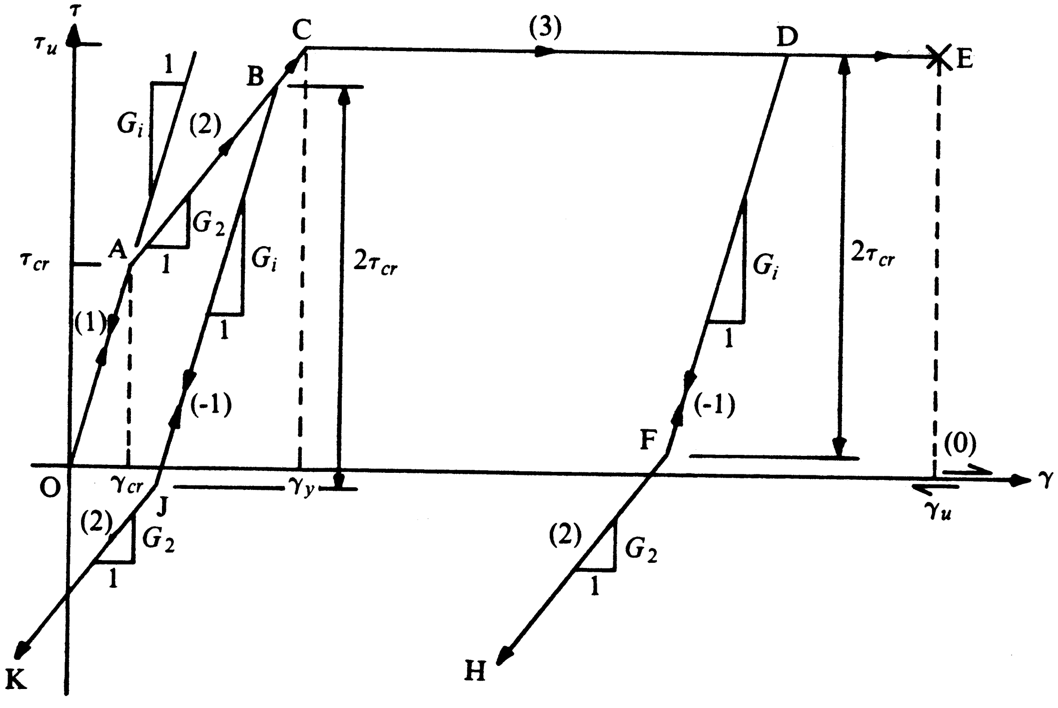

(b) RESULTING LOAD REVERSAL RESPONSE

FIG. 5.11 CONSTITUTIVE MODEL FOR SHEAR WITH LOAD REVERSAL

(0) Failed

$$\tau = 0 \ ; \ G_t = 0 \tag{5.38}$$

The superposition model discussed here is also used to represent the load reversal characteristics in the trilinear $w_4 - v_4$ relationship, as discussed next in Sec. 5.2.3.

5.2.3 $w_4 - v_4$ Relationship

The nonlinear constitutive relationship for the generalized stress w_4 and the generalized strain v_4 is obtained from a flexural analysis of the box beam cross section as a transverse reinforced concrete frame of unit width in the longitudinal direction. The transverse frame consists of four flexural members (Fig. 5.12a): the top flange, the bottom flange, the left web and the right web. The left web and the right web are assumed to have identical transverse reinforcement so that the transverse frame is symmetric about the z axis.

The cross section of each member of the frame is assumed to be reinforced with two equal layers of transverse reinforcing steel in opposite faces, placed symmetrically about the mid-depth (Fig. 5.12b). The total area of the transverse reinforcing steel in the cross section of unit width is designated as $a_t = A_t / s$, and the concrete cover to the centroid of each layer of reinforcement is designated as d'. The overall depth of the cross section, t, corresponds to the thickness of the walls of the box section. If the transverse reinforcement actually consists of only one layer at the mid-thickness of the flanges or the webs, d' becomes equal to $t/2$.

5.2.3a Moment-Curvature Relationship

The moment-curvature ($m - \phi$) relationship of the cross section in Fig. 5.12b, assumed to be under-reinforced, is idealized using a trilinear model, as shown in Fig. 5.12c. The flexural rigidity of the initial linear elastic branch prior to cracking is taken as

$$(EI)_i = E_{ci} I_g \tag{5.39}$$

where $I_g = t^3/12$ is moment of inertia of the gross concrete section about centroidal axis, neglecting reinforcement.

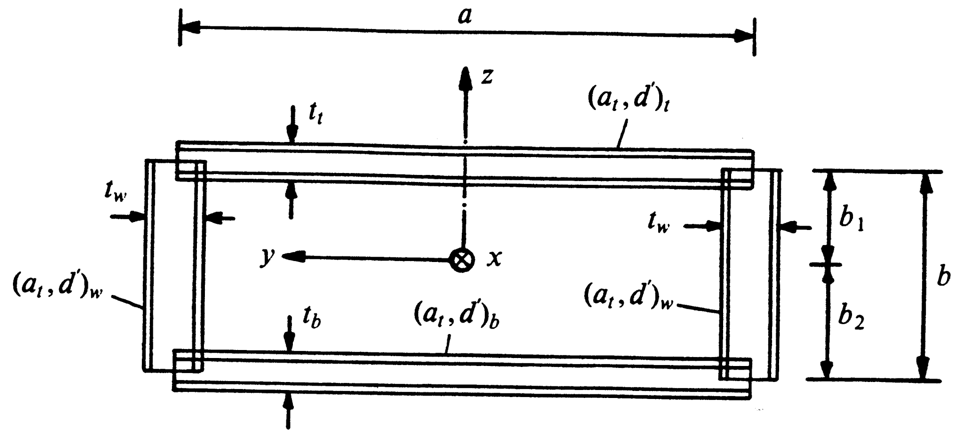

(a) TRANSVERSE FRAME

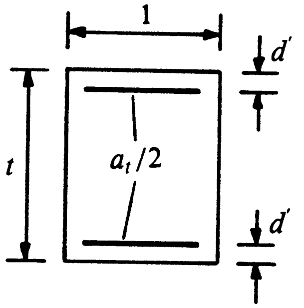

(b) CROSS SECTION OF TRANSVERSE FRAME MEMBER

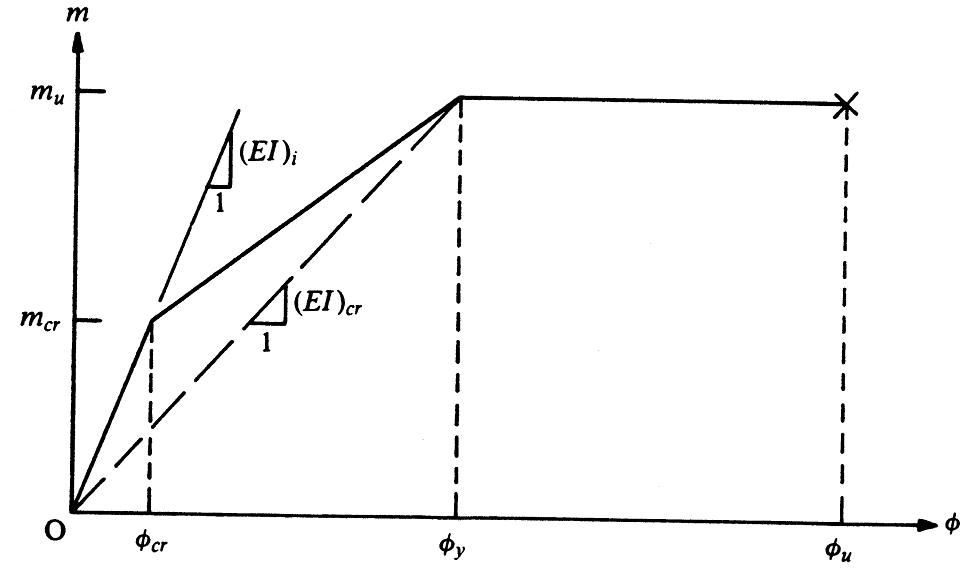

(c) TRILINEAR MOMENT-CURVATURE RELATIONSHIP OF CROSS SECTION

FIG. 5.12 IDEALIZATION OF BOX BEAM CROSS SECTION FOR TRANSVERSE BENDING ANALYSIS

Concrete cracking is assumed to occur when the extreme fiber tensile stress exceeds the tensile strength f_t of concrete, and this gives a cracking moment per unit length of

$$m_{cr} = \frac{f_t t^2}{6} \tag{5.40}$$

The cracked flexural rigidity $(EI)_{cr}$ in Fig. 5.12c is taken as

$$(EI)_{cr} = E_{ci} I_{cr} \tag{5.41}$$

where I_{cr} is moment of inertia of the cracked section transformed to concrete (Fig. 5.13a). Ignoring the small area of concrete displaced by the compression steel, analysis of the transformed section in Fig. 5.13a gives

$$I_{cr} = \frac{(kd)^3}{3} + \frac{na_t}{2}[(d - kd)^2 + (kd - d')^2] \tag{5.42}$$

$$kd = -\, na_t + \sqrt{na_t(na_t + t)} \tag{5.43}$$

where n is the modular ratio, kd is the depth of the neutral axis measured from the extreme compression fiber, and $d = t - d'$ is the distance from the extreme compression fiber to the centroid of tension reinforcement.

The ultimate moment per unit length, m_u, in Fig. 5.12c is determined based on the assumption of an equivalent rectangular concrete stress distribution, as recommended by the AASHTO [49] and ACI [50] codes. The assumed strain and stress distributions at ultimate are shown in Fig. 5.13b and c for singly reinforced ($d' = t/2$) and doubly reinforced sections, respectively. In accordance with the requirement for a practical section, the tension steel is assumed to yield at ultimate. The compression steel in the doubly reinforced section (Fig. 5.13c) will not yield in compression since the compression and tension steel areas are equal. It may however be actually in tension.

Applying conditions of equilibrium and compatibility of strains in Fig. 5.13b and c, the neutral axis depth c is obtained as follows:

For singly reinforced section,

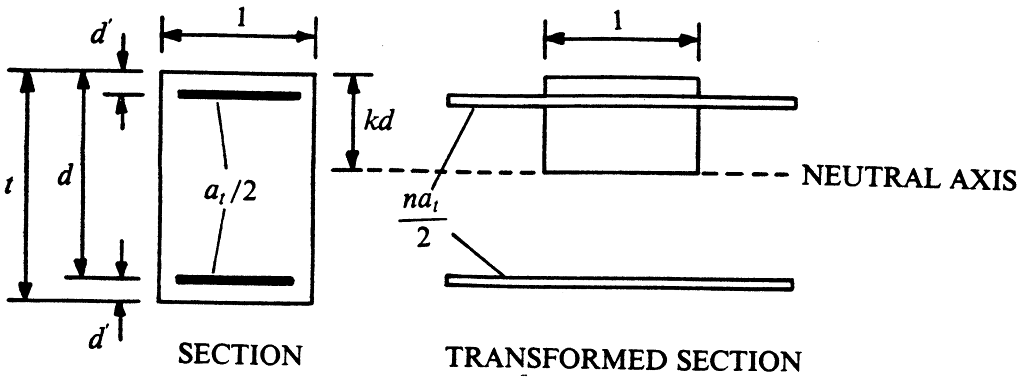

(a) CRACKED SECTION TRANSFORMED TO CONCRETE

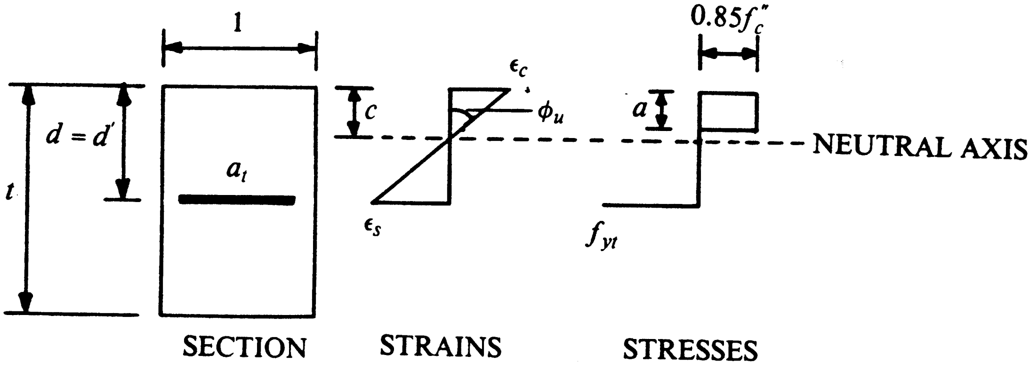

(b) STRAINS AND STRESSES AT ULTIMATE FOR SINGLY REINFORCED SECTION

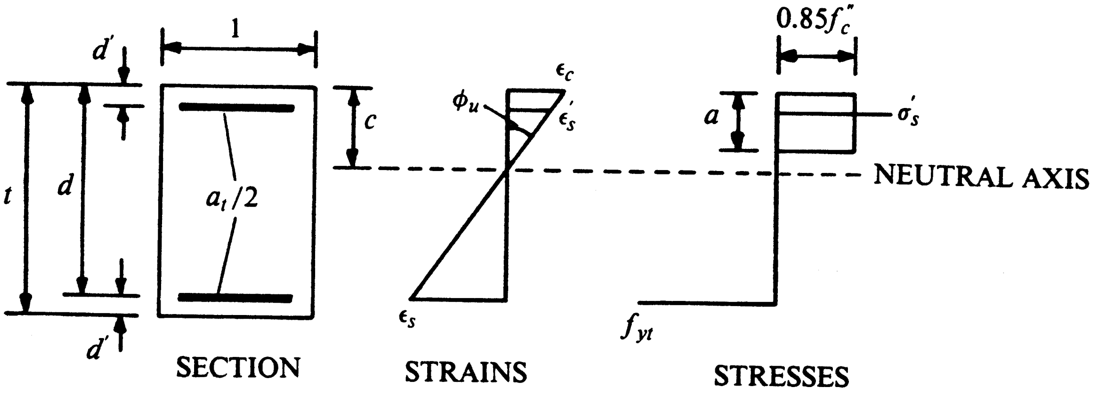

(c) STRAINS AND STRESSES AT ULTIMATE FOR DOUBLY REINFORCED SECTION

FIG. 5.13 FLEXURAL ANALYSIS OF CROSS SECTION OF TRANSVERSE FRAME MEMBER

$$c = \frac{f_{yt} a_t}{0.85 \beta_1 f_c''} \tag{5.44a}$$

For doubly reinforced section,

$$c = \frac{\sqrt{\frac{a_t^2}{4}(E_{st}\epsilon_c - f_{yt})^2 + 1.7\beta_1 f_c'' a_t E_{st}\epsilon_c d'} - \frac{a_t}{2}(E_{st}\epsilon_c - f_{yt})}{1.7\beta_1 f_c''} \tag{5.44b}$$

In Eq. (5.44) above, ϵ_c is the strain at the extreme concrete compression fiber, $\beta_1 = a/c$, a is the depth of the equivalent rectangular concrete stress block, and all other quantities are as defined previously.

The ultimate moment m_u per unit length is then given by:

For singly reinforced section,

$$m_u = a_t f_{yt}(d' - 0.5a) \tag{5.45a}$$

For doubly reinforced section,

$$m_u = 0.85 f_c'' a(d - 0.5a) + 0.5 a_t E_{st}\epsilon_c(1 - d'/c)(d - d') \tag{5.45b}$$

From the strain distributions in Fig. 5.13b and c, the ultimate curvature ϕ_u is found to be

$$\phi_u = \frac{\epsilon_c}{c} \tag{5.46}$$

In the above equations, the values of β_1 and ϵ_c need to be known. The ACI code [50] recommends that β_1 be taken as 0.85 for concrete strengths f_c' up to and including 4,000 psi, and be reduced continuously at a rate of 0.05 for each 1,000 psi of strength in excess of 4,000 psi, but β_1 shall not be taken less than 0.65. For the ultimate moment (m_u) calculations, the value of the strain at the extreme concrete compression fiber is taken as $\epsilon_c = 0.003$. For the ultimate curvature (ϕ_u) calculations , however, a value of $\epsilon_c = 0.003$ is believed to be too conservative, and hence a value of $\epsilon_c = 0.004$, suggested by Park and Paulay [51], is used.

Finally, the cracking curvature ϕ_{cr} and the yield curvature ϕ_y in Fig. 5.12c are given by:

$$\phi_{cr} = \frac{m_{cr}}{(EI)_i} \tag{5.47}$$

$$\phi_y = \frac{m_u}{(EI)_{cr}} \tag{5.48}$$

5.2.3b Trilinear Model

The $w_4 - v_4$ relationship for the transverse frame in Fig. 5.12a can now be found by imposing increasing values of the corner displacements in Fig. 2.2b corresponding to the generalized strain v_4, and then analyzing the frame for the associated generalized stress w_4. The resulting response, based on the moment-curvature characteristics in Fig. 5.12c, is shown by the dashed lines in Fig. 5.14. The initial response is linear elastic until at A, the moment per unit length at the top (m_t) or the bottom (m_b) corners of the frame exceeds the critical m_{cr} at those corners, and cracking occurs. After cracking, the response becomes nonlinear. The next major event occurs at B, when plastic hinges are formed at either the top or the bottom corners of the frame due to the moment per unit length reaching the critical m_u at those corners. Then at C, plastic hinges form at the remaining two corners, and this results in a mechanism. Beyond C, the response is perfectly plastic until failure occurs at D, when the plastic hinge rotation capacity is exceeded at either the top or the bottom corners of the frame.

In this study, an idealized trilinear model, shown by the solid lines in Fig. 5.14, is used to represent the $w_4 - v_4$ relationship. Prior to cracking, the flexural rigidities of the frame members are given by Eq. (5.39), and hence the initial generalized stiffness D_i in Fig. 5.14 is obtained as

$$D_i = \frac{24E_{ci}}{a}[I_{gt}(1 - \theta_t) + I_{gb}(1 - \theta_b)] \tag{5.49}$$

where θ_t and θ_b (Fig. 2.2b) are given by

$$\theta_t = 1 - \frac{2I_{gw}^2 a^2 + 6I_{gw} I_{gb} ab}{2I_{gt} I_{gw} ab + 3I_{gt} I_{gb} b^2 + I_{gw}^2 a^2 + 2I_{gw} I_{gb} ab} \tag{5.50}$$

$$\theta_b = 1 - \frac{2I_{gw}^2 a^2 + 6I_{gw} I_{gt} ab}{I_{gt} I_{gw} ab + 3I_{gt} I_{gb} b^2 + I_{gw}^2 a^2 + 2I_{gw} I_{gb} ab} \tag{5.51}$$

and $I_{gt} = t_t^3/12, I_{gb} = t_b^3/12, I_{gw} = t_w^3/12$ are moments of inertia of gross concrete sections for top flange, bottom flange and webs respectively.

The moments per unit length at the top and the bottom corners, prior to cracking, are

$$m_t = \frac{6E_{ci} I_{gt}}{a}(1 - \theta_t) v_4 \tag{5.52}$$

$$m_b = \frac{6E_{ci} I_{gb}}{a}(1 - \theta_b) v_4 \tag{5.53}$$

The critical cracking moment per unit length at the top corners, $m_{cr,t}$, is the minimum of the values calculated from Eq. (5.40) for the top flange and the webs. Similarly, the critical cracking moment per unit length at the bottom corners, $m_{cr,b}$, is the minimum of the values calculated from Eq. (5.40) for the bottom flange and the webs. By equating $m_{cr,t}$ and $m_{cr,b}$ to m_t and m_b respectively in Eqs. (5.52) and (5.53), two values of v_4 are obtained, and the minimum of these two values is taken as the generalized cracking strain $v_{4,cr}$ in Fig. 5.14. With $v_{4,cr}$ thus determined, the generalized cracking stress $w_{4,cr}$ is given by

$$w_{4,cr} = D_i v_{4,cr} \tag{5.54}$$

In the ultimate range ED (Fig. 5.14), the moment per unit length, $m_{u,t}$, at the top corners of the frame will be the minimum of the m_u values calculated from Eq. (5.45) for the top flange and the webs. Similarly, the moment per unit length, $m_{u,b}$, at the bottom corners of the frame will be the minimum of the m_u values calculated from Eq. (5.45) for the bottom flange and the webs. Then from the principle of virtual displacements, the generalized ultimate stress $w_{4,u}$ is easily obtained as

$$w_{4,u} = 4(m_{u,t} + m_{u,b}) \tag{5.55}$$

The generalized cracked stiffness D_{cr} in Fig. 5.14 is estimated based on an effective flexural rigidity $E_{ci} I_e$ for each frame member. The following empirical expression developed by Branson [52], and subsequently recommended by the AASHTO [49] and ACI [50] codes, is used to calculate the effective moment of inertia I_e.

$$I_e = \left[\frac{m_{cr}}{m_a}\right]^3 I_g + \left[1 - \left[\frac{m_{cr}}{m_a}\right]^3\right] I_{cr} \tag{5.56}$$

where for the present application, m_a is the maximum moment per unit length at stage defined by $(v_{4,y}, w_{4,u})$ in Fig. 5.14. For the top flange $m_a = m_{u,t}$, for the bottom flange $m_a = m_{u,b}$, and for the webs $m_a = \max\,(m_{u,t}, m_{u,b})$. The effective moment of inertia is thus calculated for each frame member, and the generalized cracked stiffness is estimated as

$$D_{cr} = \frac{24E_{ci}}{a}[I_{et}(1 - \theta_t) + I_{eb}(1 - \theta_b)] \tag{5.57}$$

where I_{et} and I_{eb} are the effective moments of inertia for the top and the bottom flanges respectively; θ_t and θ_b are again calculated from Eqs. (5.50) and (5.51) respectively, but with the gross moments of inertia replaced by the corresponding effective moments of inertia.

If it is assumed that $E_{ci}I_e$, with I_e given by Eq. (5.56), does represent the exact secant stiffness of the frame members, the value of D_{cr} calculated as above will lie between the secant stiffnesses at points B and C in Fig. 5.14. At point B, when the first two plastic hinges form at either the top or the bottom corners of the frame, the moment per unit length at the other two corners is less than the ultimate value ($m_{u,t}$ or $m_{u,b}$) at those locations. The actual value of m_a in Eq. (5.56) will then be smaller than the ultimate values ($m_{u,t}$, $m_{u,b}$) for one or more of the transverse frame members, thus resulting in a higher secant stiffness than D_{cr}. At point C, when plastic hinges just form at all four corners, the corner moments are as assumed in the calculation of D_{cr}. But D_{cr} in Eq. (5.57) is obtained from an analysis of a continuous frame (i.e., no hinges at any corner) although the response between points B and C does involve hinges at two corners. Thus the secant stiffness at C will be less than D_{cr}. In the special case when the moment-curvature relationships (Fig. 5.12c) for the top and the bottom flange sections are identical, points B, C and E in Fig. 5.14 will coincide.

The generalized yield strain $v_{4,y}$ in Fig. 5.14 is given by

$$v_{4,y} = \frac{w_{4,u}}{D_{cr}} \tag{5.58}$$

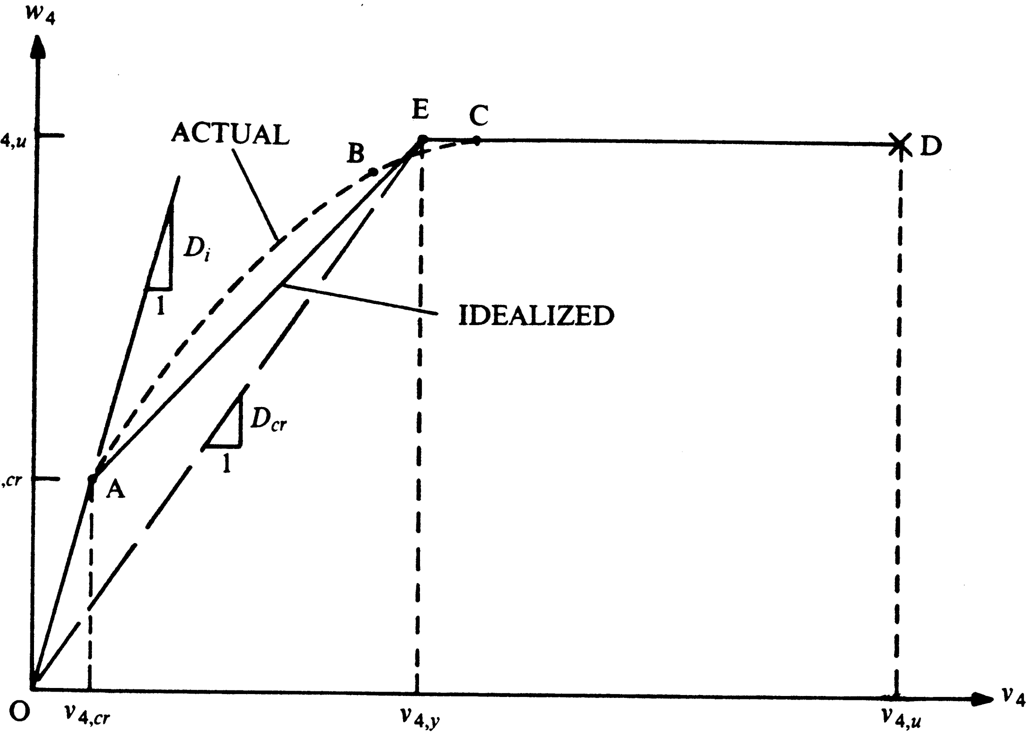

FIG. 5.14 TRILINEAR MODEL FOR w_4–v_4 RELATIONSHIP

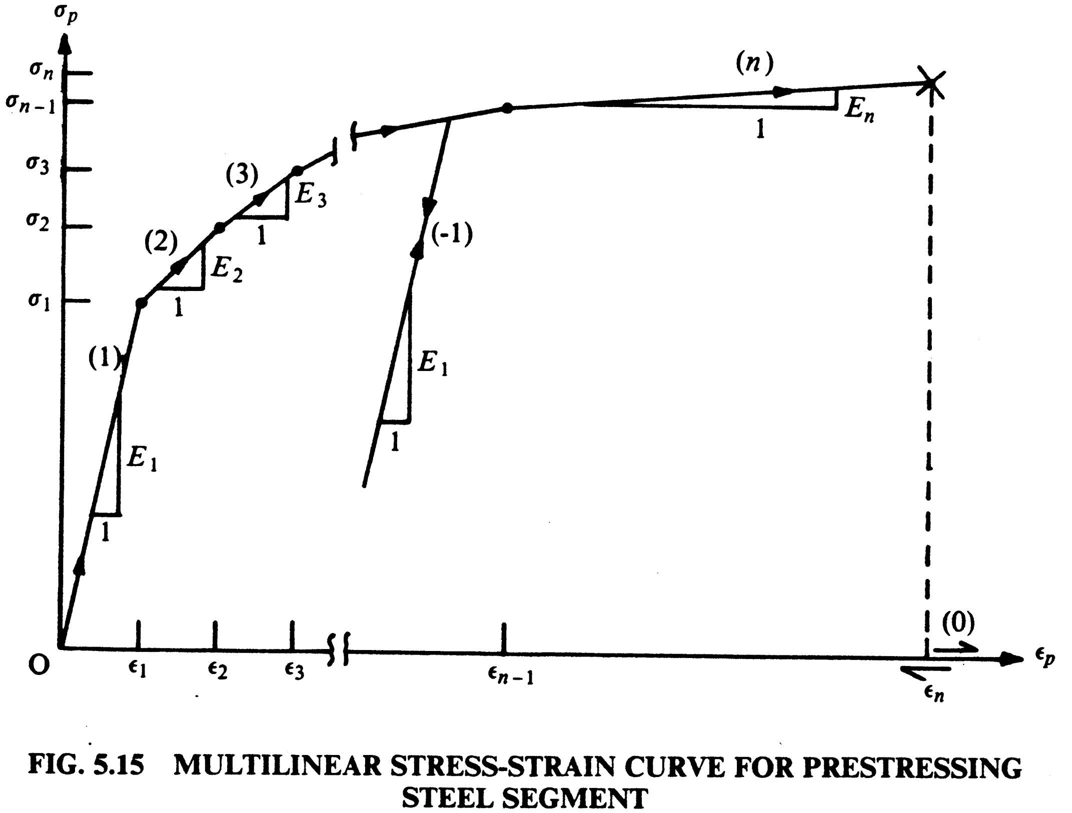

FIG. 5.15 MULTILINEAR STRESS-STRAIN CURVE FOR PRESTRESSING STEEL SEGMENT

The generalized ultimate strain, $v_{4,u}$, is governed by the rotation capacities of the plastic hinges at the four corners of the frame. As shown by Park and Paulay [51], the rotation capacity θ_p to one side of the plastic hinge in a reinforced concrete flexural member can be expressed as

$$\theta_p = (\phi_u - \phi_y)l_p \tag{5.59}$$

where ϕ_u and ϕ_y are respectively the ultimate and the yield curvatures of the section (Fig. 5.12c), and l_p is the equivalent length of the plastic hinge over which the plastic curvature $(\phi_u - \phi_y)$ is considered to be constant. Various empirical expressions have been proposed for estimating the plastic hinge length l_p. In this study, the following empirical relationship due to Corley [53] and Mattock [54] is used.

$$l_p = 0.5d + 0.05z \tag{5.60}$$

where d is the effective depth of section, and z is the distance from the critical section to the point of contraflexure. In the present application, $z = a/2$ for the critical sections at the ends of the top and the bottom flanges, $z = m_{u,t}b/(m_{u,t} + m_{u,b})$ for the critical sections at the top ends of the webs, and $z = m_{u,b}b/(m_{u,t} + m_{u,b})$ for the critical sections at the bottom ends of the webs.

After the formation of a mechanism due to plastic hinges at all four corners of the frame, a unit increase in the generalized strain v_4 produces two units of plastic hinge rotation at each corner of the frame (Fig. 2.2b). The generalized ultimate strain at failure can then be estimated as

$$v_{4,u} = v_{4,y} + 0.5\theta_u \tag{5.61}$$

where θ_u is the plastic hinge rotation at the frame corners at failure when the plastic hinge rotation capacity is first reached at either the top or the bottom corners of the frame.

The trilinear constitutive model in Fig. 5.14 is then completely defined. To model the load reversal characteristics and the associated material states, exactly the same superposition model used for shear response (Sec. 5.2.2b, Fig. 5.11) is employed.

5.3 Prestressing Steel Segment

The stress-strain curve of prestressing steel need to be known for the formulation of the prestressing steel segment properties. The stress-strain curve of prestressing steel differs from that of reinforcing steel in that it exhibits no definite yield plateau or point. The curve is initially linear until at a stress of about two-thirds of the tensile strength, yielding develops gradually. In the inelastic range, the curve continues to rise smoothly up to the tensile strength. In order to accommodate this behavior, a multilinear model (Fig. 5.15), similar to the one used by Kang [28], is used to represent the prestressing steel stress-strain curve in this study.

Since the prestressing steel is used exclusively in tension, only the tensile stress-strain curve is considered in Fig. 5.15. The strains $\epsilon_1, \epsilon_2, \ldots, \epsilon_n$ and the corresponding stresses $\sigma_1, \sigma_2, \ldots, \sigma_n$ define n linear branches with tangent moduli $E_1, E_2, \ldots, E_n$. The slope of the unloading and reloading path is assumed to be the same as the initial modulus E_1. Failure is assumed to occur when the strain exceeds ϵ_n. For a model with n linear branches, $(n + 2)$ material states are defined, as shown in Fig. 5.15. The material states 1, 2,..., n correspond to the n primary branches. The two additional material states -1 and 0 correspond respectively to unloading-reloading and failure.

5.4 Summary

The nonlinear constitutive models, which form the basis of the nonlinear material analysis in this study, were discussed in detail in this chapter. The uniaxial stress-strain curves of concrete and reinforcing steel, used to represent the behavior of the reinforced concrete box beam element under longitudinal normal strains and stresses, were modelled. The interaction between concrete and reinforcing steel due to the tension stiffening effect was considered by means of a modified stress-strain curve for the reinforcing steel. Trilinear constitutive models were developed for the shear response and the transverse flexural response of the reinforced concrete box beam element. A superposition model based on two bilinear components was used to represent the load reversal characteristics in these trilinear constitutive relationships. Finally, the stress-strain curve of the prestressing steel was modelled using a multilinear idealization.

6. NONLINEAR ANALYSIS PROCEDURE

6.1 General

Due to the nonlinearities in the constitutive relationships discussed in the previous chapter (Chapter 5), the equilibrium equations of the structure of the form

$$\underline{K}\,\underline{r} = \underline{R} \qquad (6.1)$$

will be nonlinear. This chapter deals with the details of the procedure used in this study for the solution of the nonlinear equilibrium equations above.

6.2 Solution Methods for Nonlinear Equilibrium Equations

Various numerical methods are available for the solution of the nonlinear equilibrium equations (Eq. (6.1)). These can generally be classified into three categories as follows.

6.2.1 Incremental Load Method

In this method, the vector of total loads $\underline{R}$ is divided into a number of load increments $\Delta\underline{R}$. Using the tangent stiffness at the beginning of each load increment, the corresponding displacement increments $\Delta\underline{r}$ are found. The vector of total displacements $\underline{r}$ is then obtained by summing the displacement increments $\Delta\underline{r}$. The method is shown schematically in Fig. 6.1a. The solution tends to deviate from the true path unless the load increments $\Delta\underline{R}$ are chosen to be sufficiently small.

An improvement in the incremental load method is achieved by checking the equilibrium after each load increment. The magnitude of discrepancy from the equilibrium state is represented by the unbalanced loads obtained by subtracting the internal resisting loads from the external nodal loads. The unbalanced loads for each load increment are then added to the next load increment. The result is a better approximation of the true load-displacement path, as shown in Fig. 6.1b.

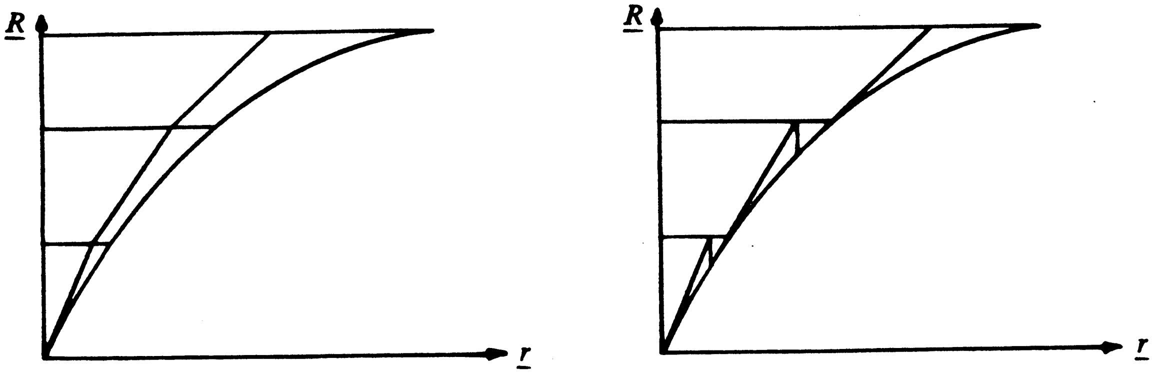

(a) INCREMENTAL LOAD METHOD WITHOUT EQUILIBRIUM CORRECTIONS

(b) INCREMENTAL LOAD METHOD WITH EQUILIBRIUM CORRECTIONS

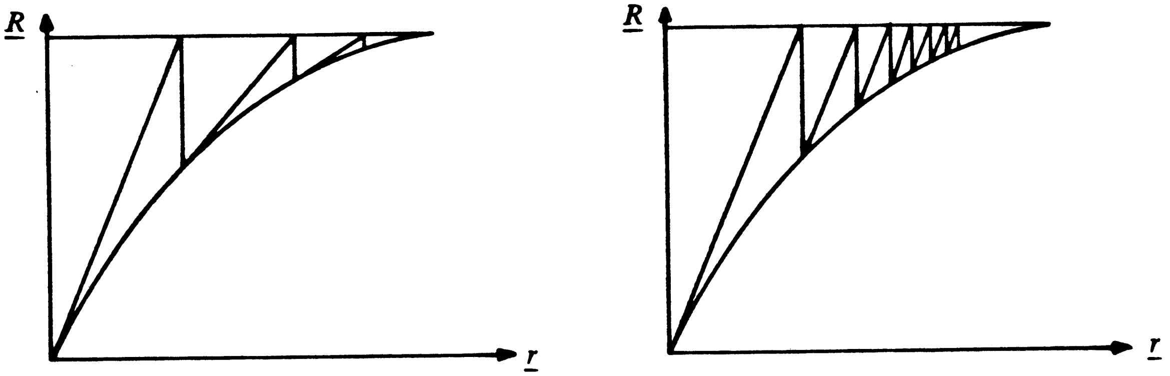

(c) ITERATIVE METHOD WITH TANGENT STIFFNESS

(d) ITERATIVE METHOD WITH INITIAL STIFFNESS

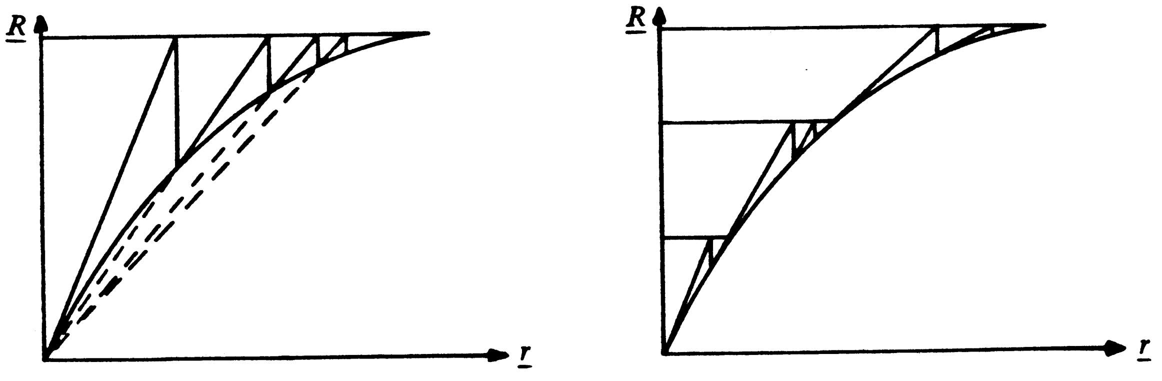

(e) ITERATIVE METHOD WITH SECANT STIFFNESS

(f) COMBINED METHOD

FIG. 6.1 SOLUTION METHODS FOR NONLINEAR EQUILIBRIUM EQUATIONS

6.2.2 Iterative Method

The total loads are applied in one step in the iterative method. A series of iterations are then performed by applying the unbalanced loads until equilibrium is satisfied to the desired degree. Depending on the stiffness matrix used for each iteration, three variations of the iterative method are available.

Tangent Stiffness Method

In this method, often referred to as the Newton-Raphson method, an updated tangent stiffness matrix is used for each iteration (Fig. 6.1c). This leads to the most rapid convergence but has the disadvantage that the tangent stiffness matrix has to be formed and triangularized for each iteration.

Initial Stiffness Method

A modification of the Newton-Raphson method is to perform all iterations with a constant stiffness matrix which is equal to the initial tangent stiffness matrix (Fig. 6.1d). An obvious advantage of this method is that the stiffness matrix has to be formed and triangularized only once. But the convergence is also slower.

Secant Stiffness Method

An attempt is made in this method to find a secant stiffness matrix at each iteration which satisfies the load-displacement relationship as shown in Fig. 6.1e. The secant stiffness matrix is then used for the iterative solution.

6.2.3 Combined Method

The incremental load method and the iterative method can be combined in a variety of ways to try and find a solution scheme best suited to any given problem. Usually the total loads are divided into load increments, and for each load increment one of the three iterative methods is used for better accuracy (Fig. 6.1f).

6.3 Solution Strategies for Present Study

In nonlinear analysis of a reinforced concrete structure, the solution is generally path-dependent mainly due to progressive cracking in tensile regions. Hence the sequence of loading must be considered in the analysis. This is done in the present study by means of a number of "load patterns" applied cumulatively in sequence. Analysis is performed successively for each load pattern, and the incremental solutions are added to the previous totals to obtain the updated cumulative solutions.

The dead load and the prestressing loads at transfer are always applied as the first load pattern. Any other external loads that are present during the transfer of prestress can also be considered as part of the first load pattern. The structure is analyzed as an ordinary reinforced concrete one for the first load pattern. The contribution of the prestressing steel to the overall structural stiffness is neglected since at this stage the steel is unbonded.

Live load history can then be simulated as the second and subsequent load patterns. The last load pattern will normally be the one under which failure analysis of the structure is desired. For the second and subsequent load patterns, the prestressing steel is assumed to be bonded to the concrete and the prestressing steel stiffnesses are included in the overall structural stiffness.

For each load pattern, either a "load control" or a "displacement control" strategy is employed for the solution of the nonlinear equilibrium equations.

6.3.1 Load Control Strategy

Conventionally, the solution of the nonlinear equilibrium equations has been achieved by controlling the loads $\underline{R}$ and solving for the corresponding displacements $\underline{r}$. The methods described in Sec. 6.2 are based on this approach. The load control strategy, as used in the present study, is a combination of the incremental and iterative methods described previously. The total loads for the load pattern are divided into a number of load steps with load increments $\Delta\underline{R}_e$, each of which may be of different magnitudes. Unbalanced load iterations are performed for each load step until certain predefined convergence criteria (Sec. 6.7) are satisfied.

For any displaced state of the structure, let $\underline{r}$ be the vector of nodal displacements, let $\underline{R}_e$ be the vector of accumulated external nodal loads, let $\underline{R}_i$ be the vector of internal resisting loads (i.e., the vector of nodal loads in equilibrium with the internal forces of the structure), and let $\underline{K}_t$ be the tangent stiffness matrix. The vector of unbalanced loads, $\underline{R}_u$, is given by

$$\underline{R}_u = \underline{R}_e - \underline{R}_i \tag{6.2}$$

and provides a measure of the solution error. The accumulated external nodal loads $\underline{R}_e$ for a load step are obtained by adding the load increments $\Delta\underline{R}_e$ to the previous $\underline{R}_e$. The iterative sequence (Fig. 6.2) for the kth iteration in a load step is then as follows:

$$\underline{R}_u^{k-1} = \underline{R}_e - \underline{R}_i^{k-1} \tag{6.3}$$

$$\Delta\underline{r}^k = (\underline{K}_t^k)^{-1}\underline{R}_u^{k-1} \text{ , for } k \le j \tag{6.4a}$$

$$\Delta\underline{r}^k = (\underline{K}_t^j)^{-1}\underline{R}_u^{k-1} \text{ , for } k > j \tag{6.4b}$$

$$\underline{r}^k = \underline{r}^{k-1} + \Delta\underline{r}^k \tag{6.5}$$

$$\underline{R}_i^k = \text{function of } \underline{r}^k \tag{6.6}$$

Eq. (6.6) above represents the "state determination" phase in which the internal forces and the resisting load vector are determined. It is apparent from Eq. (6.4) that a modification of the tangent stiffness and initial stiffness iterations is used. The tangent stiffness is used for the first j iterations, and subsequent iterations are performed with a constant stiffness equal to the tangent stiffness at the jth iteration. The value of j is determined such that a certain predefined criterion related to the convergence of the solution is satisfied (Sec. 6.5).

6.3.2 Displacement Control Strategy

In a nonlinear material analysis, the load-displacement curve of the structure can exhibit strain-softening, as shown in Fig. 6.3. The tangent stiffness matrix of the structure then becomes nonpositive definite at some point in the solution path. The conventional methods

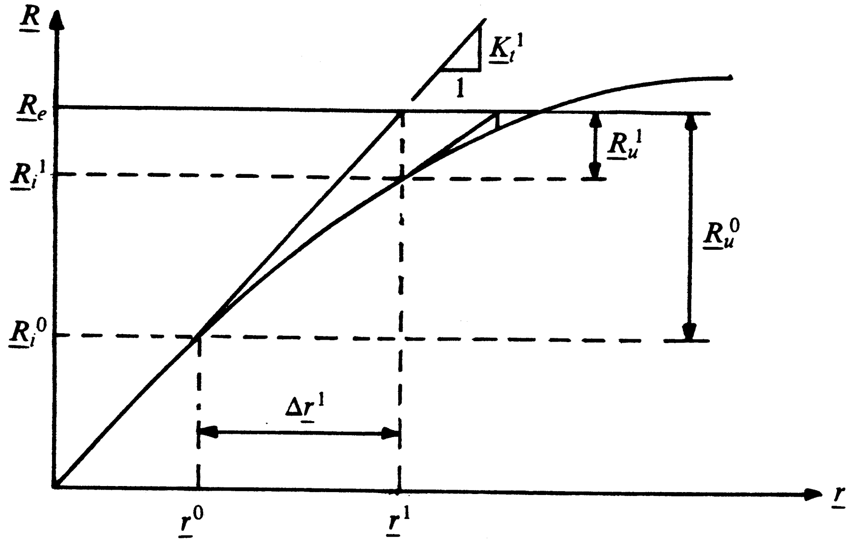

FIG. 6.2 ITERATIVE SEQUENCE FOR LOAD CONTROL STRATEGY

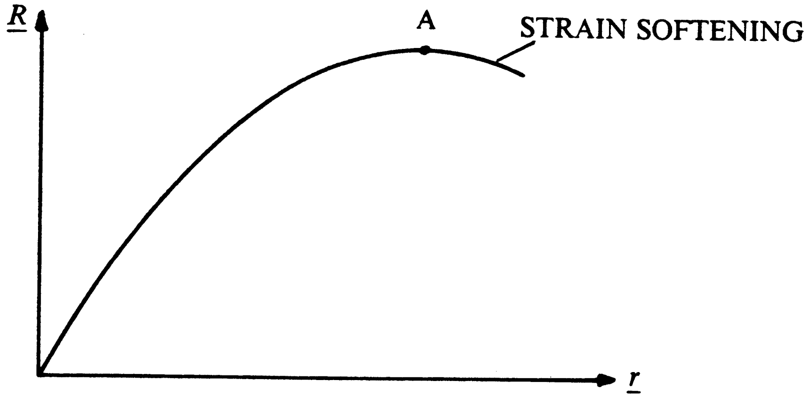

FIG. 6.3 LOAD-DEFLECTION RESPONSE WITH STRAIN-SOFTENING

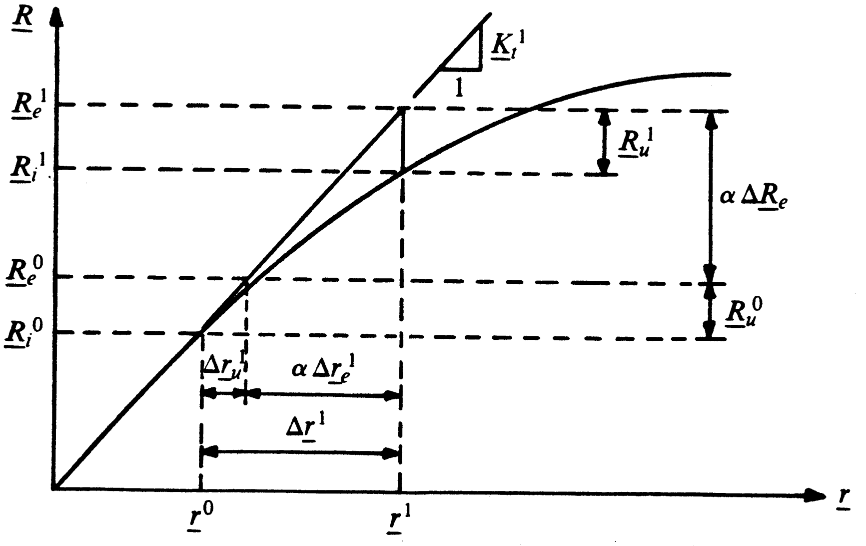

FIG. 6.4 ITERATIVE SEQUENCE FOR DISPLACEMENT CONTROL STRATEGY

for solving the nonlinear equilibrium equations, as discussed in Sec. 6.2, are not applicable in such situations without certain modifications.

Various numerical schemes have been proposed in the past to circumvent the difficulties which arise in treating the nonpositive definiteness of the stiffness matrix, and in passing over the limit point (point A in Fig. 6.3) when the determinant of the stiffness matrix changes sign. Based on a comparative study made by Chan [31], the displacement control strategy proposed by Powell and Simons [55] has been chosen for the present study.

In the displacement control strategy, the analysis for a load pattern consists of a number of displacement steps. For each displacement step, a displacement increment δ is specified at a particular degree of freedom, say n. The displacement increments δ can vary from one displacement step to another, but the controlled degree of freedom n must remain the same. In addition, an increment of external load vector, $\Delta \underline{R}_e$, is specified for the load pattern. This load increment is used to establish only a direction of motion, and hence is of arbitrary magnitude. The analysis for the displacement step is then performed using an iterative procedure based on limiting the displacement increment for the nth degree of freedom to δ. The iterations are terminated when predefined convergence criteria (Sec. 6.7) are satisfied.

At each iteration in a displacement step, separate displacement increments are calculated for $\underline{R}_u$ and $\Delta \underline{R}_e$ as follows.

$$\Delta \underline{r}_u = \underline{K}_t^{-1} \underline{R}_u \tag{6.7}$$

$$\Delta \underline{r}_e = \underline{K}_t^{-1} \Delta \underline{R}_e \tag{6.8}$$

The displacement increments for the iteration are then taken as

$$\Delta \underline{r} = \Delta \underline{r}_u + \alpha \Delta \underline{r}_e \tag{6.9}$$

The value of α must be selected to satisfy the specified limit on the displacement increment for the nth degree of freedom. In mathematical terms,

$$\underline{b}_n^T \Delta \underline{r} = \delta \text{ , for first iteration} \tag{6.10a}$$

$$\underline{b}_n^T \Delta \underline{r} = 0 \ , \text{ for subsequent iterations} \tag{6.10b}$$

where the vector $\underline{b}_n$ contains zeros except for unity at location n. Then from Eqs. (6.9) and (6.10),

$$\alpha = \frac{\delta - \underline{b}_n^T \Delta \underline{r}_u}{\underline{b}_n^T \Delta \underline{r}_e} \ , \text{ for first iteration} \tag{6.11a}$$

$$\alpha = - \frac{\underline{b}_n^T \Delta \underline{r}_u}{\underline{b}_n^T \Delta \underline{r}_e} \ , \text{ for subsequent iterations} \tag{6.11b}$$

The external load increments for the iteration corresponding to the displacement increments $\Delta \underline{r}$ are given by $\alpha \Delta \underline{R}_e$. If the value of α is negative, external loads will be removed during the iteration. This will occur for a progressively softening system. On the other hand, if the value of α is positive, external loads will be added during the iteration. This will occur for a progressively stiffening system.

It may be noted that the tangent stiffness matrix in Eqs. (6.7) and (6.8) need not be positive definite, provided it is nonsingular.

The iterative sequence (Fig. 6.4) for the kth iteration in a displacement step can be summarized as follows:

$$\underline{R}_u^{k-1} = \underline{R}_e^{k-1} - \underline{R}_i^{k-1} \tag{6.12}$$

$$\Delta \underline{r}_u^k = (\underline{K}_t^k)^{-1} \underline{R}_u^{k-1} \ , \text{ for } k \leq j \tag{6.13a}$$

$$\Delta \underline{r}_u^k = (\underline{K}_t^j)^{-1} \underline{R}_u^{k-1} \ , \text{ for } k > j \tag{6.13b}$$

$$\Delta \underline{r}_e^k = (\underline{K}_t^k)^{-1} \Delta \underline{R}_e \ , \text{ for } k \leq j \tag{6.14a}$$

$$\Delta \underline{r}_e^k = (\underline{K}_t^j)^{-1} \Delta \underline{R}_e \ , \text{ for } k > j \tag{6.14b}$$

$$\alpha = \frac{\delta - \underline{b}_n^T \Delta \underline{r}_u^k}{\underline{b}_n^T \Delta \underline{r}_e^k} \ , \text{ for } k = 1 \tag{6.15a}$$

$$\alpha = - \frac{\underline{b}_n^T \Delta \underline{r}_u^k}{\underline{b}_n^T \Delta \underline{r}_e^k} \ , \text{ for } k > 1 \tag{6.15b}$$

$$\Delta \underline{r}^k = \Delta \underline{r}_u^k + \alpha \Delta \underline{r}_e^k \tag{6.16}$$

$$\underline{R}_e^k = \underline{R}_e^{k-1} + \alpha \Delta \underline{R}_e \tag{6.17}$$

$$\underline{r}^k = \underline{r}^{k-1} + \Delta \underline{r}^k \tag{6.18}$$

$$\underline{R}_i^k = \text{function of } \underline{r}^k \tag{6.19}$$

It can be seen from Eqs. (6.13) and (6.14) above that, as in the load control strategy, the tangent stiffness is used for the first j iterations, and a constant stiffness, equal to the tangent stiffness at the jth iteration, is used for the subsequent iterations.

An important characteristic of the displacement control strategy is that the vector of accumulated external nodal loads, $\underline{R}_e$, varies from iteration to iteration and cannot be predetermined. This is in contrast to the load control strategy where $\underline{R}_e$ is predetermined and remains constant for all iterations. If the solution is desired for given external loads, the displacement control strategy cannot be used. This is the case with dead load and prestressing loads at transfer whose magnitudes are fixed and cannot be arbitrarily scaled. Since the dead load and the prestressing loads at transfer are applied as the first load pattern, the load control strategy must be used for this load pattern, unless dead load and prestressing are not included in the analysis.

6.4 State Determination

After each iteration in a load or displacement step of the analysis, the element states (strains, stresses and tangent moduli) are determined for each reinforced concrete box beam element and each prestressing steel segment. These are then used to calculate the internal resisting load vector $\underline{R}_i$ for the iteration (Sec. 6.5) and the tangent stiffness matrix $\underline{K}_t$ for the next iteration (Sec. 6.6).

The element state may be determined using either a "path-dependent" or a "path-independent" scheme. In the path-dependent scheme, the element state at the end of any iteration is determined with reference to the element state at the end of the previous iteration. The final state at the end of all iterations for a load or displacement step thus depends on the path followed during the iterations. In the path-independent scheme, the element state at the end of any iteration is determined with reference to the element state at the beginning of the iterative sequence. The final state thus depends only on the beginning state and the sum of the displacement increments for all iterations, and hence is independent of the iteration path.

If all the element strains increase monotonically during the iterations, there will be no difference between the final states calculated by the two schemes. However, in the analysis of a reinforced or prestressed concrete structure, the element strains often do not increase monotonically. This is even more so when a displacement control strategy is used [55]. Using the path-dependent scheme in such instances can lead to serious errors in the solution. Thus path-independent state determination is used in the present study.

6.4.1 Reinforced Concrete Box Beam Element

At any iteration, let $\underline{r}$ be the updated nodal displacements for the element determined from Eq. (6.5) or (6.18). The current strains can then be determined from the strain-displacement relationships.

$$\epsilon_x = \underline{B}_\epsilon \underline{r} \tag{6.20}$$

$$\gamma_{xs} = \underline{B}_\gamma \underline{r} \tag{6.21}$$

$$v_4 = \underline{B}_v \underline{r} \tag{6.22}$$

The matrices $\underline{B}_\epsilon$, $\underline{B}_\gamma$ and $\underline{B}_v$ are given respectively by Eqs. (2.50), (2.52) and (2.43) derived previously in Sec. 2.6.

The longitudinal normal strains ϵ_x are calculated from Eq. (6.20) at the mid-point of each concrete and longitudinal reinforcing steel filament (Sec. 5.2.1) for the two Gauss quadrature points along the element axis (Fig. 2.1a). The corresponding concrete filament stresses σ_c and tangent moduli E_{tc} are then determined from the nonlinear constitutive relationship described in Sec. 5.2.1a. The steel filament stresses σ_s and tangent moduli E_{ts} are determined from the nonlinear constitutive model for reinforcing steel described in Secs. 5.2.1b and 5.2.1c.

The shear strains are calculated from Eq. (6.21) at the mid-points of the four walls of the box cross section (Sec. 5.2.2) for the two Gauss quadrature points along the element axis. The trilinear $\tau-\gamma$ relationship described in Sec. 5.2.2 is then used to determine the corresponding shear stresses τ_{xs} and tangent shear stiffnesses G_t.

The generalized strains v_4 are calculated from Eq. (6.22) at the two Gauss quadrature points along the element axis. The corresponding generalized stresses w_4 and tangent rigidities D_t are then determined form the nonlinear constitutive model described in Sec. 5.2.3.

6.4.2 Prestressing Steel Segment

The initial prestressing steel segment forces are computed based on specified jacking forces at each tendon end, including the effects of friction and anchorage slip losses, as described previously in Chapter 3. The initial stresses and the corresponding initial strains and tangent moduli can then be easily obtained. These initial strains, stresses and tangent moduli represent the prestressing steel segment states at the end of the first load pattern, i.e., after the transfer of prestress. During the analysis for the subsequent load patterns, the state determination is based on a formulation of the prestressing steel segments as truss-type elements.

Consider the prestressing steel segment between two consecutive nodes i and $(i + 1)$ of the structure. In the undeformed configuration of the structure, the global coordinates (X_i^0, Y_i^0, Z_i^0) and $(X_{i+1}^0, Y_{i+1}^0, Z_{i+1}^0)$ of the two segment ends at nodes i and $(i + 1)$, respectively, are known from the specified tendon profile (Sec. 3.3). The vector

$$\underline{V}_0 = \begin{Bmatrix} X_{i+1}^0 - X_i^0 \\ Y_{i+1}^0 - Y_i^0 \\ Z_{i+1}^0 - Z_i^0 \end{Bmatrix} \tag{6.23}$$

from segment end i to $(i + 1)$ represents the original axis of the segment, and its magnitude $|\underline{V}_0| = L_0$ represents the original length of the segment.

Next, let (X_i^k, Y_i^k, Z_i^k) and $(X_{i+1}^k, Y_{i+1}^k, Z_{i+1}^k)$ be the global coordinates of segment ends i and $(i + 1)$ at the end of the kth iteration in a load or displacement step. Then the vector $\underline{V}_k$ from segment end i to $(i + 1)$ at the kth iteration is given by

$$\underline{V}_k = \begin{Bmatrix} X_{i+1}^k - X_i^k \\ Y_{i+1}^k - Y_i^k \\ Z_{i+1}^k - Z_i^k \end{Bmatrix} \tag{6.24}$$

Using small displacement theory, the current length L_k of the prestressing steel segment at the kth iteration is given by the projection of vector $\underline{V}_k$ on the original axis of the segment. That is,

$$L_k = \frac{1}{L_0} \underline{V}_0^T \underline{V}_k \tag{6.25}$$

Similarly, the length L_{k-1} at the end of the $(k - 1)$th iteration is

$$L_{k-1} = \frac{1}{L_0} \underline{V}_0^T \underline{V}_{k-1} \tag{6.26}$$

Then for any iteration k, the increment in the axial strain of the prestressing steel segment is defined as

$$\Delta\epsilon_p = \frac{L_k - L_{k-1}}{L_0} \tag{6.27}$$

Substituting Eqs. (6.25) and (6.26) in Eq. (6.27),

$$\Delta\epsilon_p = \frac{1}{L_0^2} \underline{V}_0^T (\underline{V}_k - \underline{V}_{k-1}) \tag{6.28}$$

Making use of Eq. (6.24),

$$\Delta\epsilon_p = \frac{1}{L_0^2} \underline{V}_0^T \begin{Bmatrix} \Delta X_{i+1} - \Delta X_i \\ \Delta Y_{i+1} - \Delta Y_i \\ \Delta Z_{i+1} - \Delta Z_i \end{Bmatrix} \tag{6.29}$$

where $(\Delta X_i, \Delta Y_i, \Delta Z_i)$ and $(\Delta X_{i+1}, \Delta Y_{i+1}, \Delta Z_{i+1})$ represent the increments in the global coordinates of segment ends i and $(i + 1)$, respectively, for any iteration.

Now, if $\Delta \underline{r}_j$ and $\Delta \underline{r}_{j+1}$ are the nodal displacement increments at nodes i and $(i + 1)$, the corresponding increments in the global coordinates of segment ends i and $(i + 1)$ are given by

$$\begin{Bmatrix} \Delta X_i \\ \Delta Y_i \\ \Delta Z_i \end{Bmatrix} = \underline{A}_i \, \Delta \underline{r}_j \; ; \qquad \begin{Bmatrix} \Delta X_{i+1} \\ \Delta Y_{i+1} \\ \Delta Z_{i+1} \end{Bmatrix} = \underline{A}_{i+1} \, \Delta \underline{r}_{j+1} \tag{6.30}$$

where $\underline{A}_i$ and $\underline{A}_{i+1}$ are calculated from Eq. (2.29b) with the known eccentricities (y_i, z_i) and (y_{i+1}, z_{i+1}) of the segment ends with respect to the element nodes i and $(i + 1)$.

Finally, combining Eqs. (6.29) and (6.30), the axial strain increment $\Delta \epsilon_p$ corresponding to the nodal displacement increments

$$\Delta \underline{r} = \begin{Bmatrix} \Delta \underline{r}_j \\ \Delta \underline{r}_{j+1} \end{Bmatrix} \tag{6.31}$$

for the prestressing steel segment, is obtained as

$$\Delta \epsilon_p = \underline{B}_p \, \Delta \underline{r} \tag{6.32a}$$

where

$$\underline{B}_p = \frac{1}{L_0^2} \underline{V}_0^T < -\underline{A}_i , \underline{A}_{i+1} > \tag{6.32b}$$

For the state determination after any iteration, the axial strain increment $\Delta \epsilon_p$ is first calculated from Eq. (6.32). The total strain ϵ_p is then obtained by adding $\Delta \epsilon_p$ to the previous total. Finally, the stress σ_p and the tangent modulus E_{tp} are determined from the multilinear stress-strain relationship for prestressing steel described in Sec. 5.3.

6.5 Calculation of Internal Resisting Load Vector

The internal resisting load vector, $\underline{R}_i$, is defined as the vector of nodal loads in equilibrium with the internal stresses of the structure. The internal resisting loads are calculated for each reinforced concrete box beam element and each prestressing steel segment, as described subsequently, and then assembled for the structure. In calculating the unbalanced load vector $\underline{R}_u$ by Eq. (6.3) or (6.12), the support reactions $\underline{R}_s$ (Sec. 2.10) have to be subtracted from the internal resisting loads $\underline{R}_i$, since the external nodal loads $\underline{R}_e$ do not include the reactions.

The internal resisting load vector for a reinforced concrete box beam element corresponding to a given state of stresses σ_x, τ_{xs} and w_4 is given by

$$\underline{R}_i = \int_{-1}^{1} \int_A \underline{B}_\epsilon^T \sigma_x \lambda \, dA \, d\xi + \int_{-1}^{1} \int_A \underline{B}_\gamma^T \tau_{xs} \lambda \, dA \, d\xi + \int_{-1}^{1} \underline{B}_v^T w_4 \lambda_0 \, d\xi \tag{6.33}$$

where $\lambda \, dA \, d\xi$ represents the differential volume of the element, $\lambda_0 \, d\xi$ represents the differential arc length along the element axis, and λ_0 and λ are given respectively by Eqs. (2.5c) and (2.47).

The integrations in Eq. (6.33) with respect to the natural coordinate ξ along the element axis are done numerically using two-point Gauss quadrature (Fig. 2.1a). The first integral over the cross sectional area, involving the normal stress σ_x, is evaluated using the concrete and steel filament system described in Sec. 5.2.1 (Eq. (5.1), Fig. 5.2). The second integral over the cross sectional area, involving the shear stress τ_{xs}, is evaluated separately for the four discrete walls of the cross section, as described in Sec. 5.2.2 (Eq. (5.22), Fig. 5.9).

The internal resisting load vector for a prestressing steel segment corresponding to an axial stress σ_p is calculated as

$$\underline{R}_i = \int_V \underline{B}_p^T \sigma_p \, dV = \sigma_p A_p L_0 \underline{B}_p^T \tag{6.34}$$

where A_p is the cross sectional area of the prestressing tendon to which the segment belongs, L_0 is the original length of the segment, and $\underline{B}_p$ is as given by Eq. (6.32b).

6.6 Calculation of Tangent Stiffness Matrix

The tangent stiffness matrix $\underline{K}_t$ is calculated for each reinforced concrete box beam element and prestressing steel segment, and assembled for the structure. The support spring stiffnesses are then added to the appropriate terms of the tangent stiffness matrix of the structure, as described in Sec. 2.10.

The tangent stiffness matrix for a reinforced concrete box beam element is given by

$$\underline{K}_t = \int_{-1}^{1} \int_A \underline{B}_\epsilon^T E_t \underline{B}_\epsilon \lambda \, dA \; d\xi + \int_{-1}^{1} \int_A \underline{B}_\gamma^T G_t \underline{B}_\gamma \lambda \, dA \; d\xi + \int_{-1}^{1} \underline{B}_v^T D_t \underline{B}_v \lambda_0 \, d\xi \tag{6.35}$$

The integrals are again evaluated using two-point Gauss quadrature along the element axis. The same discretization of the cross section into concrete and steel filaments and four shear elements, as used for calculating the internal resisting load vector, is employed in performing the integrations over the cross sectional area.

The contribution of a prestressing steel segment to the tangent stiffness matrix is calculated as

$$\underline{K}_t = \int_V \underline{B}_p E_{tp} \underline{B}_p \, dV = E_{tp} A_p L_0 \underline{B}_p^T \underline{B}_p \tag{6.36}$$

6.7 Convergence Criteria

Since an iterative technique is used in this study to trace the nonlinear behavior of a structure (Sec. 6.3), convergence criteria are necessary to terminate the iterative process when the solution is deemed to be sufficiently close to the equilibrium state. Two measures of convergence can be used. The first is the amount by which equilibrium is violated, which is reflected in the magnitudes of the unbalanced loads. The second possibility is to assess the accuracy of the total displacements. This can be done by monitoring the magnitudes of additional displacement increments.

In this study, magnitudes of additional displacement increments are measured in terms of a displacement ratio proposed by Kang [28]. For each load or displacement step, the two components of the displacement vector $\underline{r}$ that have the maximum absolute values of translational displacement increment and rotational displacement increment for the first iteration are selected. If a displacement control strategy is being used, the controlled degree of freedom is not considered in this selection. Suppose the ith component has the maximum displacement (translational) increment, and the jth component has the maximum rotation increment. Let r_i^{k-1} be the total displacement increment for the load or displacement step of the ith component after the $(k-1)$th iteration, and let Δr_i^k be the displacement increment of the ith component for the kth iteration. r_j^{k-1} and Δr_j^k are similarly defined for the rotation increments. After the kth iteration, two ratios ρ_d and ρ_r are calculated for the displacement and rotation increments, respectively, as follows

$$\rho_d = \left| \frac{\Delta r_i^k}{r_i^{k-1}} \right| \quad ; \quad \rho_r = \left| \frac{\Delta r_j^k}{r_j^{k-1}} \right| \tag{6.37}$$

The displacement ratio ρ is defined as

$$\rho = \max(\rho_d, \rho_r) \tag{6.38}$$

To check the convergence after each iteration, the displacement ratio ρ is compared with three specified tolerances as follows.

1. ρ_i (displacement ratio tolerance for intermediate load or displacement steps)

   If $\rho \le \rho_i$, proceed to next load or displacement step.

   If $\rho > \rho_i$, continue iteration.

2. ρ_f (displacement ratio tolerance for final load or displacement step)

   If $\rho \le \rho_f$, proceed to next load pattern.

   If $\rho > \rho_f$, continue iteration.

3. ρ_c (displacement ratio tolerance for changing stiffness)

   If $\rho \le \rho_c$, use previously formed tangent stiffness matrix for next iteration.

   If $\rho > \rho_c$, form new tangent stiffness matrix for next iteration.

By specifying appropriate values of ρ_i and ρ_f, intermediate and final results can be obtained to the desired degree of accuracy. In general, the tolerance ρ_c implies tangent stiffness iterations followed by constant stiffness iterations. If desired, however, the tangent stiffness method or the initial stiffness method can be used by specifying $\rho_c = 0$ or ρ_c = some high value, respectively.

There is a possibility that equilibrium is violated excessively even though the displacement convergence criterion is satisfied. To guard against such a case, maximum allowable unbalanced loads are specified for each of the eight nodal degrees of freedom. If the unbalanced loads are not within these allowable limits, iteration is continued.

In addition to the convergence tolerances described above, the number of iterations performed for each load or displacement step is limited in case the convergence tolerances have been set too stringently. The maximum number of iterations allowed for intermediate load or displacement steps is specified as n_i, and the maximum number of iterations allowed for the final load or displacement step is specified as n_f.

6.8 Termination of Solution

The solution is of course terminated if all the load and/or displacement steps are executed successfully. However, the solution is also terminated under the following circumstances if they occur before the completion of all the load and/or displacement steps.

If a load control strategy is being used, the solution is terminated when a negative pivot is encountered during the triangularization of the tangent stiffness matrix. The negative pivot implies that the tangent stiffness matrix is nonpositive definite, and this indicates that the ultimate load of the structure (point A in Fig. 6.3) has been reached. A nonpositive definite tangent stiffness matrix occurs either due to the strains exceeding the specified ultimate values at one or more locations, or due to extensive yielding of concrete and/or steel at strains lower than the ultimate values.

If a displacement control strategy is being used, and if an ultimate load analysis is desired, the solution is terminated at the end of the displacement step during which a negative pivot in the triangularization process is detected.

In addition to the above criteria, the solution is also terminated if a zero pivot is encountered during the triangularization of the tangent stiffness matrix. Though a zero pivot does not necessarily mean that the tangent stiffness matrix is singular, the Gaussian elimination algorithm used in this study fails, since it does not include row and column interchanges. A zero pivot, however, does imply that the tangent stiffness matrix is nonpositive definite, thus indicating that the ultimate load of the structure has been reached.

7. COMPUTER PROGRAMS

7.1 General

Two computer programs, LAPBOX and NAPBOX, have been developed incorporating the theory presented previously in Chapters 2, 3, 5 and 6. LAPBOX is intended for linear elastic analysis, whereas NAPBOX is intended for nonlinear material analysis. The linear elastic examples in Chapter 4 were analyzed with LAPBOX. NAPBOX is used to obtain the results for the nonlinear analysis examples in Chapter 8.

The computer programs LAPBOX (Linear elastic Analysis of Prestressed concrete BOX girders) and NAPBOX (Nonlinear Analysis of Prestressed concrete BOX girders) are coded in FORTRAN IV with double precision, and have been tested on the IBM 3090 computer at the University of California, Berkeley. Within each program, the blank common is dynamically dimensioned so that the central memory of the computer can be used efficiently. The equation solving is done by Gaussian elimination, and the equation solver has been adapted to solve symmetric banded matrices by triangularization and back substitution in two separate routines.

7.2 Input Requirements

Data describing the structure to be analyzed are provided in an input file of card images. The required formats of the input files for LAPBOX and NAPBOX can be found in Appendices A and C respectively. Sample input files are given in Appendix B for LAPBOX and in Appendix D for NAPBOX. Consistent units must be used for all input data.

The basic input for both programs consist of: structure geometry and boundary conditions; material properties; prestressing data; structure loading; and locations for stress output. NAPBOX additionally requires concrete and longitudinal steel filament data, transverse steel data and convergence tolerances. The input variables are defined in the input guides (Appendices A and C). Most of the input requirements are self-explanatory. However, the following discussions on certain aspects of the input data are necessary.

7.2.1 Distributed Element Load Data for LAPBOX and NAPBOX

Provisions have been made in the computer programs LAPBOX and NAPBOX for the application of uniformly distributed element loads such as those shown in Fig. 7.1. The load consists of a uniform pressure p in the Z direction acting upon a certain area of the top flange (including the side cantilevers) or the bottom flange. In the longitudinal direction, the load stretches from element *NFE* through element *NFL*. Element *NFE* is nearer to node 1 while element *NLE* is nearer to node *NN*. The transverse distribution of the load is defined by the coordinate y_m (y_{m_1} for top flange, y_{m_2} for bottom flange) to the centerline of the load and the transverse width w (w_1 for top flange, w_2 for bottom flange).

In the computer programs, the fractions

$$YMF(1) = \frac{y_{m_1}}{a + 2f} \text{ , for top flange} \qquad (7.1a)$$

$$YMF(2) = \frac{y_{m_2}}{a} \text{ , for bottom flange} \qquad (7.1b)$$

are specified as input. The transverse widths, w_1 and w_2, can be input either as fractions of the flange widths ($w_1/(a + 2f)$ and w_2/a) or as absolute values.

Proper signs must be used for p and y_m. p is taken to be positive wU[the load acts along the Z axis, and y_m is measured positive along the y axis. The distributed element loads are automatically converted into equivalent nodal loads within the programs, as discussed in Sec. 2.8.2.

7.2.2 Section Data for NAPBOX

As discussed earlier (Sec. 5.2.1, Fig. 5.2), the cross section of the box beam element is subdivided into a number of concrete and longitudinal reinforcing steel filaments for nonlinear material analysis. The filament system for each different section is described through the section data for NAPBOX.

Each wall of the cross section is subdivided into *NCL* concrete layers, and each layer

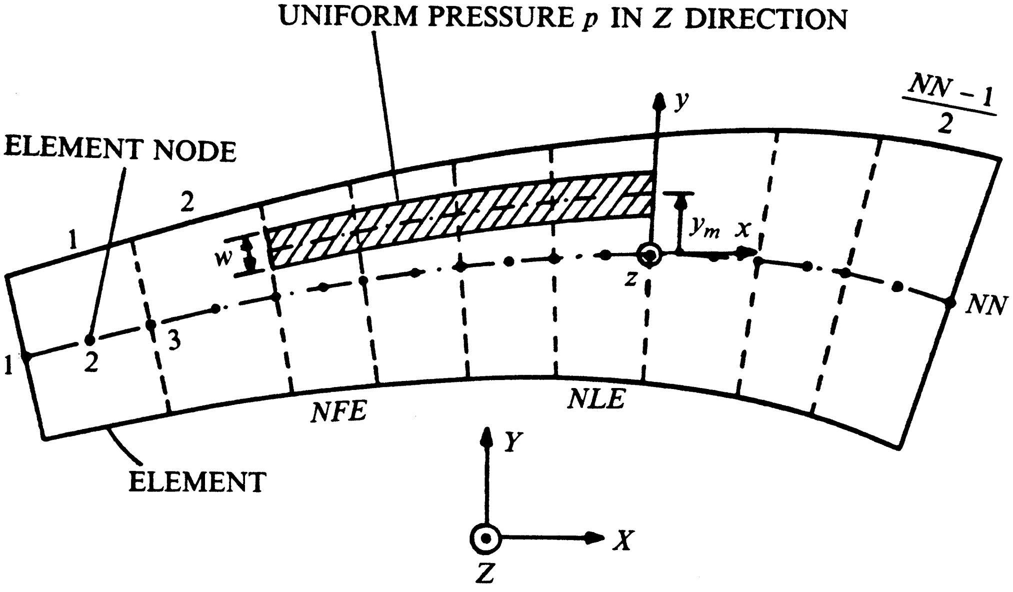

(a) PLAN VIEW

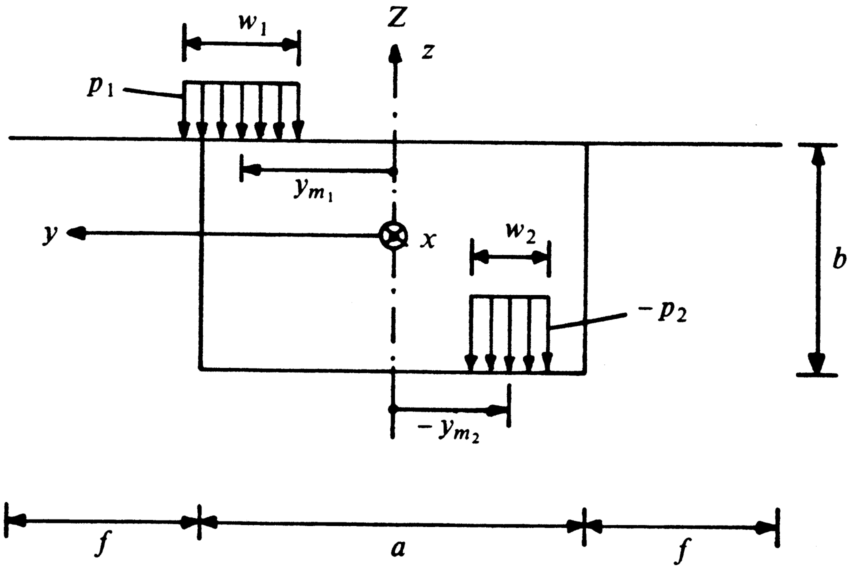

(b) CROSS SECTIONAL VIEW

FIG. 7.1 DISTRIBUTED ELEMENT LOADS

into *NCFL* concrete filaments (Fig. 7.2a). The layers and the filaments in each layer are numbered as shown in Fig. 7.2a. Then any concrete filament is uniquely identified by its location (top flange, bottom flange, left web, right web, left cantilever or right cantilever), the number of the layer to which it belongs, and its filament number within that layer. All the concrete filaments in a section are assumed to have the same material properties. The thicknesses *THS* of the concrete layers in each wall are specified as fractions of the total wall thickness. The widths *WDH* of the filaments are specified as fractions of the total wall width. Expressing *THS* and *WDH* as fractions enables the modelling of a nonprismatic element. From the above data, the area and the local y, z coordinates at the mid-point of each concrete filament can be calculated for any location along the axis of a nonprismatic element.

By appropriately specifying the fractions *THS* and *WDH*, it is possible to obtain a finer mesh of concrete filaments at certain locations of the cross section, and a coarser mesh at other locations. However, to simplify the input, an option is provided in NAPBOX to generate the concrete filaments automatically. If this option is used, filaments with equal thicknesses and equal widths are generated for each wall of the section. The generated layers and filaments are numbered as in Fig. 7.2a.

The longitudinal reinforcing steel filaments (Fig. 7.2b) are located at the mid-thickness of the cross section walls. The number of filaments *NSF* is specified for each wall. Different material properties and area can be specified for each steel filament. The area *ALF* of each filament remains constant along the longitudinal direction. The locations of the steel filaments are defined with the variable *YZSF*. For the top and bottom flanges, $YZSF = y/a$; for the left and right webs, $YZSF = (z + b_2)/b$; and for the left and right cantilevers, $YZSF = (|y| - a/2)/f$. The local y (for flanges and cantilevers) or z (for webs) coordinates of a steel filament at any location along the axis of a nonprismatic element can be determined from *YZSF*.

An option is provided in NAPBOX to generate the steel filaments automatically. If this option is used, only the total area *ALT* of the longitudinal steel need to be input for each

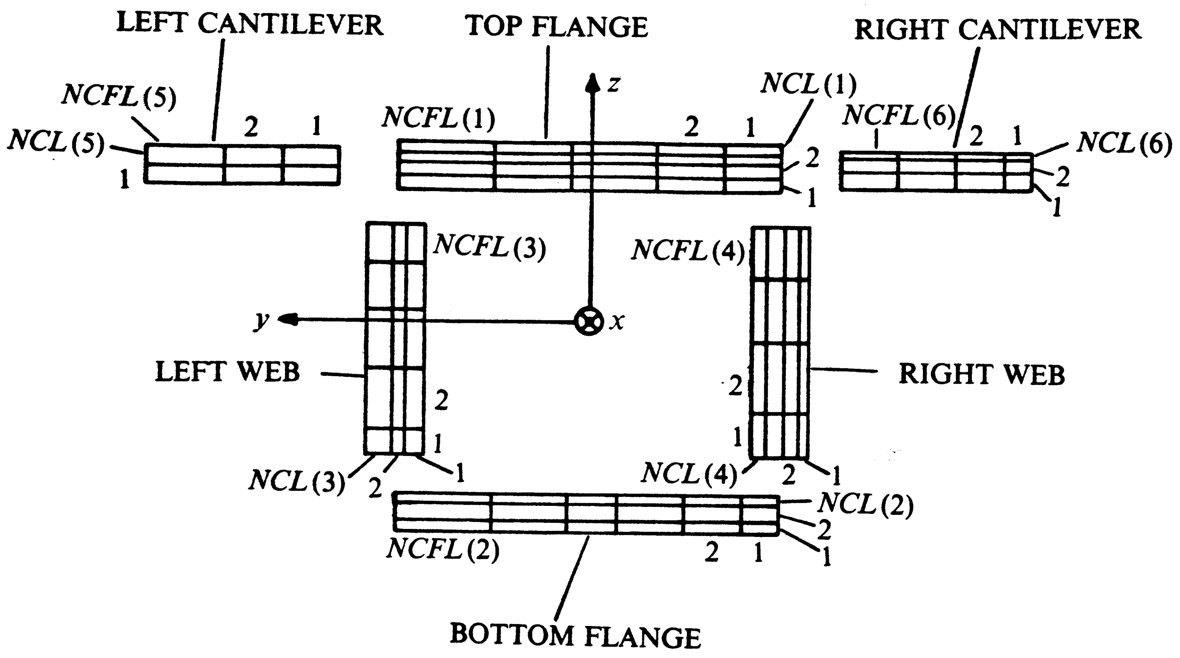

(a) CONCRETE FILAMENTS

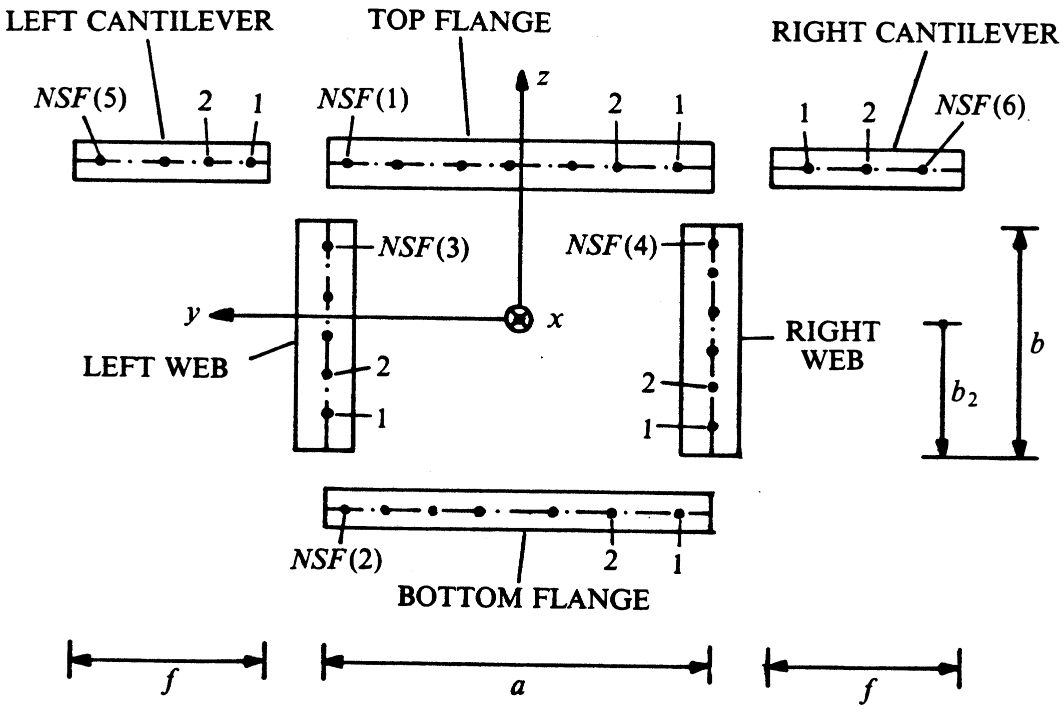

(b) STEEL FILAMENTS

FIG. 7.2 CONCRETE AND LONGITUDINAL REINFORCING STEEL FILAMENTS wall. All the steel filaments in a wall are then assumed to have the same material properties. The generated steel filaments have equal areas and are equally spaced in each wall.

When the steel filament data are input directly, there is no specific numbering system for the filaments. The filaments are simply numbered in the order in which their data are input. If the automatic generation option is used, the steel filaments are numbered as in Fig. 7.2b.

In addition to the concrete and steel filament data discussed above, the transverse steel data have to be input for each section. The input guidelines in Appendix C for the transverse steel data are self-explanatory.

7.3 Output Capabilities

Both programs provide a check printout of all the input and generated data describing the structure, the prestressing and the loads. The additional output capabilities of the two programs are described separately.

7.3.1 LAPBOX

The following final results are output by LAPBOX for each load case:

1. The eight generalized displacements in the global coordinate system at each node.

2. Support reactions in the local coordinate systems of the support springs.

3. The eight generalized forces in the global coordinate system at the end nodes, i and j, of each element. The forces at the mid node o are simply equal to the applied external loads at that node and hence are of no interest.

4. Stresses and force resultants at the two Gauss sections of each element for which stress output is requested. The normal and shear stresses are output at the four Gauss quadrature points along each wall of the cross section. The transverse bending moments per unit length at the top and bottom corners of the box section are also output. The force resultants are obtained by integrating the normal and shear stresses according to Eq. (2.41). The force resultants are output in the local coordinate system.

7.3.2 NAPBOX

The following results are output by NAPBOX for each load or displacement step in a load pattern:

1. The eight generalized displacements in the global coordinate system at each node.

2. Support reactions in the local coordinate systems of the support springs.

3. The unbalanced loads in the global coordinate system at each node.

4. The internal resisting loads in the global coordinate system at the end nodes, i and j, of each element.

5. Strains, stresses and material states for each prestressing steel segment.

6. At the two Gauss sections of each element for which stress output is requested, the following are output: generalized strain v_4 of the cross section and the corresponding stress w_4 and material state; shear strain, stress and material state for each wall of the cross section; normal strain, stress and material state for each concrete and longitudinal reinforcing steel filament; force resultants in the local coordinate system obtained by integrating the normal and shear stresses according to Eq. (2.41). The force resultants do not include the effect of the prestressing steel segment forces.

8. NONLINEAR ANALYSIS - NUMERICAL EXAMPLES

Three numerical examples of nonlinear material analysis performed with the computer program NAPBOX (Chapter 7) are presented in this chapter. These examples demonstrate the range of applicabilty of the proposed method, and its ability to capture the primary nonlinear behavior of reinforced and prestressed concrete box girders. Due to nonavailability of experimental data, the degree of accuracy of the analytical results could not be examined.

Though the computer program NAPBOX is designed specifically for box girder bridges, it can be used to analyze other thin-walled structures with rectangular single-cell box cross sections. This is demonstrated in the first example by analyzing a reinforced concrete column with hollow rectangular cross section. The dimensions of the column have been chosen such that second order effects are negligible. When second order effects are important, however, NAPBOX cannot be used to analyze columns since it does not consider geometric nonlinearities.

Two three-span continuous prestressed concrete box girder bridges, one straight and the other curved in plan, are considered as the second and third examples. Overload behavior and ultimate strength of these two bridges under increasing vehicular load are investigated.

In all the analyses, the dead load and the prestressing (if any) are applied first. External loads of increasing magnitude are then applied up to ultimate failure.

8.1 Example 8.1 - Hollow Reinforced Concrete Column

One feature of the proposed box beam element is its ability to handle problems in biaxial bending. It is the purpose of this example to demonstrate this capability, and to study the effects of warping stresses and cross sectional distortions on the response of hollow reinforced concrete columns.

8.1.1 Structure Details and Analytical Modelling

A hollow reinforced concrete column, shown in Fig. 8.1, is considered. The column is fixed into a rigid foundation at the base such that all eight degrees of freedom are restrained. At the top, the column is assumed to be completely free. The cross section (Fig. 8.1b) is a rectangular thin-walled box, and is constant along the length of the column. In the longitudinal direction, 2 layers of #10 rebars at a transverse spacing of 12 in. are provided in each wall of the box cross section. This gives a total longitudinal steel area of 96.52 in.^{2} uniformly distributed along the walls of the cross section. The transverse reinforcement in each wall consists of 2 legs of #4 stirrups at a longitudinal spacing of 5 in., which is equivalent to 0.08 in.^{2}/in. of total transverse steel area per unit longitudinal length. Concrete cover to the center of each transverse steel layer ia taken as 1.25 in. The material properties assumed in the analysis are summarized in Table 8.1.

The column is loaded at the top by a concentrated vertical load P at one of the corners of the cross section (Fig. 8.1). In the analysis, the concentrated load is replaced by a set of equivalent nodal loads determined from Eq. (2.55). The equivalent loads consist of an axial force, bending moments about the y and z axes, and a warping bimoment.

20 box beam elements of equal length are used to model the column. Each wall of the cross section is subdivided into 2 equal concrete layers with 20 equal concrete filaments per layer, which gives a total of 160 concrete filaments. 38 longitudinal steel filaments, each with an area of 2.54 in.^{2}, are used. The steel filaments are equally spaced along the mid-thickness of the walls of the box cross section.

8.1.2 Presentation and Discussion of Results

The lateral displacements, δ_Y and δ_Z, at the column top under increasing values of the load P are shown in Fig. 8.2. The load-displacement curves are practically linear up to P = 1,100 kips. At the next load step of P = 1,300 kips, initial cracking of concrete filaments was observed near the top and the base of the column. This initial cracking is reflected in the response curves of Fig. 8.2 which first become nonlinear at P = 1,300 kips. The primary source of nonlinearity in the column response is the cracking of concrete filaments. Yielding of longitudinal steel occurred only at very high load levels. Longitudinal steel first yielded in

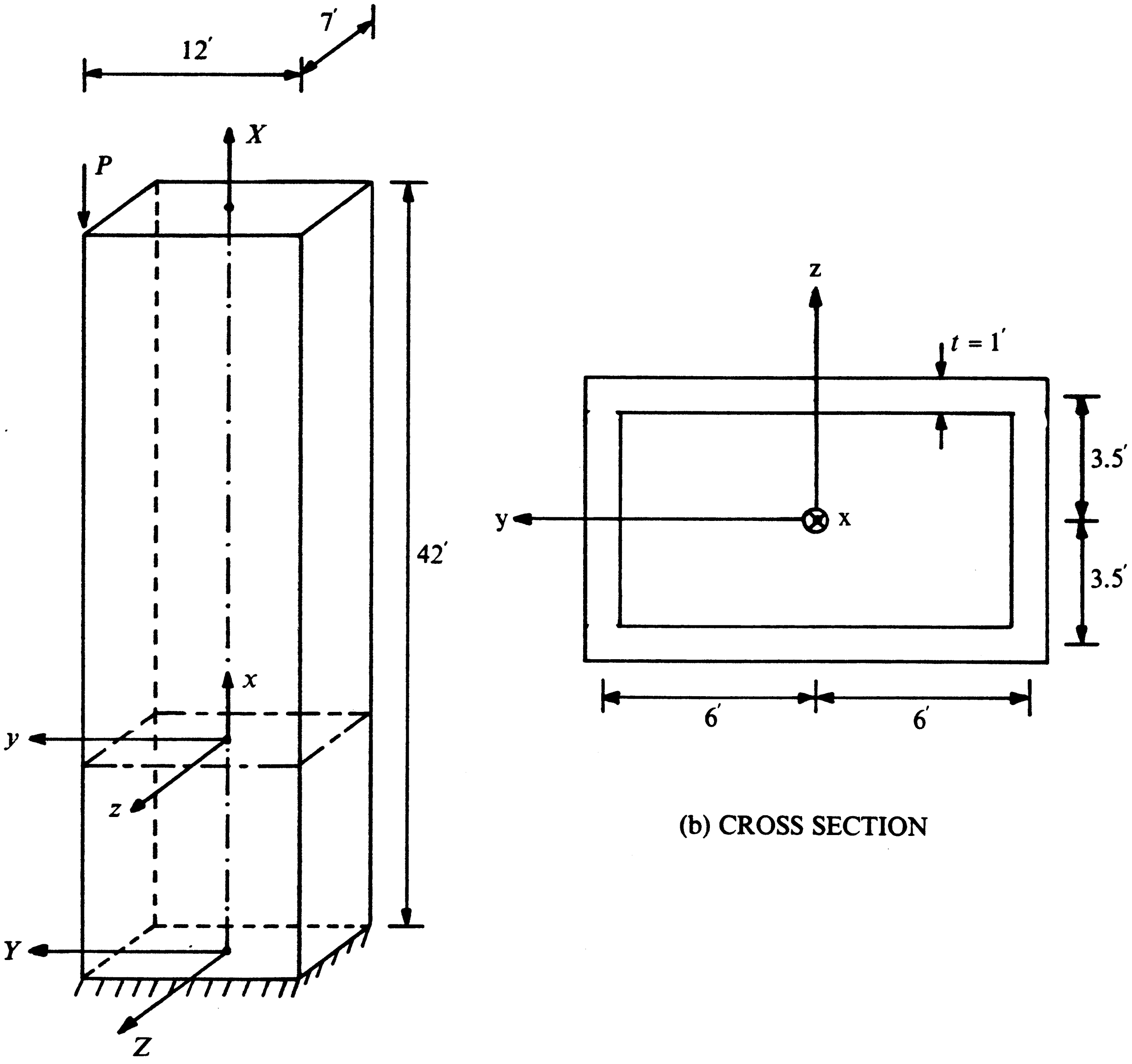

(a) ISOMETRIC VIEW

(b) CROSS SECTION

FIG. 8.1 EXAMPLE 8.1 - HOLLOW REINFORCED CONCRETE COLUMN

TABLE 8.1 EXAMPLE 8.1 - MATERIAL PROPERTIES

Concrete:

$f_c'' = 4{,}000$ psi

$E_{ci} = 3.605 \times 10^6$ psi

$f_t = 500$ psi

$\epsilon_{cu} = 0.004$

$\beta = 0.85$

$\nu = 0.20$

$\tau_{cr} = 126.5$ psi

$\beta_1 = 0.85$

Longitudinal reinforcing steel:

$f_y = 60$ ksi

$E_{s1} = 29{,}000$ ksi

$E_{s2} = 0$

$\epsilon_{su} = 0.03$

Transverse reinforcing steel:

$f_{yt} = 60$ ksi

$E_{st} = 29{,}000$ ksi

Unit weight of composite structure: $w = 155$ pcf

Tension stiffening coefficient: $k' = 57$ psi

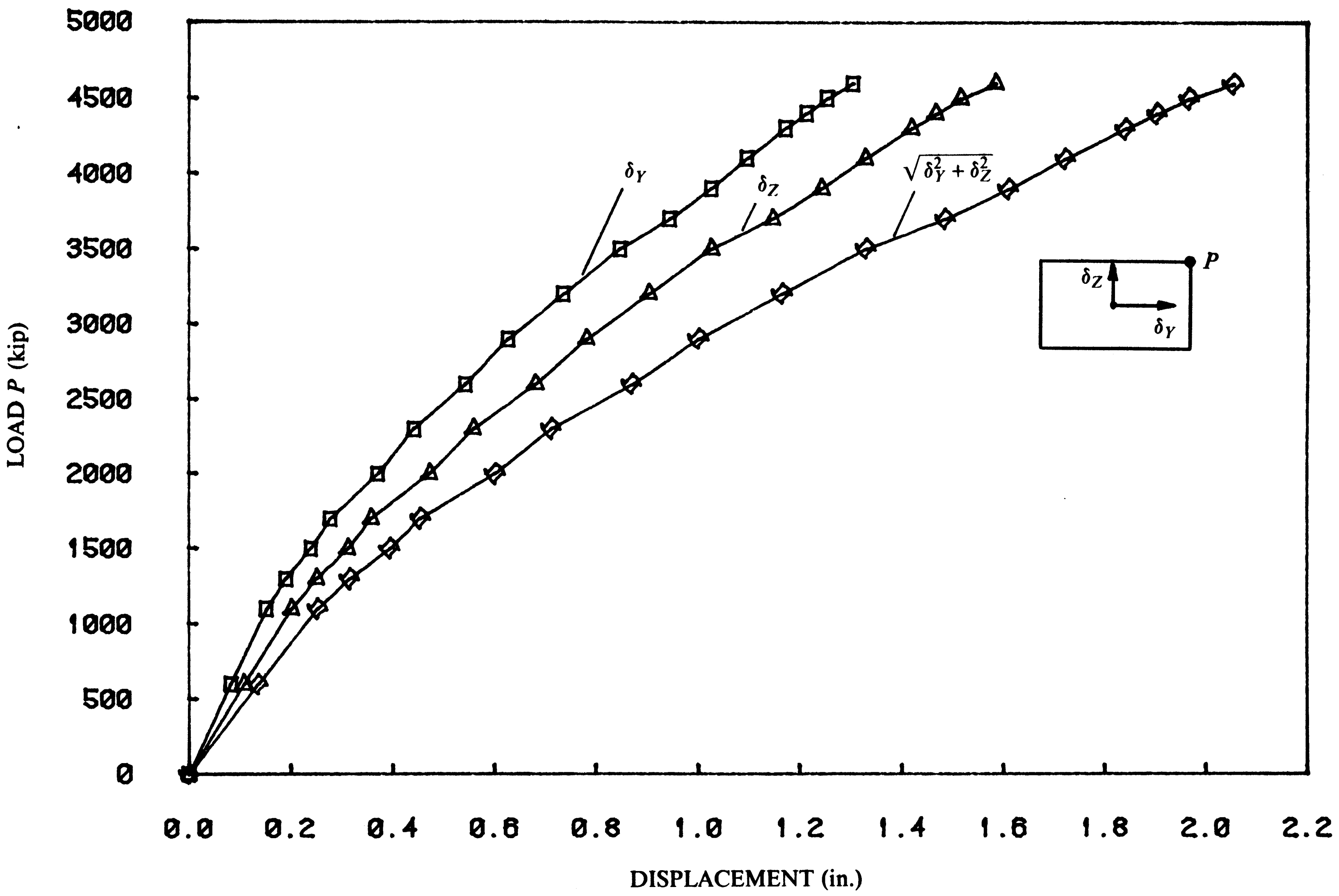

FIG. 8.2 EXAMPLE 8.1 - LOAD vs. LATERAL DISPLACEMENTS AT COLUMN TOP

compression at P = 4,100 kips near the column top. Then at P = 4,500 kips, yielding of longitudinal steel in tension was detected again near the column top. The ultimate load predicted by the analysis is P = 4,600 kips. Failure occurred due to crushing of concrete filaments at the loaded corner of the column top.

The crack patterns in the concrete filaments and the yield patterns in the concrete and longitudinal steel filaments at two sections, one near the column top and the other near the column base, are shown in Fig. 8.3 for three load levels. Effect of the warping bimoment component of the loading is evident in Fig. 8.3. Due to the warping bimoment applied at the column top, the crack patterns at the section near the top are completely different from those at the section near the base. Near the top, the warping stresses dominate over the flexural stresses, and this is reflected in the crack and yield patterns in Fig. 8.3a. The warping stresses damp out away from the top until, near the base, the flexural stresses dominate over the warping stresses. Thus the crack patterns at the section near the column base (Fig. 8.3b) resemble ordinary beam theory predictions.

It is seen from Fig. 8.3 that the failure of the column is governed by the failure of the section near the top where the warping stresses dominate. Ordinary beam theory, which does not consider the effect of warping stresses, would predict an ultimate load on the unsafe side.

Also of interest is the transverse flexural response of the column cross section. The transverse distortions of the cross section at the column top under increasing load levels are shown in Fig. 8.4. Initial cracking due to transverse flexure occurred at P = 600 kips at the column top. With increasing load levels, the transverse distortions increased rapidly near the column top. At P = 2,300 kips, transverse flexural yielding was observed at the column top. After yielding, the transverse distortions increased even more rapidly. At the ultimate load of P = 4,600 kips, the transverse flexural yielding spread to about 9.5 ft from the column top.

The results of this example indicate that warping stresses and transverse distortions of the cross section may be important considerations in the design of hollow reinforced concrete columns with thin-walled box sections. The computer program NAPBOX can be an useful

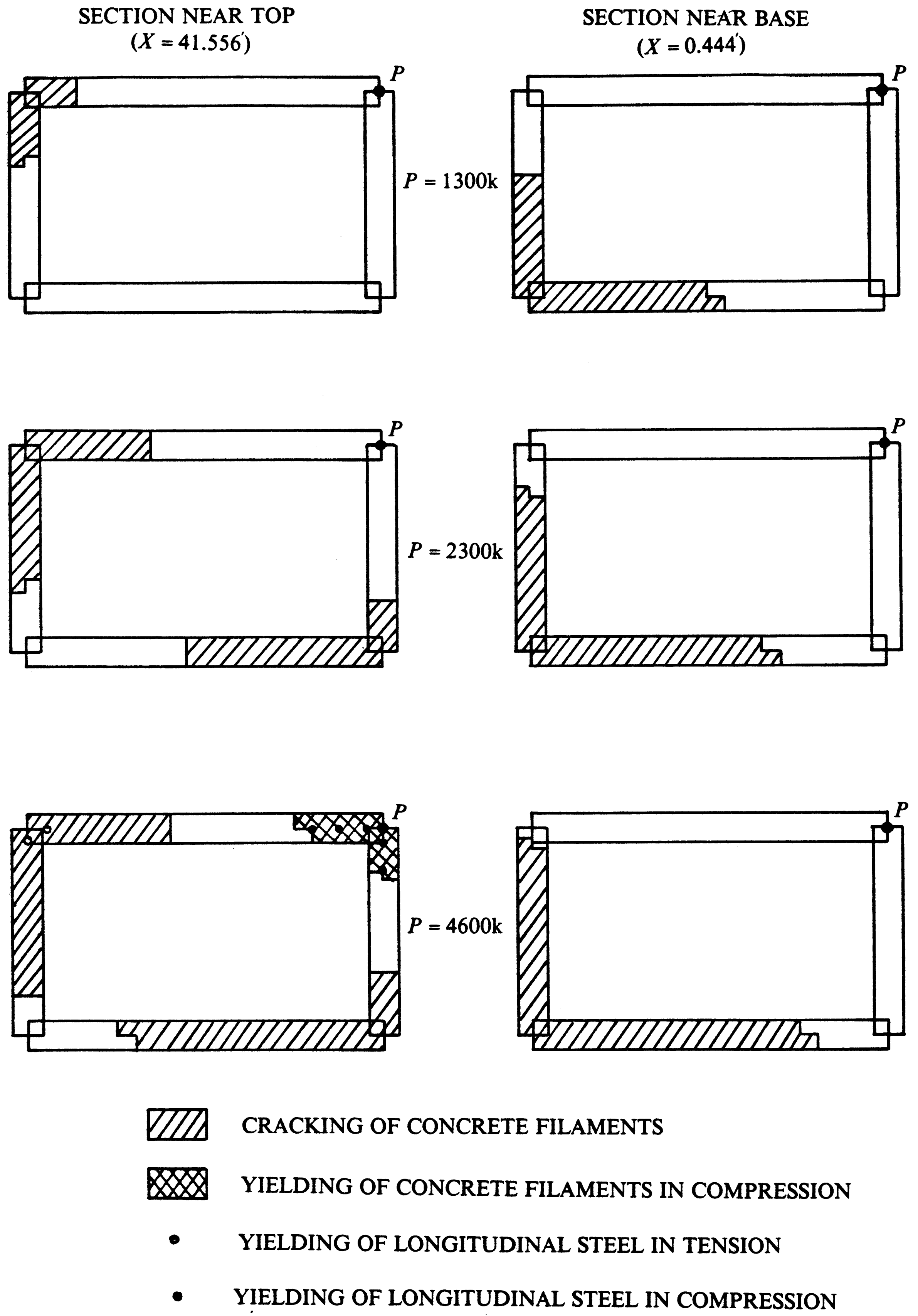

FIG. 8.3 EXAMPLE 8.1 - CRACK AND YIELD PATTERNS AT SECTIONS NEAR TOP AND BASE OF COLUMN

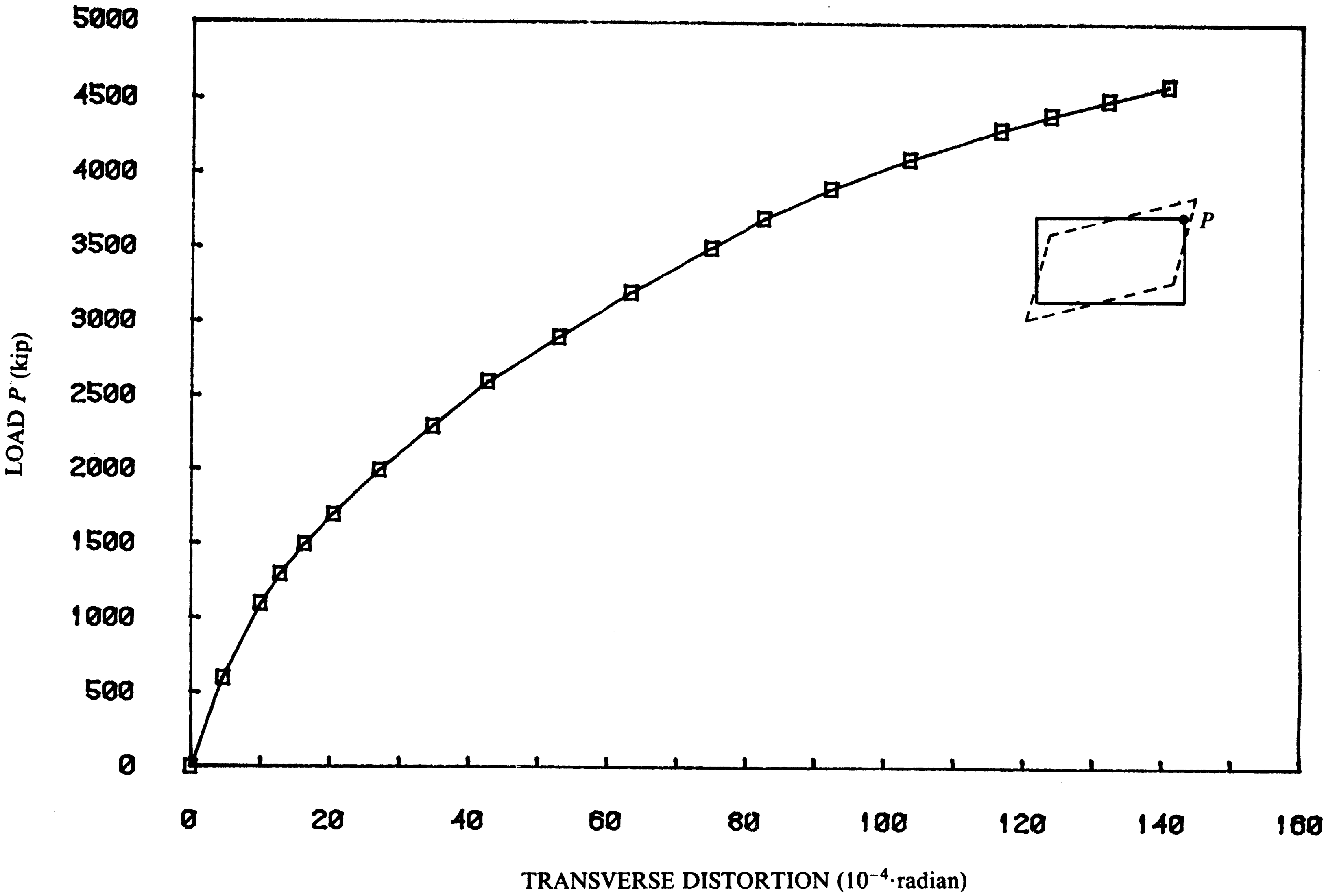

FIG. 8.4 EXAMPLE 8.1 - LOAD vs. TRANSVERSE DISTORTION AT COLUMN TOP

tool in the design of such columns.

8.2 Example 8.2 - Three-Span Straight Prestressed Concrete Bridge

This example demonstrates how the computer program NAPBOX can be used to trace the response of a continuous prestressed concrete bridge throughout the elastic, inelastic and ultimate load ranges. The effect of transverse positioning of the live load on the structural response is also investigated. The accuracy of the NAPBOX results in the case of a purely longitudinal flexural loading is checked against a previously developed computer program PCFRAME [28, 29].

8.2.1 Structure Details and Analytical Modelling

The structure considered in this example is a three-span, straight, continuous, prestressed concrete box girder bridge (Fig. 8.5). Its span arrangement (Fig. 8.5a) is symmetrical with 160 ft, 200 ft and 160 ft spans. The bridge is assumed to be fully restrained against vertical translation, twist and transverse distortion of the cross section at the four supports. No restraint against longitudinal warping of the cross section is provided.

For the sake of simplicity, the cross section (Fig. 8.5b) is assumed to be constant from end to end of the structure, although design practice often calls for thickening of the bottom flange and/or the webs in regions near supports. The total top deck width of 34 ft is typical of a two-lane highway bridge.

The prestressing in the bridge consists of two tendons in the longitudinal direction, one in each web. The prestress is achieved by post-tensioning from both ends simultaneously. After post-tensioning, the prestressing steel is grouted and hence bonded to the concrete. The tendon profile is the same in each web, and is shown in Fig. 8.5c.

The material properties assumed for the design of the bridge, and subsequently for the nonlinear analysis with NAPBOX, are given in Table 8.2. The coordinates of the multilinear stress-strain curve for prestressing steel used in the NAPBOX computer analysis are obtained by approximating a typical curve for ½ in. diameter 7-wire strands with a nominal ultimate

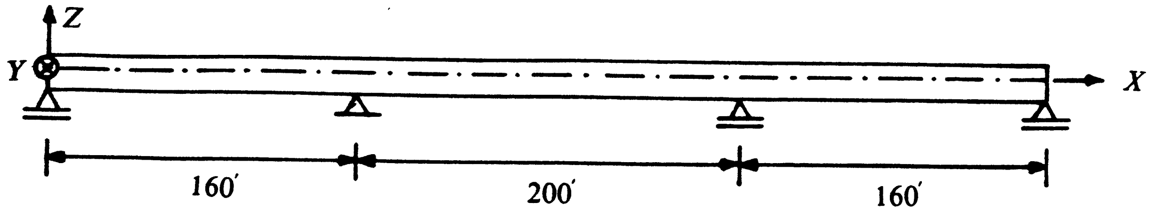

(a) SPAN ARRANGEMENT

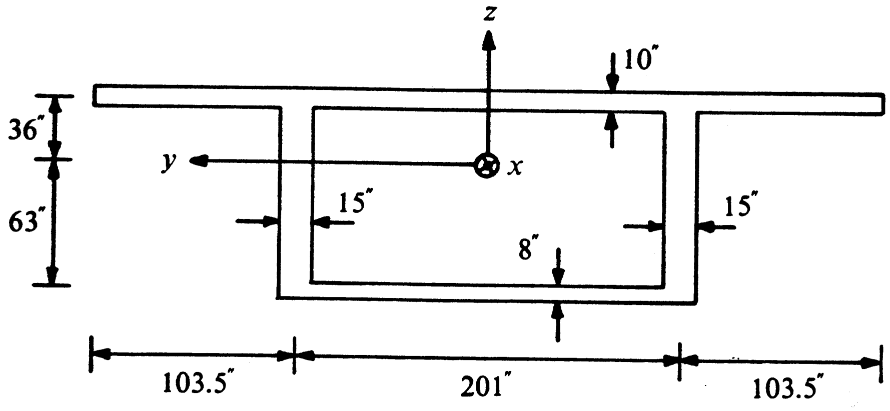

(b) CROSS SECTION

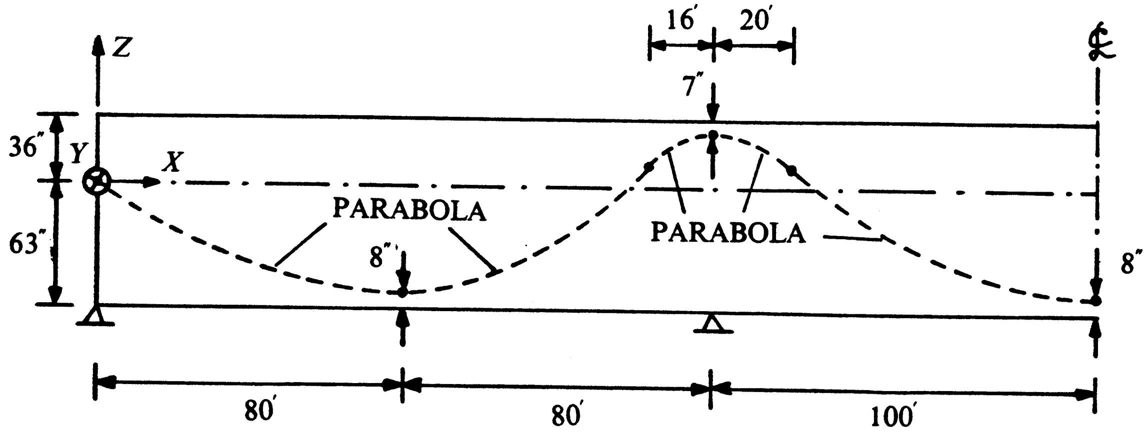

(c) PRESTRESSING TENDON PROFILE

FIG. 8.5 EXAMPLE 8.2 - THREE-SPAN STRAIGHT PRESTRESSED CONCRETE BRIDGE

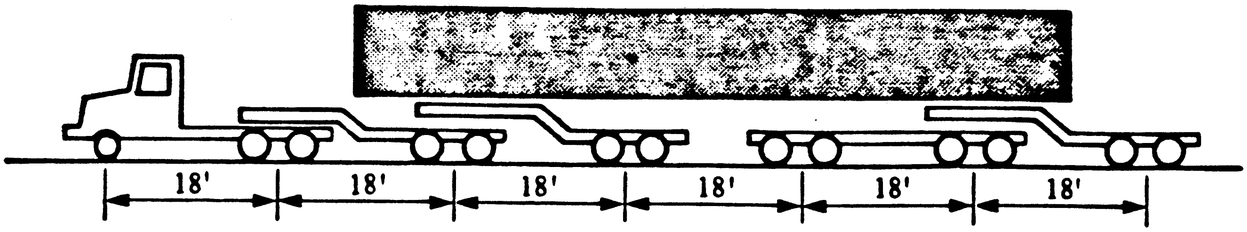

(a) TRUCK ELEVATION

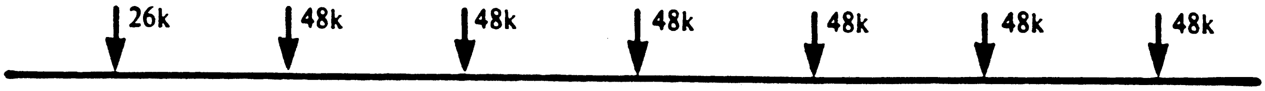

(b) TOTAL AXLE LOADS ON BRIDGE

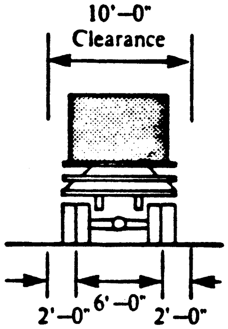

(c) TRUCK SECTION

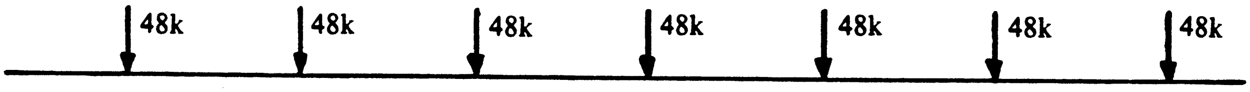

(d) SYMMETRIC APPROXIMATION USED IN ANALYSES

FIG. 8.6 P13 TRUCK LOADING

strength of 270 ksi [39].

Structural design of the box girder is based on State of California standard criteria . The prestressing steel requirements are calculated by considering HS20 lane loading in each of the two lanes, impact factors based on span lengths, and an allowable tensile stress of $6\sqrt{f_c''}$ psi in concrete after all prestresing losses have occurred. A total of 172 ½ in. diameter 7-wire strands (86 strands per web), which gives a total prestressing steel area of 26.32 in.^{2}, is provided. The required jacking force is 2660 kips per web. Ultimate strength under factored loads is checked. In the load factor design, an aditional overload vehicle, designated as P13 truck (Fig. 8.6a, b and c), is considered [56].

Longitudinal mild steel reinforcement corresponding to 0.3% of the concrete area is provided in each wall of the box cross section. This steel is not required from strength considerations, but is provided for construction purposes. The transverse reinforcement consists of 2 legs of #5 stirrups at 4 in. longitudinal spacing in each web (0.155 in.^{2}/in. total area per unit longitudinal length), and 2 legs of #5 stirrups at 10 in. longitudinal spacing in each slab (0.062 in.^{2}/in. total area per unit longitudinal length). Concrete cover to the center of each transverse steel layer is taken as 1.25 in.

The response of the bridge structure is studied under increasing levels of vehicle overload up to ultimate failure. The overload vehicle considered is the P13 truck (Fig. 8.6), which is typical of the heaviest vehicles found on California's highways. A special road use permit is required before the vehicle is allowed on a highway, and it must travel at reduced speed. In order to take advantage of the symmetry of the structure, the P13 truck loading in Fig. 8.6b is approximated with the symmetric loading in Fig. 8.6d. This symmetric truck loading is positioned in the middle of the center span of the bridge (Fig. 8.7a), and the structural load vector due to its weight is incremented until ultimate failure occurs. For convenience in presentation of results, P is used to denote the factor of truck load applied. Thus $P = 1$ represents overload due to one truck (Fig. 8.7a).

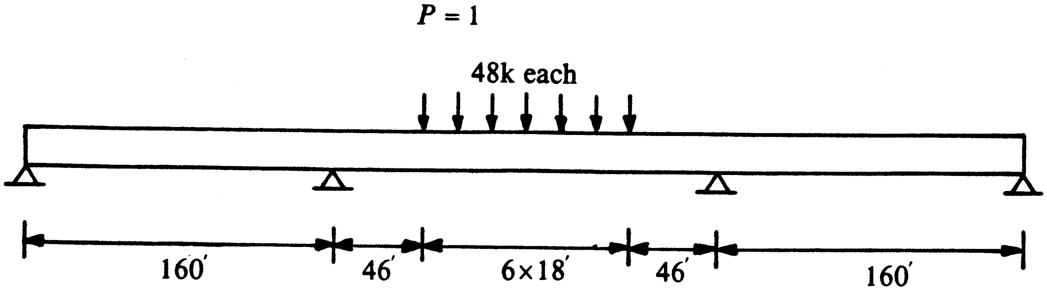

(a) LONGITUDINAL POSITION OF TRUCK LOAD
FOR LOAD CASES 1 AND 2

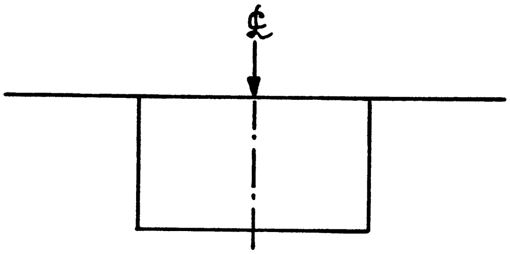

(b) TRANSVERSE POSITION OF TRUCK LOAD
FOR LOAD CASE 1

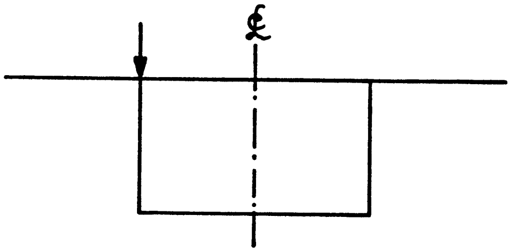

(c) TRANSVERSE POSITION OF TRUCK LOAD
FOR LOAD CASE 2

FIG. 8.7 EXAMPLE 8.2 - POSITION OF TRUCK LOAD FOR THE TWO LOAD CASES

Two different load cases are considered:

Load Case 1 - Truck load is positioned over centerline of bridge (Fig. 8.7b). This constitutes a purely longitudinal flexural loading. No transverse distortion, longitudinal warping and twist of the bridge cross section are induced in a NAPBOX analysis which represents ordinary beam theory in this particular case.

Load Case 2 - Truck load is positioned over one of the webs (Fig. 8.7c). Due to the eccentricity of this loading with respect to the centerline of the bridge, torsional, distortional and warping effects are induced in addition to longitudinal flexural effects.

Taking advantage of the symmetry of the structure and the loadings, only half the length of the bridge is analyzed. 20 box beam elements of varying lengths are used. The element subdivision is shown in Fig. 8.8. Two different discretizations of the cross section into concrete and longitudinal steel filaments, shown in Fig. 8.9, are used corresponding to the two different load cases.

8.2.2 Presentation and Discussion of Results

8.2.2a Load Case 1

The vertical displacements at the middle of the center span under increasing overload, obtained from three separate analyses, are shown in Fig. 8.10. Two analyses were performed with NAPBOX, one including shear deformations and the other excluding shear deformations. Shear deformations were excluded by manipulating the values of the Poisson's ratio, ν, and the cracking shear stress, τ_{cr}, of concrete. An additional analysis was performed with the computer program PCFRAME [28, 29] in order to verify the results from the NAPBOX analyses. PCFRAME, which is capable of performing nonlinear analysis of planar reinforced and prestressed concrete frames, has been extensively tested [28, 57]. It thus provides an useful check on the accuracy of the NAPBOX results for this special case of planar loading. Shear deformations are not considered in PCFRAME. Good agreement between the results obtained with NAPBOX and PCFRAME can be noted in Fig. 8.10.

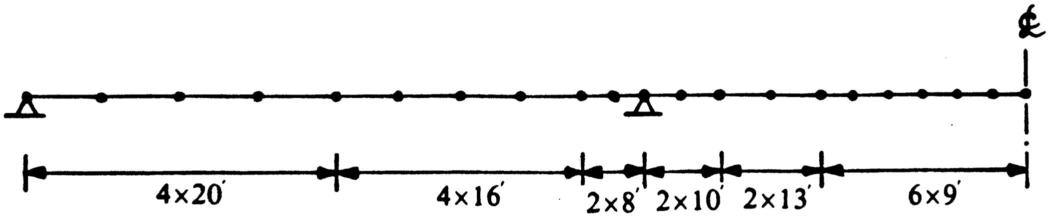

FIG. 8.8 EXAMPLE 8.2 - ELEMENT SUBDIVISION

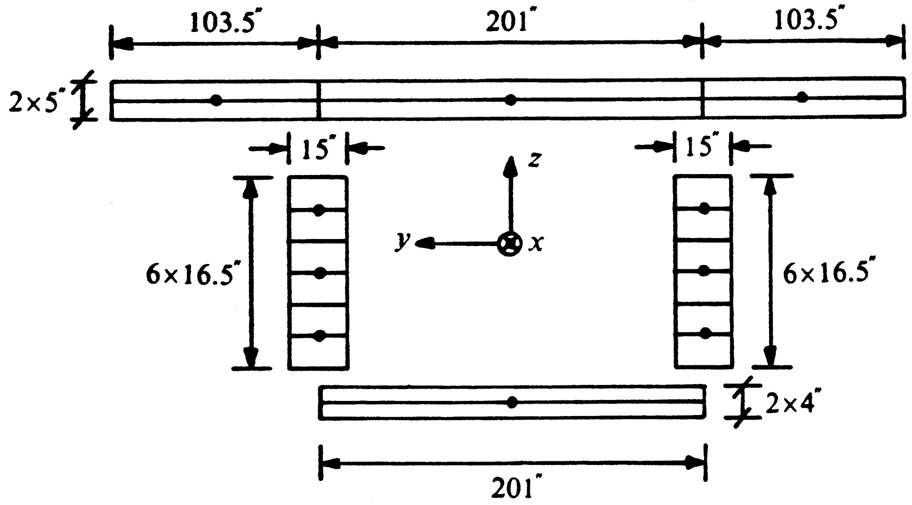

(a) LOAD CASE 1

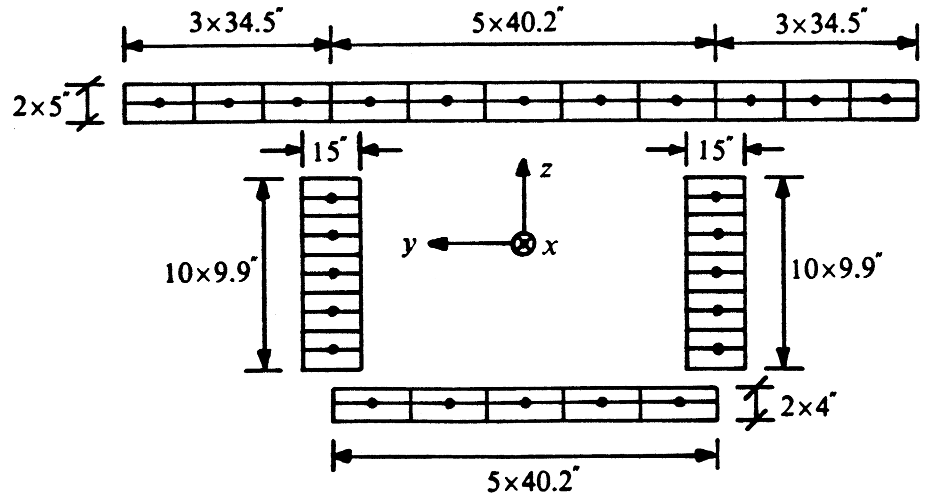

(b) LOAD CASE 2

▭ CONCRETE FILAMENT ● STEEL FILAMENT

FIG. 8.9 EXAMPLE 8.2 - DISCRETIZATION OF CROSS SECTION INTO CONCRETE AND LONGITUDINAL STEEL FILAMENTS

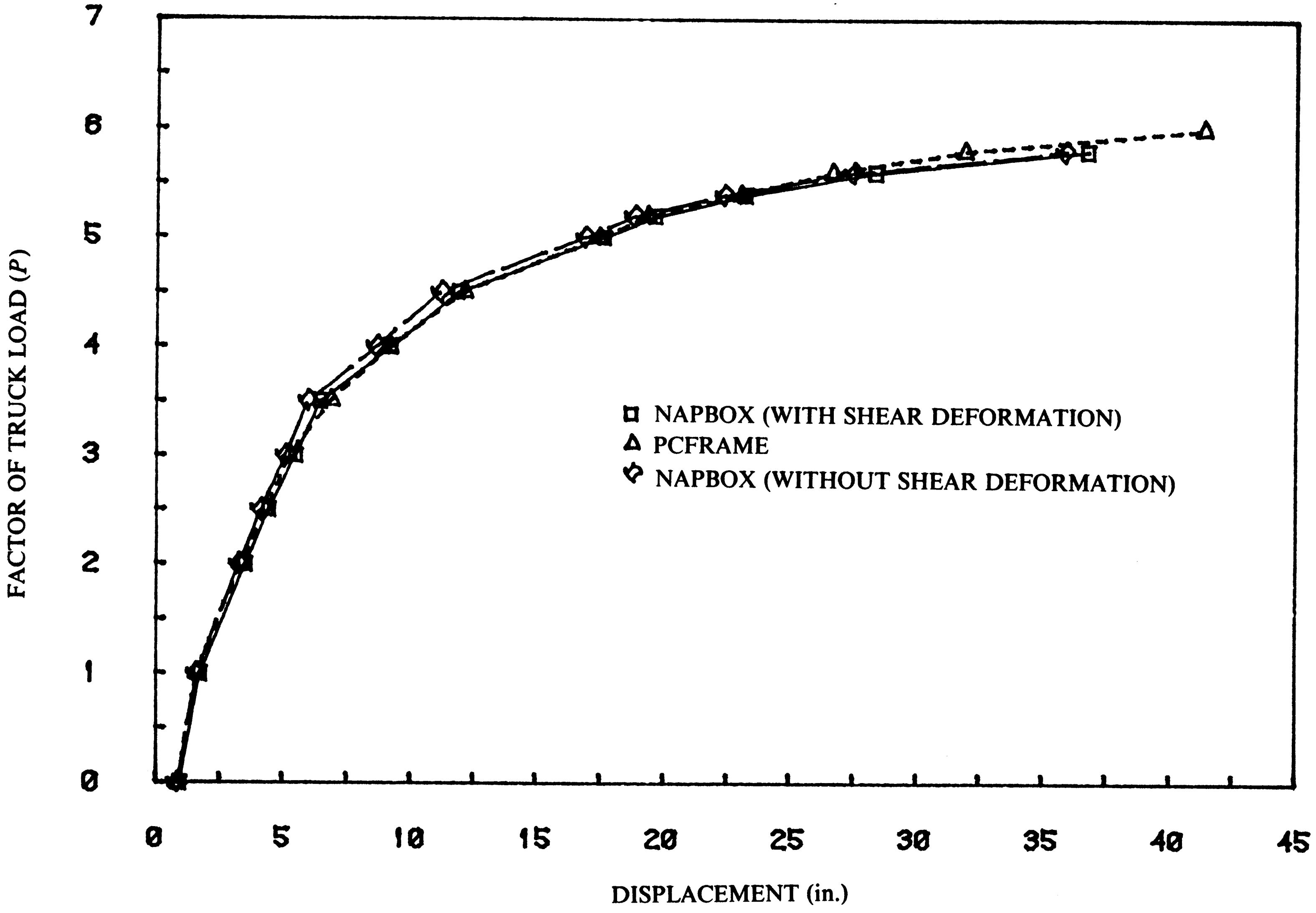

FIG. 8.10 EXAMPLE 8.2 - LOAD vs. VERTICAL DISPLACEMENT AT MIDDLE OF CENTER SPAN (LOAD CASE 1)

Comparison of the NAPBOX results for the cases with and without shear deformations indicates that the effect of shear deformations on the displacements is small.

The large overload capacity of the bridge is evident in Fig. 8.10. Even though service load design of the bridge is based on a load smaller than that due to one P13 truck, so that the P13 truck would overstress portions of the bridge, the ultimate load predicted by the two NAPBOX analyses is $P = 5.8$. Failure occurred due to yielding of concrete filaments in compression at the bottom flange over the interior support. The PCFRAME analysis predicted a slightly higher ultimate load of $P = 6.0$, which was also governed by yielding of concrete in compression over the interior support.

The internal bending moments at the middle of the center span and at the interior support under increasing truck loads are shown in Fig. 8.11. The NAPBOX results shown are from the analysis without shear deformations. The analysis with shear deformations yielded quite similar results. The agreement between NAPBOX and PCFRAME results is good. Redistribution of moments due to cracking is evident in Fig. 8.11. After cracking at the middle of the center span, at a load level of $P = 2.0$, the internal forces are redistributed such that at the middle of the center span, the rate of increase of internal bending moment with applied load becomes smaller compared to the rate prior to cracking. At the interior support, the corresponding rate becomes greater.

The effect of inelastic deformations on moment distribution can be seen in Fig. 8.12, where the longitudinal distribution of bending moments at the ultimate load of $P = 5.8$ obtained from the NAPBOX analysis is compared with that obtained from a linear elastic analysis using the computer program LAPBOX. The LAPBOX results were obtained by superposing the dead load moments, the secondary prestressing moments and the live load moments due to $P = 5.8$. Considerable redistribution of moments from the middle of the center span to the interior support is evident in Fig. 8.12. The elastic moment at the middle of the center span is reduced by 16.7%, whereas that at the interior support is increased by 23.1% (in absolute value). Such moment redistributions must be considered if an accurate

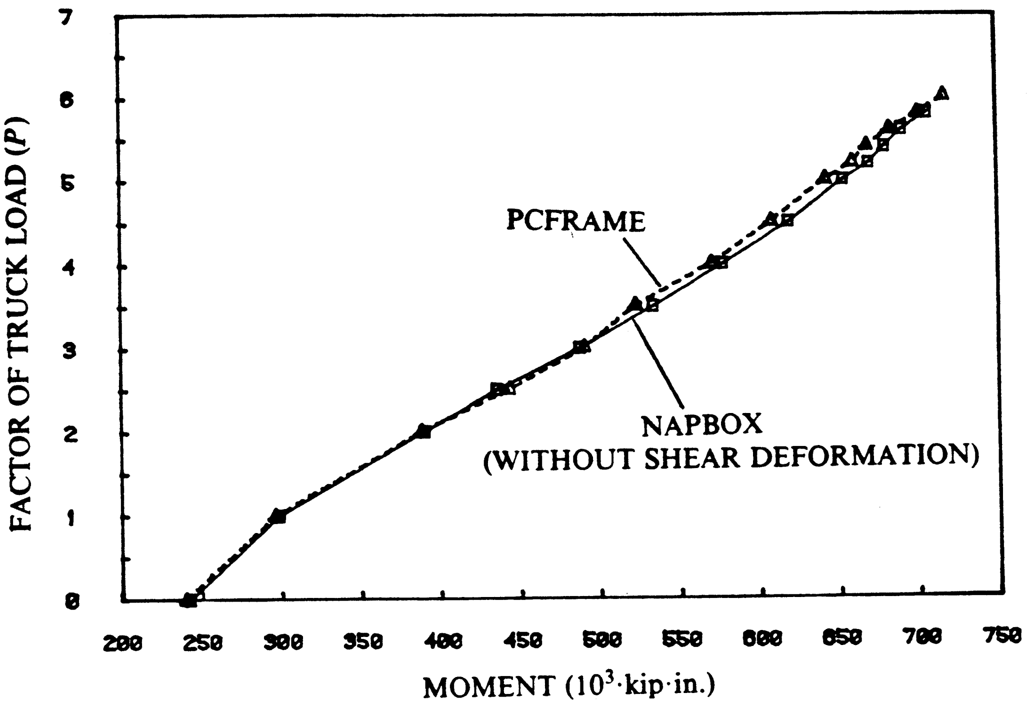

(a) NEGATIVE MOMENT AT INTERIOR SUPPORT

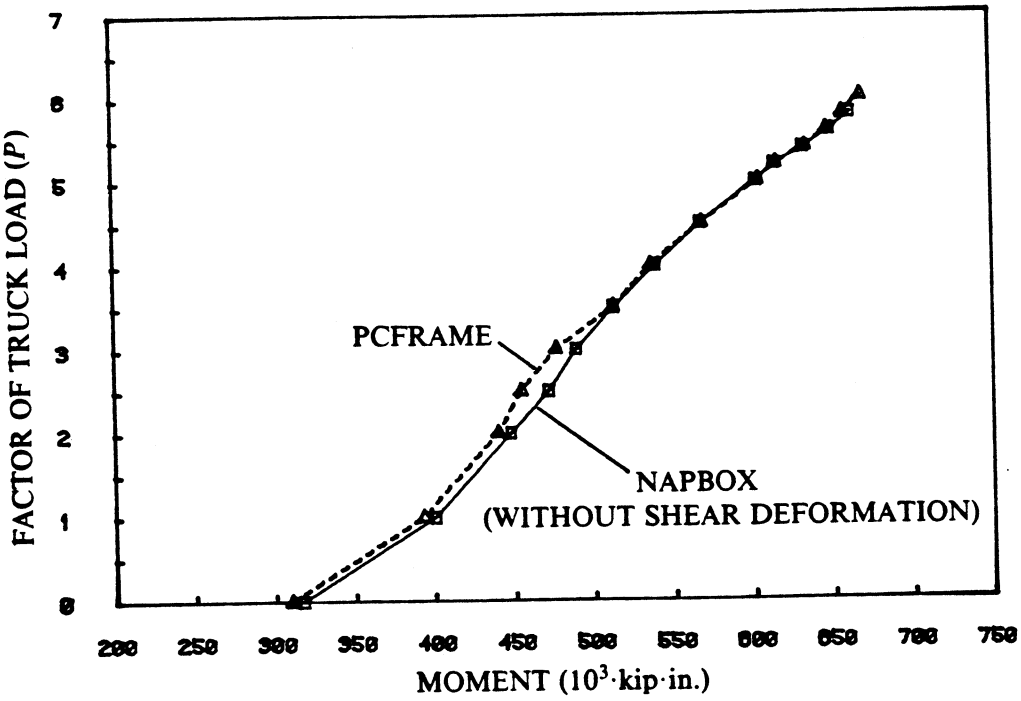

(b) POSITIVE MOMENT AT MIDDLE OF CENTER SPAN

FIG. 8.11 EXAMPLE 8.2 - LOAD vs. INTERNAL MOMENTS AT INTERIOR SUPPORT AND MIDDLE OF CENTER SPAN (LOAD CASE 1)

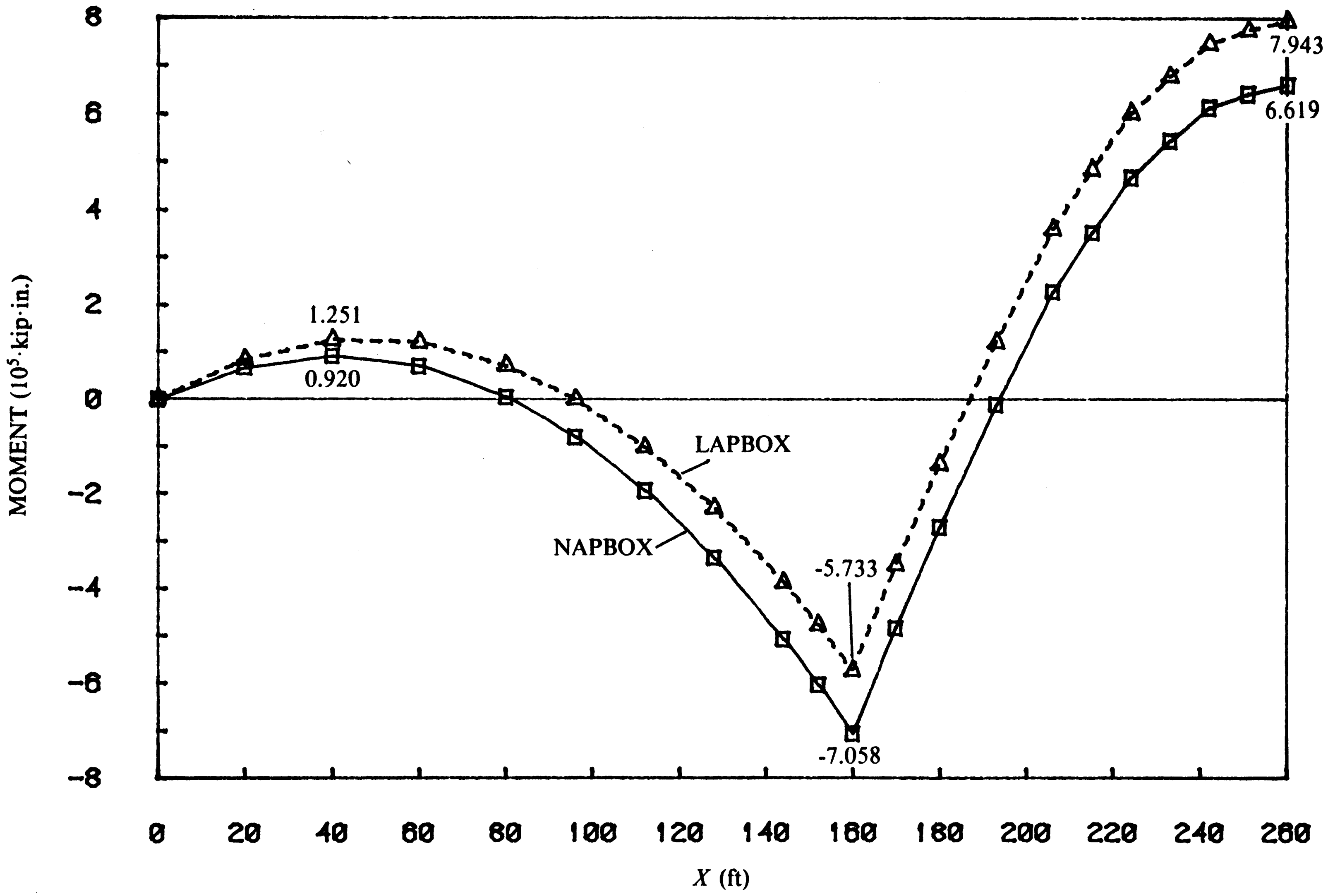

FIG. 8.12 EXAMPLE 8.2 - LONGITUDINAL DISTRIBUTIONS OF BENDING MOMENTS AT ULTIMATE LOAD P = 5.8 (LOAD CASE 1)

estimate of the ultimate load of the bridge is desired.

The increase in prestressing steel segment stresses due to vehicle overload at two critical locations, one near the middle of the center span and the other near the interior support, can be seen in Fig. 8.13. The plotted results in Fig. 8.13 are from the NAPBOX analysis including shear deformations. The results for the case without shear deformations were practically the same. Initiation of cracking at the critical sections can be identified in Fig. 8.13. The large increase in tendon stress near the middle of the center span at a load level of $P = 2.0$ corresponds to initial cracking at that location. Similarly, the large increase in tendon stress near the interior support at a load level of $P = 4.0$ corresponds to initial cracking at the interior support. After cracking, the prestressing steel segment stresses continue to increase rapidly until the ultimate load is reached.

Fig. 8.14 shows the normal stress distributions in concrete across the depth of the bridge girder at the two critical sections. The results shown correspond to the two NAPBOX analyses which gave the same concrete stresses. At $P = 0$, under the influence of dead load and prestressing alone, there is no cracking and the stress distributions are almost linear. At the ultimate load of $P = 5.8$, the compression zone in the section near the middle of the center span is located entirely within the top flange, whereas in the section near the interior support, the compression zone extends into the webs. Yielding of concrete in compression can be noticed at the interior support section, and this is an indication of impending failure.

8.2.2b Load Case 2

The vertical displacements at the middle of the center span for load case 2 under increasing overload levels are shown in Fig. 8.15. The displacements at the webs were obtained by considering the transverse distortion and twist of the cross section in addition to the centerline displacement. It is evident from Fig. 8.15 that the differences between the web displacements and the centerline displacements are small relative to the total displacements. This indicates that the distortional and torsional component of the eccentric truck loading had little influence on the overall response of the bridge.

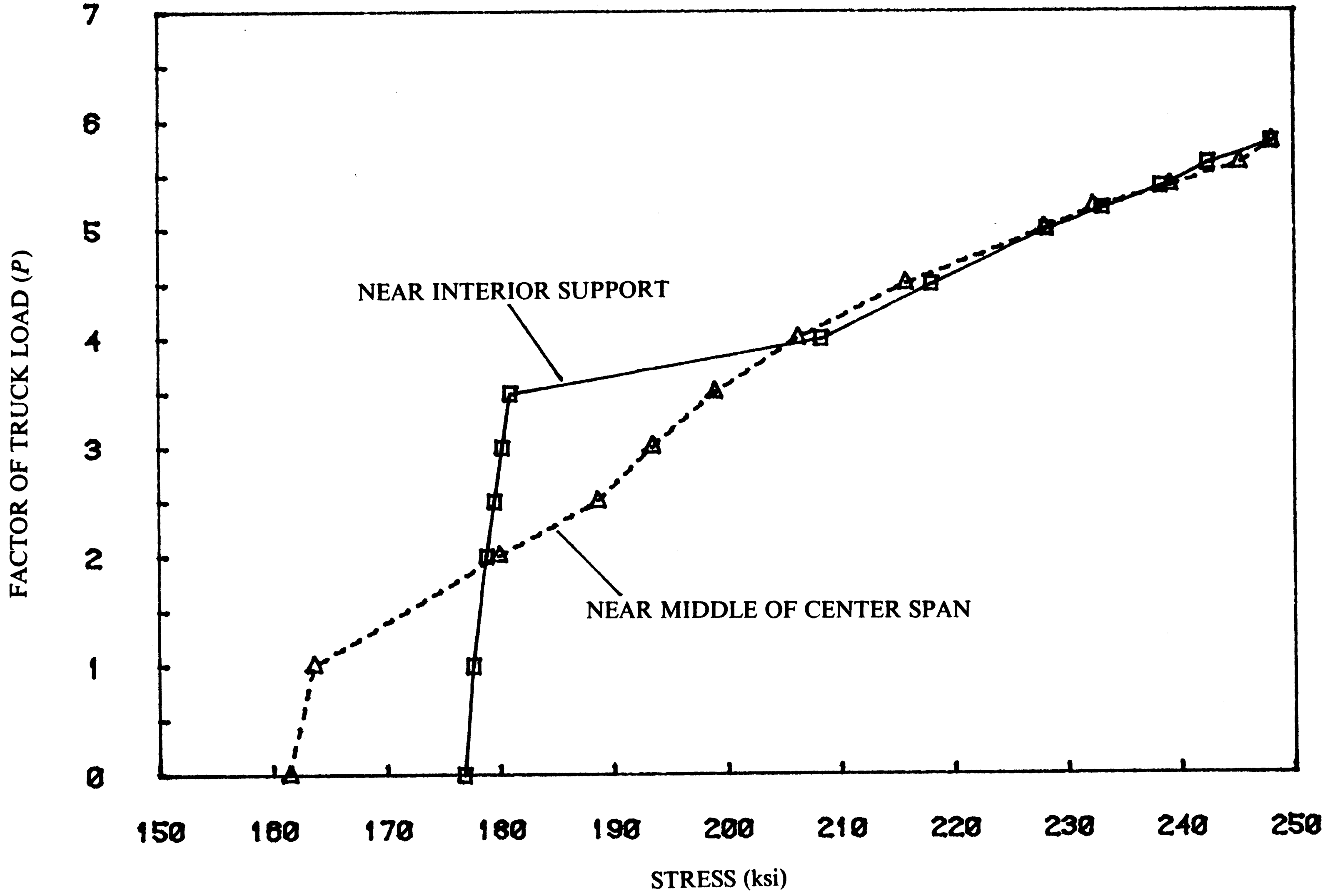

FIG. 8.13 EXAMPLE 8.2 - LOAD vs. PRESTRESSING STEEL SEGMENT STRESSES AT CRITICAL LOCATIONS (LOAD CASE 1)

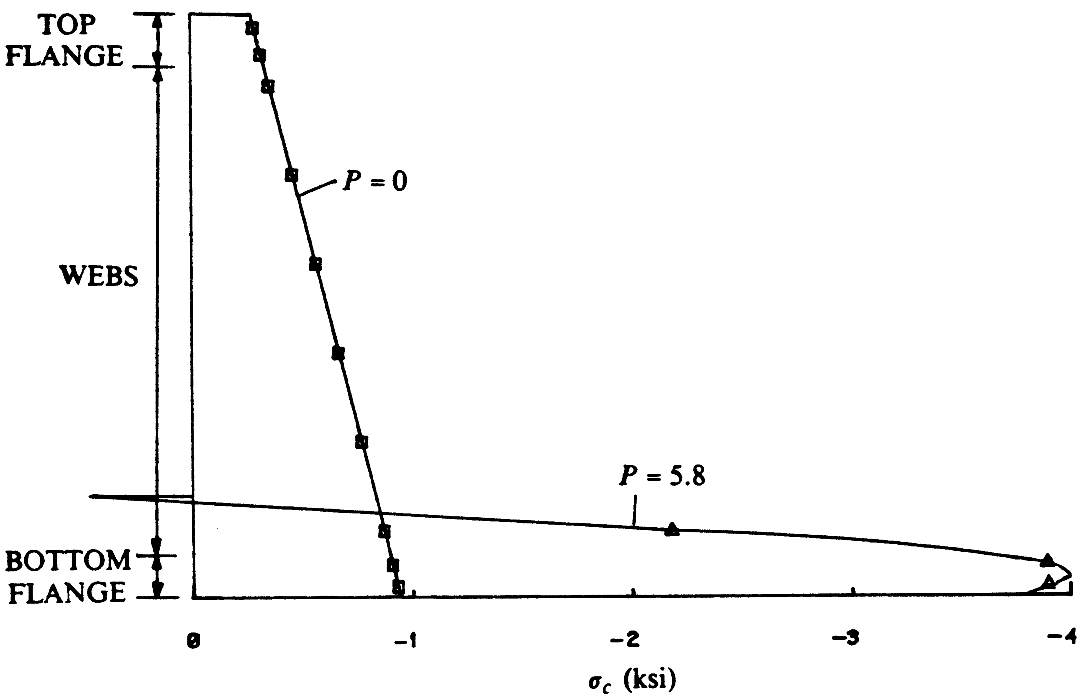

(a) SECTION NEAR INTERIOR SUPPORT (X = 158.31 ft)

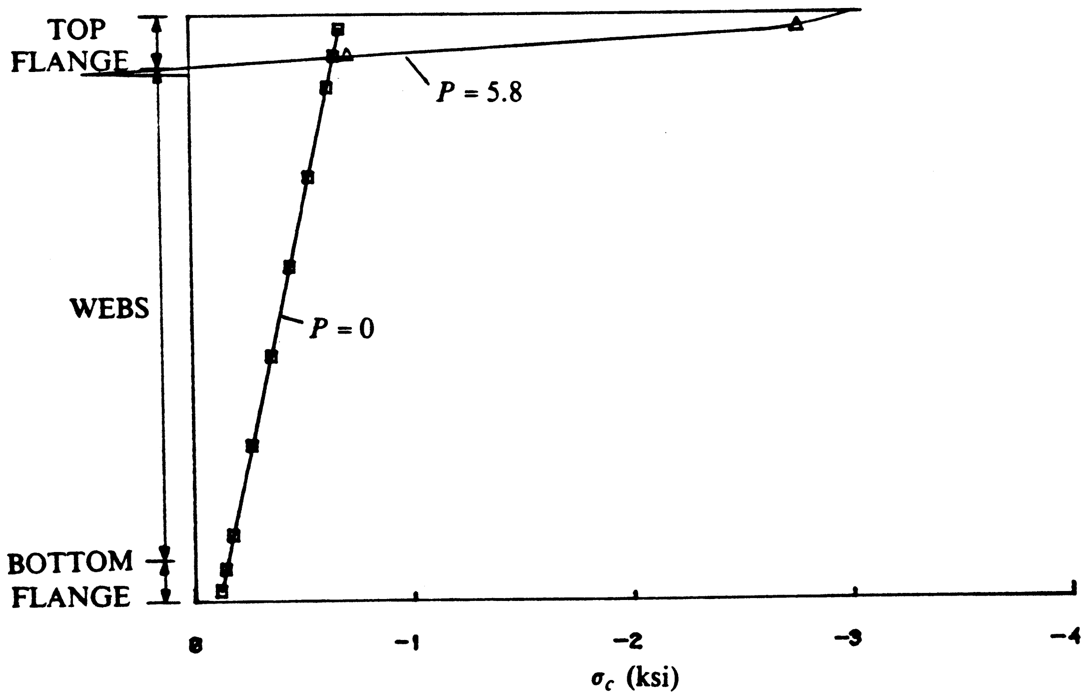

(b) SECTION NEAR MIDDLE OF CENTER SPAN (X = 258.10 ft)

FIG. 8.14 EXAMPLE 8.2 - CONCRETE STRESS DISTRIBUTIONS AT CRITICAL SECTIONS (LOAD CASE 1)

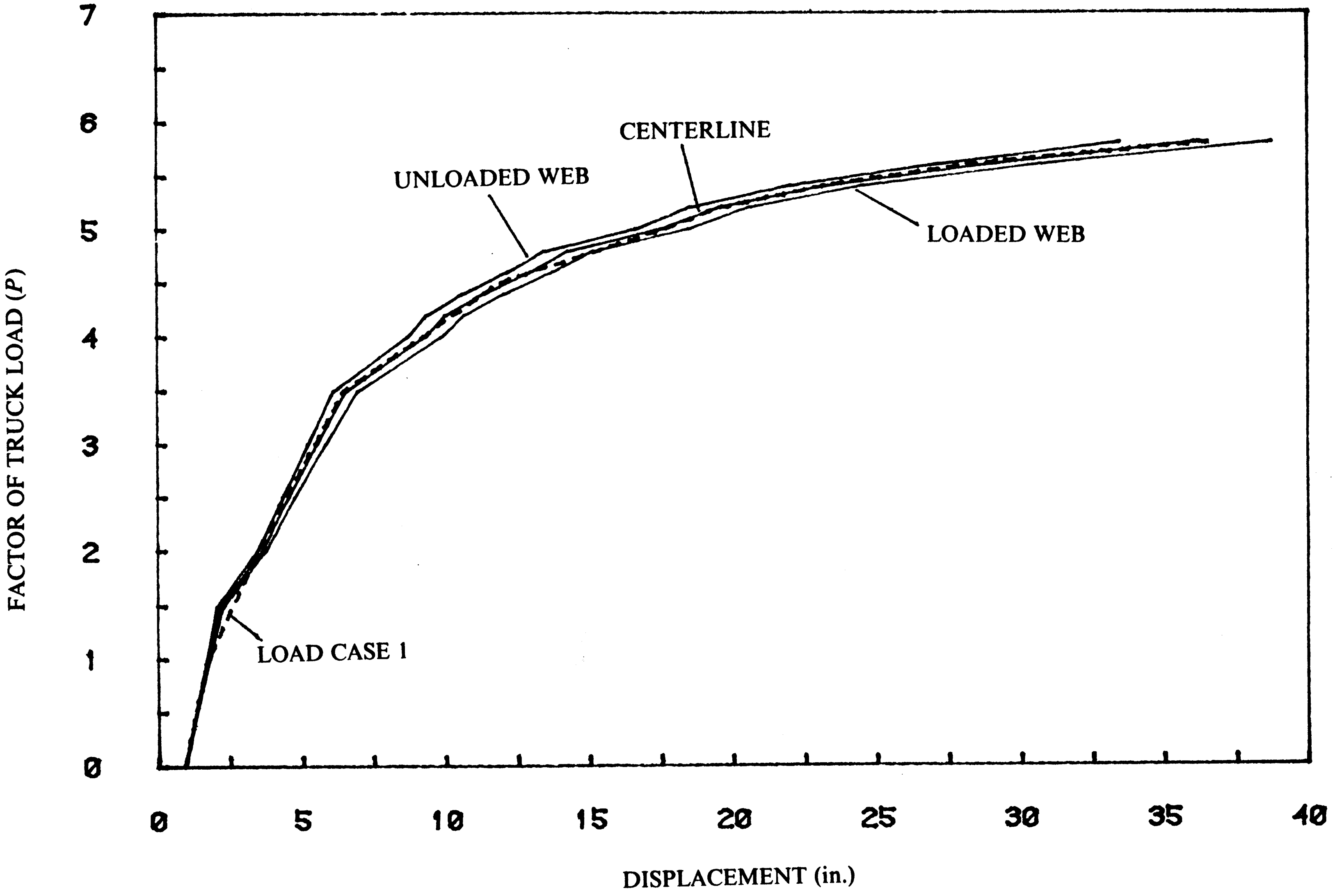

FIG. 8.15 EXAMPLE 8.2 - LOAD vs. VERTICAL DISPLACEMENTS AT MIDDLE OF CENTER SPAN (LOAD CASE 2)

Also shown in Fig. 8.15 are the vertical displacements for load case 1 (Fig. 8.10) obtained from the NAPBOX analysis including shear deformations. The results for load case 1 are seen to be very close to the centerline displacements for load case 2.

For this load case, initial cracking of concrete filaments at the middle of the center span and at the interior support occurred at load levels of $P = 2.0$ and $P = 4.0$ respectively, which are same as those for load case 1. The ultimate load of $P = 5.8$ obtained for this load case is also identical to that obtained for load case 1. Failure was again due to yielding of concrete filaments in compression at the bottom flange over the interior support. Similar agreement between the two load cases was also observed for the longitudinal bending moments and the prestressing tendon stresses. For load case 2, the tendon stresses in the loaded web were generally higher than the tendon stresses in the unloaded web, but the differences were small.

Fig. 8.16 shows transverse distributions of longitudinal normal strains at the ultimate load of $P = 5.8$. The strain distributions are shown for two sections, one near the interior support and the other near the middle of the center span. The strain values at the mid-thickness of the cross section walls have been plotted. The effect of warping strains can be seen in Fig. 8.16. At both sections, the higher strains occur in the loaded half of the box. In the tensile zones, the stresses are carried primarily by the prestressing tendons. The prestressing tendons yield considerably at the ultimate load so that large changes in strain are required to produce small changes in tendon stress. Hence the differences between the tendon stresses at the two webs are small although in the tensile zones the strains vary significantly across the width of the bridge. In the compression zones, where the stresses are carried primarily by concrete, the strain distributions are fairly uniform across the width of the bridge. The small variations in the concrete and tendon stresses across the width of the bridge demonstrate the ability of the box section to distribute the eccentrically applied load transversely.

All of the above results indicate that positioning of the truck loading over one of the webs, instead of over the centerline, did not affect the longitudinal flexural behavior of the

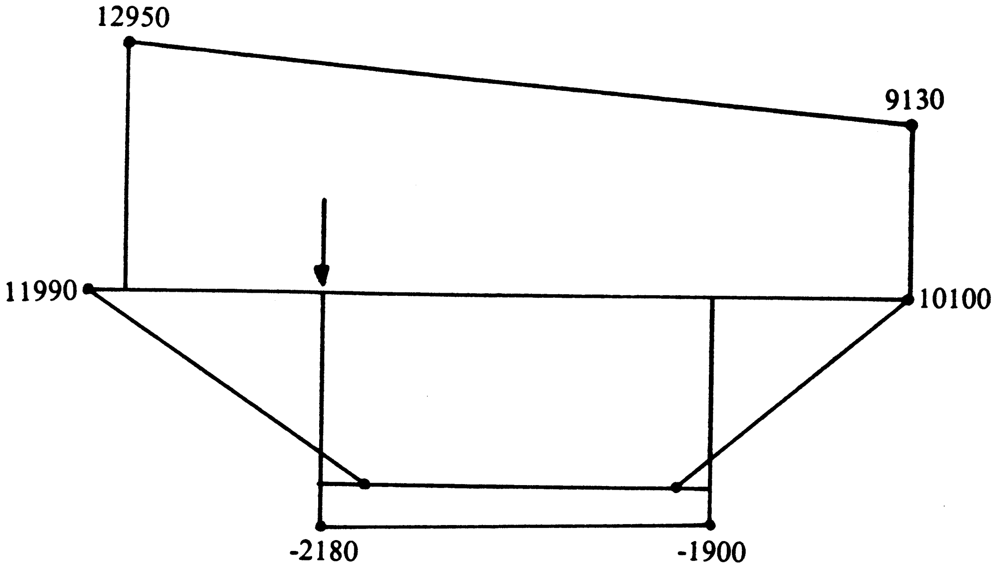

(a) SECTION NEAR INTERIOR SUPPORT (X = 158.31 ft)

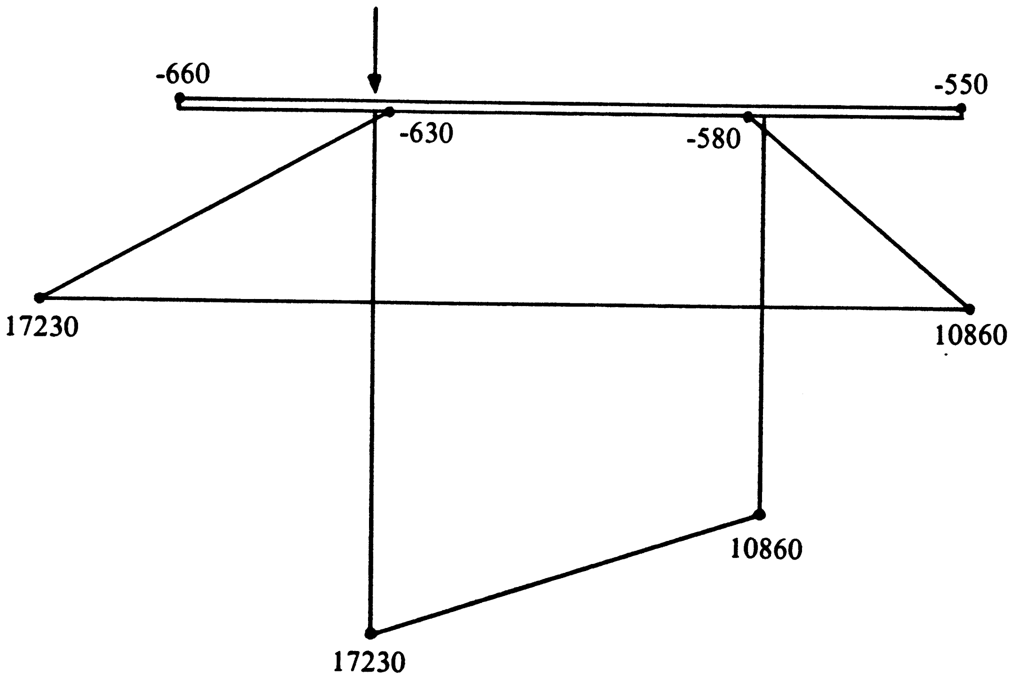

(b) SECTION NEAR MIDDLE OF CENTER SPAN (X = 258.10 ft)

ALL UNITS IN MICRO STRAIN

FIG. 8.16 EXAMPLE 8.2 - LONGITUDINAL NORMAL STRAIN DISTRIBUTIONS AT ULTIMATE AT CRITICAL SECTIONS (LOAD CASE 2)

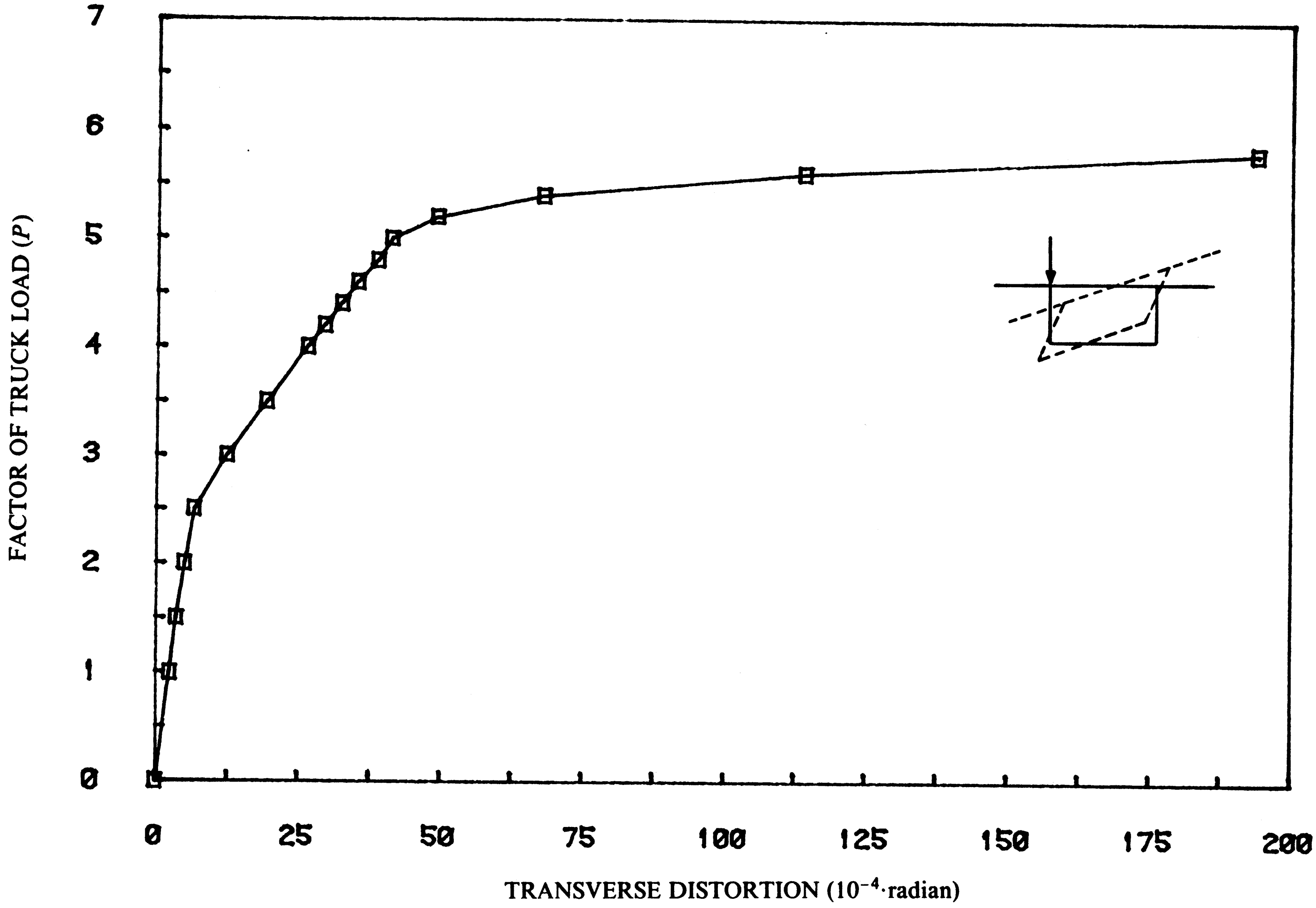

FIG. 8.17 EXAMPLE 8.2 - LOAD vs. TRANSVERSE DISTORTION OF CROSS SECTION AT MIDDLE OF CENTER SPAN (LOAD CASE 2)

bridge significantly. And it is this longitudinal flexural behavior that completely dominated the overall response of the bridge.

The transverse distortions of the cross section at the middle of the center span under increasing truck loads are shown in Fig. 8.17. Initial cracking due to transverse flexure was observed at $P = 2.5$ at the middle of the center span. This initial cracking can be identified in Fig. 8.17 as the point where the response curve first becomes nonlinear. After cracking, the transverse distortions increased more rapidly but at a nearly constant rate up to $P = 5.0$, when initial yielding due to transverse flexure occurred at the middle of the center span. After yielding, the transverse distortions increased very rapidly, and at the ultimate load of $P = 5.8$, the yielding spread out to about 60 ft from the middle of the center span. As discussed previously, the overall response of the bridge was not affected significantly in spite of the considerable transverse distortions observed near ultimate.

8.3 Example 8.3 - Three-Span Curved Prestressed Concrete Bridge

Overload behavior and ultimate strength of a curved prestressed concrete bridge are investigated in this final example. The ability of the computer program NAPBOX to predict the different response characteristics in a curved bridge induced by different overload conditions is demonstrated. Comparisons are made with the straight bridge in Example 8.2 (Sec. 8.2) where appropriate. The input data for the computer program NAPBOX used to obtain the results for load case 1 of this example are given in Appendix D.

8.3.1 Structure Details and Analytical Modelling

The three-span, curved, continuous, prestressed concrete box girder bridge considered in this example is shown in Fig. 8.18. The symmetric span arrangement of 160 ft, 200 ft and 160 ft, measured along the curved centerline, and the cross section of the bridge are identical to those for the straight bridge in Example 8.2 (Fig. 8.5). However, the axis of the bridge is now circularly curved in plan with a radius of $R = 496.5$ ft to the centerline. Full restraint against vertical translation, twist and transverse distortion of the cross section at the four

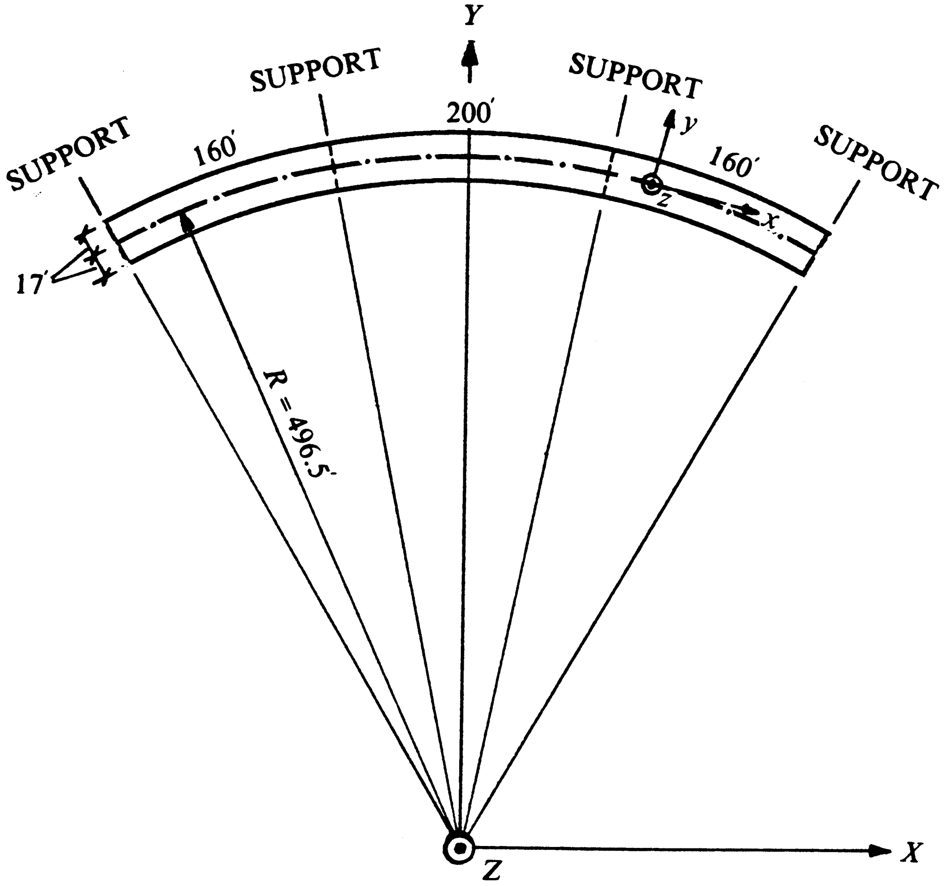

(a) PLAN

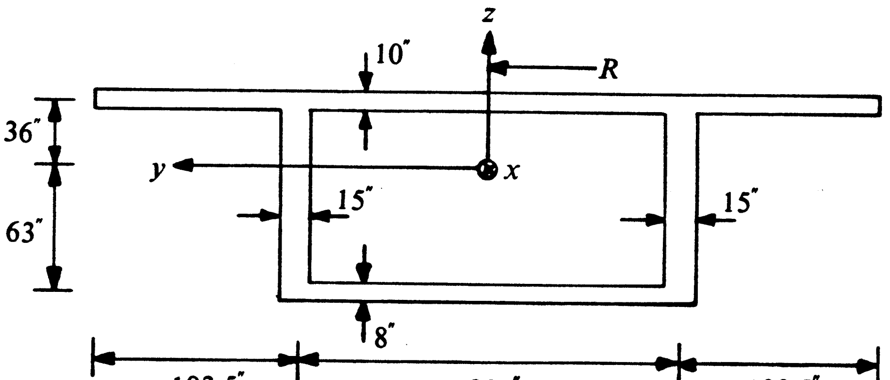

(b) CROSS SECTION

FIG. 8.18 EXAMPLE 8.3 - THREE-SPAN CURVED PRESTRESSED CONCRETE BRIDGE

TABLE 8.2 EXAMPLES 8.2 & 8.3 - MATERIAL PROPERTIES

Concrete:

$f_c'' = 4{,}000$ psi
$E_{ci} = 3.605 \times 10^6$ psi
$f_t = 500$ psi
$\epsilon_{cu} = 0.004$
$\beta = 0.85$
$\nu = 0.20$
$\tau_{cr} = 190$ psi
$\beta_1 = 0.85$

Longitudinal reinforcing steel:

$f_y = 60$ ksi
$E_{s1} = 29{,}000$ ksi
$E_{s2} = 0$
$\epsilon_{su} = 0.03$

Transverse reinforcing steel:

$f_{yt} = 60$ ksi
$E_{st} = 29{,}000$ ksi

Prestressing steel:

$\epsilon_1 = 0.00715$; $\sigma_1 = 196.6$ ksi ; $E_p = 27{,}500$ ksi
$\epsilon_2 = 0.00900$; $\sigma_2 = 220.0$ ksi
$\epsilon_3 = 0.01150$; $\sigma_3 = 240.0$ ksi
$\epsilon_4 = 0.01350$; $\sigma_4 = 245.0$ ksi
$\epsilon_5 = 0.05800$; $\sigma_5 = 270.0$ ksi

Anchorage slip at each jacking end: $\Delta_a = 0.25$ in.

Wobble friction coefficient: $K = 0.0002$/ft

Curvature friction coefficient: $\mu = 0.25$/radian

Unit weight of composite structure: $w = 155$ pcf

Tension stiffening coefficient: $k' = 0$

supports is again assumed.

Prestressing and longitudinal and transverse mild steel reinforcement for this example are assumed to be the same as for Example 8.2 (Sec. 8.2.1). The prestressing tendon profile in Fig. 8.5c is now measured along the curved webs. The same material properties (Table 8.2) are again used. Thus, except for the curvature of the bridge axis in plan, the bridge of this example is identical to the bridge of Example 8.2.

In order to study the overload behavior and the ultimate strength of the bridge under increasing vehicular load, the symmetric approximation of the P13 truck loading in Fig. 8.6, which was also used in Example 8.2, is positioned in the middle of the center span of the bridge (Fig. 8.19a), and the structural load vector due to its weight is incremented until ultimate failure occurs. For the sake of simplicity, differences between the arc lengths and the chord lengths between the points of application of the truck load are ignored. Again, for convenience in presentation and comparison of results, P is used to denote the factor of truck load applied. Thus $P = 1$ represents overload due to one truck (Fig. 8.19a).

Three different load cases are considered in this example.

Load Case 1 - Truck load is positioned over centerline of bridge (Fig. 8.19b).

Load Case 2 - Truck load is positioned over outer web (Fig. 8.19c).

Load Case 2 - Truck load is positioned over inner web (Fig. 8.19d).

Due to symmetry of the structure and the loadings, only half the length of the bridge is analyzed. The element subdivision along the bridge axis is similar to that used in Example 8.2 (Fig. 8.8), except that each of the 20 elements in Fig. 8.8 is further subdivided into 2 equal elements giving a total of 40 elements. Further, the elements are now curved rather than straight. The discretization of the cross section into concrete and longitudinal steel filaments used for all three load cases is the same as the one used in Example 8.2 for load case 2, and is shown in Fig. 8.9b.

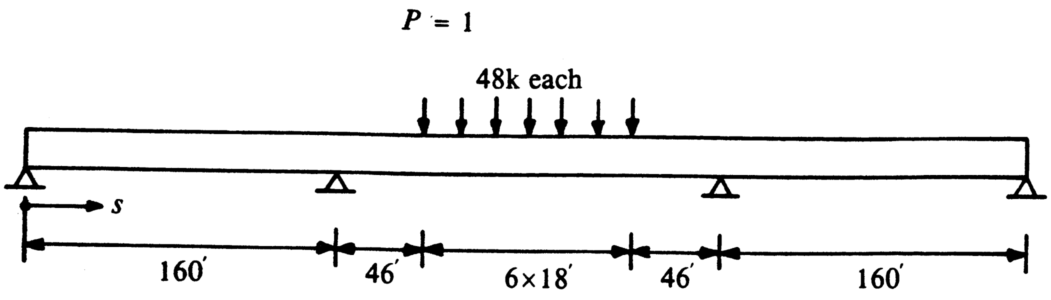

(a) LONGITUDINAL POSITION OF TRUCK LOAD FOR LOAD CASES 1, 2 AND 3

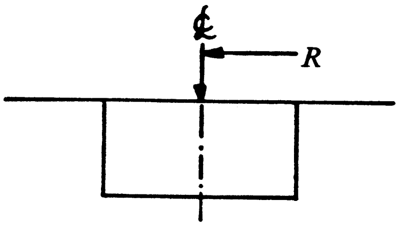

(b) TRANSVERSE POSITION OF TRUCK LOAD FOR LOAD CASE 1

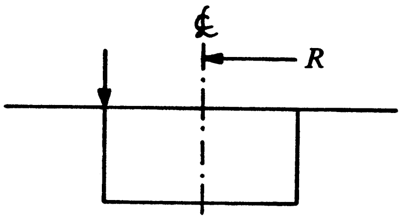

(c) TRANSVERSE POSITION OF TRUCK LOAD FOR LOAD CASE 2

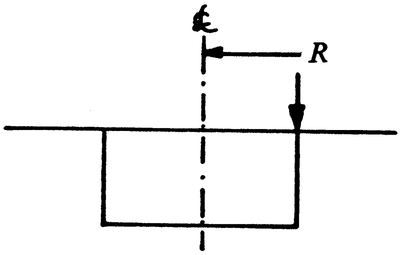

(d) TRANSVERSE POSITION OF TRUCK LOAD FOR LOAD CASE 3

FIG. 8.19 EXAMPLE 8.3 - POSITION OF TRUCK LOAD FOR DIFFERENT LOAD CASES

8.3.2 Presentation and Discussion of Results

Figs. 8.20, 8.21 and 8.22 show the vertical web displacements under increasing truck loads for load cases 1, 2 and 3 respectively. The web displacements were computed from the vertical translation (centerline displacement), transverse distortion and twist of the cross section. It is evident from the load-displacement curves that the structure responds quite differently depending upon the transverse position of the truck load.

Load case 1 (Fig. 8.20), with the truck load over the centerline, yielded the highest ultimate load of $P = 5.6$, which compares well with the ultimate of $P = 5.8$ obtained for the straight bridge in Example 8.2. Failure occurred due to yielding of concrete filaments in compression at the bottom flange over the interior support. The small differences between the vertical displacements at the two webs indicate that the overall response of the bridge was governed by its longitudinal flexural behavior.

In Fig. 8.21, the differences between the vertical displacements at the two webs are seen to be quite significant for load case 2 with the truck load positioned over the outer web. The differential web displacements, which increase with increasing load levels, are primarily due to the twist of the cross section, and were caused by rapid deterioration in the torsional stiffness of the bridge. The ultimate load of the bridge was reduced to $P = 5.2$. Failure occurred due to the shear stress reaching its ultimate value at the outer web of the section just to the inside of the interior support.

An ultimate load of only $P = 4.0$ was obtained for load case 3 (Fig. 8.22) with the truck load positioned over the inner web. This loading produced rapid deterioration in the transverse flexural rigidity of the bridge. The transverse distortion of the cross section at the middle of the center span increased rapidly, and this is reflected in the increasingly large differences between the vertical displacements at the two webs (Fig. 8.22). Failure occurred due to the transverse distortion of the cross section at the middle of the center span reaching its ultimate value. The ultimate value of the transverse distortion is of course governed by the plastic hinge rotation capacities at the four corners of the box section (Sec. 5.2.3b).

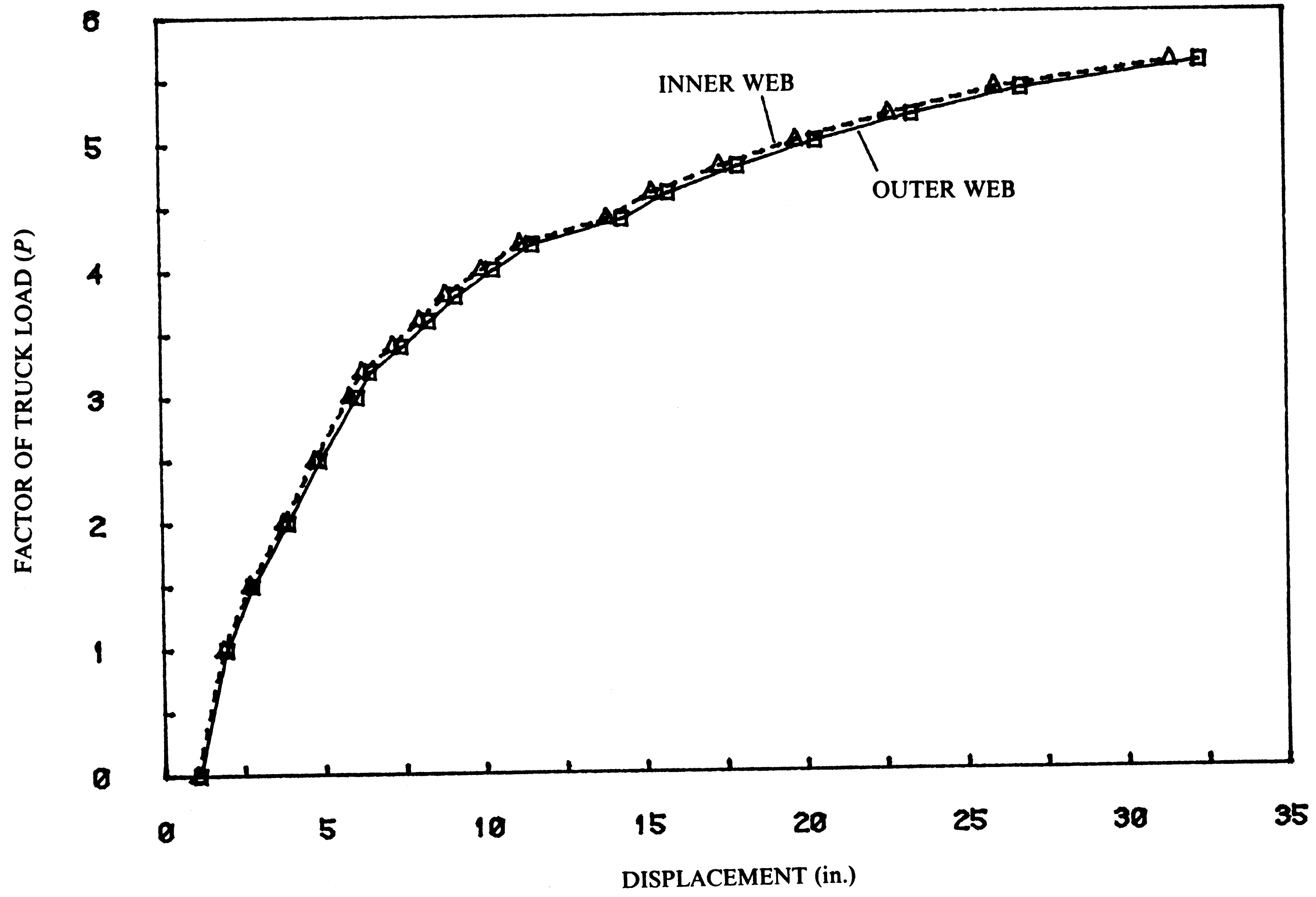

FIG. 8.20 EXAMPLE 8.3 - LOAD vs. VERTICAL WEB DISPLACEMENTS AT MIDDLE OF CENTER SPAN (LOAD CASE 1)

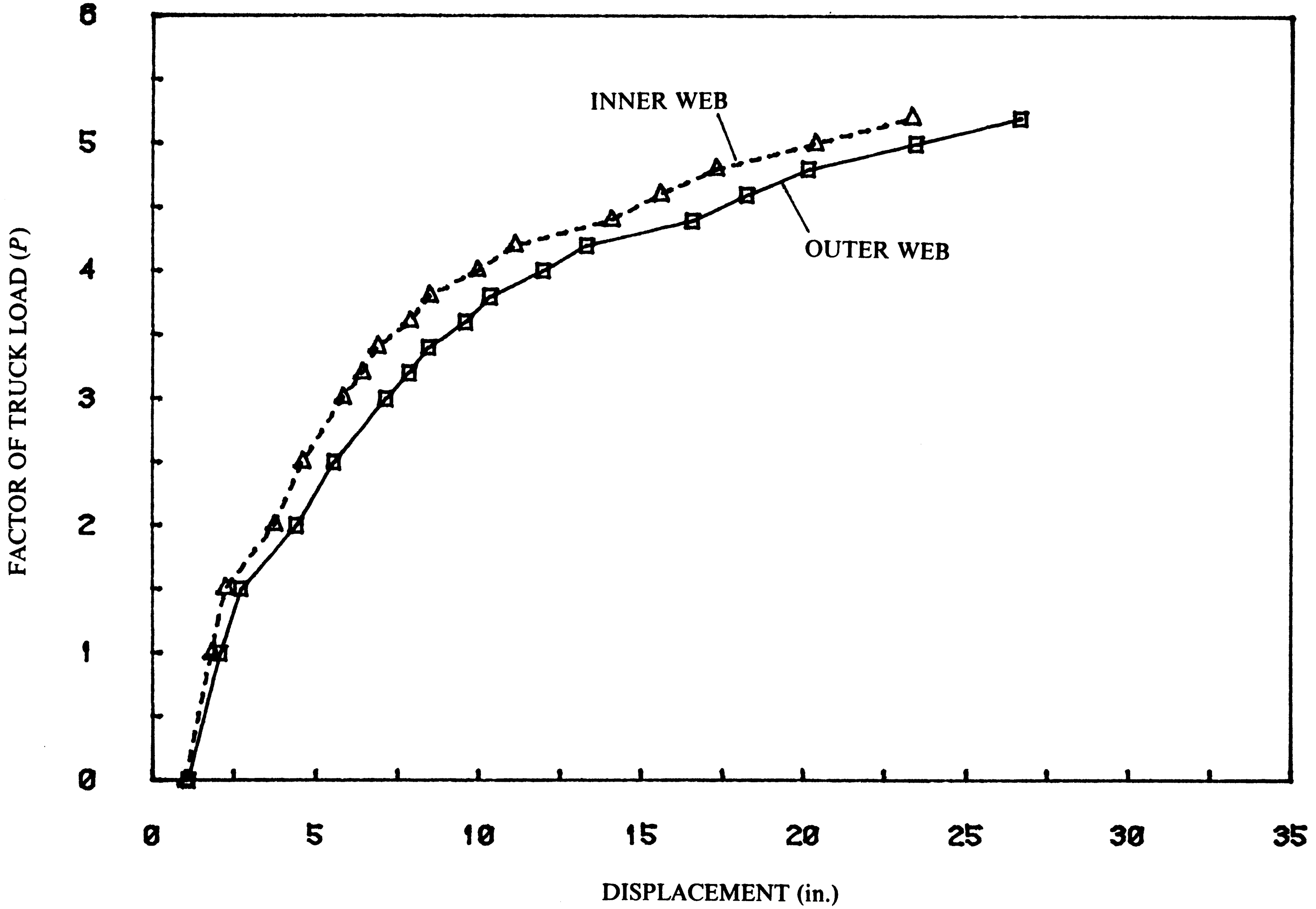

FIG. 8.21 EXAMPLE 8.3 - LOAD vs. VERTICAL WEB DISPLACEMENTS AT MIDDLE OF CENTER SPAN (LOAD CASE 2)

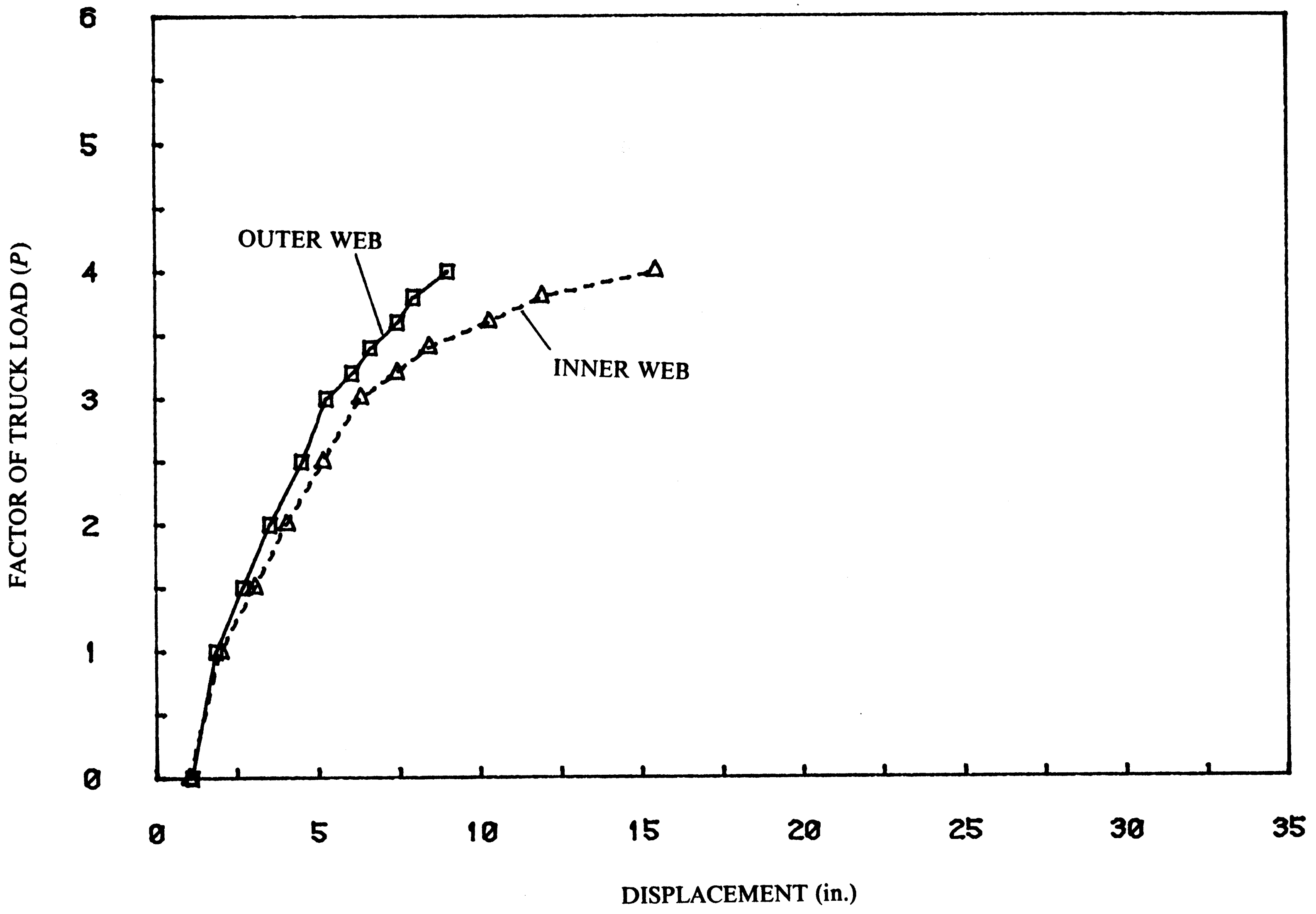

FIG. 8.22 EXAMPLE 8.3 - LOAD vs. VERTICAL WEB DISPLACEMENTS AT MIDDLE OF CENTER SPAN (LOAD CASE 3)

The cross section twists at the middle of the center span under increasing truck loads are shown in Fig. 8.23 for all three load cases. The rapid deterioration in the torsional stiffness of the bridge for load case 2 is evident in Fig. 8.23. Out of the three load cases considered, load case 2 represents the most severe torsional loading. The outer web loading tends to twist the cross section in the same direction as the dead load and prestressing, and hence produces the largest cross section twists. The deterioration in the torsional stiffness for load case 2 was enhanced by shear cracking in the bottom flange to the inside of the interior support. Initial shear cracking in the bottom flange, which was observed at $P = 1.5$ at the section just to the inside of the interior support, can be identified in Fig. 8.23 by the sudden change in the slope of the load-twist curve between $P = 1.0$ and $P = 1.5$. For all three load cases, shear cracking in the webs occurred on both sides of the interior support under the action of dead load and prestressing alone. Beyond $P = 1.5$, the cross section twist at the middle of the center span continued to increase rapidly for load case 2 as the shear cracking in the webs and the bottom flange extended longitudinally. It should be pointed out that, due to the curvature of the bridge axis, concrete filament cracking over the interior support also contributes to the cross section twist at the middle of the center span.

The load-twist curve (Fig. 8.23) for load case 1 shows a less severe torsional response of the bridge. Due to the curvature of the bridge axis, the centerline loading does tend to twist the cross section, but its effect is not as pronounced as that of load case 2. No shear cracking was observed in the bottom flange. As evident in Fig. 8.23, load case 3 represents the least severe torsional loading. The inner web loading tends to decrease the cross section twist due to dead load and prestressing. The net result is that the cross section twist remains almost constant with increasing truck load levels.

The transverse distortions of the cross section at the middle of the center span under increasing truck loads are shown in Fig. 8.24 for the three load cases. Load case 3 is now found to produce the most severe response. The inner web loading tends to distort the cross section in the same direction as the dead load and prestressing. The combined effect is to

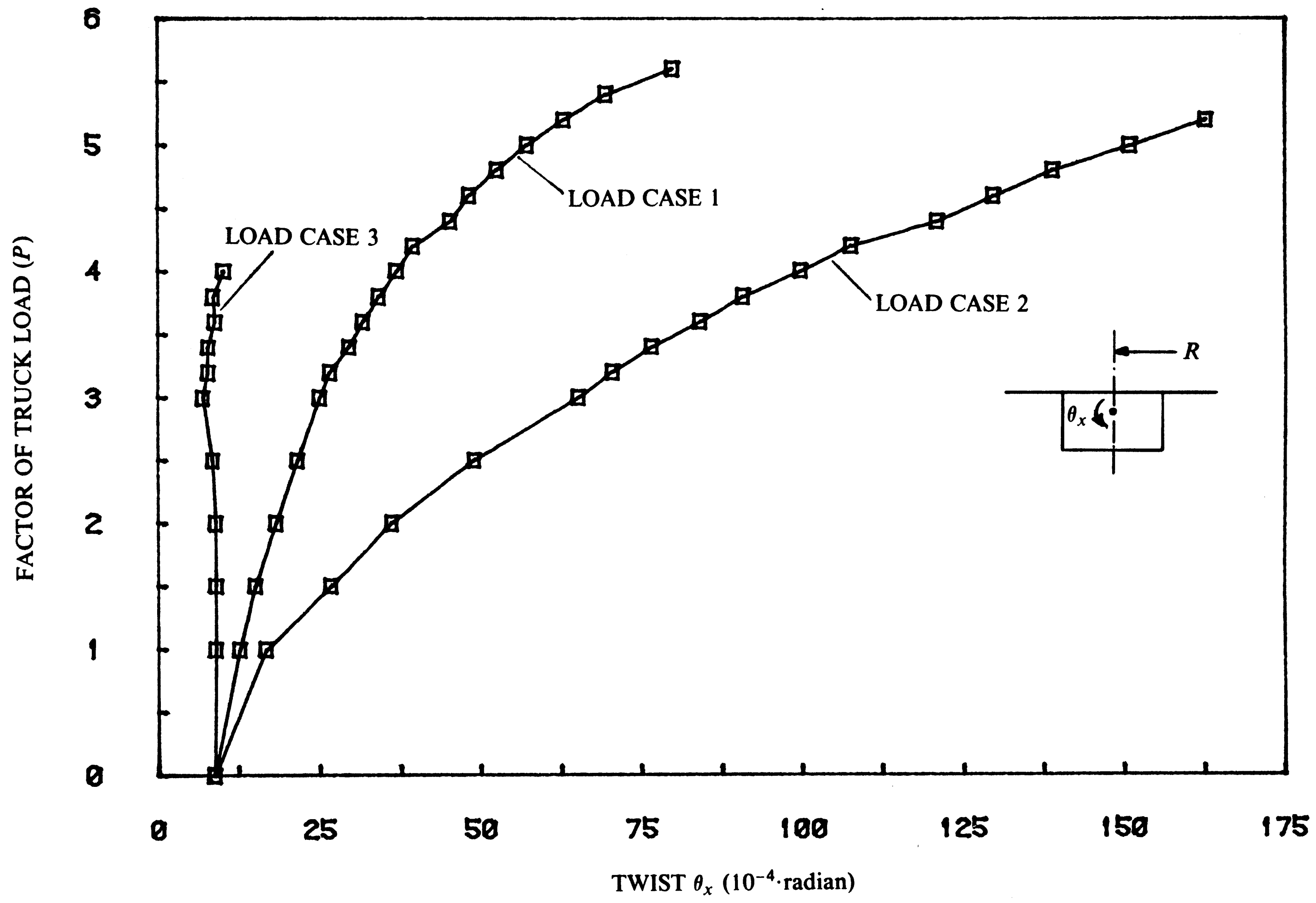

FIG. 8.23 EXAMPLE 8.3 - LOAD vs. CROSS SECTION TWIST AT MIDDLE OF CENTER SPAN (LOAD CASES 1, 2 AND 3)

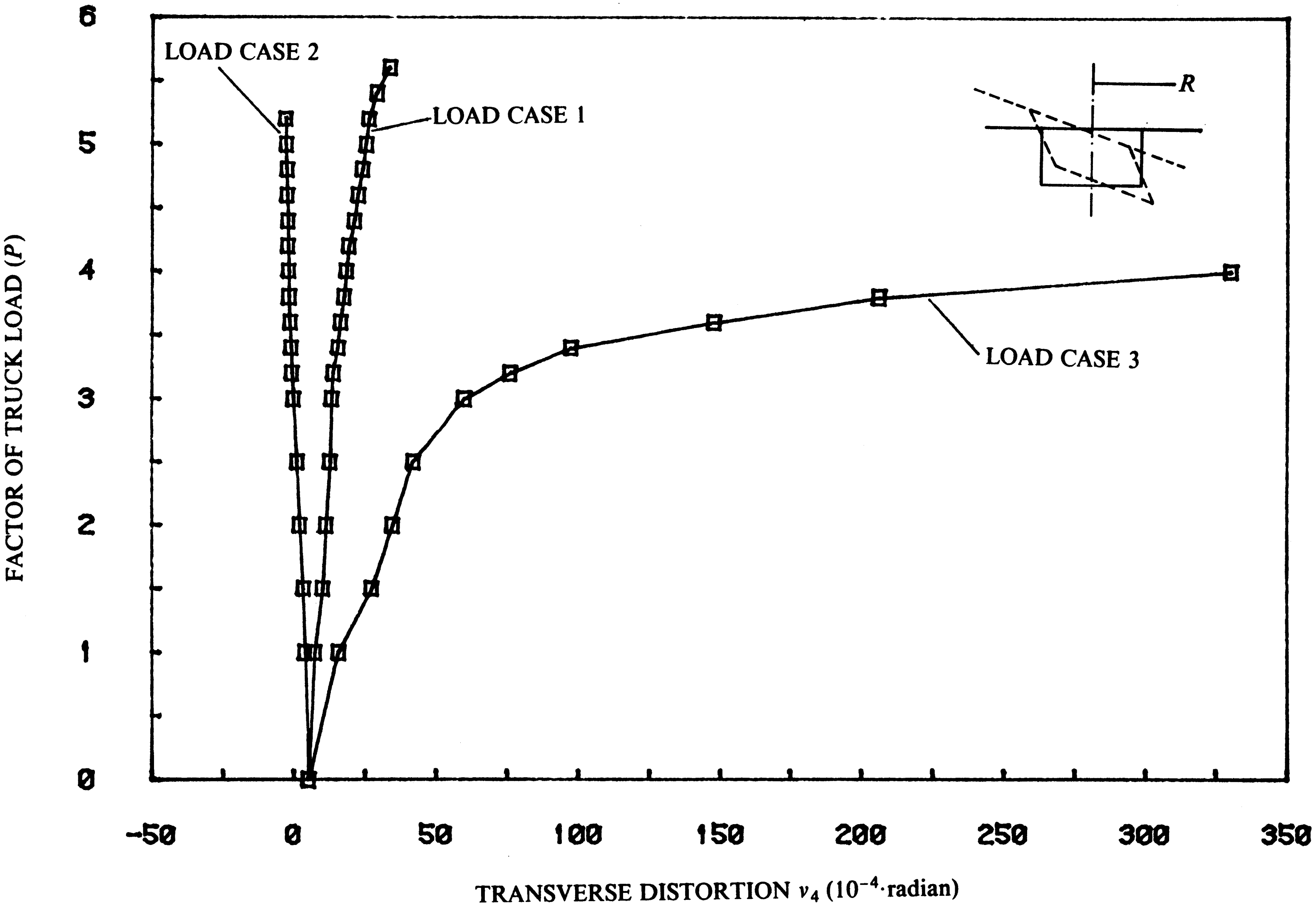

FIG. 8.24 EXAMPLE 8.3 - LOAD vs. TRANSVERSE DISTORTION OF CROSS SECTION AT MIDDLE OF CENTER SPAN (LOAD CASES 1, 2 AND 3)

cause rapid deterioration in the transverse flexural rigidity of the bridge. Initial cracking due to transverse flexure was observed at the middle of the center span at the very first load step of $P = 1.0$. This was followed by transverse flexural yielding in the middle of the center span, which first occurred at $P = 2.5$. Beyond $P = 2.5$, the transverse distorions increased rapidly as the transverse flexural yielding spread longitudinally. At the ultimate load of $P = 4.0$, the yielding spread out to about 82.5 ft from the middle of the center span.

The transverse distortions for load cases 1 and 2 are seen in Fig. 8.24 to be much smaller than those for load case 3. No serious deterioration in the transverse flexural rigidity of the bridge was observed for either of these load cases. The tendency of the outer web loading (load case 2) to distort the cross section is resisted by the dead load and prestressing which tend to distort the cross section in the opposite direction. The net result is that very little transverse distortions occur.

The prestressing steel segment stresses at two critical locations, one near the middle of the center span and the other near the interior support, are shown in Fig. 8.25 for all three load cases. For each location, the prestressing stresses in both the webs are shown. Due to additional friction losses caused by the curvature of the bridge axis, the initial prestressing stresses in Fig. 8.25 ($P = 0$) are smaller than the corresponding stresses in Fig. 8.13 that were obtained for the straight bridge in Example 8.2. Moreover, the differences between the initial prestressing stresses in the two webs are very small since the larger wobble friction losses in the outer web more or less balance out the larger curvature friction losses in the inner web.

The load levels at which initial cracking of concrete filaments was observed at the middle of the center span and at the interior support are summarized in Table 8.3. These cracking loads can be identified in Fig. 8.25 as the points where large increases in the tendon stresses occur.

The differences between the tendon stresses in the two webs, evident in Fig. 8.25, provide further insight into the behavior of the bridge under the three different loading conditions. A higher tendon stress in one or the other web indicates that a greater proportion

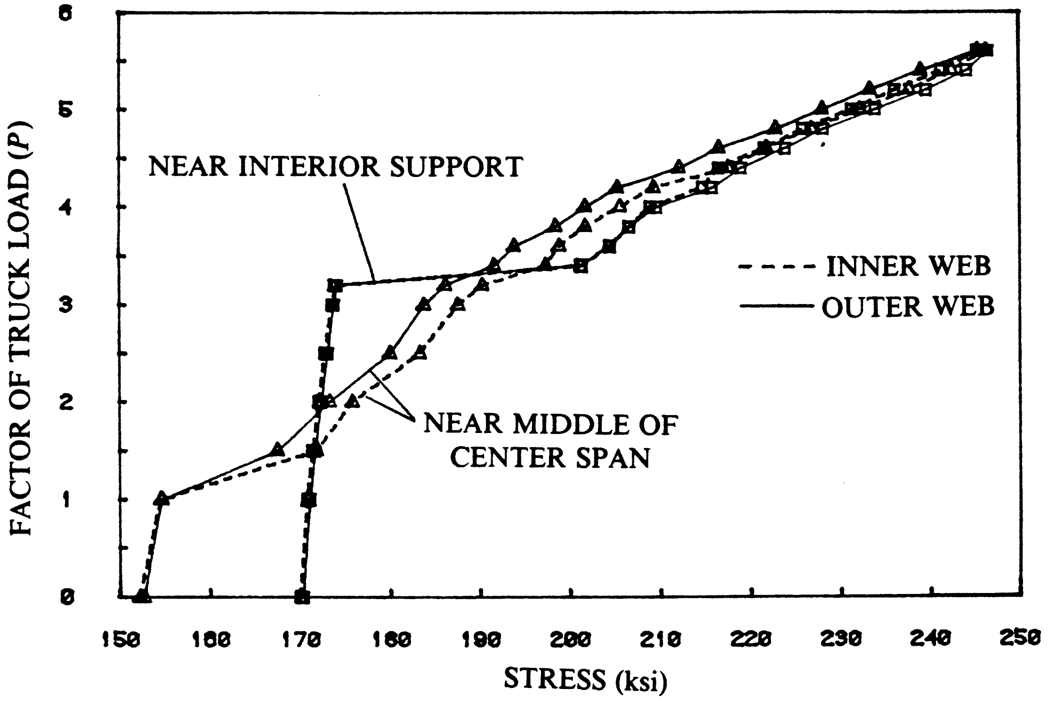

(a) LOAD CASE 1

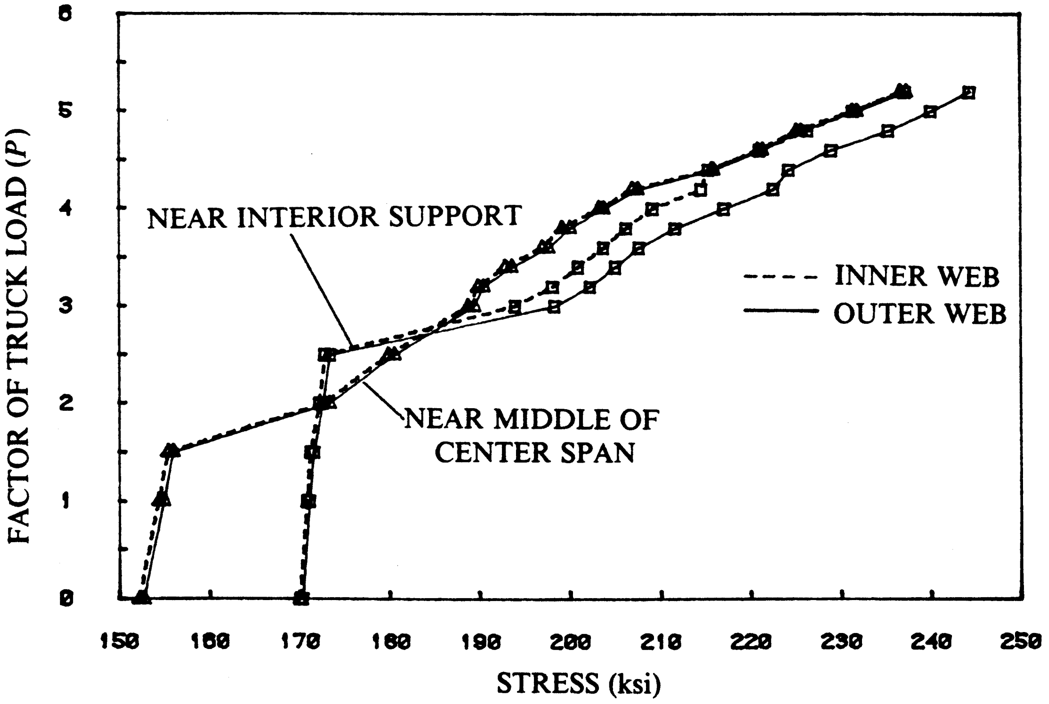

(b) LOAD CASE 2

FIG. 8.25 EXAMPLE 8.3 - LOAD vs. PRESTRESSING STEEL SEGMENT STRESSES AT CRITICAL LOCATIONS

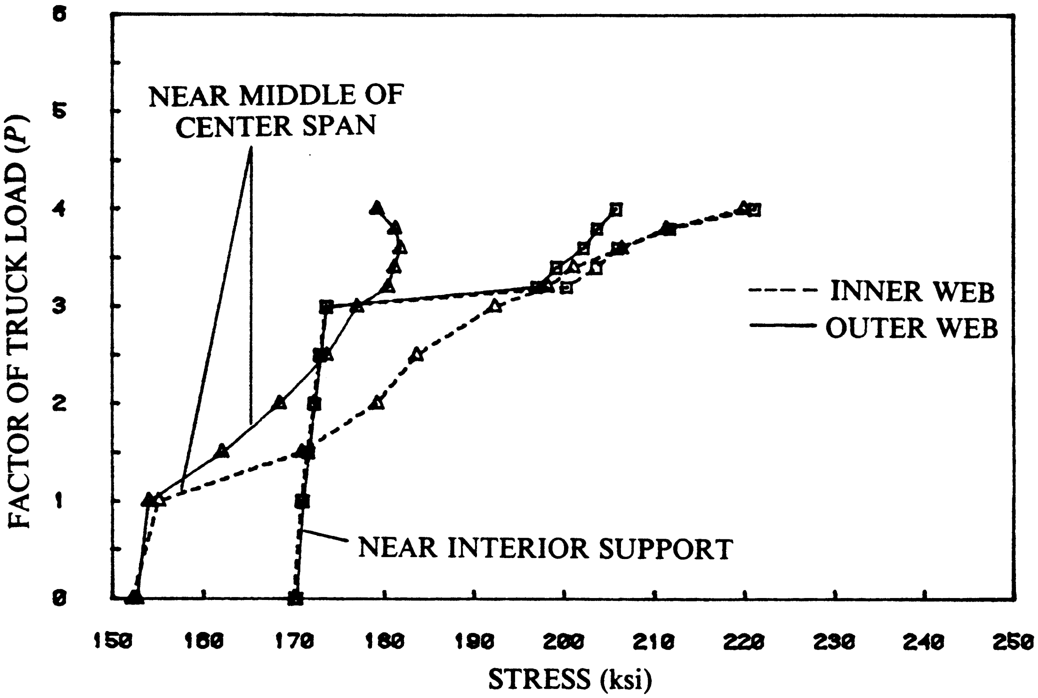

(c) LOAD CASE 3

FIG. 8.25 EXAMPLE 8.3 - LOAD vs. PRESTRESSING STEEL SEGMENT STRESSES AT CRITICAL LOCATIONS

TABLE 8.3 EXAMPLE 8.3 - SUMMARY OF CRACKING LOADS

LOAD CASE	INITIAL CRACKING AT MIDDLE OF CENTER SPAN	INITIAL CRACKING AT INTERIOR SUPPORT
CENTERLINE LOAD	$P = 1.5$	$P = 3.4$
OUTER WEB LOAD	$P = 2.0$	$P = 3.0$
INNER WEB LOAD	$P = 1.5$	$P = 3.2$

of the load is carried by that web. Fig. 8.25a shows that for load case 1, a greater proportion of the load is carried by the inner web near the middle of the center span. Near the interior support, however, the outer web carries a greater proportion of the load. But the small differences between the tendon stresses in the two webs at both locations also indicate that the centerline truck loading is distributed fairly uniformly across the width of the bridge. In Fig. 8.25b, practically equal proportions of the outer web load (load case 2) are found to be carried by the two webs near the middle of the center span. Near the interior support, the outer web carries a considerably greater proportion of the load. Fig. 8.25c shows that for load case 3, increasingly greater proportions of the inner web loading are carried by the inner web with increasing load levels. At both critical locations, the differences between the tendon stresses in the two webs increase rapidly after the initiation of concrete filament cracking. Near the middle of the center span, the outer web tendon stresses in fact start to decrease near ultimate while the inner web tendon stresses continue to increase rapidly. The increasing deterioration in the ability of the box section to distribute the eccentrically applied inner web loading transversely is due to the rapid deterioration in the transverse flexural rigidity of the bridge. The above observations on the transverse distribution of loads are also reflected in the longitudinal normal strain distributions (not reported) at the critical sections.

9. CONCLUSIONS

9.1 Summary

An efficient numerical procedure for linear elastic analysis and nonlinear material analysis of curved nonprismatic reinforced and prestressed concrete box girder bridges has been presented.

Thin-walled beam theory and the finite element method were combined to develop a curved nonprismatic thin-walled box beam element. The cross section of the element is a rectangular single-cell box with side cantilevers. The axis of the element is curved in plan. The cross sectional dimensions vary along the element axis. The three-node element has eight displacement degrees of freedom, including transverse distortion and longitudinal warping of the cross section, at each node. Small displacements and small strains were assumed in the element formulation.

Prestressing, consisting of post-tensioned tendons in the longitudinal direction, was considered. The tendons were idealized as straight prestressing steel segments between the nodes of the box beam elements. Friction and anchorage slip losses were considered. For linear elastic analysis of the structure under prestressing, the effect of prestress was represented by a set of equivalent loads applied at the nodes of the box beam elements. For the analysis at transfer of prestress in a nonlinear analysis, the prestressing was similarly represented by a set of equivalent nodal loads, and the structure was analyzed as an ordinary reinforced concrete one. The contribution of the prestressing steel to the overall structural stiffness was neglected since, at this stage, the steel is unbonded. For the subsequent application of external loads, the prestressing steel was assumed to be bonded to the concrete, and the prestressing steel stiffnesses were included in the overall structural stiffness.

For nonlinear material analysis, the uniaxial stress-strain curves of concrete, reinforcing steel and prestressing steel were modelled. The shear and the transverse flexural responses of the box beam cross section were modelled using trilinear constitutive relationships based on cracking, yielding and ultimate stages. Effect of load reversal was considered in a quasi-static manner. A composite system of concrete and longitudinal reinforcing steel filaments was constructed in order to account for varied material properties within the element cross section. Tension stiffening effect between concrete and longitudinal steel was modelled using a steel-referred method.

The nonlinear equilibrium equations were solved using an incremental method combined with unbalanced load iterations. Load control and displacement control solution strategies were included in the numerical procedure. A path-independent state determination scheme was used. The proposed nonlinear analysis procedure is capable of tracing the structural response throughout the elastic, inelastic and ultimate load ranges.

Two computer programs, LAPBOX and NAPBOX, were developed incorporating the theory. LAPBOX is intended for linear elastic analysis, whereas NAPBOX is intended for nonlinear material analysis. Various numerical studies were made using the two programs in order to demonstrate the applicability and the capabilities of the proposed method. Comparisons with other analytical and experimental results were made.

9.2 Conclusions

1. It has been demonstrated that the proposed thin-walled box beam element can predict the linear elastic response of curved nonprismatic reinforced and prestressed concrete box girder bridges quite accurately. The curved nonprismatic nature of the element makes accurate modelling of complex bridge geometries possible, so that convergence can be achieved with only a few elements.

2. The simplicity, accuracy and reduced computational effort inherent in the thin-walled box beam element make it extremely well suitable for an extension to capture nonlinear effects.

3. The proposed procedure for nonlinear material analysis has been shown to be capable of capturing the dominant structural behavior in the elastic, inelastic and ultimate

ranges. Internal strains and stresses in concrete, reinforcing steel and prestressing steel can be determined at all loading stages. Useful information on overload behavior and ultimate strength can be obtained from such a detailed analysis.

4. Depending on the structure and the loading, warping, distortional and torsional effects can influence structural behavior significantly. They not only affect the internal force distribution within the box structure, but may also govern the failure mode and the ultimate load.

5. The automatic generation schemes incorporated into the computer programs allow accurate modelling of complex bridge geometries, loadings and prestressing tendon profiles based on a few simple input parameters.

9.3 Recommendations for Future Studies

1. Selective, well-controlled experimental studies need to be carried out to assess the accuracy of the proposed numerical procedure for nonlinear material analysis.

2. The present method can be extended to include time-dependent and environmental effects of aging, creep and shrinkage of concrete, relaxation of prestressing steel, and temperature changes.

3. The proposed thin-walled box beam element can be incorporated into a computer program for analysis of segmentally erected concrete box girder bridges.

4. Inclusion of nonlinear geometry effects will extend the applicability of the present method to a wider range of thin-walled box structures.

5. The finite element formulation of the proposed thin-walled box beam element can be easily extended to an element that is curved in space.

6. The possibility of extending the present method to the analysis of multi-cell box girders, by including a greater number of deformation modes of the cross section, should be investigated.

REFERENCES

1. Scordelis, A. C., "Berkeley Computer Programs for the Analysis of Concrete Box Girder Bridges," Proceedings, NATO-Advanced Study Institute on Analysis and Design of Bridges, Cesme, Turkey, July 1982, pp. 1-71.

2. Kristek, V., "Theory of Box Girders," A Wiley-Interscience Publication, John Wiley & Sons, 1979.

3. Maisel, B. I., and Roll, F., "Methods of Analysis and Design of Concrete Boxbeams with Side Cantilevers," Technical Report 42.494, Cement and Concrete Association, London, 1974.

4. Scordelis, A. C., "Analysis of Simply Supported Box Girder Bridges," Structural Engineering and Structural Mechanics Report No. SESM 66-17, University of California, Berkeley, October 1966.

5. DeFries-Skene, A., and Scordelis, A. C., "Direct Stiffness Solution for Folded Plates," Journal of the Structural Division, ASCE, Vol. 90, No. ST3, June 1964, pp. 15-47.

6. Scordelis, A. C., and Davis, R. E., "Stresses in Continuous Concrete Box Girder Bridges," ACI Special Publication SP-26, 1971, pp. 284-319.

7. Lin, C. S., and Scordelis, A. C., "Computer Program for Bridges on Flexible Bents," Structural Engineering and Structural Mechanics Report No. UC SESM 71-24, University of California, Berkeley, December 1971.

8. Scordelis, A. C., Chan, E. C., Ketchum, M. A., and Van der Walt, P. P., "Computer Programs for Prestressed Concrete Box Girder Bridges," Structural Engineering and Structural Mechanics Report No. UCB/SESM-85/02, University of California, Berkeley, March 1985.

9. Cheung, Y. K., "Finite Strip Method Analysis of Elastic Slabs," Journal of the Engineering Mechanics Division, ASCE, Vol. 94, No. EM6, December 1968, pp. 1365-1378.

10. William, K. J., and Scordelis, A. C., "Analysis of Orthotropic Folded Plates with Eccentric Stiffeners," Structural Engineering and Structural Mechanics Report No. SESM 70-3, University of California, Berkeley, February 1970.

11. William, K. J., and Scordelis, A. C., "Analysis of Eccentrically Stiffened Folded Plates," Proceedings of IASS Symposium on Folded Plates and Prismatic Structures, Vienna, September 1970.

12. Meyer, C., and Scordelis, A. C., "Analysis of Curved Folded Plate Structures," Structural Engineering and Structural Mechanics Report No. UC SESM 70-8, University of California, Berkeley, June 1970.

13. Meyer, C., and Scordelis, A. C., "Analysis of Curved Folded Plate Structures,"Journal of the Structural Division, ASCE, Vol. 98, No. ST1, January 1972, pp. 2459-2480.

14. Kabir, A. F., and Scordelis, A. C., "Computer Program for Curved Bridges on Flexible Bents," Structural Engineering and Structural Mechanics Report No. UC SESM 74-10, University of California, Berkeley, September 1974.

15. Sorensen, S. I., and Scordelis, A. C., "Computer Program for Curved Prestressed Box Girder Bridges," Structures and Materials Research Report No. UC SESM 80-10, University of California, Berkeley, December 1980.

16. Hambly, E. C., "Bridge Deck Behaviour," Chapman and Hall, London, 1976 (Distributed in the U.S.A. by Halsted Press, a division of John Wiley & Sons, New York).

17. Seible, F., "Nonlinear Analysis and Ultimate Strength of Multi-Cell Reinforced Concrete Box Girder Bridges," Structural Engineering and Structural Mechanics Report No. UCB/SESM-82/02, University of California, Berkeley, February 1982.

18. Seible, F., and Scordelis, A. C., "Nonlinear Behavior and Failure Analysis of Multi-Cell RC Box Girder Bridges," Proceedings, CSCE International Conference on Short and Medium Span Bridges, Toronto, Canada, Vol. 1, August 1982, pp. 391-405.

19. Seible, F., and Scordelis, A. C., "Nonlinear Analysis of Multi-Cell RC Box Girder Bridges," Journal of Engineering Structures, Vol. 5, January 1983, pp. 45-57.

20. Meyer, C., and Scordelis, A. C., "Computer Program for Non-Prismatic Folded Plates with Plate and Beam Elements," Structural Engineering and Structural Mechanics Report No. UC SESM 71-23, University of California, Berkeley, December 1971.

21. Jirousek, J., Bouberguig, A., and Saygun, A., "A Macro-Element Analysis of Prestressed Curved Box-Girder Bridges," Computers & Structures, Vol. 10, No. 3, June 1979, pp. 467-482.

22. Vlasov, V. Z., "Thin-Walled Elastic Beams," Israel Program for Scientific Translations, Jerusalem, Israel, 1961.

23. Bazant, Z. P., and El Nimeiri, M., "Stiffness Method for Curved Box Girders at Initial Stress," Journal of the Structural Division, ASCE, Vol. 100, No. ST10, October 1974, pp. 2071-2090.

24. Mikkola, M. J., and Paavola, J, "Finite Element Analysis of Box Girders," Journal of the Structural Division, ASCE, Vol. 106, No. ST6, June 1980, pp. 1343-1357.

25. Zhang, S. H., and Lyons, L. P. R., "A Thin-Walled Box Beam Finite Element for Curved Bridge Analysis," Computers & Structures, Vol. 18, No. 6, 1984, pp. 1035-1046.

26. Van Zyl, S. F., "Analysis of Curved Segmentally Erected Prestressed Concrete Box Girder Bridges," Structures and Materials Research Report No. UC SESM 78-2, University of California, Berkeley, January 1978.

27. Van Zyl, S. F., and Scordelis, A. C., "Analysis of Curved Prestressed Segmental Bridges," Journal of the Structural Division, ASCE, Vol. 105, No. ST11, November 1979, pp. 2399-2417.

28. Kang, Y. J., "Nonlinear Geometric, Material and Time Dependent Analysis of Reinforced and Prestressed Concrete Frames," Structures and Materials Research Report No. UC SESM 77-1, University of California, Berkeley, January 1977.

29. Kang, Y. J., and Scordelis, A. C., "Nonlinear Analysis of Prestressed Concrete Frames," Journal of the Structural Division, ASCE, Vol. 106, No. ST2, February 1980, pp. 445-472.

30. Van Greunen, J., "Nonlinear Geometric, Material and Time Dependent Analysis of Reinforced and Prestressed Concrete Slabs and Panels," Structures and Materials Research Report No. UC SESM 79-3, University of California, Berkeley, October 1979.

31. Chan, E. C., "Nonlinear Geometric, Material and Time Dependent Analysis of Reinforced Concrete Slabs with Edge Beams," Structural Engineering and Structural Mechanics Report No. UCB/SESM-82/08, University of California, Berkeley, December 1982.

32. Chan, E. C., and Scordelis A. C., "Stability of Hyperbolic Paraboloid Gable Shells," Shell and Spatial Structures Engineering, Proceedings of the International Symposium on Shell and Spatial Structures, Rio de Janeiro, Brazil, September 1983, pp. 91-115.

33. Dabrowski, R., "Curved Thin-Walled Girders, Theory and Analysis," Springer, New York, 1968.

34. Timoshenko, S., and Woinowsky-Krieger, S., "Theory of Plates and Shells," McGraw-Hill Book Company Limited, Second Edition, 1959.

35. Zienkiewicz, O. C., "The Finite Element Method," McGraw-Hill Book Company Limited, Third Edition, 1977.

36. Barlow, J., "Optimal Stress Locations in Finite Element Models," International Journal for Numerical Methods in Engineering, Vol. 10, No. 2, 1976, pp. 243-251.

37. Hinton, E., and Campbell, J. S., "Local and Global Smoothing of Discontinuous Finite Element Functions Using a Least Squares Method," International Journal for Numerical Methods in Engineering, Vol. 8, No. 3, 1974, pp. 461-480.

38. Hinton, E., and Scott, F. C., and Ricketts, R. E., "Local Least Squares Stress Smoothing for Parabolic Isoparametric Elements," International Journal for Numerical Methods in Engineering, Vol. 9, No. 1, 1975, pp. 235-238.

39. Lin, T. Y., and Burns, N. H., "Design of Prestressed Concrete Structures," John Wiley & Sons, Third Edition, 1981.

40. Nilson, A. H., "Design of Prestressed Concrete," John Wiley & Sons, 1978.

41. Kristek, V., "Tapered Box Girders of Deformable Cross Section," Journal of the Structural Division, ASCE, Vol. 96, No. ST8, August 1970, pp. 1761-1793.

42. Bathe, K., Wilson, E. L., and Peterson, F. E., "SAP IV A Structural Analysis Program for Static and Dynamic Response of Linear Systems," Earthquake Engineering Research Center Report No. EERC 73-11, University of California, Berkeley, June 1973.

43. Hognestad, E., "A Study of Combined Bending and Axial Load in Reinforced Concrete Members," University of Illinois Engineering Experiment Station, Bulletin Series No. 399, Bulletin No. 1, November 1951.

44. ACI Committe 209, "Prediction of Creep, Shrinkage and Temperature Effects in Concrete Structures," ACI Special Publication SP-76, 1982, pp. 193-300.

45. Scanlon, A., "Time Dependent Deflections of Reinforced Concrete Slabs," PhD Dissertation, Department of Civil Engineering, University of Alberta, Edmonton, Canada, December 1971.

46. Lin, C. S., and Scordelis, A. C., "Nonlinear Analysis of RC Shells of General Form," Journal of the Structural Division, ASCE, Vol. 101, No. ST3, March 1975, pp. 523-538.

47. Gilbert, R. I., and Warner, R. F., "Tension Stiffening in Reinforced Concrete Slabs," Journal of the Structural Division, ASCE, Vol. 104, No. ST12, December 1978, pp. 1885-1900.

48. Poston, R. W., Diaz, M., Breen, J. E., and Roesset, J. M., "Design of Slender, Nonprismatic, and Hollow Concrete Bridge Piers," Research Report 254-2F, Center for Transportation Research, University of Texas, Austin, April 1983.

49. American Association of State Highway and Transportation Officials, "Standard Specifications for Highway Bridges," Twelfth Edition, 1977.

50. ACI Committee 318, "Building Code Requirements for Reinforced Concrete (ACI 318-83)," American Concrete Institute, Detroit, Michigan, 1983.

51. Park, R., and Paulay, T., "Reinforced Concrete Structures," A Wiley-Interscience Publication, John Wiley & Sons, 1975.

52. Branson, D. E., "Instantaneous and Time-Dependent Deflections of Simple and Continuous Reinforced Concrete Beams," HPR Report No. 7, Part 1, Alabama Highway Department, Bureau of Public Roads, August 1963 (1965), pp. 1-78.

53. Corley, W. G., "Rotational Capacity of Reinforced Concrete Beams," Journal of the Structural Division, ASCE, Vol. 92, No. ST5, October 1966, pp. 121-146.

54. Mattock, A. H., Discussion of "Rotational Capacity of Reinforced Concrete Beams," Journal of the Structural Division, ASCE, Vol. 93, No. ST2, April 1967, pp. 519-522.

55. Powell, G., and Simons, J., "Improved Iteration Strategy for Nonlinear Structures," International Journal for Numerical Methods in Engineering, Vol. 17, 1981, pp. 1455-1467.

56. Cassano, R. C., and Le Beau, R. J., "Correlating Bridge Design Practice with Overload Permit Policy," Transportation Research Record 664, National Research Council, Washington, D.C., 1978.

57. Hellesland, J., Choudhury, D., and Scordelis, A. C., "Nonlinear Analysis and Design of RC Bridge Columns Subjected to Imposed Deformations," Structural Engineering and Structural Mechanics Report No. UCB/SESM-85/03, University of California, Berkeley, April 1985.

APPENDIX A - INPUT GUIDE FOR LAPBOX

1. TITLE (10A8) - 1 line

Col. 1-80	Title of the problem to be printed with output, *TITLE*

2. CONTROL DATA (6I5, F10.0, I5) - 1 line

Col. 1- 5	No. of nodes, *NN* (odd no. ≥ 3)
Col. 6-10	No. of supported nodes, *NSN*
Col. 11-15	No. of transverse cantilever flanges, *NCA* (= 0 or 2)
Col. 16-20	No. of prestressing tendons, *NPT*
Col. 21-25	No. of different load cases, *NLC*
Col. 26-30	Dead load analysis code, *IDL*
	0 for excluding dead load analysis
	1 for applying dead load in positive *X* direction
	-1 for applying dead load in negative *X* direction
	2 for applying dead load in positive *Y* direction
	-2 for applying dead load in negative *Y* direction
	3 for applying dead load in positive *Z* direction
	-3 for applying dead load in negative *Z* direction
Col. 31-40	Unit weight of structure for calculating dead load, *WGT*
Col. 41-45	Data check mode option, *MODE*
	0 for execution mode
	1 for data check mode

3. NODAL DATA

The following two sets of nodal data must each be input in order of increasing node numbers.

3.1 GLOBAL COORDINATES (I5, 3F10.0) - 1 line per node

Col. 1- 5	Node number, *I*

Col. 6-15	Global X coordinate of node I, $X(I)$
Col. 16-25	Global Y coordinate of node I, $Y(I)$
Col. 26-35	Radius of curvature to next specified node, *RIF*

Note: Global coordinates for nodes omitted are generated automatically assuming equally spaced nodes along a circular curve of radius *RIF* (or along a straight if *RIF* = 0) in the $X-Y$ plane between this node and the next specified node. Data for the first and last nodes must be input. The sign of *RIF* for various curves is shown below.

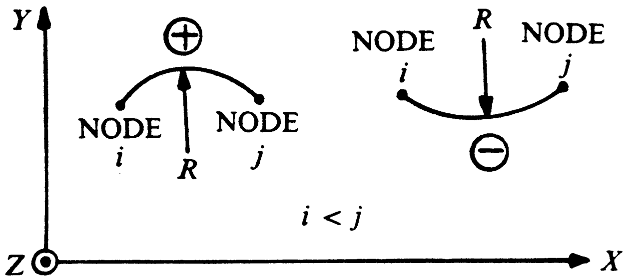

3.2 CROSS SECTIONAL DIMENSIONS - 2 lines per node (Refer to Fig. 2.1b)

First line (2I5)

Col. 1- 5	Node no., I
Col. 6-10	Automatic generation code, *IGF* 0 for no generation 1 for automatic generation of cross sectional dimensions

Second line (8F10.0)

Col. 1-10	Width of box section at node I, $A(I)$
Col. 11-20	Top depth of box section at node I, $B1(I)$
Col. 21-30	Bottom depth of box section at node I, $B2(I)$
Col. 31-40	Width of each cantilever flange at node I, $F(I)$
Col. 41-50	Thickness of cantilever flanges at node I, $TCA(I)$
Col. 51-60	Thickness of webs at node I, $TW(I)$
Col. 61-70	Thickness of top flange at node I, $TFT(I)$

Col. 71-80	Thickness of bottom flange at node I, $TFB(I)$

Note: If the automatic generation option is used, cross sectional dimensions for omitted nodes are generated automatically assuming quadratic variations between this node and the next two specified nodes. Since the node no. is used as the independent variable in determining the quadratic variations, the automatic generation option should be used only with equally spaced nodes.

4. SUPPORTED NODE DATA - 2 lines per supported node (Refer to Fig. 2.5)

First line (I5, F10.0)

Col. 1- 5	Supported node number, $JS(I)$
Col. 6-15	Angle between X and A axes measured counterclockwise from X axis to A axis in degrees, $SP(I, 9)$

Second line (8F10.0)

Col. 1-10	Translational stiffness along A axis, $SP(I, 1)$
Col. 11-20	Translational stiffness along B axis, $SP(I, 2)$
Col. 21-30	Translational stiffness along Z axis, $SP(I, 3)$
Col. 31-40	Rotational stiffness about A axis, $SP(I, 4)$
Col. 41-50	Rotational stiffness about B axis, $SP(I, 5)$
Col. 51-60	Rotational stiffness about Z axis, $SP(I, 6)$
Col. 61-70	Warping stiffness, $SP(I, 7)$
Col. 71-80	Distortional stiffness, $SP(I, 8)$

5. MATERIAL PROPERTIES (2F10.0) - 1 line

Col. 1-10	Modulus of elasticity, E
Col. 11-20	Poisson's ratio, UN

6. PRESTRESSING TENDON DATA (Skip if *NPT* = 0)

The following data are input for each prestressing tendon.

6.1 TENDON CONTROL, JACKING AND FRICTION DATA - 2 lines

First line (6I5)

Col. 1- 5 Tendon identification number, *ITN*

Col. 6-10 Tendon location code, *LCODE*

  1 for tendon located in left web

  2 for tendon located in right web

  3 for tendon located in top flange

  4 for tendon located in bottom flange

Col. 11-15 Number of spans or portions for this tendon, *NSPAN*

Col. 16-20 Smaller tendon end node number (end *A*), *NENDA*

Col. 21-25 Larger tendon end node number (end *B*), *NENDB*

Col. 26-30 Code for method of computing tendon forces, *KDTP*

  0 for method *B* (without smoothing)

  1 for method *A* (with smoothing)

Second line (8F10.0)

Col. 1-10 Jacking force at end *A*, *FENDA* (0 for end *B* jacking only)

Col. 11-20 Jacking force at end *B*, *FENDB* (0 for end *A* jacking only)

Col. 21-30 Curvature friction coefficient, *CFC*

Col. 31-40 Wobble friction coefficient, *WFC*

Col. 41-50 Area of tendon cross section, *AREA*

Col. 51-60 Modulus of elasticity of tendon, *EMOD*

Col. 61-70 Anchorage slip distance at each jacking end, *SLIP*

Col. 71-80 Force ratio (final force/initial force), *FRAT*

6.2 TENDON SPAN OR PORTION CONTROL DATA AND GEOMETRY DATA

The following data are input for each span or portion of tendon.

6.2.1 SPAN OR PORTION CONTROL DATA (4I5) - 1 line

Col. 1- 5	Span or portion identification number, *J*
Col. 6-10	Span end node number nearer to tendon end *A*, *NEND*1
Col. 11-15	Span end node number nearer to tendon end *B*, *NEND*2
Col. 16-20	Code for span geometry input mode, *KGM* 0 for parametric geometry input 1 for direct geometry input

6.2.2 PARAMETRIC GEOMETRY INPUT (6F10.0) - 1 line (Skip if *KGM* = 1)

(Refer to Fig. 3.3)

Col. 1-10	Percentage of span length from left end of span to left tendon inflection point, *RLLI*
Col. 11-20	Percentage of span length from left end of span to point of zero tendon slope, *RLLP*
Col. 21-30	Percentage of span length from right tendon inflection point to right end of span, *RLRI*
Col. 31-40	Local y (for flange) or z (for web) coordinate of tendon profile at left end of span, *YZLT*
Col. 41-50	Local y (for flange) or z (for web) coordinate of tendon profile at point of zero tendon slope, *YZLP*
Col. 51-60	Local y (for flange) or z (for web) coordinate of tendon profile at right end of span, *YZRT*

Note: Left end of span corresponds to node *NEND*1, while right end of span corresponds to node *NEND*2.

6.2.3 DIRECT GEOMETRY INPUT (5(I5, F10.0)) - 1 or more lines (Skip if *KGM* = 0)

The following data are input for each node of the span between nodes *NEND*1 and

*NEND*2 inclusive, with data for 5 nodes per line.

Col. 1- 5	Node number, *J*
Col. 6-15	Local *y* (for flange) or *z* (for web) coordinate of tendon profile at node *J*, *YZ*(*J*)

7. LOAD CASE DATA

The following data are input for each load case.

7.1 LOAD CASE TITLE (10A8) - 1 line

Col. 1-80	Title of the load case to be printed with the output, *TITLE*

7.2 LOAD CASE CONTROL DATA (3I5, 2F10.0) - 1 line

Col. 1- 5	No. of distributed element loads, *NDEL*
Col. 6-10	No. of loaded nodes, *NLN*
Col. 11-15	Stress output code, *ISCODE* 0 for no stress output <0 for stress output at all elements >0 for stress output at *ISCODE* elements
Col. 16-25	Load factor for dead load, *FDL*
Col. 26-35	Load factor for prestressing load, *FPS*

7.3 DISTRIBUTED ELEMENT LOAD DATA (4I5, 6F10.0) - *NDEL* lines

(Skip if *NDEL* = 0) (Refer to Fig. 7.1, Sec. 7.2.1)

Col. 1- 5	Distributed element load no., *NO*
Col. 6-10	No. of first element over which distributed load acts, *NFE*
Col. 11-15	No. of last element over which distributed load acts, *NLE*
Col. 16-20	Input code for load width, *IWC* 0 to input width (*W*) as an absolute value 1 to input width (*W*) as a fraction of flange width
Col. 21-30	Pressure in positive *Z* direction on top flange, *P*(1)

Col. 31-40	Fraction $y_m/(a + 2f)$ for top flange, *YMF*(1)
Col. 41-50	Width of distributed load on top flange, *W*(1)
Col. 51-60	Pressure in positive *Z* direction on bottom flange, *P*(2)
Col. 61-70	Fraction y_m/a for bottom flange, *YMF*(2)
Col. 71-80	Width of distributed load on bottom flange, *W*(2)

7.4 NODAL LOADING DATA - 2 lines per loaded node (Skip if *NLN* = 0)

First line (I5)

Col. 1- 5	Loaded node no., *LNNO*

Second line (8F10.0)

Col. 1-10	Force along *X* axis, *R*(1)
Col. 11-20	Force along *Y* axis, *R*(2)
Col. 21-30	Force along *Z* axis, *R*(3)
Col. 31-40	Moment about *X* axis, *R*(4)
Col. 41-50	Moment about *Y* axis, *R*(5)
Col. 51-60	Moment about *Z* axis, *R*(6)
Col. 61-70	Warping bimoment, *R*(7)
Col. 71-80	Distortional moment, *R*(8)

7.5 STRESS OUTPUT DATA (16I5) - 1 or more lines (Skip if *ISCODE* ≤ 0)

Element nos. for stress output, *NESTR*(*I*), *I* = 1, *ISCODE*

APPENDIX B - SAMPLE INPUT DATA FOR LAPBOX

```
LAPBOX EXAMPLE 4.5 - THREE-SPAN CURVED NONPRISMATIC PRESTRESSED CONCRETE BRIDGE
  113    4    2   14    4   -3      0.16    0
    1       0.0       0.0       0.0
   29     140.0       0.0     500.0
  113 512.32156-166.26859       0.0
    1    1
     12.0       0.0       6.0       4.0     0.667      1.25     0.667       0.6
   15
     12.7       0.0       7.0     4.225     0.667      1.25     0.667      0.95
   29    1
     13.4       0.0       8.0      4.45     0.667      1.25     0.667       1.3
   35
     13.7       0.0       6.04.54642857     0.667      1.25     0.667       1.1
   41    1
     14.0       0.0       4.04.64285714     0.667      1.25     0.667       0.9
   47
     14.3       0.0       4.04.73928571     0.667      1.25     0.667       0.7
   53    1
     14.6       0.0       4.04.83571429     0.667      1.25     0.667       0.5
   59
     14.9       0.0       4.04.93214286     0.667      1.25     0.667       0.7
   65    1
     15.2       0.0       4.05.02857143     0.667      1.25     0.667       0.9
   71
     15.5       0.0       6.0     5.125     0.667      1.25     0.667       1.1
   77    1
     15.8       0.0       8.05.22142857     0.667      1.25     0.667       1.3
   95
     16.7       0.0       7.05.51071429     0.667      1.25     0.667      0.95
  113    0
     17.6       0.0       6.0       5.8     0.667      1.25     0.667       0.6
    1       0.0
      0.0       0.0    1.E+19    1.E+19       0.0       0.0       0.0    1.E+19
   29       0.0
   1.E+19    1.E+19    1.E+19    1.E+19       0.0    1.E+19       0.0    1.E+19
   77-27.501974
      0.0       0.0    1.E+19    1.E+19       0.0       0.0       0.0    1.E+19
  113-48.128455
      0.0       0.0    1.E+19    1.E+19       0.0       0.0       0.0    1.E+19
  608256.0      0.18
    1    1    1    1   25    1
    300.0     300.0       0.2    0.0002       0.0       0.0       0.0       1.0
    1    1   25    0
      0.0      50.0       0.0     -2.47    -6.357    -4.044
    2    2    1    1   25    1
    300.0     300.0       0.2    0.0002       0.0       0.0       0.0       1.0
    1    1   25    0
      0.0      50.0       0.0     -2.47    -6.357    -4.044
    3    1    1   85  113    1
    700.0     700.0       0.2    0.0002       0.0       0.0       0.0       1.0
    1   85  113    0
      0.0      50.0       0.0    -3.646    -6.278     -2.41
    4    2    1   85  113    1
    700.0     700.0       0.2    0.0002       0.0       0.0       0.0       1.0
    1   85  113    0
      0.0      50.0       0.0    -3.646    -6.278     -2.41
    5    1    1   37   69    1
    600.0     600.0       0.2    0.0002       0.0       0.0       0.0       1.0
    1   37   69    0
      0.0      50.0       0.0    -2.473      -3.5    -2.463
    6    2    1   37   69    1
    600.0     600.0       0.2    0.0002       0.0       0.0       0.0       1.0
    1   37   69    0
```

```
       0.0      50.0       0.0    -2.473      -3.5    -2.463
    7    1    2   17   41    1
    2500.0    2500.0       0.2    0.0002       0.0       0.0       0.0       1.0
    1   17   33    0
       0.0      50.0       0.0    -3.343      -0.5      -0.5
    2   33   41    0
       0.0       0.0       0.0      -0.5      -0.5     -1.71
    8    2    2   17   41    1
    2500.0    2500.0       0.2    0.0002       0.0       0.0       0.0       1.0
    1   17   33    0
       0.0      50.0       0.0    -3.343      -0.5      -0.5
    2   33   41    0
       0.0       0.0       0.0      -0.5      -0.5     -1.71
    9    1    2   65   89    1
    3000.0    3000.0       0.2    0.0002       0.0       0.0       0.0       1.0
    1   65   81    0
       0.0      50.0       0.0     -1.84      -0.5      -0.5
    2   81   89    0
       0.0       0.0       0.0      -0.5      -0.5    -3.283
   10    2    2   65   89    1
    3000.0    3000.0       0.2    0.0002       0.0       0.0       0.0       1.0
    1   65   81    0
       0.0      50.0       0.0     -1.84      -0.5      -0.5
    2   81   89    0
       0.0       0.0       0.0      -0.5      -0.5    -3.283
   11    1    2    9   49    1
    1000.0    1000.0       0.2    0.0002       0.0       0.0       0.0       1.0
    1    9   41    0
       0.0      25.0       0.0    -2.911      -0.5      -0.5
    2   41   49    0
       0.0       0.0       0.0      -0.5      -0.5     -1.71
   12    2    2    9   49    1
    1000.0    1000.0       0.2    0.0002       0.0       0.0       0.0       1.0
    1    9   41    0
       0.0      25.0       0.0    -2.911      -0.5      -0.5
    2   41   49    0
       0.0       0.0       0.0      -0.5      -0.5     -1.71
   13    1    2   57   97    1
    1250.0    1250.0       0.2    0.0002       0.0       0.0       0.0       1.0
    1   57   89    0
       0.0      25.0       0.0     -1.71      -0.5      -0.5
    2   89   97    0
       0.0       0.0       0.0      -0.5      -0.5    -4.089
   14    2    2   57   97    1
    1250.0    1250.0       0.2    0.0002       0.0       0.0       0.0       1.0
    1   57   89    0
       0.0      25.0       0.0     -1.71      -0.5      -0.5
    2   89   97    0
       0.0       0.0       0.0      -0.5      -0.5    -4.089
LOAD CASE 1 - UNIFORM LINE LOAD ALONG CENTERLINE
    1    0   -1       0.0       0.0
    1    1   56    0    -1.E10       0.0    1.E-10       0.0       0.0       0.0
LOAD CASE 2 - DEAD LOAD
    0    0   -1       1.0       0.0
LOAD CASE 3 - PRESTRESSING
    0    0   -1       0.0       1.0
LOAD CASE 4 - UNIFORM LIVE LOAD OVER FULL WIDTH OF TOP DECK
    1    0   -1       0.0       0.0
    1   19   34    1     -0.15       0.0       1.0       0.0       0.0       0.0
```

APPENDIX C - INPUT GUIDE FOR NAPBOX

1. TITLE (10A8) - 1 line

Col. 1-80	Title of the problem to be printed with output, *TITLE*

2. CONTROL DATA - 2 lines

First line (12I5)

Col. 1- 5	No. of nodes, *NN* (odd no. ≥ 3)
Col. 6-10	No. of supported nodes, *NSN*
Col. 11-15	No. of transverse cantilever flanges, *NCA* (= 0 or 2)
Col. 16-20	No. of prestressing tendons, *NPT*
Col. 21-25	No. of different cross sections, *NSEC*
Col. 26-30	No. of different concrete material properties, *NCNC*
Col. 31-35	No. of different longitudinal steel material properties, *NSTL*
Col. 36-40	No. of different transverse steel material properties, *NSTT*
Col. 41-45	No. of points used to specify the multilinear stress-strain curve of prestressing steel excluding the origin, *NPPS*
Col. 46-50	No. of different load patterns applied cumulatively in sequence, *NLPT*
Col. 51-55	Ultimate load analysis code, *KULT* 0 to terminate execution when ultimate load is reached 1 to continue execution beyond ultimate load
Col. 56-60	Data check mode option, *MODE* 0 for execution mode 1 for data check mode

Second line (I5, 2F10.0)

Col. 1- 5	Dead load analysis code, *IDL* 0 for excluding dead load analysis 1 for applying dead load in positive *X* direction -1 for applying dead load in negative *X* direction

2 for applying dead load in positive *Y* direction

-2 for applying dead load in negative *Y* direction

3 for applying dead load in positive *Z* direction

-3 for applying dead load in negative *Z* direction

Col. 6-15	Unit weight of structure for calculating dead load, *WGT*
Col. 16-25	Tension stiffening coefficient, *TSC*

3. NODAL DATA

The following two sets of nodal data must each be input in order of increasing node numbers.

3.1 GLOBAL COORDINATES (I5, 3F10.0) - 1 line per node

Col. 1- 5	Node number, *I*
Col. 6-15	Global *X* coordinate of node *I*, *X*(*I*)
Col. 16-25	Global *Y* coordinate of node *I*, *Y*(*I*)
Col. 26-35	Radius of curvature to next specified node, *RIF*

Note: Global coordinates for nodes omitted are generated automatically assuming equally spaced nodes along a circular curve of radius *RIF* (or along a straight if *RIF* = 0) in the $X-Y$ plane between this node and the next specified node. Data for the first and the last nodes must be input. The sign of *RIF* for various curves is shown below.

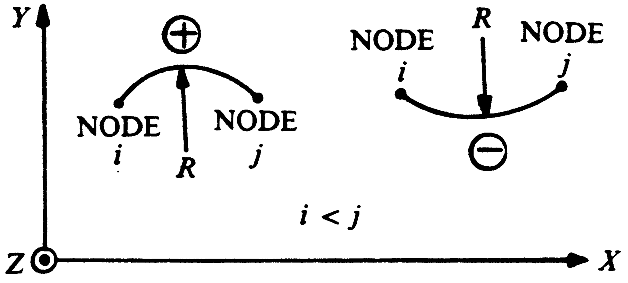

3.2 CROSS SECTIONAL DIMENSIONS - 2 lines per node (Refer to Fig. 2.1b)

First line (2I5)

Col. 1- 5	Node no., *I*

Col. 6-10	Automatic generation code, IGF 0 for no generation of cross sectional dimensions 1 for automatic generation of cross sectional dimensions

Second line (8F10.0)

Col. 1-10	Width of box section at node I, $A(I)$
Col. 11-20	Top depth of box section at node I, $B1(I)$
Col. 21-30	Bottom depth of box section at node I, $B2(I)$
Col. 31-40	Width of each cantilever flange at node I, $F(I)$
Col. 41-50	Thickness of cantilever flanges at node I, $TCA(I)$
Col. 51-60	Thickness of webs at node I, $TW(I)$
Col. 61-70	Thickness of top flange at node I, $TFT(I)$
Col. 71-80	Thickness of bottom flange at node I, $TFB(I)$

Note: If the automatic generation option is used, cross sectional dimensions for omitted nodes are generated automatically assuming quadratic variations between this node and the next two specified nodes. Since the node no. is used as the independent variable in determining the quadratic variations, the automatic generation option should be used only with equally spaced nodes.

4. SUPPORTED NODE DATA - 2 lines per supported node (Refer to Fig. 2.5)

First line (I5, F10.0)

Col. 1- 5	Supported node number, $JS(I)$
Col. 6-15	Angle between X and A axes measured counterclockwise from X axis to A axis in degrees, $SP(I, 9)$

Second line (8F10.0)

Col. 1-10	Translational stiffness along A axis, $SP(I, 1)$
Col. 11-20	Translational stiffness along B axis, $SP(I, 2)$
Col. 21-30	Translational stiffness along Z axis, $SP(I, 3)$
Col. 31-40	Rotational stiffness about A axis, $SP(I, 4)$

Col. 41-50	Rotational stiffness about *B* axis, *SP*(*I*, 5)
Col. 51-60	Rotational stiffness about *Z* axis, *SP*(*I*, 6)
Col. 61-70	Warping stiffness, *SP*(*I*, 7)
Col. 71-80	Distortional stiffness, *SP*(*I*, 8)

5. MATERIAL PROPERTIES

5.1 CONCRETE PROPERTIES (8F10.0) - *NCNC* lines (Refer to Fig. 5.3, Sec.5.2)

Col. 1-10	Maximum compressive stress, *FCDP*(*I*) (enter with negative sign)
Col. 11-20	Initial tangent modulus, *ECI*(*I*)
Col. 21-30	Tensile strength, *FTP*(*I*)
Col. 31-40	Ultimate compressive strain, *ECU*(*I*) (enter with negative sign)
Col. 41-50	Parameter β, *BETA*(*I*)
Col. 51-60	Poisson's ratio, *RNU*(*I*)
Col. 61-70	Cracking shear stress, TAUCR(I)
Col. 71-80	Parameter β_1, *BETA* 1(1)

5.2 LONGITUDINAL STEEL PROPERTIES (2(4F10.0)) - 2 sets per line

(Refer to Fig. 5.4)

Col. 1-10	Yield stress, *FYL*(*I*)
Col. 11-20	First modulus in bilinear stress-strain curve, *ES*1(*I*)
Col. 21-30	Second modulus in bilinear stress-strain curve, *ES*2(*I*)
Col. 31-40	Ultimate strain, *ESU*(*I*)

5.3 TRANSVERSE STEEL PROPERTIES (4(2F10.0)) - 4 sets per line

Col. 1-10	Yield stress, *FYT*(*I*)
Col. 11-20	Modulus of elasticity, *EST*(*I*)

5.4 PRESTRESSING STEEL PROPERTIES (8F10.0) - 1 or more lines

(Refer to Fig. 5.15)

Strain and stress values of each point in stress-strain curve excluding the origin, in order of increasing point nos., $PSE(I)$, $PSS(I)$, $I = 1, NPPS$. Data for 4 points are input per line.

6. SECTION CONTROL DATA - 1 or 2 lines for each different section

(Refer to Fig. 7.2, Sec. 7.2.2)

The following data are input for $I = 1, NSEC$ in order of increasing section numbers.

First line (12I5)

Col. 1- 5	No. of concrete layers in top flange, $NCL(I, 1)$
Col. 6-10	No. of concrete filaments per layer in top flange, $NCFL(I, 1)$
Col. 11-15	No. of longitudinal steel filaments in top flange, $NSF(I, 1)$
Col. 16-20	No. of concrete layers in bottom flange, $NCL(I, 2)$
Col. 21-25	No. of concrete filaments per layer in bottom flange, $NCFL(I, 2)$
Col. 26-30	No. of longitudinal steel filaments in bottom flange, $NSF(I, 2)$
Col. 31-35	No. of concrete layers in left web, $NCL(I, 3)$
Col. 36-40	No. of concrete filaments per layer in left web, $NCFL(I, 3)$
Col. 41-45	No. of longitudinal steel filaments in left web, $NSF(I, 3)$
Col. 46-50	No. of concrete layers in right web, $NCL(I, 4)$
Col. 51-55	No. of concrete filaments per layer in right web, $NCFL(I, 4)$
Col. 56-60	No. of longitudinal steel filaments in right web, $NSF(I, 4)$

Second line (6I5) (Skip if $NCA = 0$)

Col. 1- 5	No. of concrete layers in left cantilever flange, $NCL(I, 5)$
Col. 6-10	No. of concrete filaments per layer in left cantilever flange, $NCFL(I, 5)$
Col. 11-15	No. of longitudinal steel filaments in left cantilever flange, $NSF(I, 5)$
Col. 16-20	No. of concrete layers in right cantilever flange, $NCL(I, 6)$
Col. 21-25	No. of concrete filaments per layer in right cantilever flange,

NCFL(*I*, 6)

Col. 26-30 No. of longitudinal steel filaments in right cantilever flange, *NSF*(*I*, 6)

7. SECTION DATA (Refer to Fig. 7.2, Sec. 7.2.2)

The following data are input for $I = 1$, *NSEC* in order of increasing section numbers.

7.1 CONTROL DATA (3I5) - 1 line

Col. 1- 5 Concrete filament generation code, *ICON*

0 for concrete filament generation

1 for concrete filament data input by user

Col. 6-10 Longitudinal steel filament generation code, *ISTL*

0 for longitudinal steel filament generation

1 for longitudinal steel filament data input by user

Col. 11-15 Concrete material no., *MCNC*(*I*)

7.2 LONGITUDINAL STEEL FILAMENT GENERATION DATA - 1 or 2 lines

(Skip if $ISTL = 1$)

First line (4(I5, F10.0))

Col. 1- 5 Material no. of longitudinal steel in top flange, *MSL*(1)

Col. 6-15 Total longitudinal steel area in top flange, *ALT*(1)

Col. 16-20 Material no. of longitudinal steel in bottom flange, *MSL*(2)

Col. 21-30 Total longitudinal steel area in bottom flange, *ALT*(2)

Col. 31-35 Material no. of longitudinal steel in left web, *MSL*(3)

Col. 36-45 Total longitudinal steel area in left web, *ALT*(3)

Col. 46-50 Material no. of longitudinal steel in right web, *MSL*(4)

Col. 51-60 Total longitudinal steel area in right web, *ALT*(4)

Second line - (2(I5, F10.0)) (Skip if $NCA = 0$)

Col. 1- 5 Material no. of longitudinal steel in left cantilever flange, *MSL*(5)

Col. 6-15 Total longitudinal steel area in left cantilever flange, *ALT*(5)

Col. 16-20 Material no. of longitudinal steel in right cantilever flange, *MSL*(6)

Col. 21-30 Total longitudinal steel area in right cantilever flange, $ALT(6)$

7.3 CONCRETE FILAMENT DATA (Skip if $ICON = 0$)

7.3.1 Top flange

Layer data (8F10.0) - 1 or more lines

Thicknesses of concrete layers, expressed as fractions of total top flange thickness, in order of increasing layer nos., $THS(I, K)$, $K = 1$, $NCL(I, 1)$ (Must add up to 1). Data for 8 layers are input per line.

Filament data (8F10.0) - 1 or more lines

Widths of concrete filaments, expressed as fractions of total flange width, in order of increasing filament nos., $WDH(I, K)$, $K = 1$, $NCFL(I, 1)$ (Must add up to 1). Data for 8 filaments are input per line.

7.3.2 Bottom flange

Layer data (8F10.0) - 1 or more lines

Thicknesses of concrete layers, expressed as fractions of total bottom flange thickness, in order of increasing layer nos., $THS(I, K)$, $K = 1$, $NCL(I, 2)$ (Must add up to 1). Data for 8 layers are input per line.

Filament data (8F10.0) - 1 or more lines

Widths of concrete filaments, expressed as fractions of total flange width, in order of increasing filament nos., $WDH(I, K)$, $K = 1$, $NCFL(I, 2)$ (Must add up to 1). Data for 8 filaments are input per line.

7.3.3 Left web

Layer data (8F10.0) - 1 or more lines

Thicknesses of concrete layers, expressed as fractions of total web thickness, in order of increasing layer nos., $THS(I, K)$, $K = 1$, $NCL(I, 3)$ (Must add up to 1). Data for 8 layers are input per line.

Filament data (8F10.0) - 1 or more lines

Widths of concrete filaments, expressed as fractions of total web depth, in order of increasing filament nos., $WDH(I, K)$, $K = 1$, $NCFL(I, 3)$ (Must add up to 1). Data for 8 filaments are input per line.

7.3.4 Right web

Layer data (8F10.0) - 1 or more lines

Thicknesses of concrete layers, expressed as fractions of total web thickness, in order of increasing layer nos., $THS(I, K)$, $K = 1$, $NCL(I, 4)$ (Must add up to 1). Data for 8 layers are input per line.

Filament data (8F10.0) - 1 or more lines

Widths of concrete filaments, expressed as fractions of total web depth, in order of increasing filament nos., $WDH(I, K)$, $K = 1$, $NCFL(I, 4)$ (Must add up to 1). Data for 8 filaments are input per line.

7.3.5 Left cantilever flange (Skip if $NCA = 0$)

Layer data (8F10.0) - 1 or more lines

Thicknesses of concrete layers, expressed as fractions of total cantilever flange thickness, in order of increasing layer nos., $THS(I, K)$, $K = 1$, $NCL(I, 5)$ (Must add up to 1). Data for 8 layers are input per line.

Filament data (8F10.0) - 1 or more lines

Widths of concrete filaments, expressed as fractions of total cantilever flange width, in order of increasing filament nos., $WDH(I, K)$, $K = 1$, $NCFL(I, 5)$ (Must add up to 1). Data for 8 filaments are input per line.

7.3.6 Right cantilever flange (Skip if $NCA = 0$)

Layer data (8F10.0) - 1 or more lines

Thicknesses of concrete layers, expressed as fractions of total cantilever flange thickness, in order of increasing layer nos., $THS(I, K)$, $K = 1$, $NCL(I, 6)$ (Must add up to 1). Data for 8 layers are input per line.

Filament data (8F10.0) - 1 or more lines

Widths of concrete filaments, expressed as fractions of total cantilever flange width, in order of increasing filament nos., $WDH(I, K)$, $K = 1, NCFL(I, 6)$ (Must add up to 1). Data for 8 filaments are input per line.

7.4 LONGITUDINAL STEEL FILAMENT DATA (Skip if $ISTL = 0$)

7.4.1 Top flange (3(I5, 2F10.0)) - 1 or more lines

The following data are input for each longitudinal steel filament with data for 3 filaments per line.

Col. 1- 5	Material no. of longitudinal steel filament K, $MSLF(I, K)$
Col. 6-15	y/a ratio of longitudinal steel filament K, $YZSF(I, K)$
Col. 16-25	Area of longitudinal steel filament K, $ALF(I, K)$

7.4.2 Bottom flange (3(I5, 2F10.0)) - 1 or more lines

The following data are input for each longitudinal steel filament with data for 3 filaments per line.

Col. 1- 5	Material no. of longitudinal steel filament K, $MSLF(I, K)$
Col. 6-15	y/a ratio of longitudinal steel filament K, $YZSF(I, K)$
Col. 16-25	Area of longitudinal steel filament K, $ALF(I, K)$

7.4.3 Left web (3(I5, 2F10.0)) - 1 or more lines

The following data are input for each longitudinal steel filament with data for 3 filaments per line.

Col. 1- 5	Material no. of longitudinal steel filament K, $MSLF(I, K)$
Col. 6-15	$(z + b_2)/b$ ratio of longitudinal steel filament K, $YZSF(I, K)$
Col. 16-25	Area of longitudinal steel filament K, $ALF(I, K)$

7.4.4 Right web (3(I5, 2F10.0)) - 1 or more lines

The following data are input for each longitudinal steel filament with data for 3 filaments per line.

Col. 1- 5	Material no. of longitudinal steel filament K, $MSLF(I, K)$
Col. 6-15	$(z + b_2)/b$ ratio of longitudinal steel filament K, $YZSF(I, K)$

Col. 16-25	Area of longitudinal steel filament K, $ALF(I, K)$

7.4.5 Left cantilever flange (3(I5, 2F10.0)) - 1 or more lines (Skip if $NCA = 0$)

The following data are input for each longitudinal steel filament with data for 3 filaments per line.

Col. 1- 5	Material no. of longitudinal steel filament K, $MSLF(I, K)$
Col. 6-15	$(\|y\| - a/2)/f$ ratio of longitudinal steel filament K, $YZSF(I, K)$
Col. 16-25	Area of longitudinal steel filament K, $ALF(I, K)$

7.4.6 Right cantilever flange (3(I5, 2F10.0)) - 1 or more lines (Skip if $NCA = 0$)

The following data are input for each longitudinal steel filament with data for 3 filaments per line.

Col. 1- 5	Material no. of longitudinal steel filament K, $MSLF(I, K)$
Col. 6-15	$(\|y\| - a/2)/f$ ratio of longitudinal steel filament K, $YZSF(I, K)$
Col. 16-25	Area of longitudinal steel filament K, $ALF(I, K)$

7.5 TRANSVERSE STEEL DATA - 1 or 2 lines

First line (3(I5, 2F10.0))

Col. 1- 5	Material no. of transverse steel in top flange, $MST(I, 1)$
Col. 6-15	Total transverse steel area per unit longitudinal length in top flange, $ATS(I, 1)$
Col. 16-25	Concrete cover to center of one of the two transverse steel layers in top flange, $DPR(I, 1)$
Col. 26-30	Material no. of transverse steel in bottom flange, $MST(I, 2)$
Col. 31-40	Total transverse steel area per unit longitudinal length in bottom flange, $ATS(I, 2)$
Col. 41-50	Concrete cover to center of one of the two transverse steel layers in bottom flange, $DPR(I, 2)$
Col. 51-55	Material no. of transverse steel in webs, $MST(I, 3)$
Col. 56-65	Total transverse steel area per unit longitudinal length in each web,

	ATS(*I*, 3)
Col. 66-75	Concrete cover to center of one of the two transverse steel layers in each web, *DPR*(*I*, 3)

Second line (I5, F10.0) (Skip if *NCA* = 0)

Col. 1- 5	Material no. of transverse steel in cantilever flanges, *MST*(*I*, 4)
Col. 6-15	Total transverse steel area per unit longitudinal length in each cantilever flange, *ATS*(*I*, 4)

Note: By default, two transverse steel layers with equal concrete covers are assumed for each flange and web. If there is only one transverse steel layer at the mid-thickness, specify *DPR* = 0. The cover *DPR* is specified as an absolute value and not as a fraction.

8. ELEMENT DATA (16I5) - 1 or more lines

Section nos. of elements in order of increasing element nos., *MSEC*(*I*), *I* = 1, *NE*. Data for 16 elements are input per line.

9. PRESTRESSING TENDON DATA (Skip if *NPT* = 0)

The following data are input for each prestressing tendon.

9.1 TENDON CONTROL, JACKING AND FRICTION DATA - 2 lines

First line (6I5)

Col. 1- 5	Tendon identification number, *ITN*
Col. 6-10	Tendon location code, *LCODE* 1 for tendon located in left web 2 for tendon located in right web 3 for tendon located in top flange 4 for tendon located in bottom flange
Col. 11-15	Number of spans or portions for this tendon, *NSPAN*
Col. 16-20	Smaller tendon end node number (end *A*), *NENDA*
Col. 21-25	Larger tendon end node number (end *B*), *NENDB*

Col. 26-30 Code for method of computing tendon forces, *KDTP*

0 for method *B* (without smoothing)

1 for method *A* (with smoothing)

Second line (7F10.0)

Col. 1-10 Jacking force at end *A*, *FENDA* (0 for end *B* jacking only)

Col. 11-20 Jacking force at end *B*, *FENDB* (0 for end *A* jacking only)

Col. 21-30 Curvature friction coefficient, *CFC*

Col. 31-40 Wobble friction coefficient, *WFC*

Col. 41-50 Area of tendon cross section, *AREA*

Col. 51-60 Anchorage slip distance at each jacking end, *SLIP*

Col. 61-70 Force ratio (final force/initial force), *FRAT*

9.2 TENDON SPAN OR PORTION CONTROL DATA AND GEOMETRY DATA

The following data are input for each span or portion of tendon.

9.2.1 SPAN OR PORTION CONTROL DATA (4I5) - 1 line

Col. 1- 5 Span or portion identification number, *J*

Col. 6-10 Span end node number nearer to tendon end *A*, *NEND*1

Col. 11-15 Span end node number nearer to tendon end *B*, *NEND*2

Col. 16-20 Code for span geometry input mode, *KGM*

0 for parametric geometry input 1 for direct geometry input

9.2.2 PARAMETRIC GEOMETRY INPUT (6F10.0) - 1 line (Skip if *KGM* = 1)

(Refer to Fig. 3.)

Col. 1-10 Percentage of span length from left end of span to left tendon inflection point, *RLLI*

Col. 11-20 Percentage of span length from left end of span to point of zero tendon slope, *RLLP*

Col. 21-30 Percentage of span length from right tendon inflection point to right end of span, *RLRI*

Col. 31-40	Local y (for flange) or z (for web) coordinate of tendon profile at left end of span, *YZLT*
Col. 41-50	Local y (for flange) or z (for web) coordinate of tendon profile at point of zero tendon slope, *YZLP*
Col. 51-60	Local y (for flange) or z (for web) coordinate of tendon profile at right end of span, *YZRT*

Note: Left end of span corresponds to node *NEND*1, while right end of span corresponds to node *NEND*2.

9.2.3 DIRECT GEOMETRY INPUT (5(I5, F10.0)) - 1 or more lines (Skip if *KGM* = 0)

The following data are input for each node of the span between nodes *NEND*1 and *NEND*2 inclusive, with data for 5 nodes per line.

Col. 1- 5	Node number, *J*
Col. 6-15	Local y (for flange) or z (for web) coordinate of tendon profile at node J, $YZ(J)$

10. LOAD PATTERN DATA

The following data are input for each load pattern.

10.1 LOAD PATTERN TITLE (10A8) - 1 line

Col. 1-80	Title of the load pattern to be printed with the output, *TITLE*

10.2 LOAD PATTERN CONTROL DATA (7I5) - 1 line

Col. 1- 5	No. of loaded nodes, *NLN*
Col. 6-10	No. of distributed element loads, *NDEL*
Col. 11-15	Nonlinear strategy code, *NSC* 0 for load control 1 for displacement control
Col. 16-20	No. of load or displacements steps, *NLDS*
Col. 21-25	Maximum no. of iterations for intermediate load or displacements steps, *NITI*

Col. 26-30 Maximum no. of iterations for final load or displacement step, *NITF*

Col. 31-35 Stress output code, *ISCODE*

0 for no filament stress output

<0 for filament stress output at all elements

>0 for filament stress output at *ISCODE* elements

Note: A load control strategy ($NSC = 0$) must be used for the first load pattern if $IDL \neq 0$ or $NPT \neq 0$.

10.3 NODAL LOADING DATA - 2 lines per loaded node (Skip if $NLN = 0$)

First line (I5)

Col. 1- 5 Loaded node no., *LNNO*

Second line (8F10.0)

Col. 1-10 Force along X axis, $R(1)$

Col. 11-20 Force along Y axis, $R(2)$

Col. 21-30 Force along Z axis, $R(3)$

Col. 31-40 Moment about X axis, $R(4)$

Col. 41-50 Moment about Y axis, $R(5)$

Col. 51-60 Moment about Z axis, $R(6)$

Col. 61-70 Warping bimoment, $R(7)$

Col. 71-80 Distortional moment, $R(8)$

10.4 DISTRIBUTED ELEMENT LOAD DATA (4I5, 6F10.0) - *NDEL* lines (Skip if $NDEL = 0$) (Refer to Fig. 7.1, Sec. 7.2.1)

Col. 1- 5 Distributed element load no., *NO*

Col. 6-10 No. of first element over which distributed load acts, *NFE*

Col. 11-15 No. of last element over which distributed load acts, *NLE*

Col. 16-20 Input code for load width, *IWC*

0 to input width (W) as an absolute value

1 to input width (W) as a fraction of flange width

Col. 21-30	Pressure in positive Z direction on top flange, $P(1)$
Col. 31-40	Fraction $y_m/(a + 2f)$ for top flange, $YMF(1)$
Col. 41-50	Width of distributed load on top flange, $W(1)$
Col. 51-60	Pressure in positive Z direction on bottom flange, $P(2)$
Col. 61-70	Fraction y_m/a for bottom flange, $YMF(2)$
Col. 71-80	Width of distributed load on bottom flange, $W(2)$

10.5 DISPLACEMENT CONTROL DATA (2I5, F10.0) - 1 line (Skip if $NSC = 0$)

Col. 1- 5	Node with controlled displacement, NCD
Col. 6-10	Controlled d.o.f. at node NCD, $NCDOF$ 1 for controlling X displacement 2 for controlling Y displacement 3 for controlling Z displacement 4 for controlling X rotation 5 for controlling Y rotation 6 for controlling Z rotation 7 for controlling longitudinal warping 8 for controlling transverse distortion
Col. 11-20	Magnitude of controlled displacement, $CDISM$ (Must have proper sign)

10.6 LOAD/DISPLACEMENT STEP DATA (8F10.0) - 1 or more lines

(Skip for first load pattern if $IDL \neq 0$ or $NPT \neq 0$)

Factors for load/displacement steps in order of increasing step nos., $FLDS(I), I = 1, NLDS$. Data for 8 steps are input per line.

10.7 TOLERANCE DATA - 2 lines

First line (8F10.0)

Col. 1-10	Maximum allowable unbalanced X-force, $TOLL(1)$
Col. 11-20	Maximum allowable unbalanced Y-force, $TOLL(2)$
Col. 21-30	Maximum allowable unbalanced Z-force, $TOLL(3)$

Col. 31-40	Maximum allowable unbalanced X-moment, *TOLL*(4)
Col. 41-50	Maximum allowable unbalanced Y-moment, *TOLL*(5)
Col. 51-60	Maximum allowable unbalanced Z-moment, *TOLL*(6)
Col. 61-70	Maximum allowable warping bimoment, *TOLL*(7)
Col. 71-80	Maximum allowable distortional moment, *TOLL*(8)

Second line (3F10.0)

Col. 1-10	Displacement ratio tolerance for intermediate load or displacement steps, *TOLI*
Col. 11-20	Displacement ratio tolerance for final load or displacement, *TOLF*
Col. 21-30	Displacement ratio tolerance for changing stiffness, *TOLC*

10.8 STRESS OUTPUT DATA (16I5) - 1 or more lines (Skip if $ISCODE \leq 0$)

Element nos. for stress output in order of increasing element nos., *NESTR*(*I*), $I = 1$, *ISCODE*.

APPENDIX D - SAMPLE INPUT DATA FOR NAPBOX

```
NAPBOX EXAMPLE 8.3 - THREE-SPAN CURVED PRESTRESSED CONCRETE BRIDGE (LOAD CASE 1)
   81    3    2    2    1    1    1    1    5    2    0    0
   -3   8.97E-5       0.0
    1 -2979.345  5159.580    5958.0
   17 -2112.994  5570.729    5958.0
   33 -1379.371  5796.128    5958.0
   41 -1191.903  5837.562    5958.0
   49  -955.851  5880.826    5958.0
   57  -646.723  5922.796    5958.0
   81       0.0    5958.0       0.0
    1    1
     201.0      36.0      63.0     103.5      10.0      15.0      10.0       8.0
   41
     201.0      36.0      63.0     103.5      10.0      15.0      10.0       8.0
   81
     201.0      36.0      63.0     103.5      10.0      15.0      10.0       8.0
    1 30.003832
       0.0       0.0    1.E+20    1.E+20       0.0       0.0       0.0    1.E+20
   41 11.539935
       0.0       0.0    1.E+20    1.E+20       0.0       0.0       0.0    1.E+20
   81       0.0
    1.E+20    1.E+20       0.0       0.0    1.E+20    1.E+20    1.E+20       0.0
      -4.0    3605.0       0.5     -.004      0.85       0.2     0.190      0.85
      60.0   29000.0       0.0      0.03
      60.0   29000.0
   0.00715     196.6     0.009     220.0    0.0115     240.0    0.0135     245.0
     0.058     270.0
    2    5    5    2    5    5    1   10    5    1   10    5
    2    3    3    2    3    3
    0    0    1
    1      6.03    1     4.824    1     4.455    1     4.455
    1     3.105    1     3.105
    1     0.062      1.25    1     0.062      1.25    1     0.155      1.25
    1     0.062
    1    1    1    1    1    1    1    1    1    1    1    1    1    1    1    1
    1    1    1    1    1    1    1    1    1    1    1    1    1    1    1    1
    1    1    1    1    1    1    1    1
    1    1    2    1   81    1
    2660.0       0.0      0.25 1.6667E-5     13.16      0.25       1.0
    1    1   41    0
       0.0      50.0      10.0       0.0     -55.0      29.0
    2   41   81    0
      20.0     100.0       0.0      29.0     -55.0     -55.0
    2    2    2    1   81    1
    2660.0       0.0      0.25 1.6667E-5     13.16      0.25       1.0
    1    1   41    0
       0.0      50.0      10.0       0.0     -55.0      29.0
    2   41   81    0
      20.0     100.0       0.0      29.0     -55.0     -55.0
LOAD PATTERN 1 - DEAD LOAD AND PRESTRESS AT TRANSFER
    0    0    0    1   20   20    3
       1.0       1.0       1.0      10.0      10.0       1.0     100.0       1.0
      0.01      0.01       0.0
   20   21   40
LOAD PATTERN 2 - P13 TRUCK LOAD IN MIDDLE OF CENTER SPAN OVER CENTERLINE
    4    0    0   24   30   30    3
   57
       0.0       0.0     -48.0       0.0       0.0       0.0       0.0       0.0
```

```
65
    0.0       0.0     -48.0       0.0       0.0       0.0       0.0       0.0
73
    0.0       0.0     -48.0       0.0       0.0       0.0       0.0       0.0
81
    0.0       0.0     -24.0       0.0       0.0       0.0       0.0       0.0
    1.0       0.5       0.5       0.5       0.5       0.2       0.2       0.2
    0.2       0.2       0.2       0.2       0.2       0.2       0.2       0.2
    0.2       0.2       0.2       0.2       0.2       0.2       0.2       0.2
    1.0       1.0       1.0     100.0     100.0      10.0     500.0      10.0
   0.01      0.01       0.0
20   21   40
```